2005

Optimization Of An Unstructured Finite Element Mesh For Tide And Storm Surge Modeling Applications In The Western North Atlantic Ocean

Satoshi Kojima
University of Central Florida

STARS Citation
Kojima, Satoshi, "Optimization Of An Unstructured Finite Element Mesh For Tide And Storm Surge Modeling Applications In The Western North Atlantic Ocean" (2005). *Electronic Theses and Dissertations, 2004-2019*. 457.
https://stars.library.ucf.edu/etd/457

OPTIMIZATION OF AN UNSTRUCTURED FINITE ELEMENT MESH FOR TIDE AND STORM SURGE MODELING APPLICATIONS IN THE WESTERN NORTH ATLANTIC OCEAN

by

SATOSHI KOJIMA
B.S. Chuo University, Tokyo, Japan, 2001

A thesis submitted in partial fulfillment of the requirements
for the degree of Master of Science
in the Department of Civil and Environmental Engineering
in the College of Engineering and Computer Science
at the University of Central Florida
Orlando, Florida

Summer Term
2005

ABSTRACT

Recently, a highly resolved, finite element mesh was developed for the purpose of performing hydrodynamic calculations in the Western North Atlantic Tidal (WNAT) model domain. The WNAT model domain consists of the Gulf of Mexico, the Caribbean Sea, and the entire portion of the North Atlantic Ocean found west of the 60° W meridian. This high resolution mesh (333K) employs 332,582 computational nodes and 647,018 triangular elements to provide approximately 1.0 to 25 km node spacing. In the previous work, the 333K mesh was applied in a Localized Truncation Error Analysis (LTEA) to produce nodal density requirements for the WNAT model domain.

The goal of the work herein is to use these LTEA-based element sizing guidelines in order to obtain a more optimal finite element mesh for the WNAT model domain, where optimal refers to minimizing nodes (to enhance computational efficiency) while maintaining model accuracy, through an automated procedure. Initially, three finite element meshes are constructed: 95K, 60K, and 53K. The 95K mesh consists of 95,062 computational nodes and 182,941 triangular elements providing about 0.5 to 120 km node spacing. The 60K mesh contains 60,487 computational nodes and 108,987 triangular elements. It has roughly 0.5 to 185 km node spacing. The 53K mesh includes 52,774 computational nodes and 98,365 triangular elements. This is a particularly coarse mesh, consisting of approximately 0.5 to 160 km node spacing. It is important to note that these three finite element meshes were produced automatically, with each employing the bathymetry and coastline (of various levels of resolution) of the 333K mesh, thereby enabling progress towards an optimal finite element mesh.

Tidal simulations are then performed for the WNAT model domain by solving the shallow water equations in a time marching manner for the deviation from mean sea level and depth-integrated velocities at each computational node of the different finite element meshes. In order to verify the model output and compare the performance of the various finite element mesh applications, historical tidal constituent data from 150 tidal stations located within the WNAT model domain are collected and examined. These historical harmonic data are applied in two types of comparative analyses to evaluate the accuracy of the simulation results. First, qualitative comparisons are based on visual sense by utilizing plots of resynthesized model output and historical tidal constituents. Second, quantitative comparisons are performed via a statistical analysis of the errors between model response and historical data. The latter method elicits average phase errors and goodness of average amplitude fits in terms of numerical values, thus providing a quantifiable way to present model error.

The error analysis establishes the 53K finite element mesh as optimal when compared to the 333K, 95K, and 60K meshes. However, its required time step of less than ten seconds constrains its application. Therefore, the 53K mesh is manually edited to uphold accurate simulation results and to produce a more computationally efficient mesh, by increasing its time step, so that it can be applied to forecast tide and storm surge in the Western North Atlantic Ocean on a real-time basis.

Never give up your dreams.

Nothing is impossible to a determined mind even if there are many difficulties.

夢を諦めるな。

例えそこに棘の道があろうとも、

断固たる決意があれば不可能なことなどない。

小島　郷史

ACKNOWLEDGMENTS

I would like to appreciate following people for their assistance and guidance to accomplish this research. I would like to appreciate Dr. Scott C. Hagen for his appropriate advice and guidance for this project. In addition, I am really grateful for his patience and understanding to study at the University of Central Florida. I am also thankful for Dr. Gour-Tsyh Yeh and Dr. Manoj B. Chopra for acceptance on my thesis committee; Peter Bacopoulos for his help on not only my research but also my thesis editor. Although he has his own project, he spent immeasurable time to edit my thesis for me. I am really proud of him. I am thankful for Yuji Funakoshi for his many advice for my research; Mike Salisbury for his assistance with not only this project but also to improve my English skills; and many thanks to former colleague Daniel Dietsche, Ryan Murray, and Michael Parrish.

I also would like to appreciate my family who gave me a chance to go on an overseas study program in the United State; Chris Poplin, who has been my roommate since I came to the United State, for his kindness and to teach me English and American culture.

This research was in part conducted under award NA04NWS4620013 from the National Oceanic and Atmospheric Administration (NOAA), U.S. Department of Commerce, and Award N00014-02-1-0150 from the National Oceanographic Partnership Program (NOPP). The statements, findings, conclusions, and recommendations are those of the authors and do not necessarily reflect the views of NOAA, the Department of Commerce, or NOPP and its affiliates.

TABLE OF CONTENTS

LIST OF TABLES

CHAPTER 2

CHAPTER 3

CHAPTER 4

CHAPTER 5

CHAPTER 6

CHAPTER 7

LIST OF FIGURES

CHAPTER 1

CHAPTER 2

CHAPTER 3

CHAPTER 4

CHAPTER 5

CHAPTER 6

CHAPTER 7

LIST OF ABBREVIATIONS

ADCIRC-2DDI	Advanced Circulation Model for Oceanic, Coastal, and Estuarine Waters, Two-Dimensional Depth-Integrated
CP	Carte Parallelogrammatique
CWRS	Compaq Water Resources Simulation
GWCE	The Generalized Wave Continuity Equation
IHO	The International Hydrographic Organization
UCF	University of Central Florida
LTEA	Localized Truncation Error Analysis
MSL	Mean Sea Level
NOS	The National Ocean Service
SMS	Surfacewater Modeling System
WNAT	Western North Atlantic Tidal
333K	Finite Element Mesh for WNAT which includes approximately 333,000 Computational Nodes
95K	Finite Element Mesh for WNAT which includes approximately 95,000 Computational Nodes
60K	Finite Element Mesh for WNAT which includes approximately 60,000 Computational Nodes
53K	Finite Element Mesh for WNAT which includes approximately 53,000 Computational Nodes
48K	Finite Element Mesh for WNAT which includes approximately 48,000 Computational Nodes

CHAPTER 1

INTRODUCTION

Past civilizations and recent societies have dealt with a great variety of natural disasters throughout history and still today, including earthquakes, volcanic eruptions, hurricanes, flooding, ground subsidence, and mud slides, to name a few. Prediction of the effects caused by such catastrophic events can provide further protection to our lives and property by allowing for the necessary evacuation and preparation procedures to be enacted in a timelier manner. A singular product of the following thesis will enable real-time forecasting of one of the most disastrous occurrences on earth, storm surge. The focus of this research is to demonstrate and enhance an automated procedure that can be used to optimize a finite element mesh for the Western North Atlantic Ocean for simulation of astronomical tides including storm surge. It is assumed that an “optimal” mesh for astronomical tides will perform well in storm surge simulations, whereby “optimal” is defined as achieving maximum computational efficiency while maintaining a high level of model accuracy.

The Western North Atlantic Tidal (WNAT) model domain encompasses the Gulf of Mexico, the Caribbean Sea, and the entire portion of the North Atlantic Ocean found west of the 60º W meridian (Figure 1-1). The open-ocean boundary lying along the 60° W meridian extends from the area of Glace Bay, Nova Scotia, Canada to the vicinity of Corocora Island in eastern Venezuela and is situated almost entirely in the deep ocean. Bounded on the north, west, and south by the North, Central, and South American coastlines, respectively, this large scale computational domain covers an area of approximately 8.4 million km^2. Due to the vast size of the WNAT model domain, with deep ocean regions accounting for more than three quarters of the area and the remaining portions consisting of shallow coastal shelf seas, an unstructured, finite element mesh is recommended for application towards producing sufficient tidal circulation predictions.

Previous efforts by Parrish (2001) and Mukai et al. (2002) have resulted in the development of a highly resolved finite element mesh (333K) for tidal computations in the WNAT model domain.

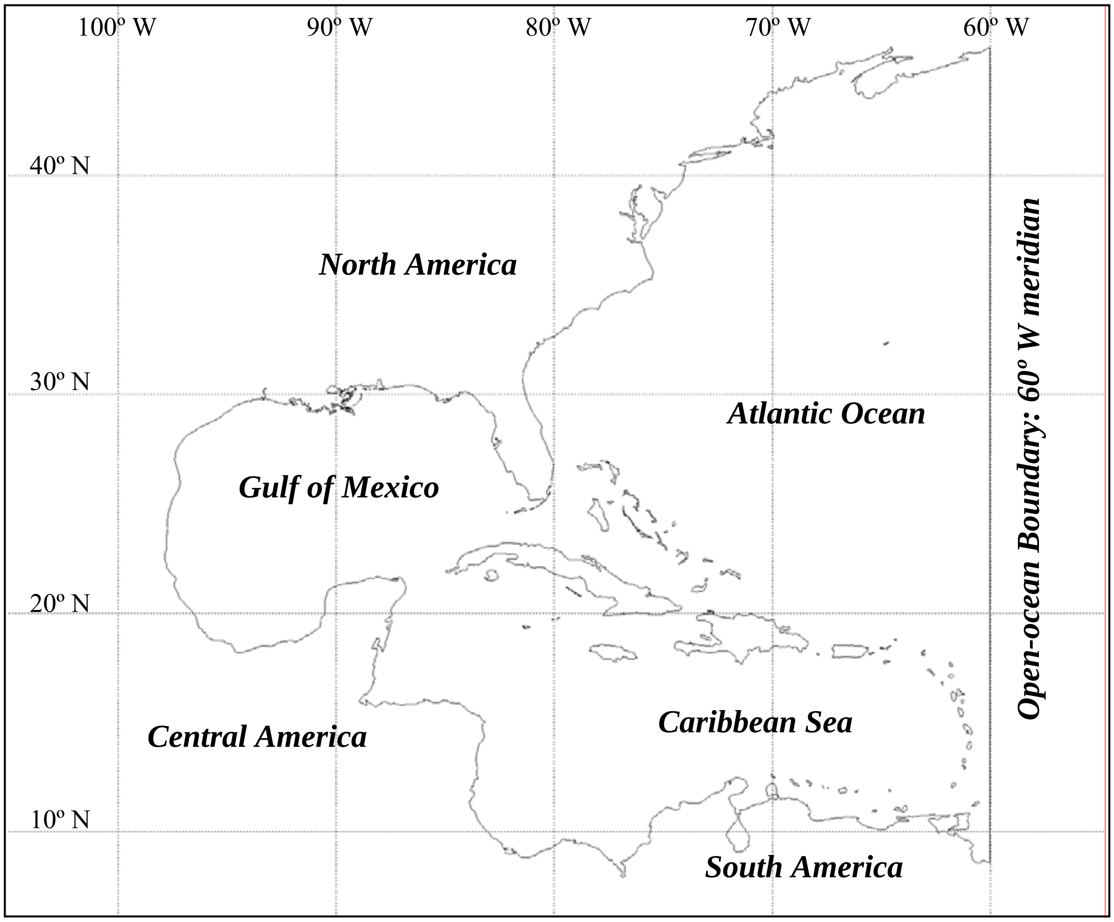

Figure 1-1: WNAT model domain with boundary.

This original grid contains 332,582 computational nodes and 647,018 triangular elements, providing a very detailed description of the physical system with node spacing ranging from 1.0 to 25 km. This fine resolution mesh yields tidal simulation results with a high level of accuracy; however, it requires approximately 13.3 days to complete a full 90-day simulation (on a twelve-node cluster of 600 MHz processors running in parallel), which is considered an unreasonable amount of time to deliver computational results on a real-time basis. Hence, a more computationally efficient mesh must be generated in order to reduce this simulation run time. Therefore, three finite element meshes (of decreasing levels of resolution) are developed using node spacing guidelines generated from a Localized Truncation Error Analysis (LTEA) to provide simulation results in a timelier manner while preserving the numerical integrity of the computational output.

In order compare the performance of the different finite element mesh applications, 150 tidal stations within the WNAT model domain are identified and examined. Historical tidal constituent data collected at these 150 tidal stations are compared to harmonically decomposed elevation output generated by each of the model runs to provide a quantified measure of the model accuracies that are achieved. Finally, a manual editing procedure is demonstrated to arrive at an “optimal” finite element mesh for tidal computations in the WNAT model domain. This final variation of the finite element mesh exceeds the model accuracy and computational efficiency of a standard grid that is commonly employed in real-time forecasting systems (Roe, 1998; Westerink et al., 1993).

CHAPTER 2

LITERATURE REVIEW

Two-dimensional numerical modeling of oceans and coastal seas involves the use of the shallow water equations to reproduce water surface elevations and currents due to long wave processes. Recently, the development and successful implementation of large domain models that describe shallow water flow physics have provided accurate and robust hydrodynamic circulation predictions for expansive ocean basins and marginal shelf seas (Lynch, 1983; Le Provost and Vincent, 1986; Flather, 1987; Foreman, 1988; Vincent and Le Provost, 1988; Gray, 1989; Kolar et al., 1994a; Kolar et al., 1996; Walters and Werner, 1989; Werner and Lynch, 1989; Westerink and Gray, 1991; Blain et al., 1994a; Westerink et al., 1994a; Funakoshi et al., 2004; Kojima et al., 2005). While the focus of the research presented herein pertains to the automatic generation and optimization of unstructured, finite element meshes for tidal computations within a large domain, the following literature reviews covers four main topics directly related to this study. First, an explanation of the dynamic features of the ocean surface is necessary to better understand the physical system and internal processes being modeled. Next, the historical and current states of ocean measurement capabilities are discussed to provide a review of the data collection procedures followed in the past and those used today. Following, recent progress in hydrodynamic modeling using large domains is documented to highlight past advancements and demonstrate the need for more effective modeling methods. Finally, a section dedicated to the harmonic analysis of tidal elevations permits for the discussion of tidal constituents and their role in describing the tides.

2.1 Dynamic Features of the Ocean Surface

Sea levels and the associated hydrodynamics vary by factors that extend over a wide range of space and time scales (Figure 2-1). Over relatively long geological time durations, corresponding to the right side of Figure 2-1, tectonic processes preside over long-term sea level changes; in the bottom left-hand corner of the space-time map, over much shorter time periods, local wind waves dominate small-scale rapid changes in sea levels. In this study, focus is concentrated on those processes affecting sea levels that occur between these two extremes. Within this range, sea levels are governed by twice-daily fluctuations due to the tides, weather effects (surges), and seasonal variations. In addition, the long wave motion excited by a tsunami, including other non-tidal effects may change sea levels within this range of space and time scales.

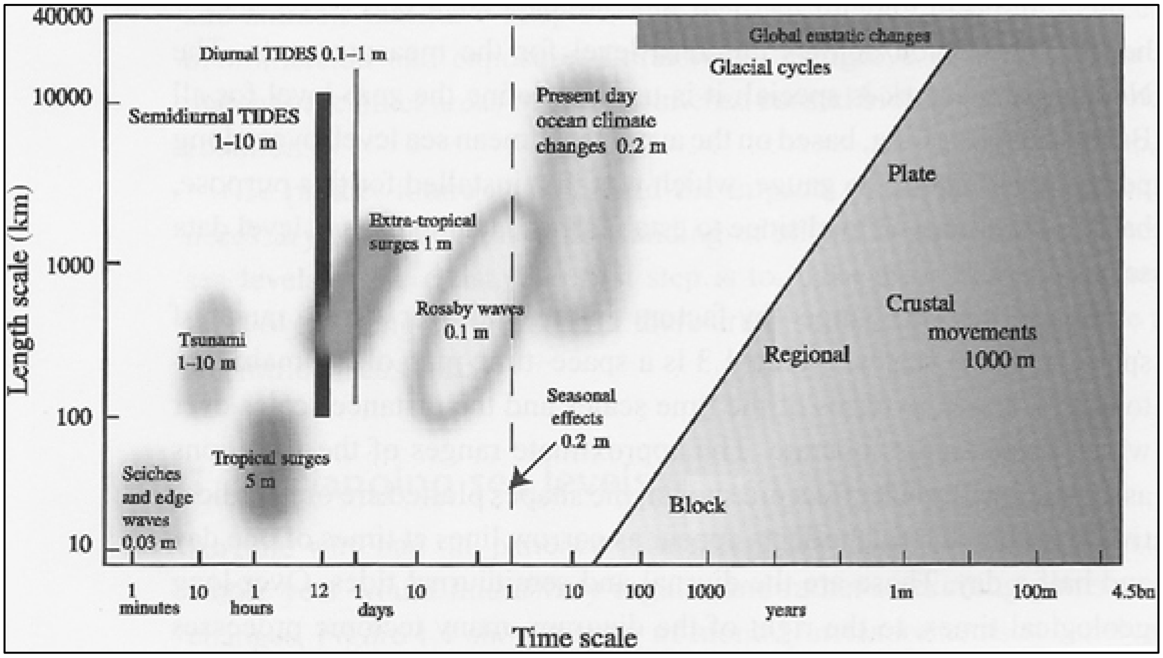

Figure 2-1: A map of the factors that change sea levels in space and time
(after Pugh, 2004).

2.1.1 Sea Surface Reference Datums

According to Pugh (2004), mean sea level (MSL) is defined as the average level of the sea surface, measured relative to a fixed level on the land, identified by a network of fixed benchmarks. Typically, MSL is calculated as the average over a long period of time in order to remove tidal influences, weather effects, and short-period waves. It is important to note that MSL is a time dependent measure over geological time scales; however, for the purposes of this study, MSL is considered to be only spatially variant with negligible temporal variance over the applied model time scales.

To provide a better understanding of the geodetic reference datums used to measure the sea surface, it is necessary to define the following geophysical features. The geoid relates to an equipotential surface that endures only gravitational forces (i.e., all forces are acting perpendicular to this equipotential surface). The exact shape of the geoid depends on the mass distribution within the earth and the rate of rotation of the earth about its own axis (Garland, 1965; Jeffreys, 1976). An alternative explanation of the geoid involves the conditions that no tidal forces are present, no differences in fluid density exist, no currents are driven, and no atmospheric influences are occurring. Under these conditions, no horizontal forces would be induced and the sea surface would remain undisturbed. It is important to note that these conditions do not accurately reflect the natural setting of the earth, and hence, MSL may deviate from the geoid by a considerable measure.

As another approximation, the earth is a rotating sphere. However, over geological time, the earth has adjusted its shape to the planetary rotation by extending its equatorial radius and reducing its polar radius. This polar flattening can be computed by the ratio of the difference between the equatorial and polar radii to the equatorial radius. The shape generated by this rotational distortion is called an ellipsoid of revolution. Li and Gotze (2001) provide a thorough background on a variety of reference ellipsoids developed in previous years. It is important to note that for an earth of uniform density, the geometric ellipsoid would closely approximate the geoid; however, due to the uneven mass distribution of the earth, the actual geoid contains

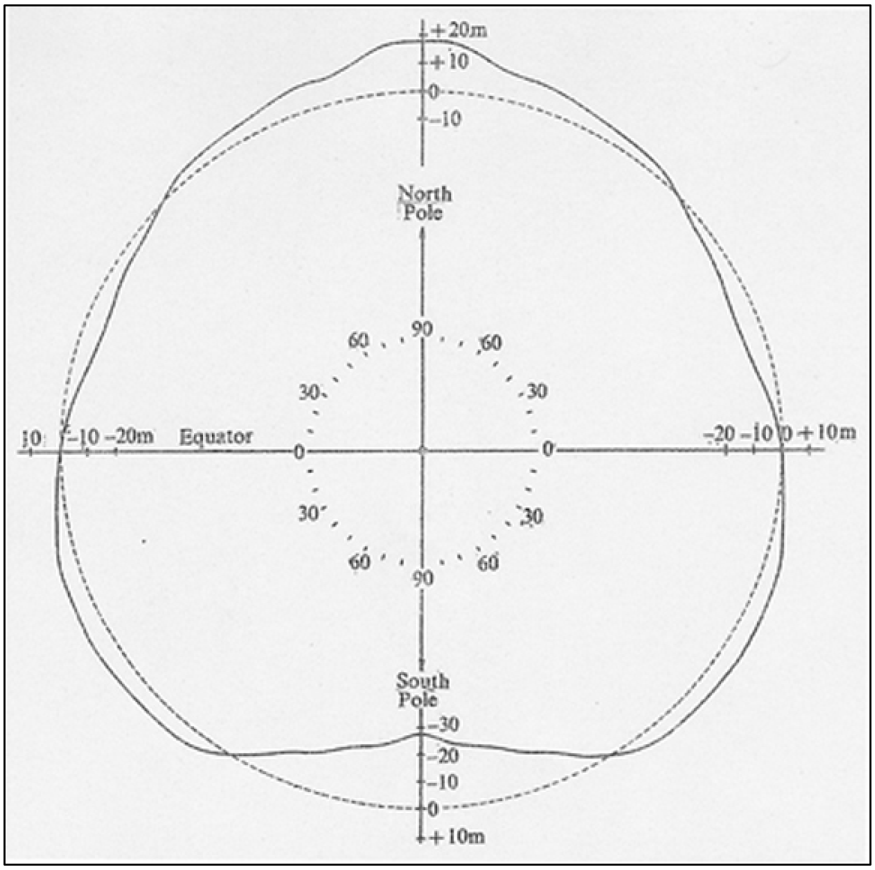

Figure 2-2: Height of the longitude-averaged meridional profile of the geoid (solid line) relative to a geometric ellipsoid with a polar flattening value of 1/298.25 (dashed line) (after King-Hele et al., 1980).

positive and negative digressions of several tens of meters from the geometric ellipsoid (Figure 2-2). While these deviations within the geoid are thought to be due to density differences deep inside the earth, variations of mass distribution near the earth's surface give rise to local mean sea level differences. These local variations in mean sea level are of particular importance to physical oceanographers, as such water level differences produce horizontal pressure gradients which may influence ocean and coastal circulation patterns.

2.1.2 Tides

Deacon (1997) and Cartwright (1999) detail several explanations of the tides that were current in the first half of the seventeenth century: the magnetic or attractive hypothesis of Stevin, Gilbert, and Kepler; the argument from the movement of the earth, as principally developed by Galileo; Descartes' theory that the ocean and atmosphere are compressed by the passage of the moon. Later in history, Darwin (1911) defined the tides as the rising and falling of the ocean waters as caused by the attractions of the sun and moon. It is therefore accepted that modern tidal theory began with, and remains founded upon, Newton's formulation of the Law of Gravitational Attraction.

While the attractive forces of the sun and moon produce tidal movements in all of earth's media, including the atmosphere and solid earth, the following discussion on tides deals solely with the periodic fluctuations of the ocean waters. Of importance, since these tidal motions are quite regular, then it is assumed that their tide-generating forces can be precisely formulated based on the periodicity of the observed tidal oscillations.

To facilitate this discussion on tide-generating forces, one must consider that these resulting forces are produced from two celestial systems: earth-moon; earth-sun. The earth and moon behave as a single system rotating about a common center of mass with a period of 27.3 days (Figure 2-3). It is necessary to differentiate the eccentric motion described in Figure 2-3 from the earth's rotation about its own axis. Similarly, the centrifugal forces resulting from the eccentric motion (which are equal at all locations on earth) should not be confused with the centrifugal forces caused by the earth's spin (which increase with distance from the axis of rotation). To establish equilibrium, the total of the centrifugal forces acting on the earth-moon system exactly balances the gravitational forces exerted between the two celestial bodies. The centrifugal forces arising from the rotation of the earth-moon system are directed parallel to the plane of rotation. The gravitational forces vary in both magnitude and direction with location on the earth's surface. Points nearest the moon experience a greater gravitational response than those sites located on the opposite side of the earth. In addition, the gravitational response at all points on earth is directed towards the moon's center. The resultant of the centrifugal and gravitational forces

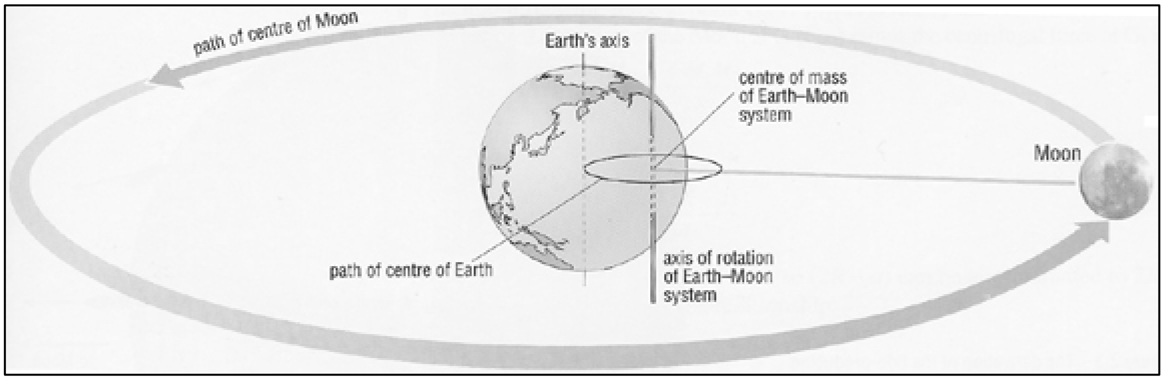

Figure 2-3: Rotation of the earth-moon system (after Open University, 2000).

corresponds to the tide-generating force which consists of two components (directed in relation to the surface of the earth): vertical; horizontal. The vertical part of this composite effect is insufficient to overcome gravity and is therefore ineffective in moving the ocean waters. Contrastingly, the horizontal portion of the resulting tide-generating force acts to promote ocean and coastal circulation (Figure 2-4).

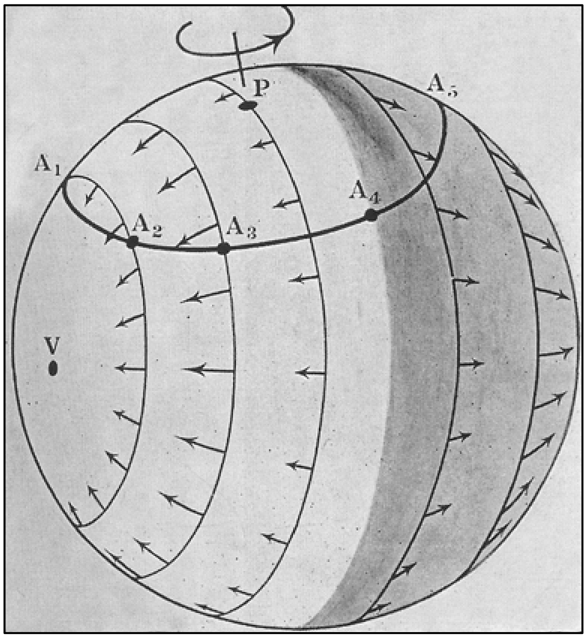

Figure 2-4: Horizontal tide-generating force (after Darwin, 1911).

As a result of the tidal motion that is induced by the horizontal tide-generating force, an ellipsoid with its two bulges directed towards and away from the moon develops. Figure 2-5 shows the resulting distribution of the tides under these equilibrium conditions assuming an earth completely covered with water. According to the equilibrium theory of the tides (which was first proposed by Newton) and considering the various rotational speeds of the earth-moon system, the length of time for the tidal bulges shown in Figure 2-5 to cycle the earth equals the period of the earth's rotation with respect to the moon, a lunar day (or about 24 hours and 50 minutes).

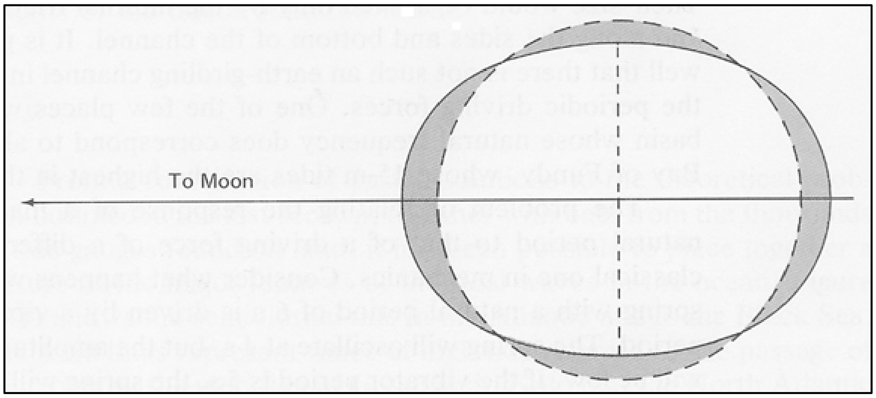

Figure 2-5: Exaggerated equilibrium tidal ellipsoid for a water-covered earth where the dashed line represents the equilibrium surface under no tidal forces and the solid line represents the equilibrium surface under tidal forces (after Knauss, 1978).

The relative positions and orientations of the earth and moon are not constant, which produce variations of the lunar-induced tides according to three main interacting cycles. Figure 2-6 shows the simultaneous changes in the moon's phase, distance from the earth, and declination, all corresponding to the month of March in the year 2002. The phase of the moon is dictated by the degree of alignment between the moon, earth, and sun. Over the lunar month (or about 29.5306 days) shown in Figure 2-6, a fourteen-day cycle between the new and full moon phases is apparent. (This fortnightly cyclical period has a major influence on the tidal ranges of the ocean waters and will be emphasized later.)

Lunar distance varies over an anomalistic month (or about 27.5546 days) as a consequence of the moon's elliptical orbit about the earth-moon center of mass. When the moon is closest to earth, it is said to be in perigee, and the moon's tide-generating force is increased by up to 20% above the average value; when the moon is furthest from the earth, it is said to be in apogee, and the tide-generating force is reduced by about 20% below the average value (Open University, 2000). Further, the moon's elliptical orbit revolves (in an opposite sense of rotation to that of the earth's spin and moon's orbit about the earth-moon center of mass) about the earth-moon center of mass over 18.6 years to complete a full precession cycle. It is important to note that this 18.6-year precession cycle affects all of the lunar characteristics that are displayed in Figure 2-6, the details of which are beyond the scope of this literature review.

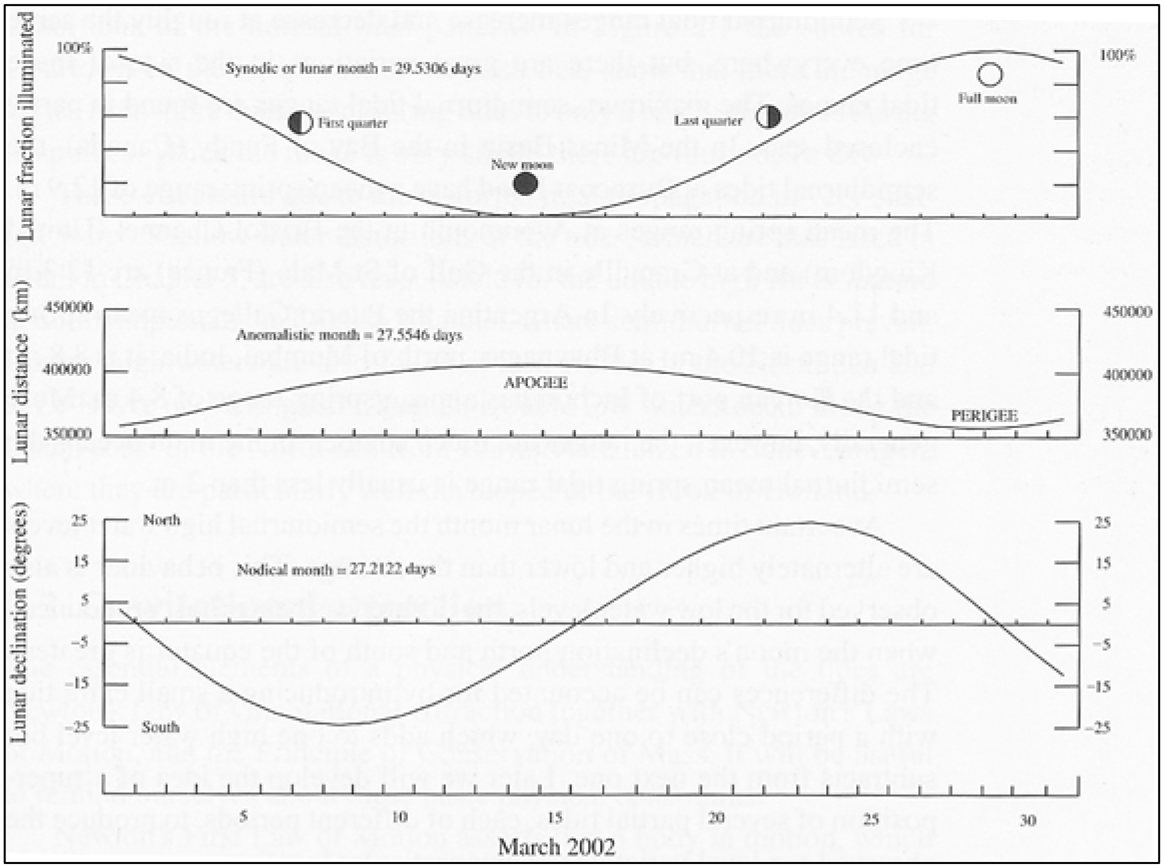

Figure 2-6: Three main interacting cycles influencing the lunar-induced tides, all corresponding to the month of March in the year 2002 (after Pugh, 2004).

The plane of the moon's orbit is inclined at an angle of 28.6° from the equatorial plane of the earth resulting in a successive rise and fall of the moon's path across the night sky over a nodical month (or about 27.2122 days). Of significance, when the moon is at any angle of declination other than zero, the plane of the two tidal bulges will be offset with respect to the equatorial plane of the earth (Figure 2-7). Thus, at any given latitude (e.g., along line P'P in Figure 2-7), the surface heights reached by the semi-diurnal (i.e., twice daily) high tides show a diurnal (i.e., daily) inequality.

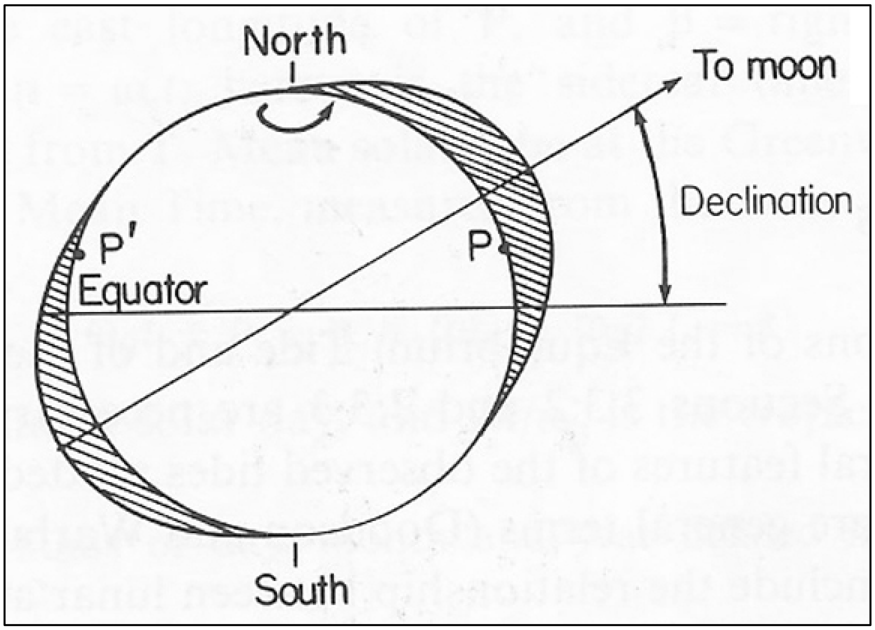

Figure 2-7: Diurnal inequality of the lunar-induced tides at mid-latitude locations consequent upon the moon's declination (after Pugh, 1987).

Another celestial system to consider in the production of tide-generating forces is that between the earth and sun. Applying equilibrium tidal theory to the earth-sun system and considering the earth-sun distance and mass of the sun, one computes the magnitude of the sun's tide-generating force to be about 0.46 times that of the moon. Due to the earth's spin, which requires 24 hours to complete a full rotation, the equilibrium tides produced by the sun have a semi-diurnal period of 12 hours.

Similar to the variations observed in the lunar-induced tides, the solar tides are affected by the sun's declination and orbital geometry. The sun's declination ranges up to 23.4° (also the angle of tilt of the earth's axis of rotation) from the equatorial plane of the earth over the seasonal annual cycle causing a diurnal inequality in the solar tides. Analogous to the moon's orbit around the earth, the orbit of the earth around the sun is elliptical. The eccentricity of the orbit allows for two extremes to develop: perihelion, which corresponds to the minimum distance between the earth and sun (January 3); aphelion, which corresponds to the maximum distance between the earth and sun (July 4). While this solar distance varies over the seasonal annual cycle to affect the sun's tide-generating force, it should be noted that the difference in the earth-sun distance between perihelion and aphelion is only about 4%, as compared to an approximate 13% difference in the earth-moon distance between perigee and apogee (Open University, 2000).

The interaction between the lunar and solar tides results in a 14-day modulation in the semidiurnal tidal ranges of the ocean waters. To simplify this discussion, consider the conditions that both the moon and sun have a zero angle of declination and are positioned, with respect to the earth, in the orientations shown in Figure 2-8. In Figure 2-8(a), the lunar and solar equilibrium tides are coincident (i.e., the tide-generating forces produced by the moon and sun are acting along the same axis) resulting in a tidal range that is larger than average. Such tides are known as spring tides (i.e., higher high tides and lower low tides are experienced). At new moon, the moon and sun are said to be in conjunction; at full moon, the moon and sun are said to be in opposition. Collectively, corresponding to both of these situations, the moon is said to be in syzygy.

Conversely, Figure 2-8(b) shows the tidal conditions resulting from the moon being positioned at right angles to the earth-sun alignment (also known as lunar quadrature). When the moon is in

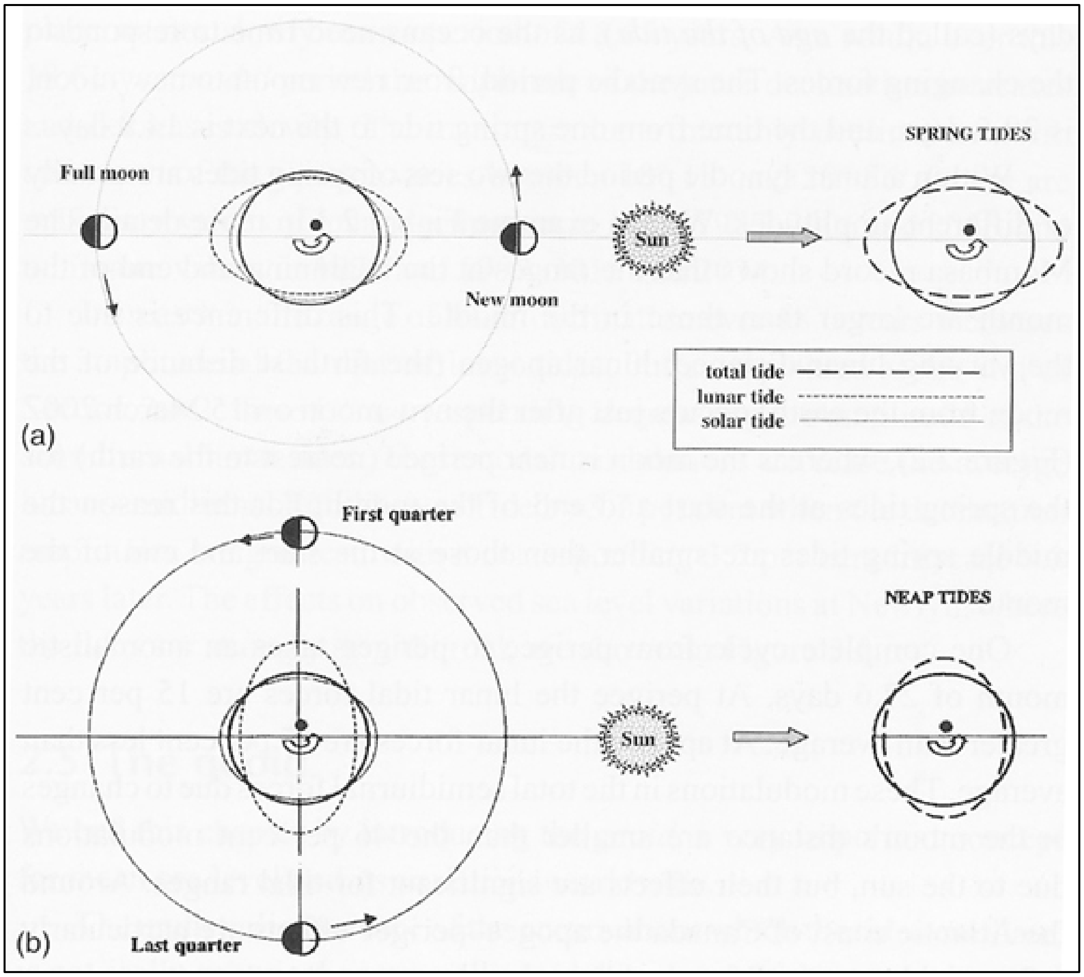

Figure 2-8: (a) Spring tide conditions when the moon is in syzygy and (b) neap tide conditions when the moon is in quadrature (after Pugh, 2004).

quadrature, the tide-generating forces produced by the moon and sun are out of phase and tend to cancel. Thus, the tidal range is correspondingly smaller. Such tides are known as neap tides (i.e., lower high tides and higher low tides are experienced).

While equilibrium tidal theory provides satisfactory insight into the tide-generating forces and the resulting response of the sea surface, discrepancies exist between the equilibrium tides and observed tidal heights. Historically, this prompted the need for a more rigorous description of the tides as they occur in reality. Laplace was the first to suggest such a dynamic theory of the tides; one in which considers the tides as waves driven by the periodic fluctuations of the tide-generating forces. Further interpretations of the dynamic theory of the tides include differentiating the observed tidal dynamics from the equilibrium tides by considering the inertial effects of the forced wave action. In the real oceans then, a complete description of the tides must recognize the relationship between the periodic external forces and the natural frequencies and frictional characteristics of the interconnected ocean basins. More detailed discussion on the topics of dynamical oceanography and ocean tides can be found in Darwin (1911), Proudman (1953), Defant (1960), Dietrich and Kalle (1963), McLellan (1965), Macmillan (1966), Neumann and Pierson (1966), Phillips (1966), Pickard (1975), and LeBlond and Mysak (1978).

2.1.3 Storm Surge and Tsunamis

Storm surge is a meteorologically induced long wave motion which results from the combined action of extreme wind stress and, to a lesser degree, reduced atmospheric pressure on shallow coastal shelf seas. Reid (1990) states that there are four basic mechanisms that drive storm surge development at or near the shoreline: 1) inverted barometer effect; 2) set-up due to onshore winds; 3) geostrophic tilt resulting from wind-driven alongshore currents; 4) short wave set-up. For the coastal regions along the east coast of the United States and surrounding the Gulf of Mexico, storm surge is primarily generated by approaching tropical storm systems; these hurricanes are compact in size with varying degrees of intensity producing exceptionally high flood levels within a confined local area (Simpson, 2003).

The inverted barometer effect acts to lift the sea surface upward in regions of low atmospheric pressure; it can account for not more than about 1 meter of rise centered at the hurricane eye and depends directly on the central pressure deficit relative to outside ambient atmospheric pressure (Reid, 1990). This inverted barometer effect is equally effective over deep or shallow water provided that the ocean surface area is large relative to the spatial scale of the hurricane (Pugh, 1987). Set-up by onshore wind stress is most effective in shallow water and depends directly on the wind stress, the distance over which it acts, and inversely on depth (Reid, 1990). The geostrophic tilt resulting from wind-driven alongshore winds develops to provide the required equilibrium balance between the alongshore current and increased sea levels along the coastline. Figure 2-9 illustrates this geostrophic balance within an idealized domain: for time, $t \geq 0$, a wind stress (F_S) acting parallel to a (no cross-boundary flow) coastline of a semi-infinite sea of constant depth (D) induces a flow current (u) in the direction of the acting wind stress which increases steadily with time at a rate inversely proportional to the water depth (as limited by bottom friction); in response (due to mass conservation and Ekman transport), a sea level gradient $\left(\frac{\partial\zeta}{\partial y}\right)$ normal to the coastline develops to maintain a geostrophic equilibrium with the flow current at all times. (Note that in Figure 2-9, f stands for the Coriolis parameter accounting for the inertial effects generated by the rotation of the earth and g stands for the acceleration due to gravity.) Short wave set-up is caused by the radiation stress (i.e., the excess flux of momentum carried towards the shore) associated with short surface waves that are also generated by the storm winds (Reid, 1990); this phenomenon is confined to the nearshore region where the waves crest and break (referred to as the surf zone).

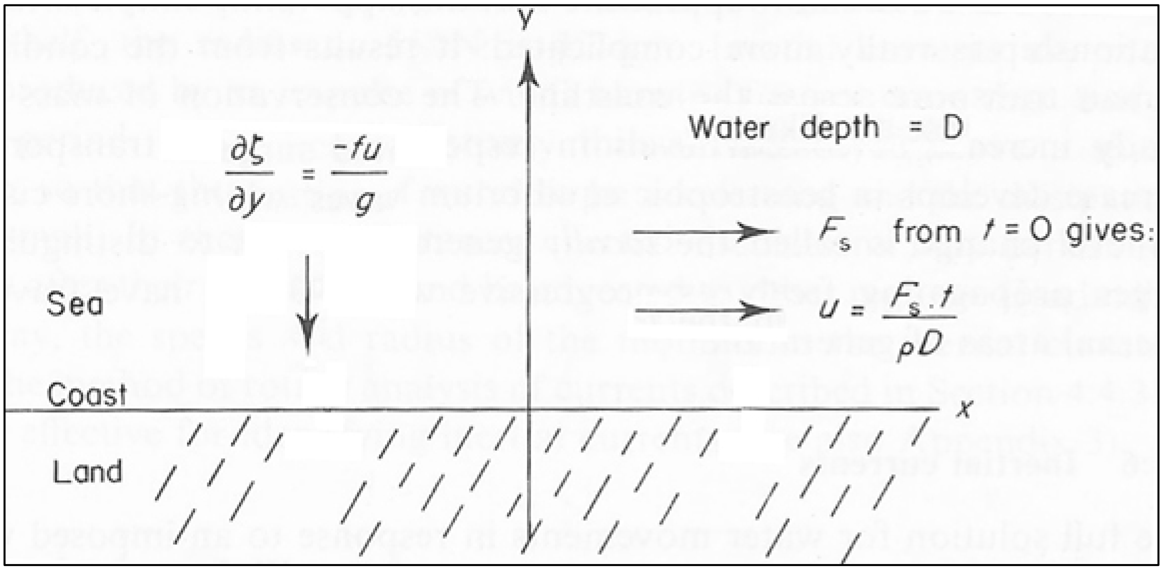

Figure 2-9: Response of an idealized coastal sea to an acting alongshore wind stress (after Pugh, 1987).

Tsunamis are rare wave events generally resulting from seismic or other geologic activity, and therefore, fall outside of the two principal categories of forces responsible for sea level changes: tides and weather (Murty, 1977; Loomis, 1978). Pond and Pickard (1978) translate the word *tsuanami* from a Japanese word meaning “harbor wave” (as distinct from the regular rise and fall of the tides), and it is now generally used to refer to long-period water waves generated by sea bottom movements associated with earthquakes. The alternative term *seismic sea wave* is also commonly used. Tsunamis are generated by submarine earthquakes, but landslides into the sea, and submarine slumping (e.g., of sediments on the continental slope) may occasionally be responsible. There are three distinct aspects of tsunamis that may be considered: 1) their generation by earthquakes; 2) their propagation in deep water; 3) their behavior where they impinge on coasts and the surrounding shallow water regions.

Not all submarine earthquakes produce tsunamis. The important driving element appears to be a vertical crustal movement which displaces the sea bed (Pugh, 2004). After the sea bed is displaced, a tsunami is generated by the horizontal pressure gradients in the water acting as a restoring force. The resulting wave characteristics depend on the amplitude of the displacement and the dimensions of the sea basin involved. Horizontal displacements of the sea bed are relatively ineffective for producing tsunamis because water is not displaced vertically.

Tsunamis propagate through deep water as long-period water waves with typical wave periods of ten minutes or longer (Pugh, 1987). Thus, the speed of tsunami wave propagation may be estimated by the same function used to approximate the speed of long-period, shallow water, nondispersive waves (Knauss, 1978):

$$c = \sqrt{gh} \quad \text{(2.1)}$$

where c = wave speed; h = bathymetric depth. Also, the amplitude of the tsunami wave as it propagates through deep water is small, perhaps not more than 1 m, and as a result, these waves can pass unnoticed by ships at sea.

Although the arrival time of a tsunami can be predicted accurately, the amplitude of the wave which hits a particular length of coast is much less certain. This is because in shallow coastal waters, in addition to the normal amplification of the wave height as it slows down over the continental shelf, the tsunami wave undergoes reflection and refraction. This uncertainty results in widespread catastrophe along the coasts bordering seismically active ocean basins upon the arrival of a tsunami; see Neumann and Pierson (1966) and O'Loughlin and Lander (2003) for reviews of tsunami accounts in the Pacific Ocean and Caribbean Sea, respectively. In addition, further reading related to the generation, propagation through deep water, and transformations on the continental shelf, of tsunamis can be found in the papers of Podyapolsky (1969), Braddock (1969), and Nekrasov (1969), respectively.

2.2 Historical and Current States of Ocean Measurement Capabilities

The following section of this literature review serves to provide a background on the observational methods used in the past and those practiced today to measure ocean conditions. The extent of the following background information entails only those measurement techniques used to record sea levels, which can be divided into two categories: those appropriate for coastal measurements; those which can be used offshore (Forrester, 1983; Howarth and Pugh, 1983). It is important to recognize the relevance of this section, as a great deal of historical water level data is applied in the following study in order to quantify model performance.

2.2.1 Coastal Water Level Measurements

Three different water level measurement instruments are generally used in coastal measurements of sea level (Dietrich and Kalle, 1963): 1) lath gages; 2) float gages; 3) air pressure gages. The lath gage, or more commonly referred to as tide poles or staffs, is an inexpensive water level measurement instrument that can be installed nearly anywhere with relative ease. These vertical rulers are used in a similar sense to the way the ancient Egyptians linked their Nilometers to their temples in order for the priests to provide warnings of imminent flooding (Pugh, 1987). For these, and for all water level measurements, there should be a careful connection of the gage zero to a permanently fixed shore benchmark. As is often practiced, taking the average water level between the crests and troughs over a short period, perhaps 20 seconds, averages out surface wave fluctuations. Reading accuracy may be further increased by fitting a transparent hollow tube alongside the tide pole, which connects to the sea through a narrower tube preventing immediate response to external water level changes. Tide poles are frequently the best choice for short-term surveys of limited accuracy, but the tedium involved and errors associated with the readings over longer time periods make tide poles unsuitable for long-term surveys.

Over the past 150 years, and until quite recently, float gages were the standard method of measuring and automatically recording sea levels (Pugh, 2004). Of historical significance, the first self-recording float gage began operation at Sheerness in the Thames estuary (Palmer, 1831).

A float gage consists of a system of wires, pulleys, and gears to provide either direct mechanical registration or electronic transmission of its water level measurements through a recording drum (Figure 2-10). Such a float gage requires a vertical structure to support the recording drum above the stilling well, a vertical shaft long enough to cover the entire range of the tides at the site. The entire length of the stilling well is closed except for some small openings at the bottom to allow for water entry and exit. These small openings remain through the use of either orifices or pipe inlets to provide sufficient damping of the short surface waves and more accurate measurement of the longer period variations (e.g., those induced by the tides); several stilling well arrangements are possible (Lennon, 1971; Noye, 1974; Seelig, 1977). Although float gages are robust and relatively simple to operate, the accuracy of the stilling-well system is limited by two fundamental factors: water density differences (due to salinity and temperature variations) between the inside and outside (with respect to the stilling well) waters lead to differences in the measured water levels; in the presence of strong flow currents, pressure distortions in the vicinity of the well openings can permit drawdown in the stilling-well water levels.

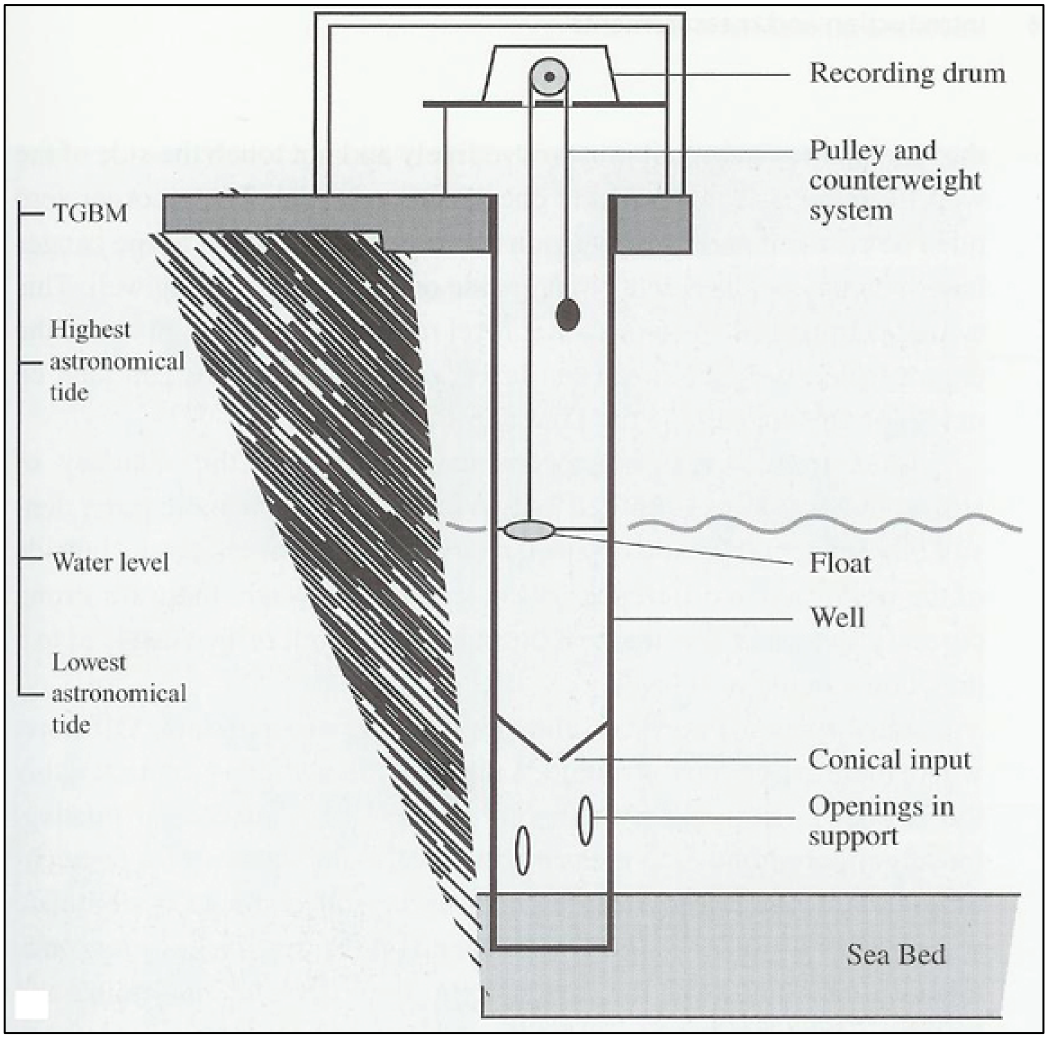

Figure 2-10: Working principle of a float gage (after Pugh, 2004).

An alternative approach is to measure the pressure at some fixed point below the sea surface and to convert this pressure into an equivalent water level through use of the basic hydrostatic relationship (Pugh, 1987):

$$P = P_A + \rho g D \qquad (2.2)$$

where P = measured pressure at the transducer depth; P_A = atmospheric pressure acting on the water surface; ρ = mean density of the overlying water column; D = water level above the transducer. A gas bubbling system, as shown in Figure 2-11, is a simple tide gage with good overall accuracy and datum stability. Compressed air or nitrogen gas from a cylinder is reduced in pressure through one or two valves to allow for a small steady flow through a connecting tube to escape through an orifice in an underwater canister, called a pressure-point. The level of the orifice defines the gage zero. At this underwater outlet, for low rates of gas escape, the gas pressure is equal to the water pressure; this is also the pressure that is transmitted up the connecting tube for measurement and record. Normal procedures call for a differential transducer which responds to the pressure difference (system pressure minus atmospheric pressure) to

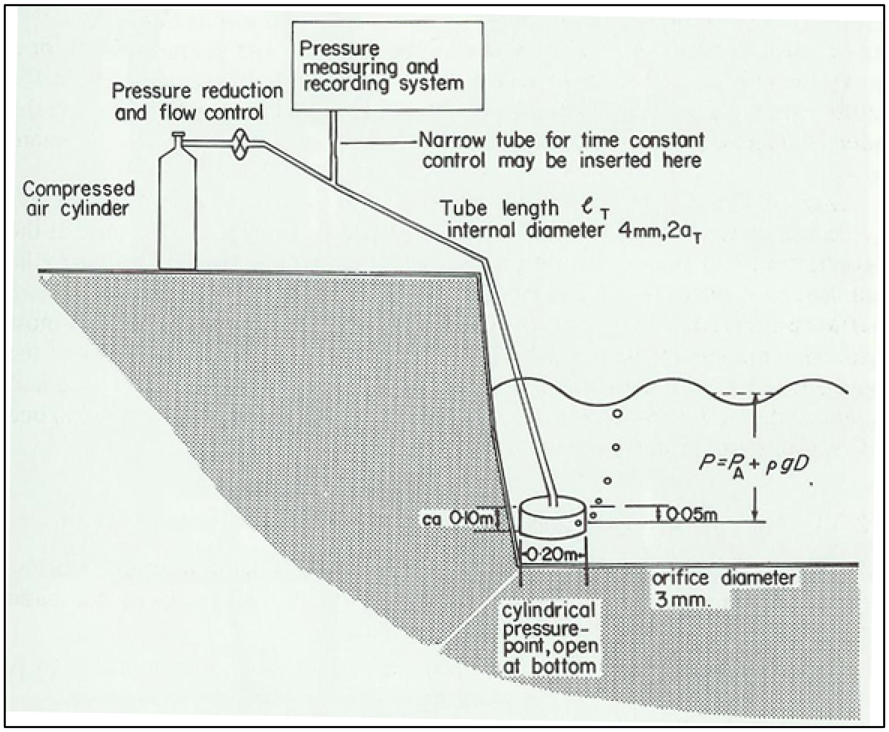

Figure 2-11: A basic pneumatic bubbling system for tube lengths less than 200 m (after Pugh, 1972).

provide a pressure head reading that relates more directly to the height of the overlying water column through the basic hydrostatic relationship given in Equation (2.2).

2.2.2. Offshore Water Level Measurements

In measuring sea levels in the deep regions of the ocean, the only stable reference point from which to supply measurements is the sea bed. (Of course, this corresponds to the case when it is not possible to attach an observation device directly to an offshore structure.) As such, specialized bottom-mounted, self-contained pressure measuring and recording systems have been designed to provide water level observations based on its pressure measurements. Operation of these gages requires a high level of technical skill for deployment and recovery of the equipment and to ensure reliability and precise calibration (Cartwright et al., 1980). These measurement instruments cannot be applied towards long-term sea level studies because there is no geodetic datum control; however, regular water level fluctuations (e.g., those produced by the tides) can be extracted by analysis to provide tidal observations in the open sea. Also, it is important to employ sufficient calibration techniques in order to best correct the measurements for density differences induced by temperature variations.

Measurements supplied by satellite altimetry have revolutionized the methods of measuring sea surface elevations and the analysis and scientific interpretation of these observations. This alternative approach to measuring water levels offers enormous quantities of data; the complexities of interpreting these altimeter-derived data requires physical oceanographers to pay particular attention to the accurate determination of satellite orbits and the exact shape of the mean-sea-level surface (Robinson, 1985). The most important satellites for sea level studies include the TOPEX/Poseidon and JASON missions (Pugh, 2004).

The basic principle of timing a reflected pulse is based on the speed of the signal as it travels through a known medium and the corresponding length of travel. For instance, the time of travel for an electromagnetic pulse to travel from a satellite altimeter to the sea surface and back again is related to a measured height (or length of travel) through the following relationship:

$$t = \frac{2l}{C_e} \qquad (2.3)$$

where l = length of travel; C_e = velocity of an electromagnetic wave traveling through air. Figure 2-12 shows this height (or length of travel) as h_1. For oceanographic work, the sea level required (h_4) is measured relative to the geoid. In addition, satellite elevations (h_2) can be fixed relative to a reference ellipsoid. Lastly, and as previously discussed, deviations exist between the surfaces of the geoid and reference ellipsoid; these differences are measured as h_3. The techniques employed to arrive at these measurements with accuracies approaching 1 cm are beyond the scope of this literature review; see Fu and Cazenave (2001) for further reading on these methods and procedures. Information regarding correction factors for surface wave heights, and for electromagnetic effects in the ionosphere and gases in the atmosphere, and orbital geometry of the satellite track is given by Chelton et al. (1990).

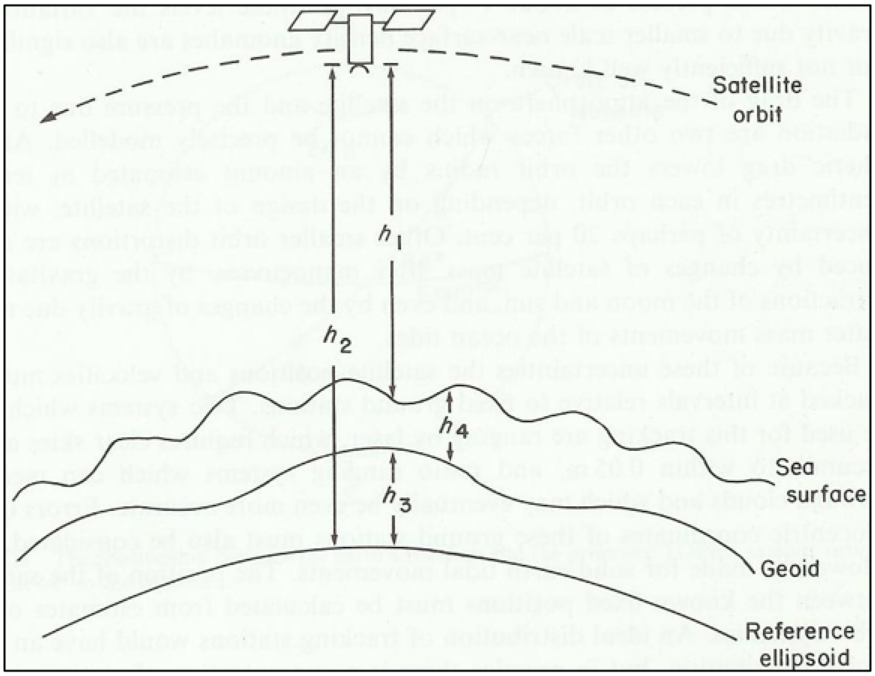

Figure 2-12: Schematic diagram of the parameters which must be known to determine the sea level relative to the geoid by satellite altimetry (after Pugh, 1987).

2.3 Hydrodynamic Modeling using Large Domains

Recent trends in coastal and ocean hydrodynamic modeling have been directed towards using larger computational domains which extend up to or beyond the continental break and slope (Lynch, 1983; Westerink and Gray, 1991). For example, Flather (1987), Gerritsen and Bijlsma (1988), and Vincent and Le Provost (1988) have all developed tidal and/or storm surge models to cover a large portion of the northeastern quadrant of the Atlantic Ocean. Foreman (1988), Gray (1989), Walters and Werner (1989), and Werner and Lynch (1989) have all demonstrated success in applying large domains to reproduce tidal circulation patterns in expansive ocean basins and marginal shelf seas. Furthermore, Westerink et al. (1991), Westerink et al. (1993), Westerink et al. (1994a), and Westerink et al. (1995) show the advantages of using unstructured, graded grids to cover a large expanse of the deep ocean in addition to the continental margin waters of interest. Further studies by Foreman (1986), Kolar et al. (1994b), Westerink et al. (1994b), and Kolar et al. (1996) explain various implementations of these large domain hydrodynamic models. A progress of research presented by Westerink et al. (1992a), Blain et al. (1994a), Blain et al. (1994b), Blain et al. (1994c), and Blain et al. (1995) details the benefits of employing large computational domains towards producing hurricane storm surge predictions.

While a large domain increases the predictive capabilities of coastal and ocean hydrodynamic models, it complicates the process of computational node placement. Large domains require a strategic placement of computational nodes in order to maintain acceptable levels of accuracy for a given computational cost. However, the actual gridding of larger, more complex domains relies on crude mesh resolution criteria and results in computational grids that are user-dependent and indirectly related to the flow physics of the system being modeled (Le Provost and Vincent, 1986; Frey, 1987; Lohner, 1987; Ho-Le, 1988; Ramaswamy and Akin, 1990; Thacker et al., 1990; Jones and Richards, 1992; Kashiyama and Okada, 1992; Taniguchi et al., 1992; Turner and Baptista, 1993; Knupp and Steinberg, 1994; Roache, 1994). More recently, methods that more directly incorporate tidal flow and circulation physics into the mesh generation procedure have resulted in highly variable, graded computational grids that better locally refine areas of high sensitivity (Westerink et al., 1992b; Westerink et al., 1994c; Hagen and Westerink, 1995; Luettich and Westerink, 1995; Hagen, 1998; Hagen et al., 2000; Hagen, 2001; Hagen et al., 2001; Hagen et al., 2002; Hagen and Parrish, 2004; Kojima et al., 2005). These areas of high sensitivity include shallow water regions containing higher localized wave number content and locations with steep bathymetric gradients. In addition, two-dimensional response structures associated with complicated shorelines, variable bottom topography, amphidromes (the intersection of all phase lines and a point at which all cotidal lines meet), and resonant bays also require increased grid resolution.

The remaining focus of this section of the literature review concentrates on an effective numerical technique that has been shown to provide robust element sizing guidelines for large domains (Hagen, 1998; Hagen et al., 2000; Hagen, 2001; Hagen et al., 2001; Hagen et al., 2002): the localized truncation error analysis (LTEA). The basis of the concept behind the LTEA is directly related to the mesh refinement scheme described by Berger and Colella (1986). However, the LTEA extends the truncation error estimation used by Berger and Colella (1986) by analyzing the first four orders of the truncation error series in full detail. It is this truncation error that is used in developing the necessary local refinement and relaxation of nodal density for the computational grid. The goal, which is achieved through a repositioning of the computational nodes, is to force the level of truncation error to be constant throughout the entire domain. This LTEA-based approach leads to a more robust error estimation for long wave propagation problems, as it evaluates the truncation error series using solutions that have achieved dynamic steady state conditions. Hagen (1998) and Hagen et al. (2000) thoroughly detail the model formulation, LTEA-based node spacing requirements, and grid development for a one-dimensional, shallow water modeling application. Hagen (2001), Hagen et al. (2001), and Hagen et al. (2002) then extend this analysis to a two-dimensional setting. It is important to note that all (except for the original) of the computational grids employed in this study are generated using element sizing guidelines provided by application of the LTEA.

2.4 Harmonic Representation of the Tides

In the most basic sense, the analysis of tidal records is a special case of time series study; the idea is to condense a long-term record of observations to a brief collection of constants. Due the regularity of the tide-generating forces, periodicities contained within a tidal record may be extracted in order to describe the tidal displacement at a location as a sum of the associated harmonics. For a historical review, various methods of analysis devised by Darwin (1911), Doodson (1928), and Horn (1960) are primarily aimed at determining the amplitude and phase properties of the predominant harmonics. More recently, attempts have been made to evaluate the contribution of non-tidal phenomena present in the record of observation in order to provide a quantitative estimate of the variability in the tidal record (Munk and Cartwright, 1966). The following section of this literature review covers a brief review of the mathematics involved in the analysis of the tides and a discussion regarding harmonic constants and their role in representing the tides.

Fourier series forms the basis of the analysis of the tides; a superposition of multiple waves, each with its own properties (e.g., interval of recurrence and those associated with the amplitude and phase of the tidal component), to form a total tidal signal. Therefore, tidal variations can be represented by a finite number N of harmonic terms of the form (Pugh, 2004):

$$H_n \cos \omega_n t - g_n \qquad (2.4)$$

where n = component index; H_n = component amplitude; ω_n = component angular speed = $2\pi/T_n$; T_n = component period; g_n = component phase lag relative to some defined time zero (commonly taken as the phase lag on the Equilibrium Tide phase at the Greenwich Meridian, in which case it is called G_n). Use of the Equilibrium Tide is also helpful in determining the angular speed of the various tidal components. These are found by an expansion of the Equilibrium Tide into harmonic terms; the speeds of these terms are found to have the general form (Pugh 2004):

$$\omega_n = i_a\omega_1 + i_b\omega_2 + i_c\omega_3 + \left(\omega_4, \omega_5, \omega_6 \text{ terms}\right) \qquad (2.5)$$

where the values of ω_1 to ω_6 are the angular speeds related to the astronomical parameters shown in Table 2-1 and the coefficients i_a to i_c are small integers, usually in the range between -2 and 2.

Table 2-1: The basic speeds and origins of the astronomical arguments (ω_n) that give the frequencies of the harmonic components (after Pugh, 2004).

Origin	Period	Degrees per mean solar hour	Symbol
Mean solar day (msd)	1.0000 msd	15.0000	ω_0
Mean lunar day	1.0351 msd	14.4921	ω_1
Sidereal month	27.3217 msd	0.5490	ω_2
Tropical year	365.2422 msd	0.0411	ω_3
Moon's perigee	8.85 years	0.0046	ω_4
Regression of moon's nodes	18.61 years	0.0022	ω_5
Perihelion	20942 years	–	ω_6

At this point in the harmonic analysis, the individual harmonic components (herein referred to as constituents) are derived by considering the associated periodicity of the corresponding tide-generating forces. For example, the M_2 tidal constituent is representative of the semi-diurnal (with a period of 12 hours and 25 minutes) tide resulting from the moon's revolution about the earth in a circular orbit. The naming convention follows that M represents the moon and the subscript 2 shows that the tide occurs twice a day. Similarly, the semi-diurnal tide generated by the sun (as being on the equatorial plane of the earth) has a period of exactly 12 hours, and hence, the S_2 tidal constituent is represented. Furthermore, the interaction between the M_2 and S_2 tides produces the spring-neap tidal cycle.

These concepts are now related to the actual movements of the moon and sun by considering each individual modulation as an effect produced by a separate phantom satellite (Pugh, 2004). For instance, the astronomical expressions can be expanded for declination and distance mathematically to determine the periods and theoretical amplitudes of the extra terms. The concept is then extended to include longer period variations of the moon and sun, which results in annual, semi-annual, and diurnal tidal constituents.

The main divisions in the pattern of tidal constituents are the number of cycles per day (governed by i_a), where each division is called a tidal species. In the complete astronomical expansion, i_b is used to fit the monthly modulations, which varies between -5 and 5 and defines the group within each tidal species. Within each group, i_c fits the annual modulations; it also varies between -5 and 5 and is said to define the constituent. The modulations in ω_4, ω_5, and ω_6 are affected by longer period astronomical cycles and cannot be resolved as independent harmonics from a year of observations. Therefore, variations in these astronomical arguments are represented in the harmonic expansions by small adjustment factors, f and u, to the amplitude and phase, respectively.

In applying the harmonic method of analysis to a tidal record, a tidal function $T(t)$ is fit to the sea level observations (Pugh, 2004):

$$T(t) = Z_0 + \sum_N H_n f_n \cos[\omega_n t - g_n + (V_n + u_n)] \qquad (2.6)$$

where the unknown parameters are Z_0 and the series of constituent amplitudes and phases (H_n, g_n). Z_0 is included here as a variable to be fitted in the analysis, but it commonly represents local mean sea level and is therefore a known parameter. The nodal adjustment factors are given as f_n and u_n and the terms $\omega_n t$ and V_n together determine the phase angle of the Equilibrium constituent. V_n is the Equilibrium phase angle for the constituent at the arbitrary time origin. The accepted convention is to take V_n as for the Greenwich Meridian and to take t in the standard time zone of the observation station. A least-squares fitting procedure is then employed to determine the amplitudes and phases of the tidal constituents corresponding to the particular measurement site. This least-squares fitting procedure serves to minimize the square of the residual differences between the observed $O(t)$ and computed tidal elevations, when summed over all observations (Pugh, 2004):

$$S(t) = O(t) - T(t) \qquad (2.7)$$

The least-squares fitting procedure provides the following benefits (Pugh, 1987): gaps in the observation data are permissible; any length of data may be treated; no assumptions are made about data outside the interval to which the fit is made; transient phenomena are eliminated (i.e., only variations with a coherent phase at tidal frequencies are extracted); fitting can be applied using any time step. Foreman (1977) and Foreman and Henry (1979) offer a more detailed explanation of the harmonic analysis of tidal heights and high and low water observations, respectively. Additionally, Godin (1972) offers an excellent text covering the fundamental mathematical basis of tidal analysis, traditional and applied methods of analysis, shallow water tides, and the inference of constituents.

CHAPTER 3

MODEL DESCRIPTION

Chapter 3 includes three categories: 1) governing equations, 2) model parameterizations and boundary condition specifications, and 3) domain definition and bathymetric features.

3.1 Governing Equations

ADCIRC-2DDI (Advanced Circulation Model for Oceanic, Coastal, and Estuarine Waters-Two Dimensional Depth Integrated option) has been developed for the specific purpose of generating long time periods of two dimensional hydrodynamic calculations along shelves, coasts, and within estuaries (Luettich et al., 1992). Advances in ADCIRC-2DDI enable the code to produce long-term numerical simulations for quite large computational domains (e.g., the model domain applied in this study). ADCIRC-2DDI applies the depth integrated equations of mass and momentum conservation, subject to the hydrostatic pressure, incompressibility, and Boussinesq approximations, neglecting baroclinic terms and lateral diffusion/dispersion effects. Under these assumptions, a physically-based continuity equation (the primitive continuity equation) and two physically-based momentum equations (the primitive momentum equations in latitudinal and longitudinal directions), expressed in a spherical coordinates system (Flather, 1988; Kolar et al., 1992), are set up into the ADCIRC-2DDI computer code to solve hydrodynamic problems in order to describe shallow water tidal flow.

The primitive continuity equation, expressed in a spherical coordinate system, is represented as:

$$\frac{\partial \zeta}{\partial t}+\frac{1}{R\cos\phi}\left[\frac{\partial UH}{\partial \lambda}+\frac{\partial (VH\cos\phi)}{\partial \phi}\right]=0 \quad \text{......}(3.1)$$

The primitive momentum equation in the latitudinal direction, expressed in a spherical coordinate system, is represented as:

$$\begin{aligned}&\frac{\partial U}{\partial t}+\frac{1}{R\cos\phi}U\frac{\partial U}{\partial \lambda}+\frac{1}{R}V\frac{\partial U}{\partial \phi}-\left(\frac{\tan\phi}{R}U+f\right)V \\ &\quad=-\frac{1}{R\cos\phi}\frac{\partial}{\partial \lambda}\left[\frac{p_s}{\rho_0}+g(\zeta-\eta)\right]+\frac{\tau_{s\lambda}}{\rho_0 H}-\tau_* U\end{aligned} \quad \text{......}(3.2)$$

The primitive momentum equation in the longitudinal direction, expressed in the spherical coordinate system, is represented as:

$$\begin{aligned}&\frac{\partial V}{\partial t}+\frac{1}{R\cos\phi}U\frac{\partial V}{\partial \lambda}+\frac{1}{R}V\frac{\partial V}{\partial \phi}+\left(\frac{\tan\phi}{R}U+f\right)U \\ &\quad=-\frac{1}{R}\frac{\partial}{\partial \phi}\left[\frac{p_s}{\rho_0}+g(\zeta-\eta)\right]+\frac{\tau_{s\phi}}{\rho_0 H}-\tau_* V\end{aligned} \quad \text{......}(3.3)$$

where

t = time

λ = degrees longitude, east of Greenwich positive

ϕ = degrees latitude, north of Equator positive

ζ = free surface elevation, relative to the geoid

U = depth averaged velocity in the λ direction

V = depth averaged velocity in the ϕ direction

R = radius of the Earth

H = $h+\zeta$ = total height of the water column

h = bathymetric depth, relative to the geoid

f = $2\Omega \sin\phi$ = Coriolis parameter

Ω = angular speed of the Earth

p_s = atmospheric pressure at the free surface

ρ_0 = reference density of water

g = acceleration due to gravity

η = Newtonian equilibrium tide potential

$\tau_{s\lambda}$ = applied free surface stress in the λ direction

$\tau_{s\phi}$ = applied free surface stress in the ϕ direction

τ_* = $C_f \frac{\sqrt{U^2+V^2}}{H}$ = quadratic bottom stress

C_f = bottom friction coefficient

Reid (1990) established the effective Newtonian equilibrium tide potential and is written as:

$$\eta(\lambda,\phi,t) = \sum_{n,j} \alpha_{jn} C_{jn} f_{jn}(t_0) L_j(\phi) \cos\left[\frac{2\pi(t-t_0)}{T_{jn} + j\lambda + \nu_{jn}(t_0)}\right] \text{..(3.4)}$$

where

t_0 = reference time

C_{jn} = constant characterizing the amplitude of tidal constituent *n* of species *j*

T_{jn} = period of constituent *n* of species *j*

α_{jn} = effective earth elasticity factor for tidal constituent *n* of species *j*

f_{jn} = time-dependent nodal factor

ν_{jn} = time-dependent astronomical argument

j = 0, 1, 2 = tidal species

(j = 0, declinational; j = 1, diurnal; j = 2, semidiurnal)

$$L_0 = 3\sin^2(\phi) - 1 \qquad (3.5)$$

$$L_1 = \sin(2\phi) \qquad (3.6)$$

$$L_2 = \cos^2(\phi) \qquad (3.7)$$

In addition, Reid (1990) consolidated the value of the effective earth elasticity factor, α_{jn}, which is typically applied as 0.69 for all tidal constituents (Schwiderski, 1980; Hendershott, 1981) even though the value has been shown to be slightly constituent dependent (Wahr, 1981).

It is convenient to work with the finite element discretization of the shallow water equations in an alternative coordinate system, which is named the Carte Parallelogrammatique (CP) projection (Westerink et al., 1993). The following transformation equations exist to convert the governing equations from a spherical coordinate system to the CP projection:

$$x' = R(\lambda - \lambda_0)\cos\phi_0 \qquad (3.8)$$

$$y' = R\phi \qquad (3.9)$$

where λ_0 and ϕ_0 correspond to the center point of the projection.

The primitive continuity equation, expressed in the CP coordinate system, is represented as:

$$\frac{\partial \zeta}{\partial t}+\frac{\cos\phi_0}{\cos\phi}\frac{\partial UH}{\partial x'}+\frac{1}{\cos\phi}\frac{\partial\left(VH\cos\phi\right)}{\partial y'}=0 \qquad (3.10)$$

The primitive momentum equation in the latitudinal direction, expressed in the CP coordinate system, is represented as:

$$\begin{aligned}\frac{\partial U}{\partial t}+\frac{\cos\phi_0}{\cos\phi}U\frac{\partial U}{\partial x'}+V\frac{\partial U}{\partial y'}-\left(\frac{\tan\phi}{R}U+f\right)V \\ =-\frac{\cos\phi_0}{\cos\phi}\frac{\partial}{\partial x'}\left[\frac{p_s}{\rho_0}+g\left(\zeta-\eta\right)\right]+\frac{\tau_{s\lambda}}{\rho_0 H}-\tau_* U\end{aligned} \qquad (3.11)$$

The primitive momentum equation in the longitudinal direction, expressed in the CP coordinate system, is represented as:

$$\begin{aligned}\frac{\partial V}{\partial t}+\frac{\cos\phi_0}{\cos\phi}U\frac{\partial V}{\partial x'}+V\frac{\partial V}{\partial y'}+\left(\frac{\tan\phi}{R}U+f\right)U \\ =-\frac{\partial}{\partial y'}\left[\frac{p_s}{\rho_0}+g\left(\zeta-\eta\right)\right]+\frac{\tau_{s\phi}}{\rho_0 H}-\tau_* V\end{aligned} \qquad (3.12)$$

The Generalized Wave Continuity Equation (GWCE) is derived by uniting a time-differentiated form of the primitive continuity equation and a spatially differentiated form of the two primitive momentum equations recast into conservative form, reformulating the convective terms into non-conservative form, and adding the primitive form of the continuity equation multiplied by a constant in time and space, τ_0 (Lynch et al., 1979; Kinnmark, 1984; Luettich, et al., 1992).

The GWCE, expressed in a spherical coordinate system is represented as:

$$
\begin{aligned}
&\frac{\partial^2 \zeta}{\partial t^2} + \tau_0 \frac{\partial \zeta}{\partial t} \\
&+ \frac{1}{R\cos\phi}\frac{\partial}{\partial \lambda}\left\{ U\frac{\partial \zeta}{\partial t} - \frac{1}{R\cos\phi} UH \frac{\partial U}{\partial \lambda} - \frac{1}{R} VH \frac{\partial U}{\partial \phi} + \left(\frac{\tan\phi}{R} U + f \right) VH \right. \\
&\qquad \left. - \frac{H}{R\cos\phi}\frac{\partial}{\partial \lambda}\left[\frac{p_s}{\rho_0} + g(\zeta - \eta) \right] + \frac{\tau_{s\lambda}}{\rho_0} - (\tau_* - \tau_0) UH \right\} \\
&+ \frac{1}{R}\frac{\partial}{\partial \phi}\left\{ V\frac{\partial \zeta}{\partial t} - \frac{1}{R\cos\phi} UH \frac{\partial V}{\partial \lambda} - \frac{1}{R} VH \frac{\partial V}{\partial \phi} - \left(\frac{\tan\phi}{R} U + f \right) UH \right. \\
&\qquad \left. - \frac{H}{R}\frac{\partial}{\partial \phi}\left[\frac{p_s}{\rho_0} + g(\zeta - \eta) \right] + \frac{\tau_{s\phi}}{\rho_0} - (\tau_* - \tau_0) VH \right\} - \frac{\tan\phi}{R}\left(\frac{\partial VH}{\partial t} + \tau_0 VH \right) = 0
\end{aligned}
$$

....(3.16)

The GWCE, expressed in the CP coordinate system is represented as:

$$
\begin{aligned}
&\frac{\partial^2 \zeta}{\partial t^2} + \tau_0 \frac{\partial \zeta}{\partial t} \\
&+ \frac{\cos\phi_0}{\cos\phi}\frac{\partial}{\partial x'}\left\{ U\frac{\partial \zeta}{\partial t} - \frac{\cos\phi_0}{\cos\phi} UH \frac{\partial U}{\partial x'} - VH \frac{\partial U}{\partial y'} + \left(\frac{\tan\phi}{R} U + f \right) VH \right. \\
&\qquad \left. - H\frac{\cos\phi_0}{\cos\phi}\frac{\partial}{\partial x'}\left[\frac{p_s}{\rho_0} + g(\zeta - \eta) \right] + \frac{\tau_{s\lambda}}{\rho_0} - (\tau_* - \tau_0) UH \right\} \\
&+ \frac{\partial}{\partial y'}\left\{ V\frac{\partial \zeta}{\partial t} - \frac{\cos\phi_0}{\cos\phi} UH \frac{\partial V}{\partial x'} - VH \frac{\partial V}{\partial y'} - \left(\frac{\tan\phi}{R} U + f \right) UH \right. \\
&\qquad \left. - H\frac{\partial}{\partial y'}\left[\frac{p_s}{\rho_0} + g(\zeta - \eta) \right] + \frac{\tau_{s\phi}}{\rho_0} - (\tau_* - \tau_0) VH \right\} - \frac{\tan\phi}{R}\left(\frac{\partial VH}{\partial t} + \tau_0 VH \right) = 0
\end{aligned}
$$

....(3.17)

The GWCE is solved in conjunction with the primitive momentum equations in non-conservative form. GWCE-based finite element solutions to the shallow water equations result in excellent numerical amplitude and phase propagation characteristics (Westerink et al., 1993).

3.2 Model Parameterizations and Boundary Condition Specifications

The set up of the circulation code used in this study is discussed in this section. Inconsistent model input parameters, which do not cause fatal error, will be found automatically and set by default to a more consistent value, then, execution will be continued. The model input files set the simulations to occur in a spherical coordinate system. Next, information about the bottom stress parameterization is specified in the input files. In this research, the hybrid bottom friction formulation is utilized. The bottom friction coefficient for deep water is constant and a quadratic bottom friction law results. Contrary, the bottom friction coefficient increases as the depth decreases in shallower waters. Finally, the current simulations enable finite amplitude terms and the wetting and drying of elements. Initial water surface elevations are set equal to the bathymetric water depth in the grid file (fort.14 file) (Westerink, 2000).

The ADCIRC-2DDI model sets up to compute a spatially variable Coriolis parameter, which is 0.0. In this study, seven tidal potential forcings (K_1, K_2, M_2, N_2, O_1, Q_1, and S_2) are applied over the entire domain, and the open-ocean boundary is depth-forced with tidal elevation data corresponding to eight tidal constituents (K_1, K_2, M_2, N_2, O_1, Q_1, S_2, and *Steady*). Table 3-1 displays the definitions and angular speeds of the tidal constituents that are used to force the ADCIRC-2DDI model. The global ocean model provided by Le Provost et al. (1998) defines these harmonic data used to force the deep-ocean nodes located along the 60º W meridian. The acceleration due to gravity, g, is 9.81m/s^2, and the GWCE weighting factor, τ_0, is set to -0.01. The time weighting factors for the GWCE are 0.35, 0.30, and 0.35 (at time levels k+1, k, and k-1, respectively). The minimum bathymetric depth corresponding to the of wetting and drying elements, H_0, is set to 0.1m. The following hybrid bottom friction parameters are specified: the bottom friction coefficient, C_f, is set to 0.0025, the break depth, H_{break}, is set to 1.0m, and the two dimensionless parameters are set accordingly: $\theta = 10$ and $\lambda = 1/3$. Eddy viscosity, E_{h2}, is set to 5.00m^2/s. 90-day simulations are begun from a cold start and boundary forcings are ramped via a hyperbolic ramping function over a period of 20 days to promote solution stability. A four second time step is applied for the high resolution mesh, and a five second time step is applied to the remaining three coarser meshes. Finally, a harmonic analysis is applied to the last 45 days of simulated water surface elevations. The ADCIRC-2DDI parameter input file for the 333K simulation (fort.15) is represented in Appendix B.

Table 3-1: Tidal constituents used to force the ADCIRC-2DDI model.

Symbol	Definition	Period [hr]	Frequency [rad/s]
K_1	Lunar diurnal constituent	23.93	0.000072934778604
K_2	Luni-solar semidiurnal constituent	11.97	0.000145808625898
M_2	Principal lunar semidiurnal constituent	12.42	0.000140525704669
N_2	Larger lunar elliptic semidiurnal constituent	12.66	0.000137861710268
O_1	Lunar diurnal constituent	25.82	0.000067596020604
Q_1	Larger lunar elliptic diurnal constituent	26.87	0.000064954568366
S_2	Principal solar semidiurnal constituent	12.00	0.000145444104333
Steady	Steady	∞	0.000000000000000

3.3 Domain Definition and Bathymetric Features

The Western North Atlantic Tidal (WNAT) model domain encompasses the Gulf of Mexico, the Caribbean Sea, and the entire portion of the North Atlantic Ocean found west of the 60º W meridian. Several studies in the past have proven that extending the open-ocean boundary in deep water is advantageous as compared to placement on the continental shelf[§] or the shelf break (Dietsche, 2004). The open-ocean boundary lying along the 60º W meridian extends from the

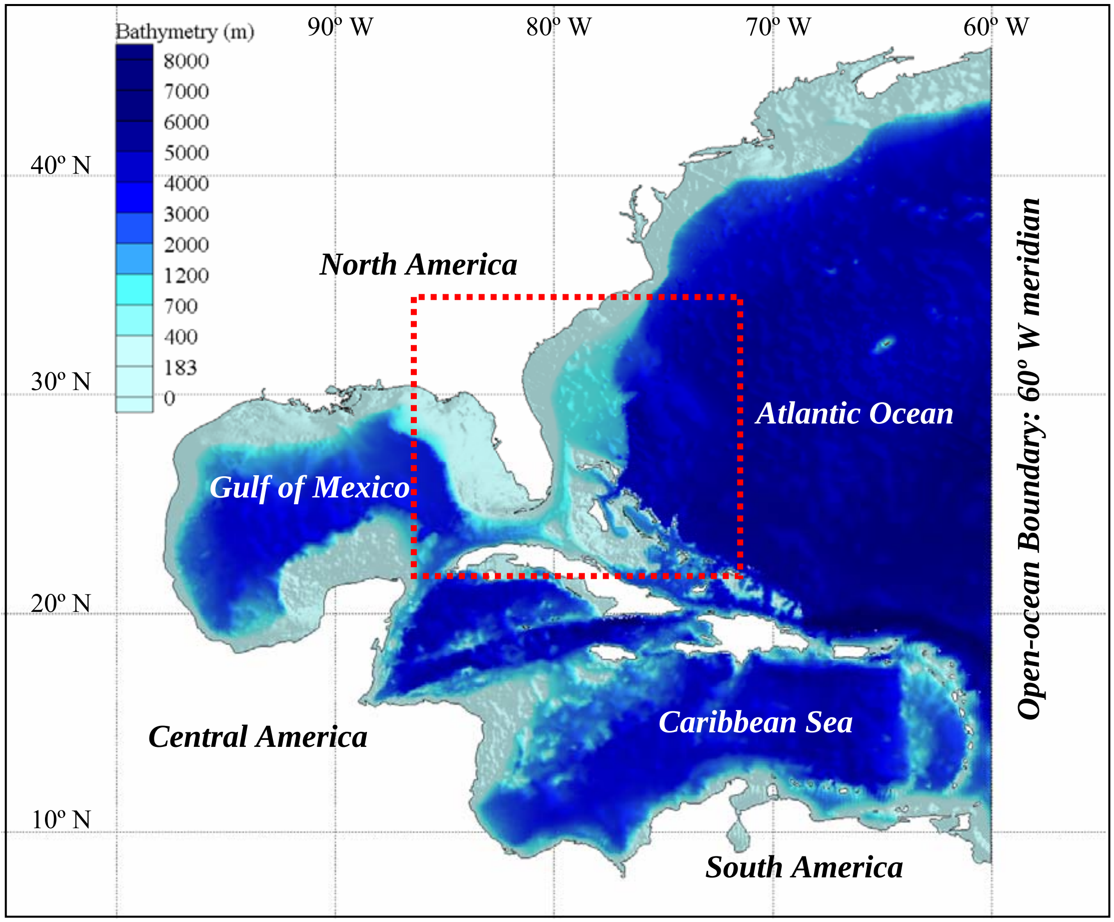

Figure 3-1: WNAT model domain with bathymetry (in meters).

[§] The continental shelf is conventionally defined as being that part of the ocean floor above a depth of 100 fathoms (600 ft or 182.88 m) (Runcorn 1967). Alternatively, the continental shelf is conceived of as having a gentle slope (about 1º) whereas the continental slope is conceived of as having a slope of 3º to 6º (Bates 1980).

area of Glace Bay, Nova Scotia, Canada to the vicinity of Corocora Island in eastern Venezuela and is situated almost entirely in the deep ocean. The area of the WNAT model domain is quite large, covering an area of approximately 8.347×10^6 km^2. Due to the vast size of the WNAT model domain, with deep ocean regions accounting for more than three quarters of the area and the remaining portions consisting of shallow coastal shelf seas, an unstructured, finite element mesh is recommended for application towards producing sufficient tidal circulation predictions.

Figure 3-1 shows the WNAT model domain with bathymetric contours, labeled in meters. It illustrates the deepest regions of the model domain, as located on the north side of Puerto Rico (Puerto Rico Trench) with depths reaching roughly 8,000 meters. Much of the coastlines surrounding the deep ocean basins employ bathymetric depths of zero. In deeper regions, flow behavior is generally linear with minimal gradients of change. However, flow behavior becomes nonlinear in shallow water areas as the tidal wave interacts with the complicated shorelines, variable bottom topography, and itself.

Figure 3-2 represents bathymetry corresponding to the inset region of Figure 3-1. Some important physical features that influence tidal flow are: the Bahamas Bank region around Andros Island, the continental shelf break at near the 183 meter contour, and the edge of Blake's Escarpment at near the 1200 meter contour, all of which are located roughly to the east of Florida. The minimum distance from the mainland shoreline to the continental shelf break is roughly 10 km around Lake Worth Pier, Atlantic Ocean, FL. In the same way, the maximum distance is approximately 150 km around Fernandina Beach, Amelia River, FL. The area of the continental shelf is about 110,000 km^2. The minimum distance from the mainland shoreline to the edge of Blake's Escarpment is roughly 100 km around Sea Level, Core Sound, NC. The maximum distance is approximately 400 km around Fernandina Beach, Amelia River, FL. The area of Blake's Escarpment is about 190,000 km^2.

The area between the mainland shoreline and the continental shelf break is characterized by relatively shallow water regions. Since, in general, shallower water has higher localized wave number content than deeper water, higher mesh resolution is required in these shallow water regions. Furthermore, it has been shown that the computed response is highly sensitive to grid resolution in regions with steep bathymetric gradients (Hagen, 1998; Hagen et al., 2004).

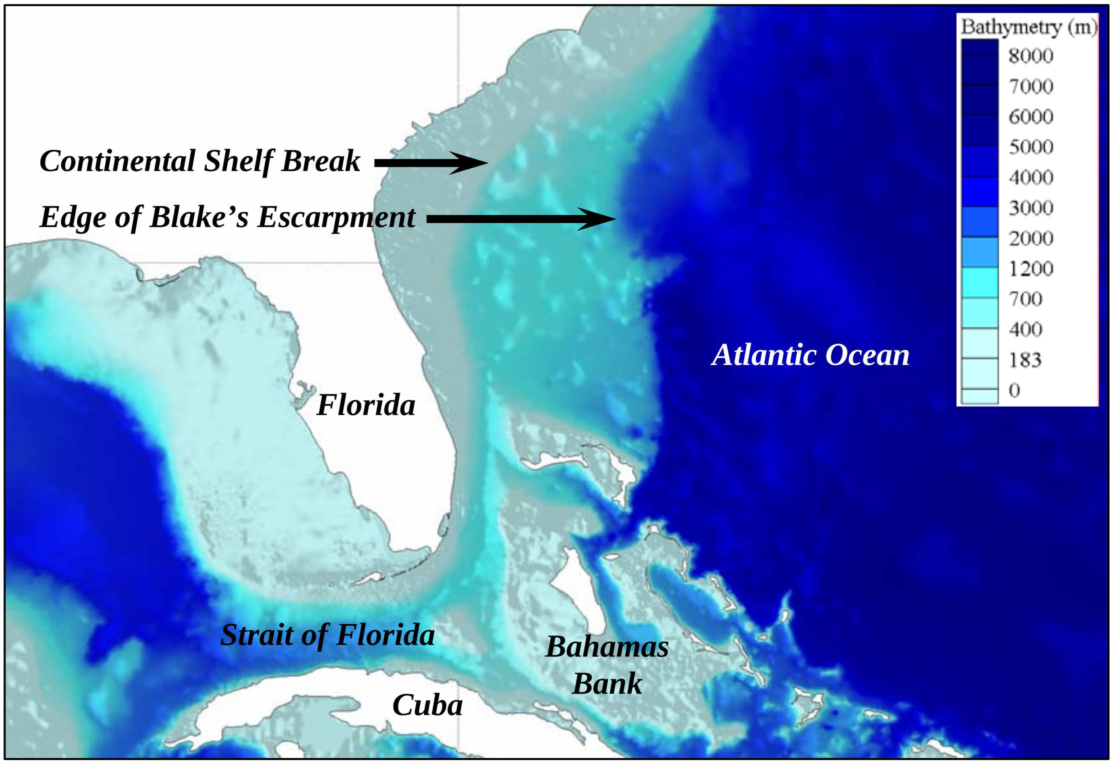

Figure 3-2: Bathymetry for the Inset (red, dotted line) Region of Figure 3-1.

CHAPTER 4

FINITE ELEMENT MESH DEVELOPMENT

Finite element mesh development techniques are described in this chapter. After the standard computational grid (333K finite element mesh) is explained, details are provided on the construction of three computationally efficient computational grids (95K, 60K and 53K finite element meshes). The LTEA technique is applied to develop these computationally efficient finite element meshes.

4.1 Standard Computational Grid (333K Finite Element Mesh)

Previous research by Parrish (2001) and Mukai et al. (2002) have resulted in the development of a highly resolved computational grid, designated as the 333K finite element mesh, for astronomical tidal computations in the WNAT model domain (Figure 4-1). The name of the finite element mesh corresponds to the total number of computational nodes. The standard finite element mesh contains 332,582 computational nodes and 647,018 triangular elements, providing a very detailed description of the physical system with node spacing ranging from 1.0 to 25 km. Minimum node spacing (smallest triangular elements) exists in the area surrounding Andros Island, the west side of the Port of Spain, and the continental shelf located in the west side of the Florida Peninsula. Maximum node spacing (largest triangular elements) is present in the Atlantic Ocean. In addition, the average node spacing for the boundary is approximately 1.0 km, and the total number of boundary nodes is 18,679. Figure 4-5 provides contours of the node spacing for this finite element mesh, labeled in kilometers. Needless to say, the node spacing is considerably small within the entire domain.

The 333K finite element mesh simulation yielded accurate results at almost every single tidal station as shown by comparisons, between historical data and simulated output (Parrish, 2001; Parrish et al., 2002); however, it is not computationally efficient. The computational time to run one complete 90-day simulation with a twelve-node cluster of 600 MHz processors running in parallel was approximately 13.3 days. A real-time forecast of the coastal hydrodynamics due to a storm event requires this computational time to be drastically reduced. Hence, more computationally efficient finite element meshes are developed as follows. It should be noted that the 333K mesh is utilized to generate the following three coarser meshes by employing the LTEA technique.

4.2 Development of Large-Scale Computational Efficient Finite Element Meshes

Previously, Hagen et al. (2004) applied an LTEA technique to the expansive WNAT model domain (see Figures 3-1 and 3-2). The goal of the LTEA procedure is to relax a high resolution mesh in areas where truncation errors are low, e.g. in the Atlantic Ocean, in order to reduce computational time, thereby driving the truncation error for the new mesh to a more constant value throughout the entire domain. The LTEA technique was performed using results from an application of the 333K finite element mesh.

The LTEA procedure creates a spatial dataset of relative element size guidelines for the WNAT model domain. Although the LTEA by Hagen et al. (2004) resulted in elemental sizing requirements that range from 1.0 to 1120 km, these nodes spacing guidelines are scalable. Thus, the elemental sizing requirements can ultimately be interpreted as the lower the value, the smaller the element should be. In addition, since the LTEA procedure does not produce values on or near boundaries, it does not include node spacing guidelines along the coastline; see Hagen (1998) for further information regarding this boundary issue.

It should be noted that the 333K finite element mesh was a product of years of painstaking efforts to adequately represent the complicated geometries found within the WNAT model domain (Hagen et al., 2004). Hand placement of nodes determined geometric element sizes and interior nodal density. While consuming an enormous amount of time, this method does little to prevent over resolving areas of the domain. The research presented herein presumes that many of the nodes created are actually redundant at best and restrictive at worst.

In order to generate a finite element mesh consisting of a minimum number of required computational nodes, the devised algorithm makes use of the LTEA-generated relative element size guidelines, in combination with a mesh paving algorithm (Lohner et. al., 1996; George, et. al., 1994; George et. al., 1991) created to take advantage of such spatially varying node spacing requirements (Sullivan, et. al., 1997; Johnston, et. al., 1992). The method, which has been implemented into the two-dimensional Surface-water Modeling System (SMS) (Zundel, 2005), provides the option of allowing the user to specify the mesh resolution along the coastline, therefore, permitting computational grids of various mesh resolutions to include similar boundary curve specifications. A minimum and maximum edge length and a maximum size transition from one element to its neighbor round out the required input options.

The algorithm (Fugal, 2000) distributes nodes throughout the interior of the domain using a paving approach. Starting with the domain boundary, which consists of the coastline, islands, and the open-ocean edge at 60º W meridian, the approach generates an offset boundary inside the domain by creating near-equilateral triangles for each segment of the boundary and connecting these sequentially to form a new layer. After trimming this new layer to eliminate inverted areas, the nodes are redistributed along the new layer boundary to conform to the underlying elemental sizing guidelines. This prepares for the next iteration of offsetting. The process is repeated, working from the most recent layer definition, until the entire domain is paved. At this point in the process, the nodes are connected to form a mesh while relaxing (Canann, 1996; Howlett, 2005) their locations to more closely approximate the LTEA-generated node spacing requirements.

In many portions of the WNAT model domain, the target node spacing recommended by the LTEA changes very quickly. This is especially true along the continental shelf, and in areas around the islands of the Caribbean Sea. Applying the paving process described above to these values to generate a mesh results in elements that change in size very quickly and therefore have a very poor shape factor. Limitations in the distance between areas desiring low resolution and areas desiring high resolution preclude the possibility of honoring the needs of both areas. In this situation, the algorithm gives precedence to the area requesting higher resolution. This assures that adequate resolution is provided to represent the complexities contained within the numerical solution. In order to communicate this precedence to the paving algorithm, the spatial function values were adjusted using a gradient smoothing process. Starting from the point with the smallest recommended element size, the neighboring point's node spacing requirement is adjusted based on its distance from the initial point and a specified area transition. In this case, a transition is specified such that no element has an area smaller than 50% (or larger than 200%) of it neighbor's area. This process ensures that the elemental sizing guidelines vary gradually enough to be honored throughout the entire domain. Note that the gradient smoothing process (Howlett, 2005) does not adjust the minimum node spacing (areas of highest resolution). In this case, the maximum extremes have been reduced. Given more space to transition, higher relative element sizes can be reached.

The LTEA-generated spatial function values are obviously not well suited for direct use as element sizes. The approach used in this research includes scaling these values to bring the minimum up to approximately the finest resolution desired away from the domain boundary. This study includes three variations of an unstructured, finite element mesh generated using the methodology described above. Each utilizes the bathymetric definition of the fine resolution mesh (Figure 4-1) with nearly identical boundary specifications. In the first pass at optimizing the mesh, a scale factor of 0.29 was applied to the LTEA data. This represents a minimum target resolution of around 290 m varying up to about 320 km. However, for the finite element mesh developed, a maximum edge length of 120 km was imposed to limit transitioning from deep to shallow water elements. From these scaled elemental sizing guidelines and a coastal boundary definition with approximately 6.0 km node spacing, the algorithm generated a mesh consisting of 95,062 computational points and 182,941 triangular elements (Figure 4-2). This computational grid is identified as the 95K finite element mesh. Figure 4-6 represents contours of node spacing corresponding to this finite element mesh. There are limited locations where the color range is red (approximately 0 to 20 km): near the boundary, around islands, the continental shelf, and the edge of Blake's Escarpment. Particularly, the smallest node spacing exists around Andros Island, the continental shelf, and the edge of Blake's Escarpment since there are the highest localized truncation error points. The minimum node spacing around these locations is approximately 500 m. Contrary, a green zone, which represents approximately 120 km node spacing, exists in the Atlantic Ocean, the Gulf of Mexico, and Caribbean Sea. In fact, these locations have much larger node spacing than the 333K finite element mesh.

The second pass mesh utilized a scale factor of 0.50 and a boundary spacing of approximately 5 km. This represents a minimum target resolution of around 500 m varying up to about 560 km. A finite element mesh consisting of 60,487 computational nodes and 108,987 triangular elements (Figure 4-3) resulted from these input parameters. This computational grid is named the 60K finite element mesh. Figure 4-7 shows contours of the node spacing associated with the 60K finite element mesh. This figure describes the continental shelf and the edge of Blake's Escarpment clearly with color range of red (approximately 0 to 20 km). In fact, these locations have high truncation error and require smaller node spacing, near 500 m. There is a particular feature in the Atlantic Ocean where the maximum node spacing is limited to approximately 185 km, which is illustrated in blue. This is the largest node spacing out of the four variations of the unstructured, finite element mesh, and it has over seven times as the maximum node spacing of the 333K finite element mesh.

To evaluate the relative importance of interior refinement verses boundary resolution, the final pass mesh utilized the scale factor from the second pass (0.50), but used the coarser boundary spacing of the first pass (6 km). This represents a minimum target resolution of around 500 m varying up to about 560 km. However, this finite element mesh applies a maximum edge length of 160 km. This produced a finite element mesh consisting of 52,774 computational nodes and 98,365 triangular elements, as illustrated in Figure 4-4. This computational grid is entitled the 53K finite element mesh. Figure 4-8 displays contours of node spacing corresponding to the 53K finite element mesh. This finite element mesh also has minimum node spacing (500 m) around Andros Island, the continental shelf, and the edge of Blake's Escarpment. A major benefit of this finite element mesh includes the smoothness of the element transitions found in the interior of the domain (e.g., within the Atlantic Ocean, as compared to the 95K and 60K finite element meshes). In fact, we assume that the 53K finite element mesh leads to the best computational results because of this opportunity.

In order to verify the compliance of the finite element mesh to the underlying spatial function, several values are computed at each node. First, the target spatial function values are interpolated to the node locations. Second, the grid spacing is computed at each node as the average of the lengths of the edges connected to the respective node. Third, these two values are differenced resulting in an absolute node spacing error. For this mesh, the average error was 457 meters. Finally, to compute a percentage error, the absolute node spacing error was divided by the target element sizes. Figure 4-9 shows the contours of the computed percentage errors. For the coarsest mesh, the average percentage error was 5.03% with the significant mismatches occurring in the areas of largest recommended element sizes.

As stated above, the algorithm requires the user to define the domain limits, and then includes the option of forcing the user specified boundary spacing into the final finite element mesh. We utilized this option for this work to ensure consistent boundary forcing of the tidal elevations for all of the applied finite element meshes. However, in this type of situation, particular note should be taken of the transition from the user specified boundary to the automatically generated node spacing requirements of the interior. A gradient smoothing process is applied to the spatial function to enforce a smooth size transition. This modification also adjusts the desired spacing of boundary nodes, but forced boundary spacing overrides this spatial function. Therefore, a desired interior node spacing that includes significant differences (smaller or larger) from the specified boundary spacing results in less favorable element size transitions. For the three computational grids utilized in this study, this concern applies mostly to the 95K finite element mesh. This finite element mesh enforces a coarse boundary resolution, but utilizes a high number of interior nodes. Therefore, the resulting size transition is not optimal.

All computational grids resolve the boundary with approximately the same curve. The 333K finite element mesh employs 18,679 boundary nodes, including all islands and the mainland. The

95K and 53K finite element meshes use identical boundaries with 7,111 island and mainland boundary nodes. The 60K finite element mesh uses 11,915 nodes to represent the island and mainland boundaries.

Figures 4-10 and 4-11 display the bathymetry as represented by each of the four finite element meshes of Figures 4-1 through 4-4. Clearly the 95K, 60K, and 53K finite element meshes smooth out the bathymetric features as represented by the 333K finite element mesh. More topographic features of the 333K finite element mesh are contained in the 95K finite element mesh than are retained in the 60K or 53K finite element meshes. The 53K finite element mesh provides a higher resolution of the 333K interior than does the 60K finite element mesh, since the 60K finite element mesh employs 4,804 more island and mainland boundary nodes, while having only 7,713 more total nodes than the 53K finite element mesh. Distinguishable bathymetric features are particularly illuminated in the Caribbean Sea and deep Atlantic Ocean areas.

Table 4-1: Details for four finite element meshes.

	333K	95K	60K	53K
Model domain surface area	8.347×10^6 km^2			
Number of computational nodes	332,582	95,062	60,487	52,774
Number of triangular elements	647,018	182,941	108,987	98,365
Scaling factor for LTEA data	N/A	0.29	0.50	0.50
Minimum target resolution	N/A	0.29 km	0.50 km	0.50 km
Maximum target resolution	N/A	320 km	560 km	560 km
Minimum node spacing	1.0 km	0.5 km	0.5 km	0.5 km
Maximum node spacing	25 km	120 km	185 km	160 km
Average boundary spacing	1.0 km	6.0 km	5.0 km	6.0 km
Computational boundary nodes	18,679	7,111	11,915	7,111

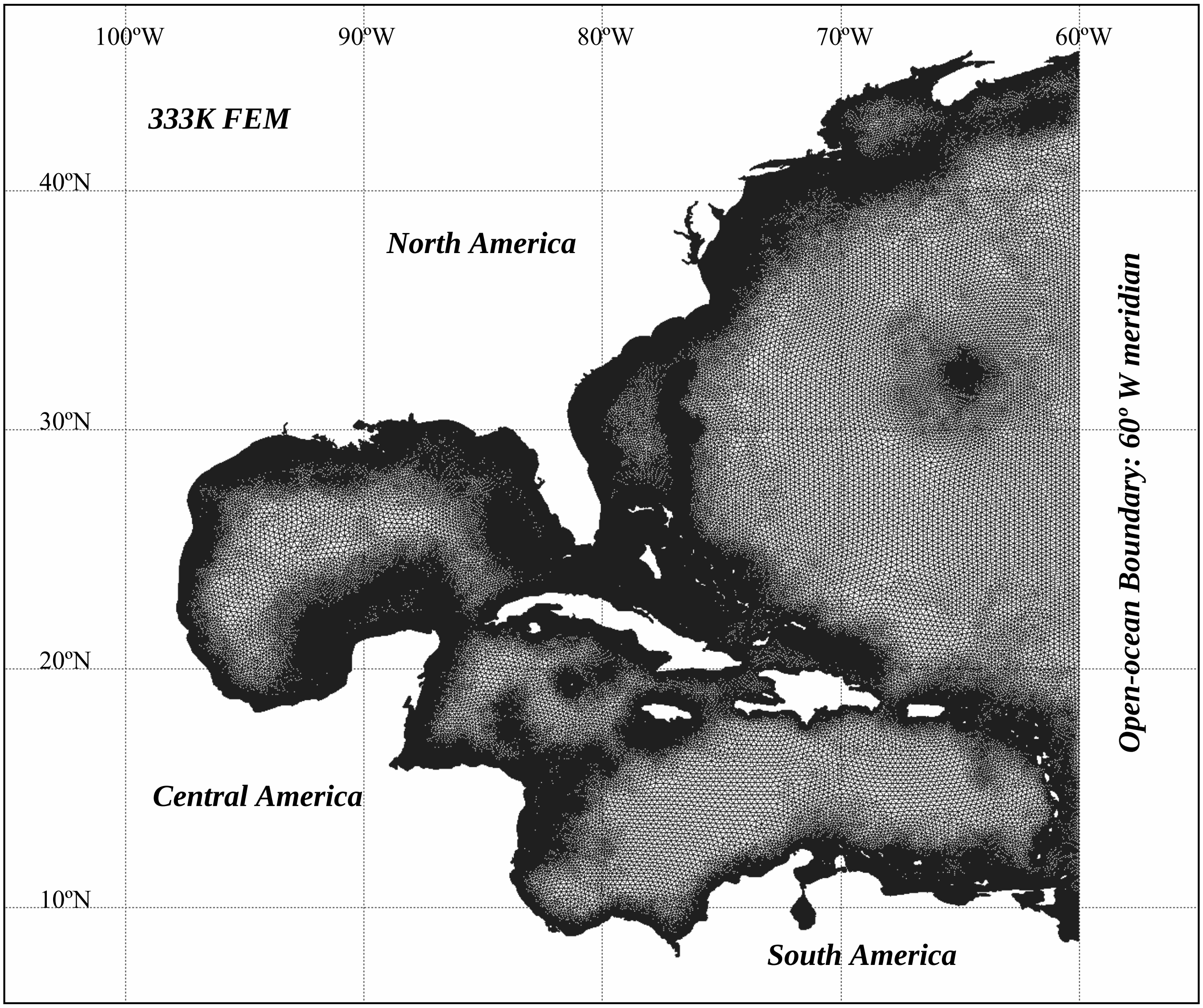

Figure 4-1: The unstructured, 333K finite element mesh for the WNAT model domain.

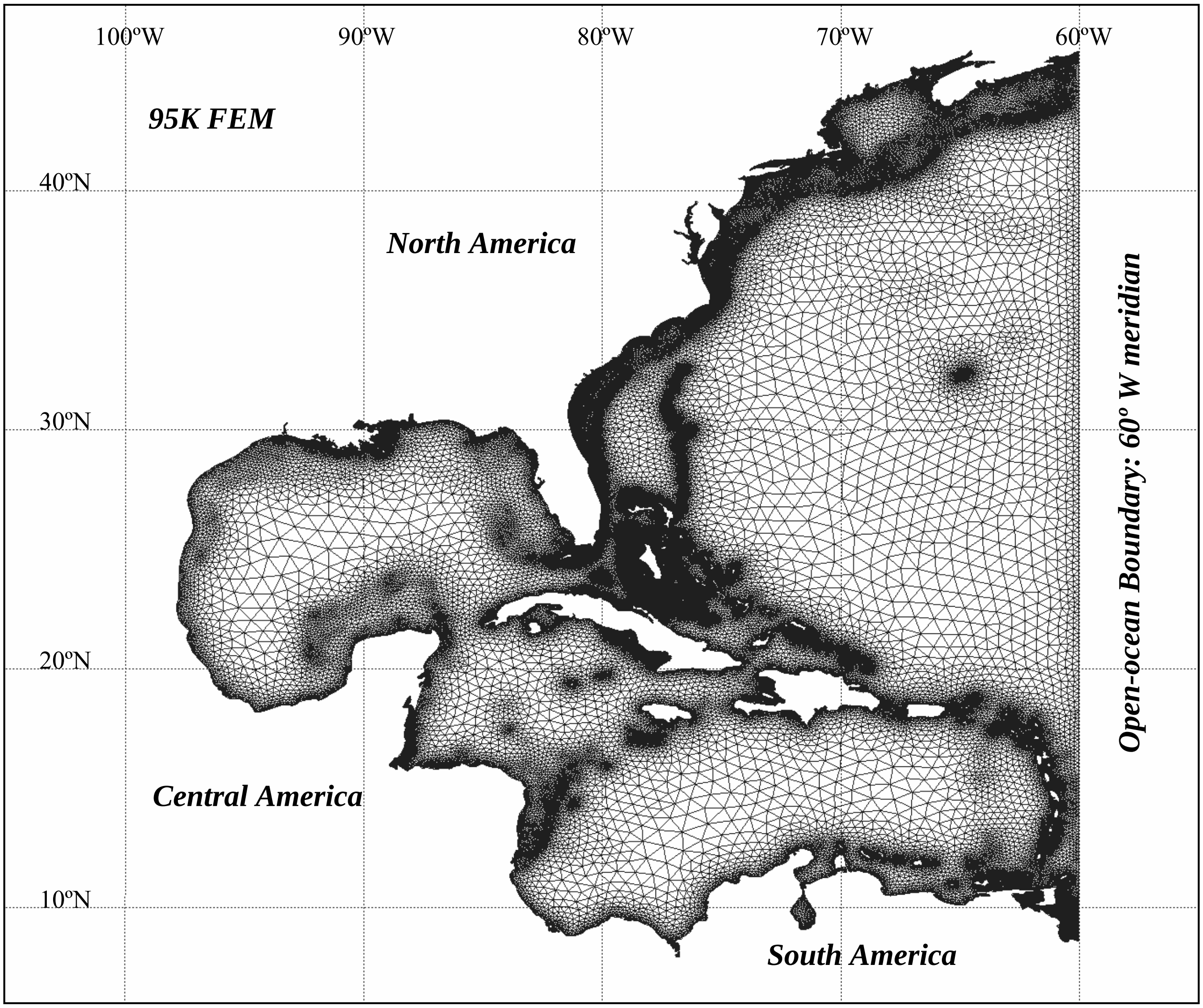

Figure 4-2: The unstructured, 95K finite element mesh for the WNAT model domain.

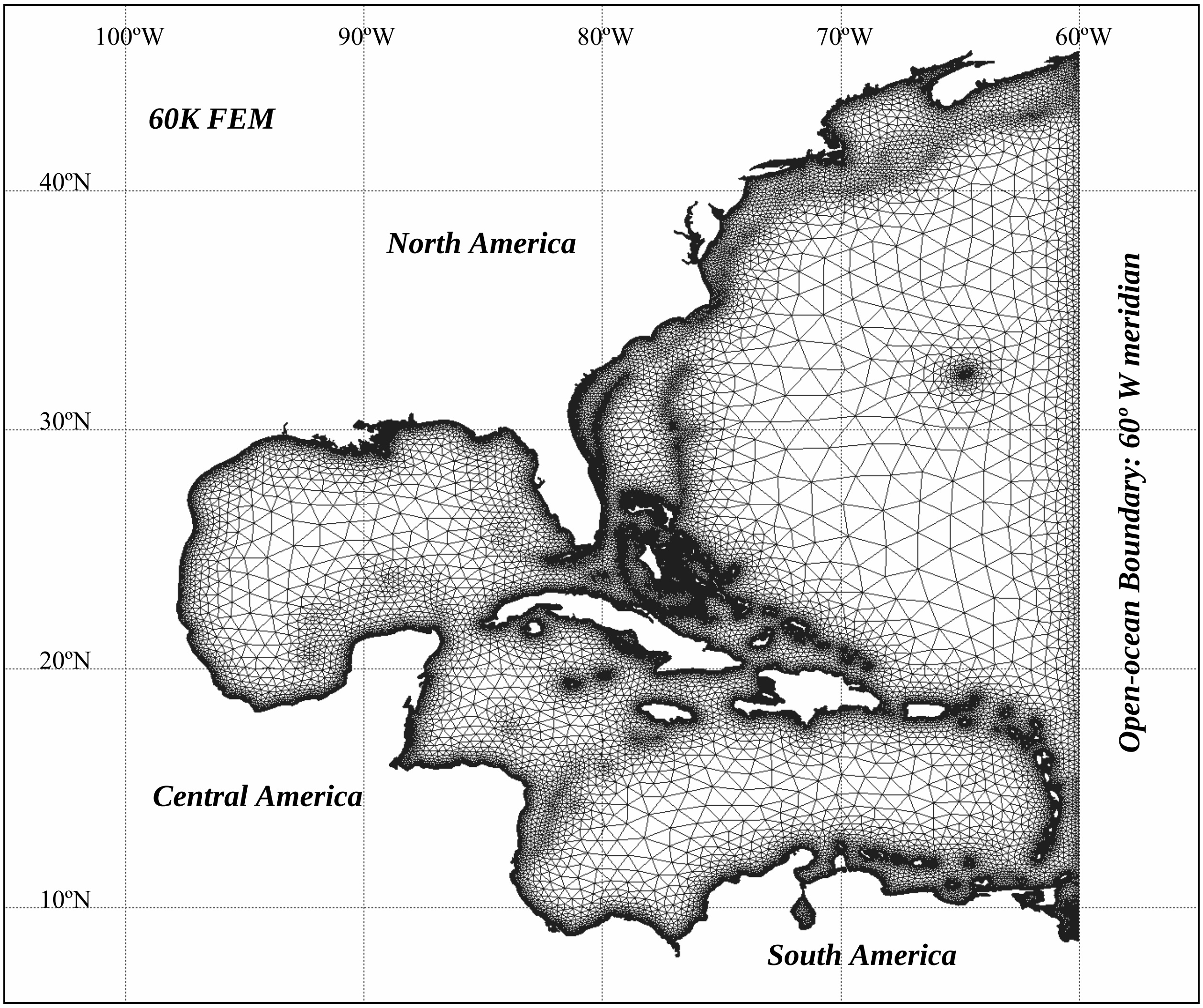

Figure 4-3: The unstructured, 60K finite element mesh for the WNAT model domain.

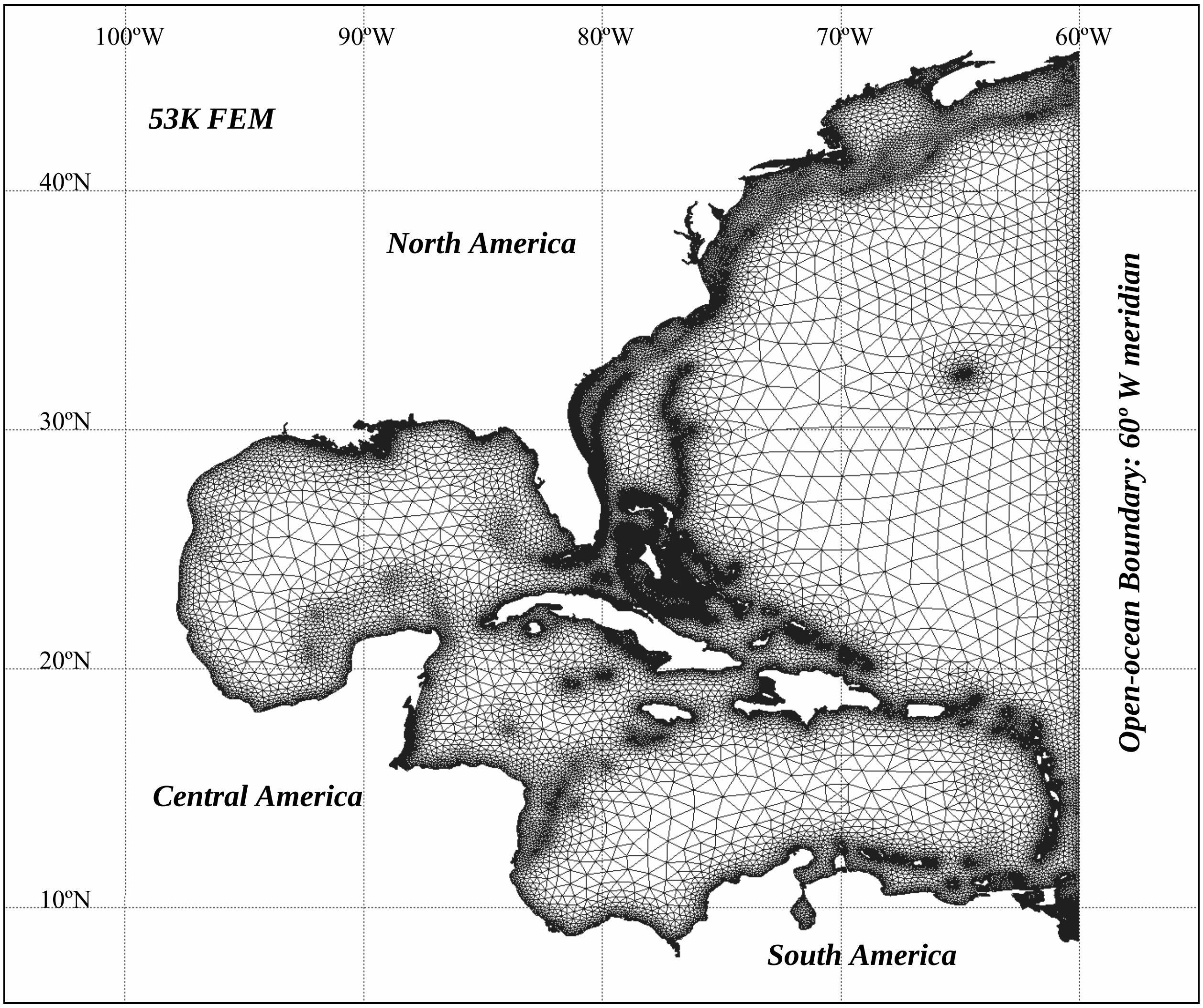

Figure 4-4: The unstructured, 53K finite element mesh for the WNAT model domain.

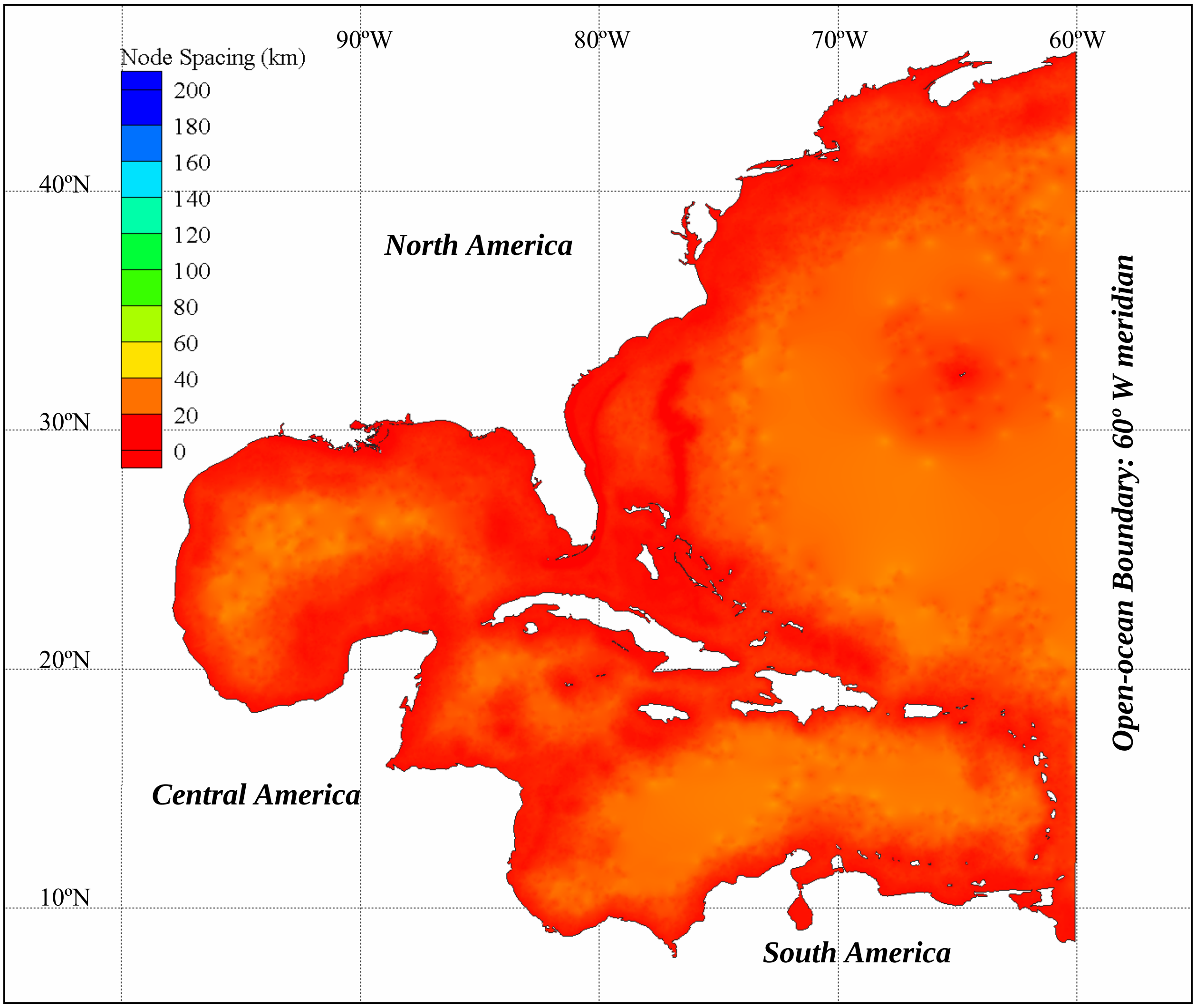

Figure 4-5: Contours of node spacing for the 333K finite element mesh.

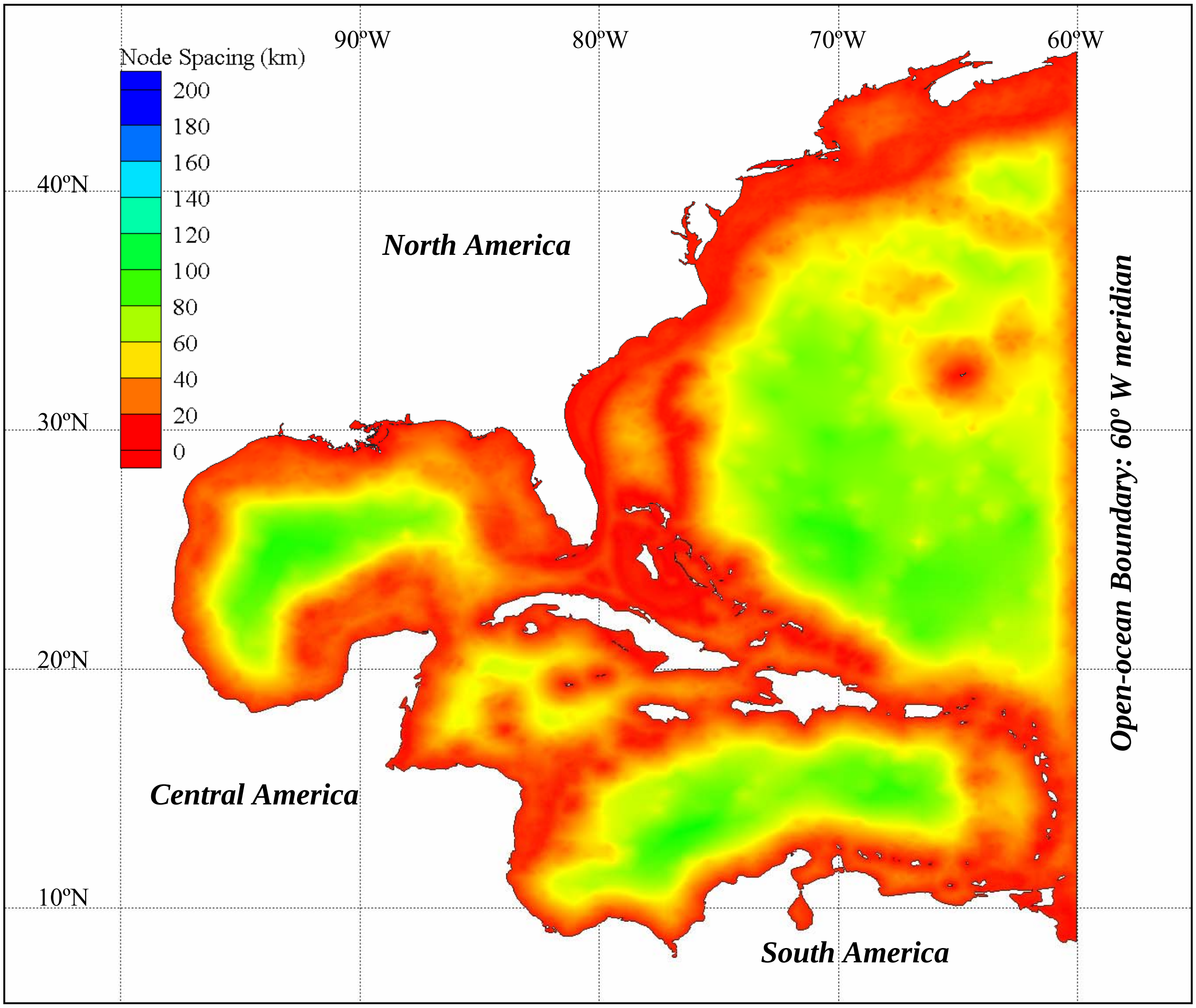

Figure 4-6: Contours of node spacing for the 95K finite element mesh.

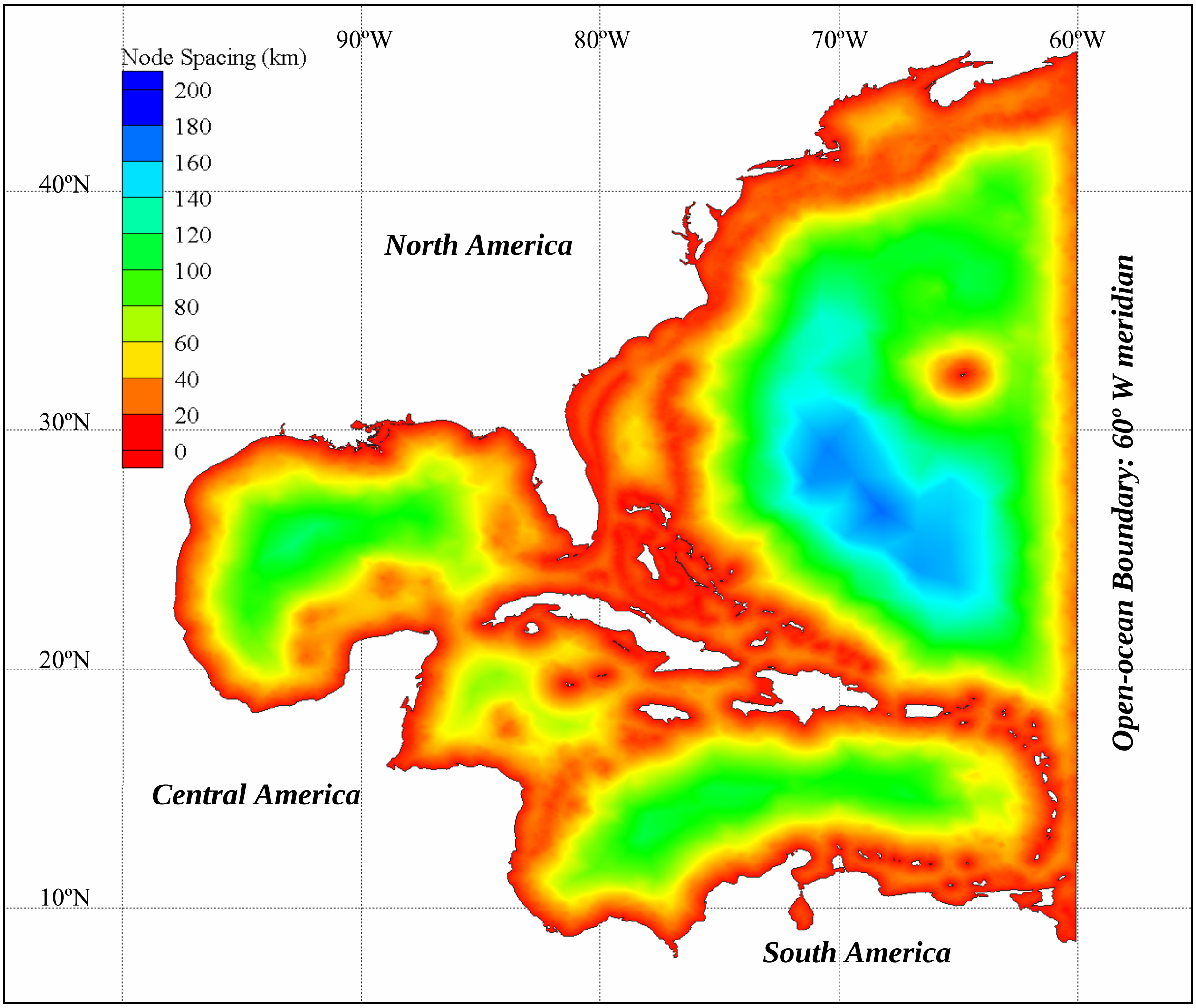

Figure 4-7: Contours of node spacing for the 60K finite element mesh.

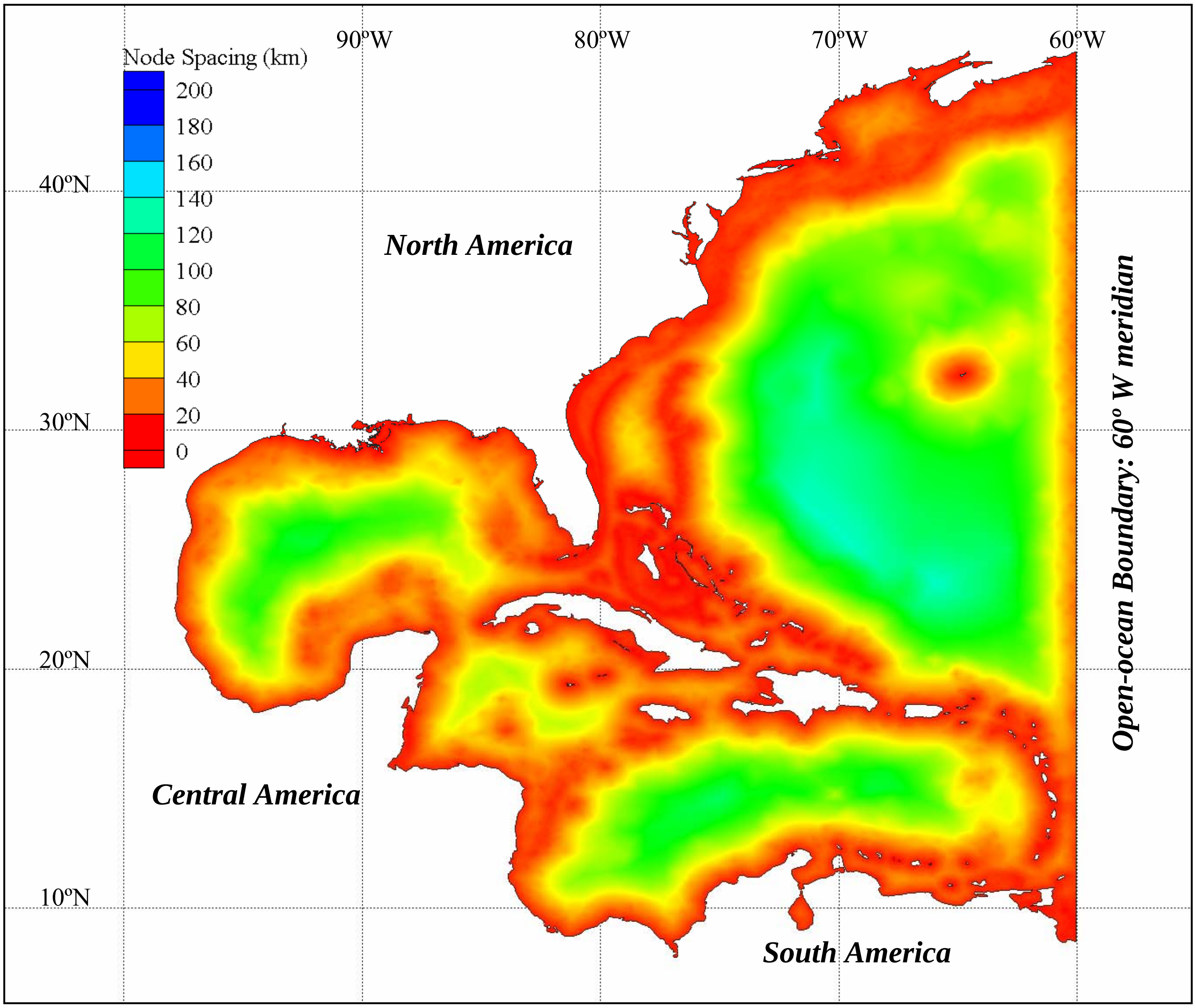

Figure 4-8: Contours of node spacing for the 53K finite element mesh.

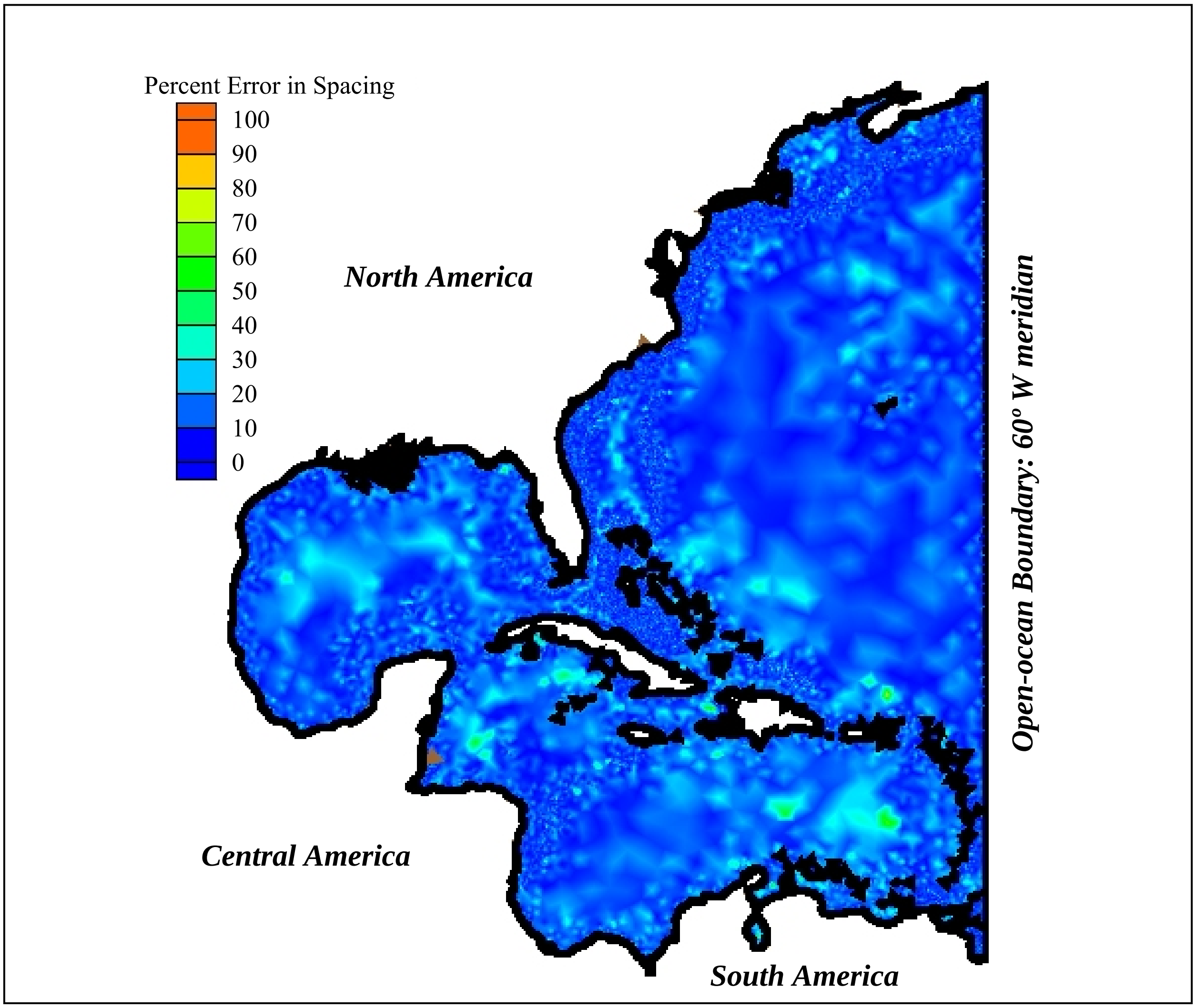

Figure 4-9: Contours of the computed percentage errors in grid spacing relative to the target element sizes for the 53K finite element mesh.

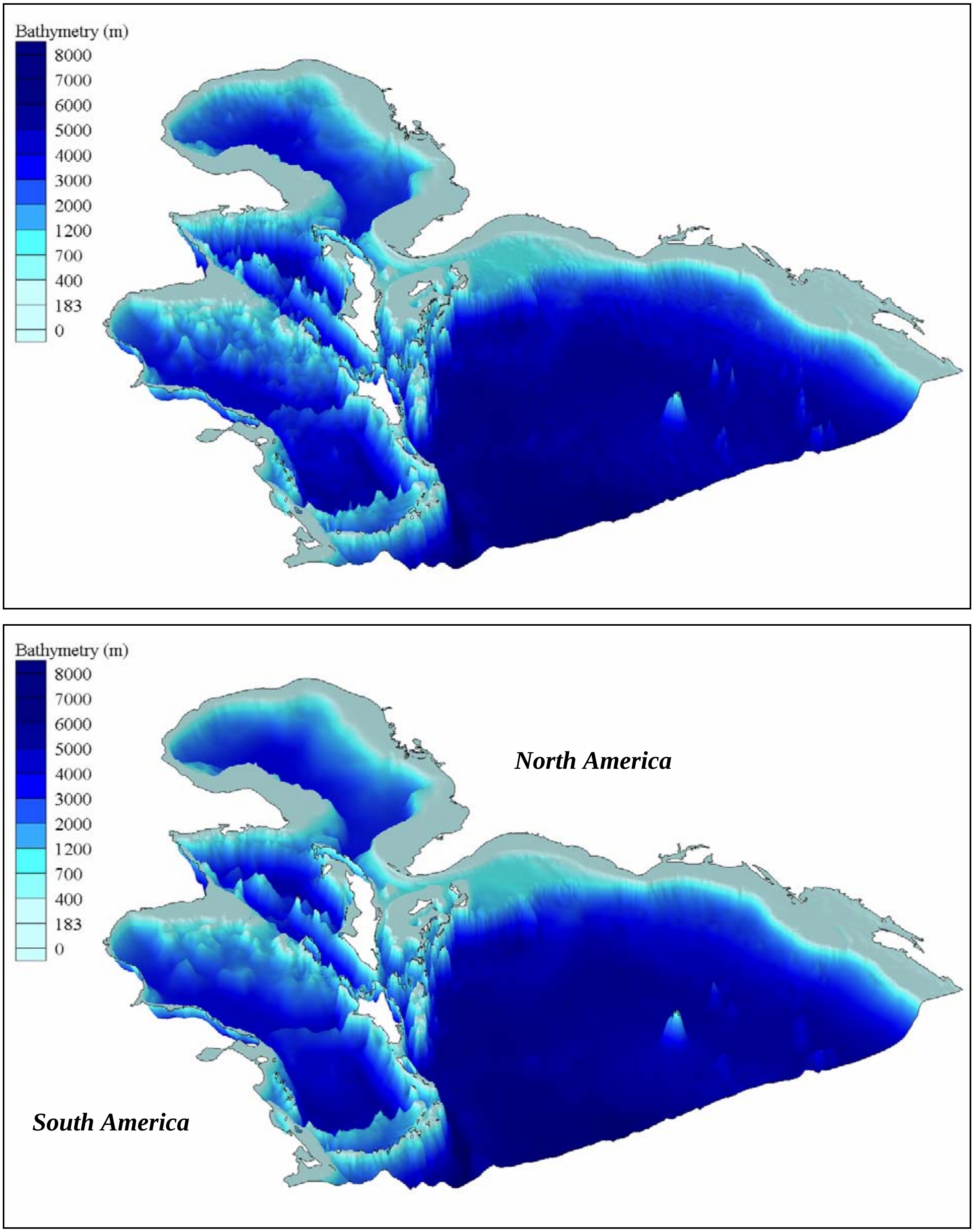

Figure 4-10: 3-D bathymetric plots of the 333K (top) and 95K (bottom) finite element meshes.

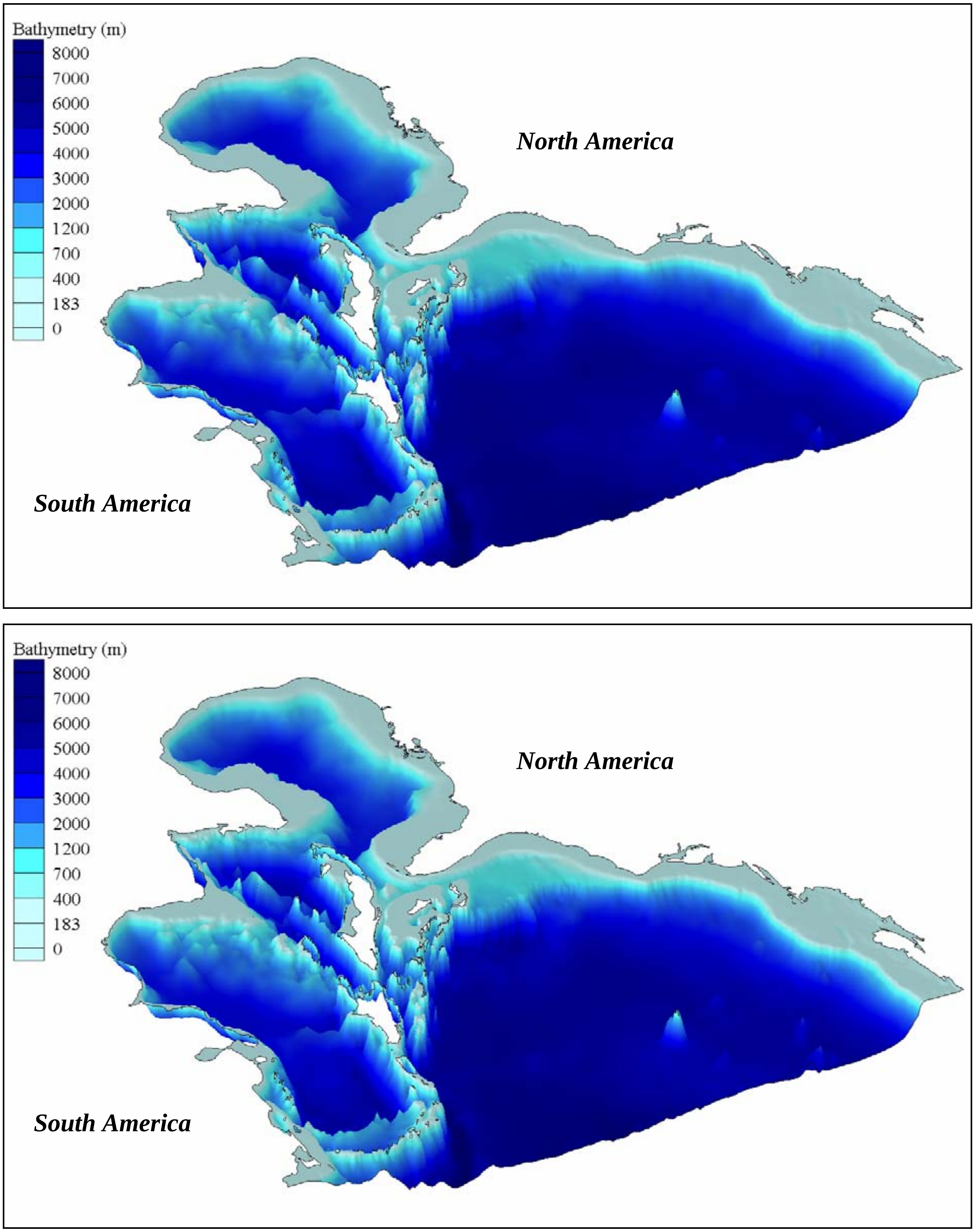

Figure 4-11: 3-D bathymetric plots of the 60K (top) and 53K (bottom) finite element meshes.

CHAPTER 5

HISTORICAL TIDAL STATIONS

Chapter 5 presents historical data collection, identification of relevant tidal stations, and explanation of the historical tidal constituents that are used in this study. Initially, 203 historical tidal stations are obtained within or near the boundaries of the WNAT model domain in order to verify simulation output. After they are examined, 150 historical tidal stations are deemed appropriate for use in assessing the accuracy of the simulation results.

5.1 Historical Data Collection

In order to verify the simulation results, 203 tidal stations within or near the boundaries of the WNAT model domain are examined. Each tidal station is represented by a tidal station name, its geographic location, and the corresponding overseeing agency. (Detailed information regarding these 203 tidal stations can be found in Appendix C.) Table 5-1 presents three tidal stations as an example.

Table 5-1: Example tidal stations.

Station number	Tidal station name	Longitude [decimal deg.]	Latitude [decimal deg.]	Overseeing agency
2	630 St. John, New Brunswick	66.05000 W.	45.26666 N.	IHO
37	8570283 OCEAN CITY INLET , MD	75.09167 W.	38.32833 N.	NOS
154	14 Ciudad Madero, Mexico	97.85833 W.	22.21666 N.	GOM

The first column shows the tidal station number. The second column represents the tidal station name, which is decided by overseeing agency. The third and fourth columns provide the geographical coordinates corresponding to the location of the tidal station. The final column corresponds to the overseeing agency. It should be noted IHO stands for the International Hydrographic Organization (http://www.iho.shom.fr/), NOS indicates the National Ocean Service (http://www.co-ops.nos.noaa.gov/data_res.html), and GOM comes from research of Reid et al. (1981).

5.2 Elimination of Irrelevant Tidal Stations

The 203 tidal stations are screened according to four conditions. The first condition is that the tidal station is located within a bay or inlet that is not described by one or more of the four finite element meshes used in this study. A tidal station, which is located in or near the river and is influenced by freshwater flow, i.e., there exists a tide and freshwater flow interaction, constitutes a second rejection condition. The third condition that warrants the elimination of a particular tidal station is hydraulic connectivity, e.g. the tidal station is located within a canal that is not included in one or more of the four finite element meshes used in this study. Finally, if an element that contained a tidal station went dry during the harmonic analysis portion of the simulation, then that tidal station is excluded. Figure 5-1 displays the locations of the final 150 historical tidal stations that are applied in the error analysis presented herein. It should be noted the first and third conditions can be fixed by applying many computational nodes (by increasing the local nodal density) in order to describe more specific geographic features. However, it is not required in this research because this study is focused on the large-scale tidal model domain, not local areas of interest. Therefore, tidal stations meeting these criteria are eliminated.

Two organizations account for the 150 historical tidal stations employed in this study. The IHO provides harmonic data for 44 tidal stations. The remaining 106 tidal stations are overseen by the NOS. For each tidal station, the respective organization provides historical harmonic data for multiple tidal constituents. Figure 5-1 shows that the 150 stations provide good coverage throughout the WNAT model domain and will permit for an extensive analysis of mesh performance by comparing model output from each of the four meshes to a resynthesis of the historical tidal constituents at each station.

Figure 5-2 displays the 53 eliminated tidal stations, with Figures 5-3 through 5-6 showing four example tidal stations. The location of the first example is Sea Level, Core Sound, NC (Figure 5-3). The reason for its elimination is that the station is situated inside of the inlet (first condition). The second example is Chesapeake City, MD (Figure 5-4). It is easy to recognize that this station is located in the river and may have a strong freshwater influence (second condition). The third location is Buzzards Bay (RR Bridge), Cape Cod Canal, MA (Figure 5-5). The reason for its elimination is that the station is positioned in the canal (third condition). The last example is Cat Island, MS (Figure 5-5). The surrounding region is very shallow and every simulation was drying out at this location. Hence, this tidal station is eliminated (fourth condition).

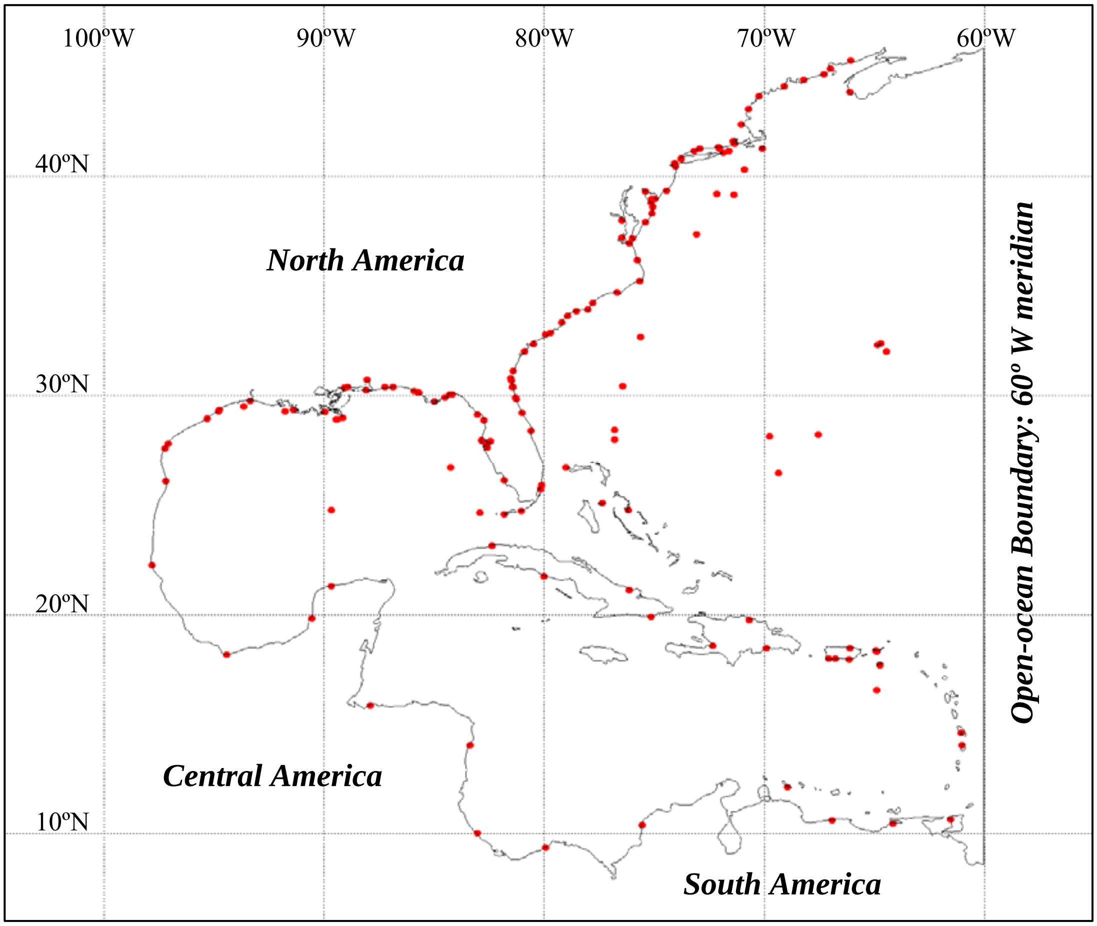

Figure 5-1: WNAT tidal model domain with 150 tidal stations.

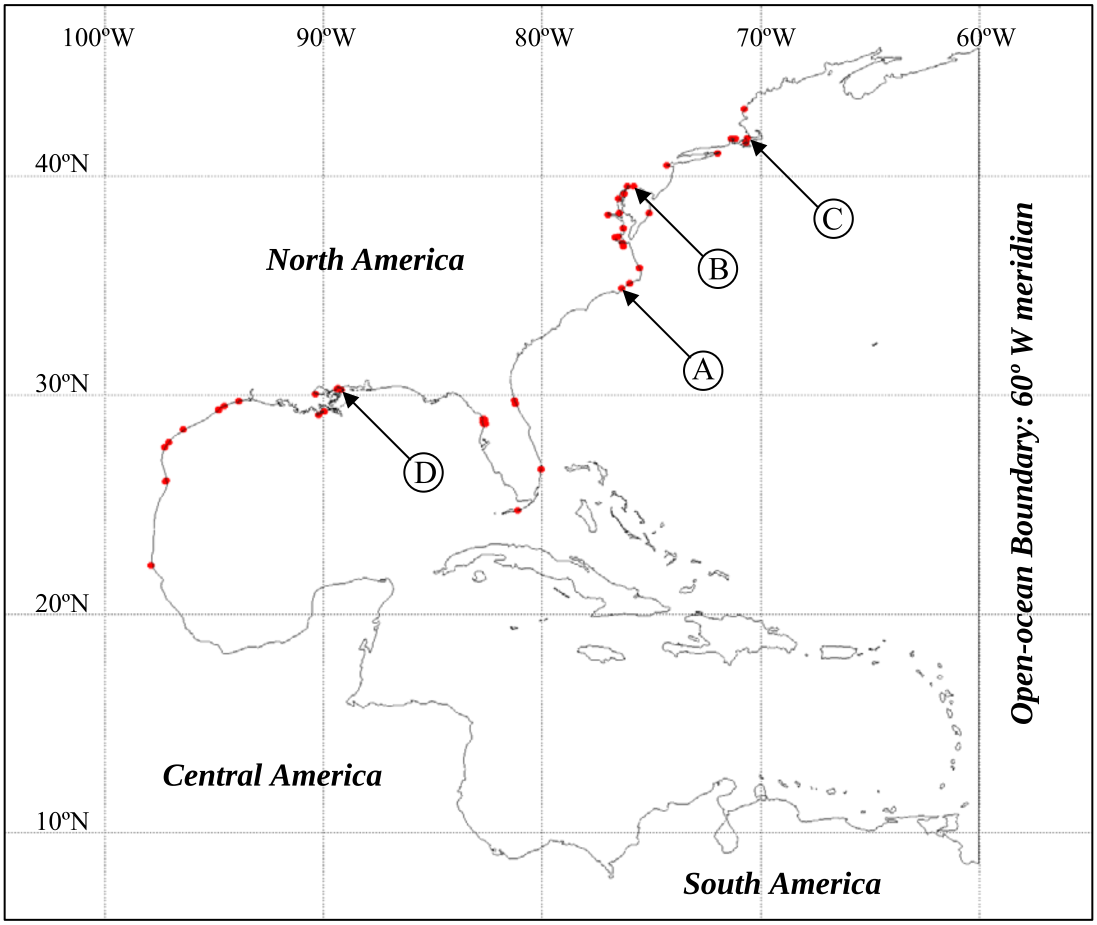

Figure 5-2: WNAT tidal model domain with eliminated 53 tidal stations.

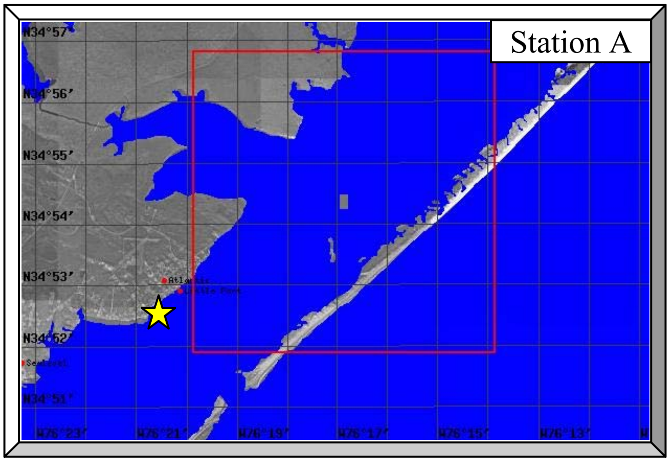

Sea Level, Core Sound, NC	
Continuous station number	58
Overseeing agency	NOS
Longitude [decimal deg.]	76.34 W.
Latitude [decimal deg.]	34.88 N.
Reason for elimination	Inside of the inlet

Figure 5-3: Example tidal station for elimination near the Sea level, Core Sound, NC.

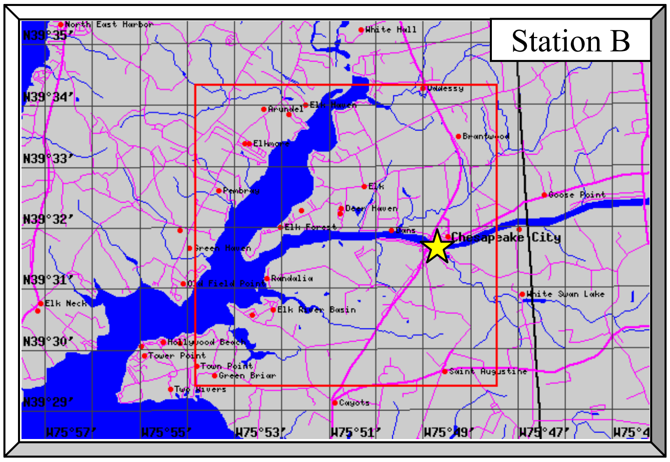

Chesapeake City, MD	
Continuous station number	41
Overseeing agency	NOS
Longitude [decimal deg.]	75.81 W.
Latitude [decimal deg.]	39.53 N.
Reason for elimination	In the river

Figure 5-4: Example tidal station for elimination near the Chesapeake City, MD.

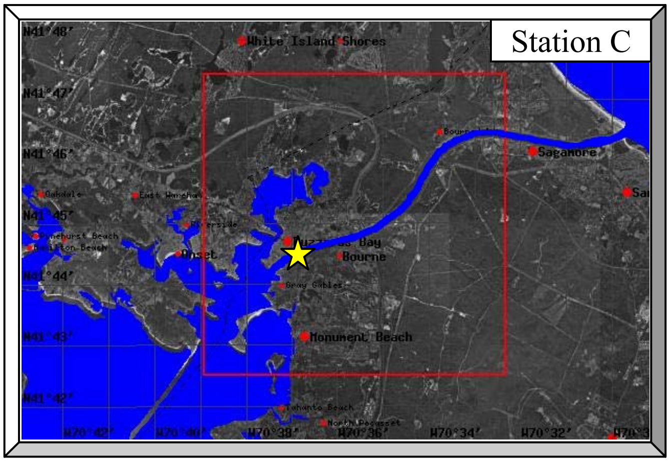

Buzzards Bay (RR Bridge), Cape Cod Canal, MA	
Continuous station number	11
Overseeing agency	NOS
Longitude [decimal deg.]	70.62 W.
Latitude [decimal deg.]	41.74 N.
Reason for elimination	In the canal

Figure 5-5: Example tidal station for elimination
near the Buzzards Bay (RR Bridge), Cape Cod Canal, MA.

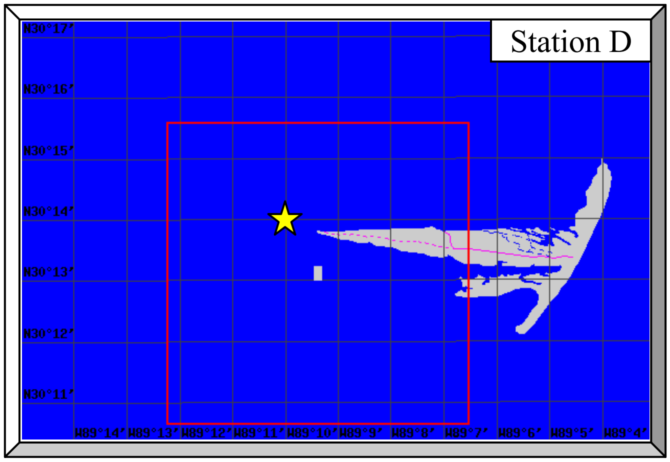

Cat Island, MS	
Continuous station number	126
Overseeing agency	IHO
Longitude [decimal deg.]	89.17 W.
Latitude [decimal deg.]	30.23 N.
Reason for elimination	Drying out

Figure 5-6: Example tidal station for elimination near the Cat Island, MS.

The remaining 49 eliminated tidal stations are shown with their geographic map and other information in Appendix D.

5.3 Historical Tidal Constituents

Historical tidal constituents are employed in the following study. The NOS tidal stations contain a total of thirty-seven historical tidal constituents. The IHO tidal stations, however, have only seven total historical tidal constituents. These constituents are composed of phase (in degrees) and amplitude (in meters) information. Table 5-2 represents information about all of the historical tidal constituents that are applied in this study.

Table 5-2: Historical tidal constituents.

Symbol	Definition	Period [hr]	Frequency [rad / s]
M_2	Principal lunar semidiurnal constituent	12.42	0.000140525704669
S_2	Principal solar semidiurnal constituent	12.00	0.000145444104333

Symbol	Definition	Period [hr]	Frequency [rad / s]
N_2	Larger lunar elliptic semidiurnal constituent	12.66	0.000137861710268
K_1	Lunar diurnal constituent	23.93	0.000072934778604
M_4	Shallow water overtides of principal lunar constituent	6.21	0.000281051409339
O_1	Lunar diurnal constituent	25.82	0.000067596020604
M_6	Shallow water terdiurnal	4.14	0.000421577114008
MK_3	Shallow water terdiurnal	8.18	0.000213365434229
S_4	Shallow water overtides of principal solar constituent	6.00	0.000290888208666
MN_4	Shallow water quarter diurnal constituent	6.27	0.000278361922168
NU_2	Larger lunar evectional constituent	12.63	0.000138189172763
S_6	Shallow water overtides of principal solar constituent	4.00	0.000436332312999
$MU_2=2MS_2$	Variational constituent	12.87	0.000135612218492
$2N_2$	Lunar elliptical semidiurnal second-order constituent	12.91	0.000135192041208
OO_1	Lunar diurnal	22.31	0.000078230804661
LAM_2	Smaller lunar evectional constituent	12.22	0.000142825634369
S_1	solar diurnal constituent	24.00	0.000072722052166
M_1	Smaller lunar elliptic diurnal constituent	24.83	0.000070291149899
J_1	Smaller lunar elliptic diurnal constituent	23.10	0.000075555378874
MM=MN	Lunar monthly constituent	661.31	0.000002639199849
SSA	Solar semiannual constituent	4382.91	0.000000398212432
SA	Solar annual constituent	8765.82	0.000000199106216
MSF=SM	Lunisolar synodic fortnightly constituent	354.37	0.000004925160854
MF	Lunisolar fortnightly constituent	327.86	0.000005323397950
RHO	Larger lunar evectional diurnal constituent	26.72	0.000065319208533
Q_1	Larger lunar elliptic diurnal constituent	26.87	0.000064954568366
T_2	Larger solar elliptic constituent	12.02	0.000145202100831
R_2	Smaller solar elliptic constituent	11.98	0.000145686915859
$2Q_1$	Larger elliptic diurnal	28.01	0.000062310933666
P_1	Solar diurnal constituent	24.07	0.000072510563024
$2SM_2$	Shallow water semidiurnal constituent	11.61	0.000150329823600
M_3	Lunar terdiurnal constituent	8.28	0.000210788557004
$L_2=2MN_2$	Smaller lunar elliptic semidiurnal constituent	12.19	0.000143177133059
$2MK_3$	Shallow water terdiurnal constituent	8.39	0.000208024940643

Symbol	Definition	Period [hr]	Frequency [rad / s]
K_2	Lunisolar semidiurnal constituent	11.97	0.000145808625898
M_8	Shallow water eighth diurnal constituent	3.11	0.000561199116397
MS_4	Shallow water quarter diurnal constituent	6.10	0.000286119549507

The first column presents the symbol of tidal constituent. Subscript in the symbol shows total number of ebbs and flows, e.g. the subscript one shows ebb and flow occur approximately once a day, and the subscript two means there are about two times of ebbs and flows per day. The second column provides the definitions of the tidal constituents. The third column presents the period corresponding to the tidal constituents. This period has a relationship with the subscript in the symbol, e.g. diurnal constituents have approximately 24 hours period, and semidiurnal constituents have about 12 hours period. The final column defines the frequency of the tidal constituents.

It should be noted that the NOS tidal stations have a maximum of 37 historical tidal constituents, which are shown in above table. The IHO tidal stations have maximum 7 historical tidal constituents, which are K_1, K_2, M_2, N_2, O_1, Q_1, and S_2. Although IHO tidal stations have only seven historical tidal constituents, they may still be compared with simulation results. Since these are dominant seven tidal constituents in the astronomical tide, significant resynthesized plots can be generated.

CHAPTER 6

SIMULATED AND HISTORICAL COMPARISONS AND COMPUTATIONAL PERFORMANCE

Chapter 6 includes a verification of the attained simulation results and the computational performance of the various finite element mesh applications. In order to examine the accuracy of the simulation results, two types of comparisons are utilized: qualitative comparisons, which are based on visual interpretations of resynthesized plots; quantitative comparisons, which are premised on statistics.

6.1 Comparisons between Simulated and Historical Results

Each of the four finite element meshes described in Chapter 4 are employed in fully nonlinear simulations of the astronomic tides, as detailed in Chapter 3. The present section assesses a resynthesis of the harmonic constituents derived from the model results (corresponding to a total of 23 tidal constituents) by using harmonic constituents from 150 historical tidal stations (employing a maximum of 37 tidal constituents). Table 6-1 represents the 23 tidal constituents applied in the resynthesized model output. It should be noted that 37 historical harmonic constituents have been described in Chapter 5 (see Table 5-2).

Table 6-1: 23 tidal constituents applied in resynthesized model output.

Symbol	Definition	Period [hr]	Frequency [rad/s]
M_2	Principal lunar semidiurnal constituent	12.42	0.000140525704669
S_2	Principal solar semidiurnal constituent	12.00	0.000145444104333
N_2	Larger lunar elliptic semidiurnal constituent	12.66	0.000137861710268
K_1	Lunar diurnal constituent	23.93	0.000072934778604
M_4	Shallow water overtides of principal lunar constituent	6.21	0.000281051409339
O_1	Lunar diurnal constituent	25.82	0.000067596020604
M_6	Shallow water terdiurnal	4.14	0.000421577114008
MN_4	Shallow water quarter diurnal constituent	6.27	0.000278361922168
$MU_2 = 2MS_2$	Variational constituent	12.87	0.000135612218492
$MM = MN$	Lunar monthly constituent	661.31	0.000002639199849
$MSF = SM$	Lunisolar synodic fortnightly constituent	354.37	0.000004925160854
Q_1	Larger lunar elliptic diurnal constituent	26.87	0.000064954568366
P_1	Solar diurnal constituent	24.07	0.000072510563024
$2SM_2$	Shallow water semidiurnal constituent	11.61	0.000150329823600
$L_2 = 2MN_2$	Smaller lunar elliptic semidiurnal constituent	12.19	0.000143177133059
K_2	Lunisolar semidiurnal constituent	11.97	0.000145808625898
M_8	Shallow water eighth diurnal constituent	3.11	0.000561199116397
MS_4	Shallow water quarter diurnal constituent	6.10	0.000286119549507
$STEADY$	Principal water level	∞	0.000000000000000
MNS_2	Arising from the interaction between MN and S_2	13.13	0.000132954497700
$2MN_6$	Shallow water twelfth diurnal constituent	4.17	0.000418917504500
MSN_6	Arising from the interaction between M_2, N_2, and S_2	4.12	0.000423842706300
M_{10}	Shallow water tenth diurnal constituent	2.48	0.000702594512500

The first column represents the symbol of the tidal constituent. The second column describes the tidal constituent. The third and fourth columns correspond to the angular speed of the tidal constituent

Harmonic constituents from the historical tidal stations result from only the astronomic tides; the model only simulates astronomic tides. In fact, both historical and simulated tidal constituents do not include other factors (e.g., freshwater inflow). Figure 6-1 shows the locations of 150 historical tidal stations throughout the WNAT model domain with identification of nine selected stations. The assessment is performed first, qualitatively, by visually inspecting resynthesized plots (Figures 6-2 through 6-4), and then, quantitatively, by examining phase and amplitude

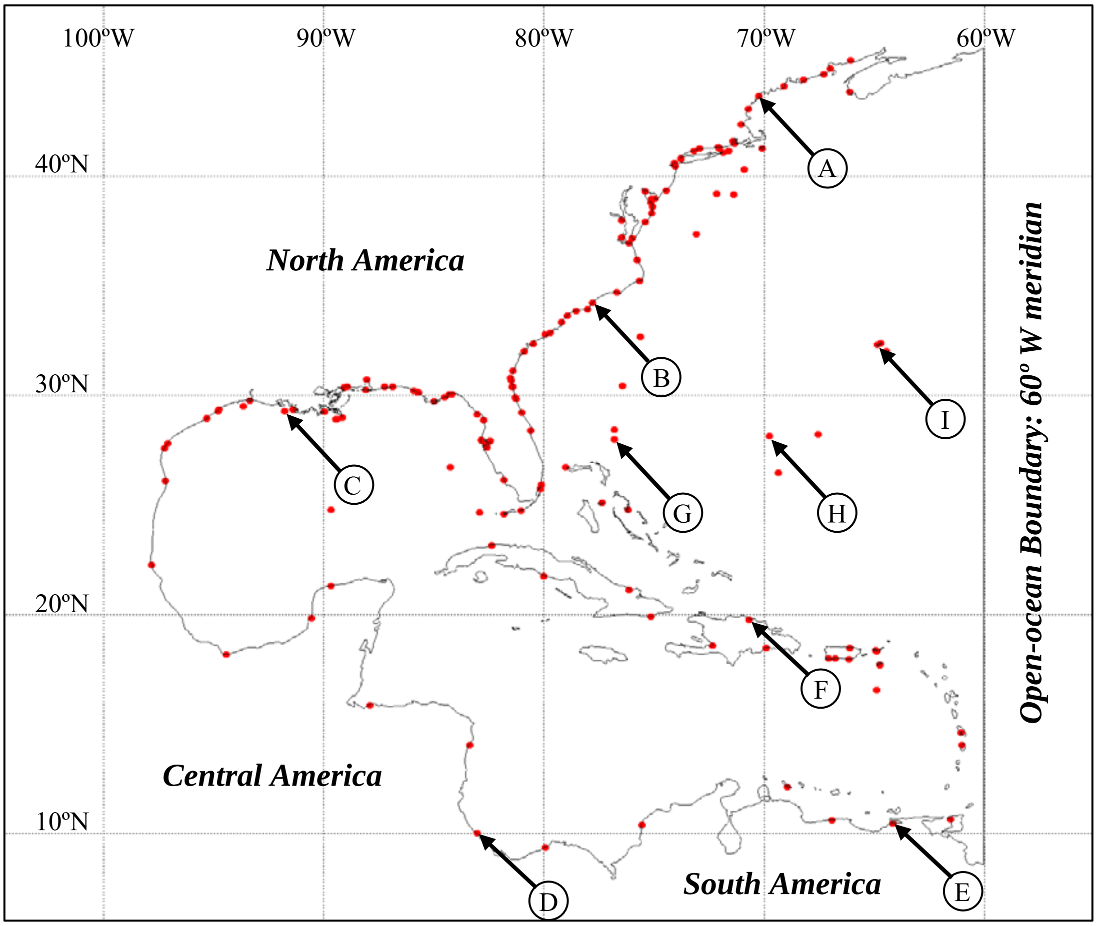

Figure 6-1: Location of 150 historical tidal stations throughout the WNAT model domain with identification of nine selected stations (A-I) for resynthesized plots.

performance through a statistical analysis (Table 6-2), using these nine selected tidal stations found within the WNAT model domain. Additionally, quantitative comparisons are made at all 150 stations throughout the WNAT model domain (Tables 6-3 through 6-7). It should be noted that the qualitative and quantitative comparison results at each single tidal station are illustrated in Appendix E. Although the resynthesized plots consist of only historical data and the best simulation results, these plots give an indication of every single simulation performance since there is an insignificant difference between each of the simulation results.

Figures 6-2 through 6-4 display plots of the resynthesized model output and historical tidal constituents for the nine selected stations shown in Figure 6-1. Each plot is a presentation of the deviation of the water surface elevation from mean sea level (MSL) in meters (Y-axis) versus a 14-day duration into the resynthesis (X-axis). (Fourteen days are chosen because that length of time will contain a complete spring-neap tidal cycle.) All plots include a blue thick solid curve to represent the resynthesized historical harmonic data and a red thin solid curve that is characteristic of all four finite element mesh applications (i.e., the curves for each of the four finite element mesh applications are indistinguishable). The intent of this visual presentation is to show how well the four finite element meshes perform throughout the domain; however, in this manner, it is impossible to determine overall superior performance of the individual finite element meshes.

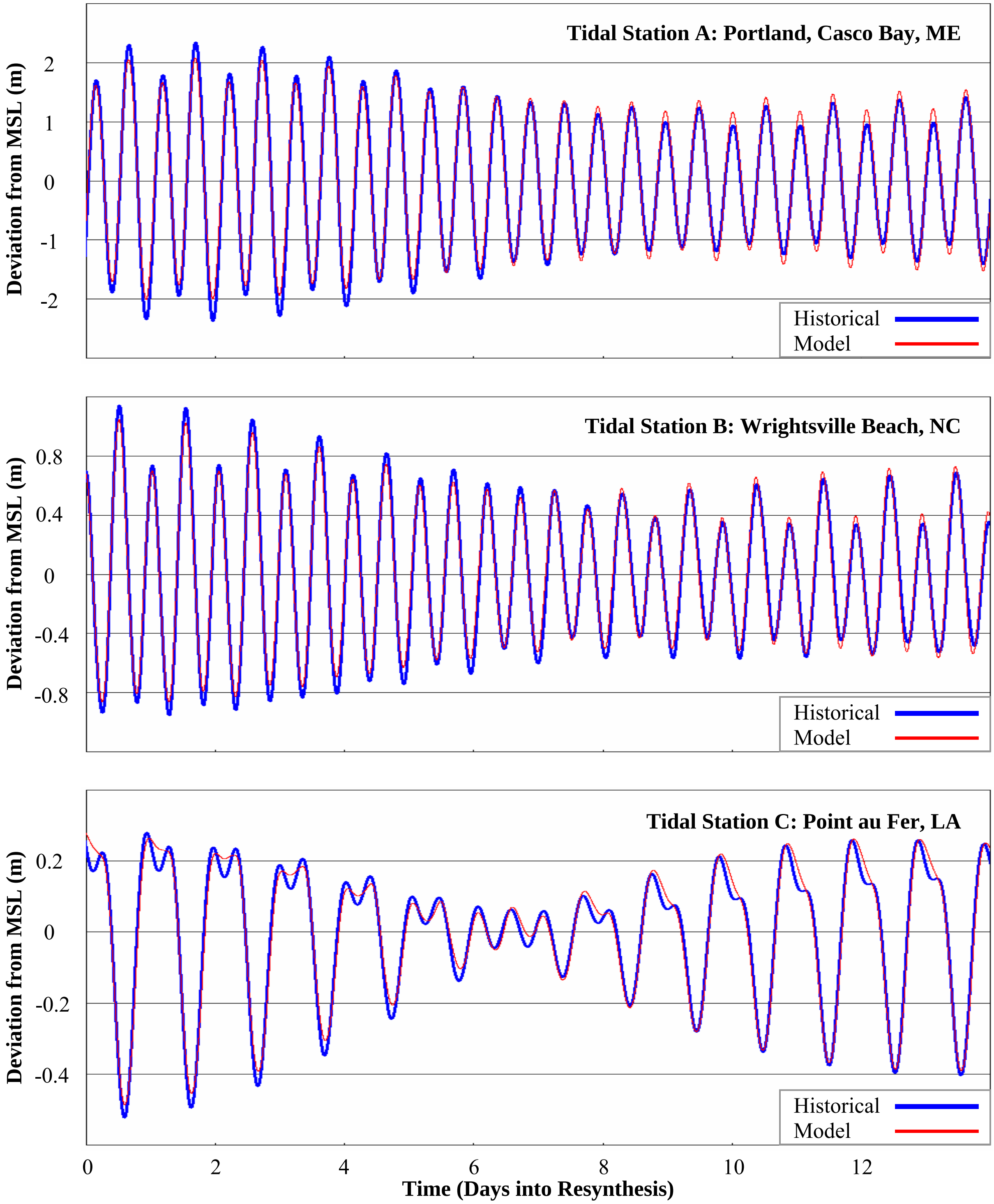

Figure 6-2: A resynthesis of historical and modeled tidal constituents
for a complete spring and neap tidal cycle at selected stations A, B, and C
(see Figure 6-1 for station locations)

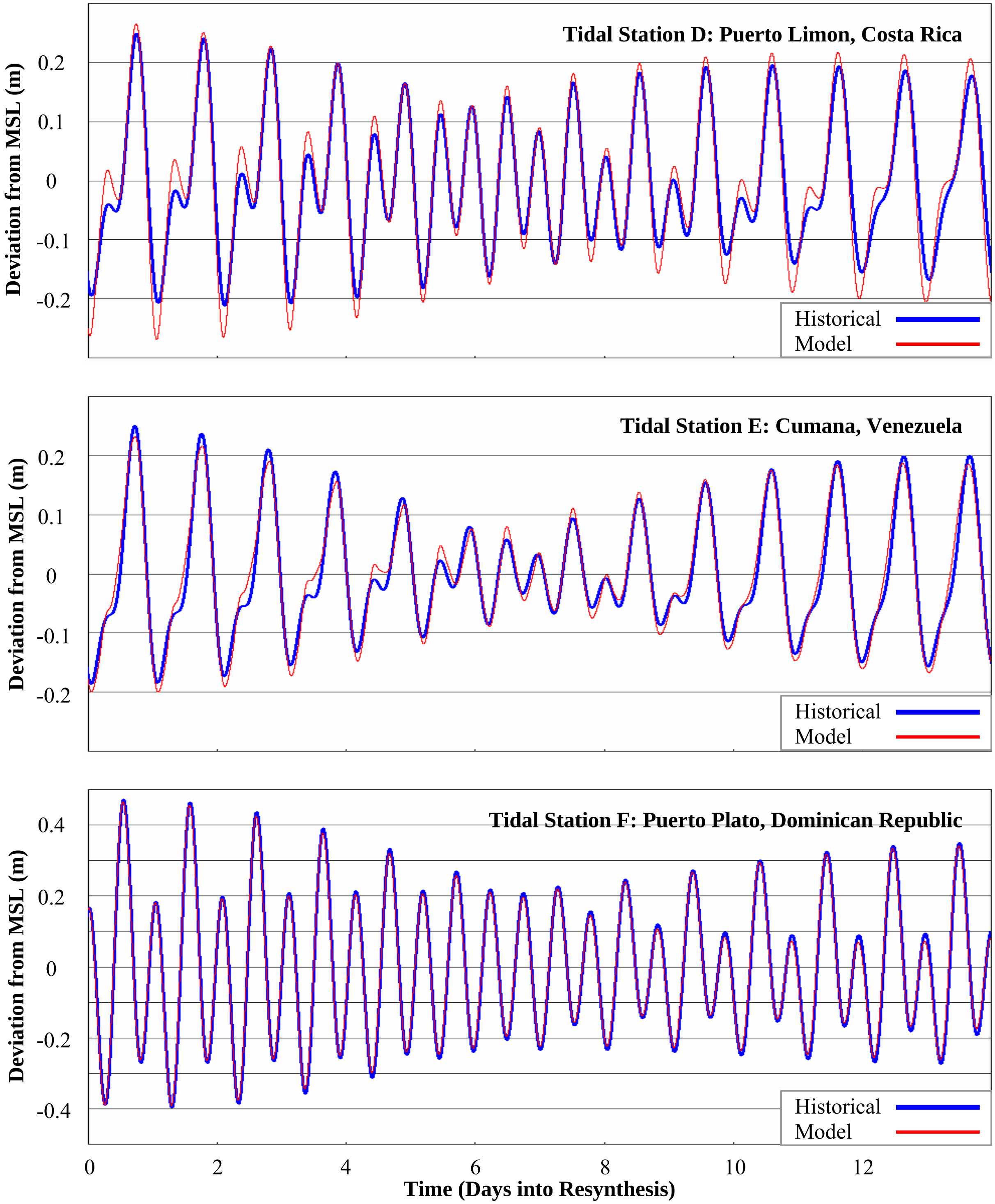

Figure 6-3: A resynthesis of historical and modeled tidal constituents
for a complete spring and neap tidal cycle at selected stations D, E, and F
(see Figure 6-1 for station locations)

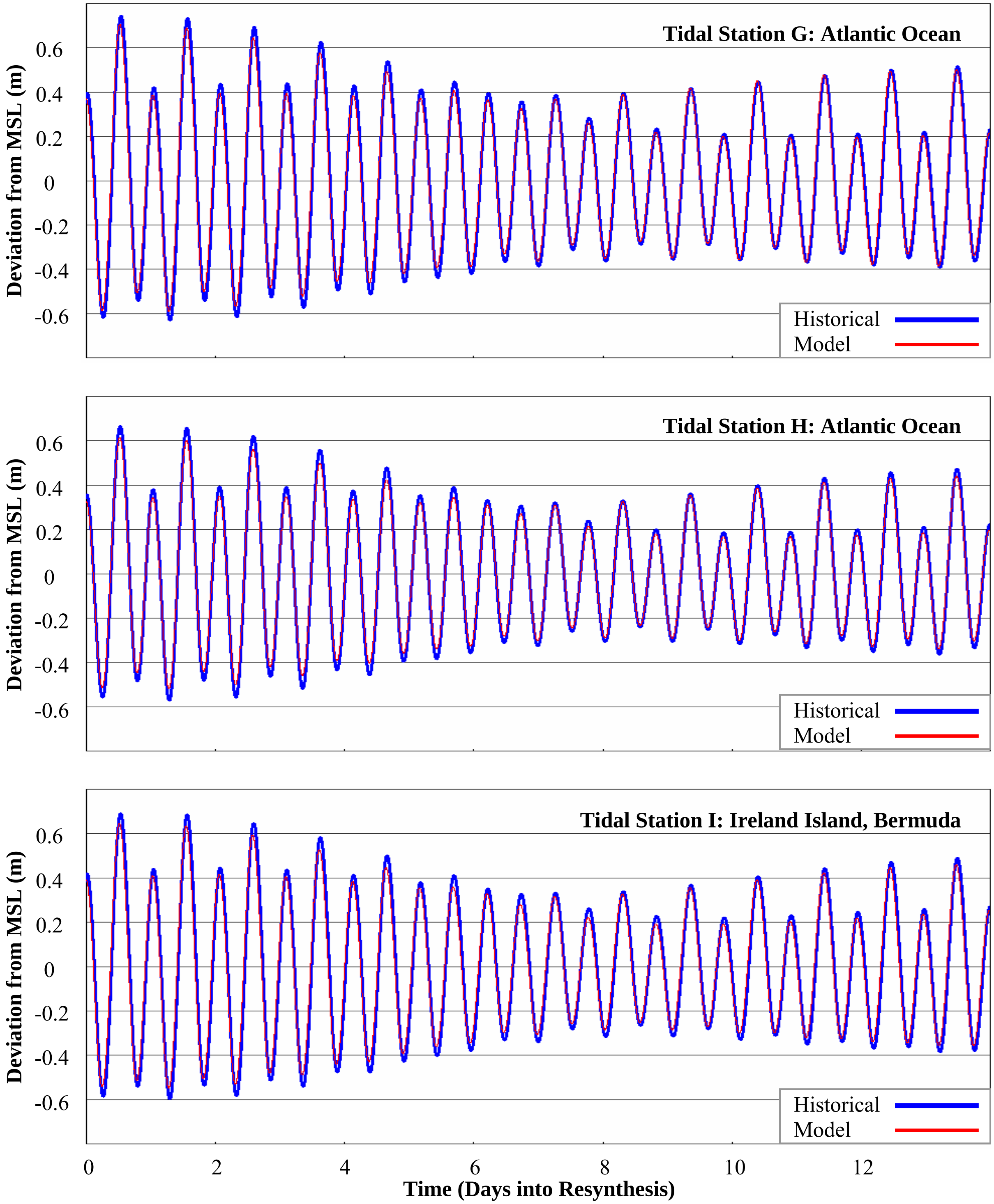

Figure 6-4: A resynthesis of historical and modeled tidal constituents for a complete spring and neap tidal cycle at selected stations G, H, and I (see Figure 6-1 for station locations)

Individual finite element mesh performance is assessed over the same 14-day period. Phase errors are computed by averaging the difference between the times of cyclical high and low tides for the historical and model resynthesized tidal signals. It is noted that for a tide with a period of 12.4 hours, a phase error of 10.0° corresponds to a time lag of 20 minutes and 40 seconds. Water surface elevations are assessed at one-minute intervals, after the model result has been corrected for phase error. A goodness of the amplitude fit (also known as the coefficient of determination) between the historical and model amplitudes is expressed as:

$$R^2 = \left[1 - \frac{SSE}{SS_{yy}}\right] = \left[1 - \frac{\sum (y_i - \hat{y}_i)^2}{\sum (y_i - \bar{y})^2}\right] = \left[1 - \frac{\sum (Hist_i - Mod_i)^2}{\sum \left(Hist_i - \overline{Hist}\right)^2}\right] \text{..............................} (6.1)$$

where R^2 represents the goodness of the amplitude fit between the historical and model elevations, i is the index of time, $Hist_i$ refers to the historical elevation at time i, Mod_i is the model elevation at time i, and $\overline{Hist}$ is the average historical elevation. It should be noted that an R^2 value of 1.00 corresponds to a direct correlation between the resynthesized model output and historical harmonic data (i.e., the model describes the historical tides without any degree of error).

Table 6-2 presents the phase errors and R^2 values at each of the nine tidal stations identified in Figure 6-1. From Table 6-2, the poorest overall phasing is exhibited at Station G; however, since the model response is only approximately 23 minutes out of phase with the historical resynthesized tidal signal, it is difficult to distinguish poor phasing over the 14-day period using any of the nine stations. Conversely, the poorer amplitude performance that is recorded in Table 6-2 for Stations D and E is recognized as such in the resynthesis plots shown in Figure 6-3.

Table 6-2: Phase errors and R^2 values corresponding to the resynthesis plots shown in Figures 6-2 through 6-4.

		333K mesh	95K mesh	60K mesh	53K mesh
Station A	Phase error [º]	3.2	3.5	5.2	4.2
	R^2 value [-]	0.98	0.98	0.98	0.99
Station B	Phase error [º]	5.5	3.2	4.6	3.2
	R^2 value [-]	0.99	0.99	0.99	0.98
Station C	Phase error [º]	10.1	13.1	1.9	8.3
	R^2 value [-]	0.98	0.98	0.98	0.98
Station D	Phase error [º]	2.2	1.7	2.4	1.9
	R^2 value [-]	0.94	0.93	0.94	0.93
Station E	Phase error [º]	3.2	3.7	3.5	3.5
	R^2 value [-]	0.95	0.95	0.95	0.95
Station F	Phase error [º]	5.9	5.9	5.8	5.7
	R^2 value [-]	1.00	1.00	1.00	1.00
Station G	Phase error [º]	11.2	11.7	11.4	11.6
	R^2 value [-]	0.99	0.99	0.99	0.99
Station H	Phase error [º]	3.4	3.6	3.3	3.5
	R^2 value [-]	0.99	0.99	0.99	0.99
Station I	Phase error [º]	11.3	11.3	11.0	11.4
	R^2 value [-]	0.99	0.99	0.99	0.99

Table 6-3 provides overall model performance for each of the four finite element mesh applications by examining errors with respect to phase. For all 150 tidal stations, average phase errors of $10.0°$, $10.5°$, $10.3°$, and $10.2°$ for the 333K, 95K, 60K, and 53K finite element meshes indicate that all of the finite element meshes performed well with respect to phasing. Clearly the

333K mesh performed best overall; however, it is intriguing that the 53K mesh performed better on average, although only slightly, than its LTEA-based counterparts that had more nodes.

Table 6-3: Phase errors for 150 tidal stations.

	333K mesh	95K mesh	60K mesh	53K mesh
Lowest phase error [º]	0.2	0.0	0.0	0.2
Highest phase error [º]	31.8	45.5	33.9	35.9
Average phase error [º]	10.0	10.5	10.3	10.2

Table 6-4 provides an overall assessment of the water surface elevations produced by each of the four finite element meshes by presenting a goodness of the amplitude fit between the historical and model amplitudes, i.e., R^2 value. All finite element mesh applications resulted in average R^2 values of 0.97. As is seen in the overall phase errors, Table 6-4 indicates that all of the finite element meshes performed well.

Table 6-4: R^2 values for 150 tidal stations.

	333K mesh	95K mesh	60K mesh	53K mesh
Lowest R^2 value [-]	0.58	0.55	0.58	0.58
Highest R^2 value [-]	1.00	1.00	1.00	1.00
Average R^2 value [-]	0.97	0.97	0.97	0.97

Tables 6-5 and 6-6 are included to differentiate the distribution of phase errors and R^2 values in an attempt to further distinguish individual finite element mesh performance. Phase errors (Table 6-3) and R^2 values (Table 6-4) are each sorted into seven categories that represent superior ($0^\circ \leq$ phase error $\leq 2^\circ$ and $0.98 \leq R^2$ value ≤ 1) to unacceptable results ($50^\circ <$ phase error and R^2 value < 0.50). None of the four finite element mesh applications exhibit unacceptable results according to the previously defined performance categories. Over half of all tidal stations, regardless of the finite element mesh that was applied, yielded phase errors of less than 10 degrees: 88 for the 333K; 81 for the 95K; 86 for the 60K; and 87 for the 53K. A clear majority of all tidal stations, regardless of the finite element mesh that was applied, exhibited R^2 values of 0.90 or higher: 125 for the 333K; 118 for the 95K; 123 for the 60K; and 125 for the 53K.

Table 6-5: Breakdown of phase errors (P.E.) for 150 tidal stations.

	333K mesh	95K mesh	60K mesh	53K mesh
Interval	0° ≤ P.E. ≤ 2°	0° ≤ P.E. ≤ 2°	0° ≤ P.E. ≤ 2°	0° ≤ P.E. ≤ 2°
Number of stations	21	16	19	18
Lowest [°]	0.2	0.0	0.0	0.2
Highest [°]	1.8	1.8	2.0	1.9
Average [°]	1.0	0.9	1.1	1.1
Interval	2° < P.E. ≤ 5°	2° < P.E. ≤ 5°	2° < P.E. ≤ 5°	2° < P.E. ≤ 5°
Number of stations	33	37	35	36
Lowest [°]	2.1	2.2	2.1	2.1
Highest [°]	5.0	5.0	5.0	4.9
Average [°]	3.6	3.5	3.7	3.5
Interval	5° < P.E. ≤ 10°	5° < P.E. ≤ 10°	5° < P.E. ≤ 10°	5° < P.E. ≤ 10°
Number of stations	34	28	32	33
Lowest [°]	5.3	5.1	5.2	5.2
Highest [°]	10.0	10.0	9.5	9.9
Average [°]	7.3	7.4	6.8	7.5
Interval	10° < P.E. ≤ 20°	10° < P.E. ≤ 20°	10° < P.E. ≤ 20°	10° < P.E. ≤ 20°
Number of stations	40	51	40	41
Lowest [°]	10.1	10.2	10.1	10.2
Highest [°]	19.3	19.8	19.5	19.1
Average [°]	14.5	14.7	14.4	14.0

	333K mesh	95K mesh	60K mesh	53K mesh
Interval	$20^{\circ} < \text{P.E.} \leq 30^{\circ}$	$20^{\circ} < \text{P.E.} \leq 30^{\circ}$	$20^{\circ} < \text{P.E.} \leq 30^{\circ}$	$20^{\circ} < \text{P.E.} \leq 30^{\circ}$
Number of stations	20	15	22	19
Lowest [º]	20.1	21.2	20.2	20.1
Highest [º]	29.1	29.7	29.7	29.9
Average [º]	23.8	24.6	24.2	23.8
Interval	$30^{\circ} < \text{P.E.} \leq 50^{\circ}$	$30^{\circ} < \text{P.E.} \leq 50^{\circ}$	$30^{\circ} < \text{P.E.} \leq 50^{\circ}$	$30^{\circ} < \text{P.E.} \leq 50^{\circ}$
Number of stations	2	3	2	3
Lowest [º]	31.1	30.5	30.9	31.5
Highest [º]	31.8	45.5	33.9	35.9
Average [º]	31.4	36.2	32.4	33.6
Interval	$50^{\circ} < \text{P.E.}$	$50^{\circ} < \text{P.E.}$	$50^{\circ} < \text{P.E.}$	$50^{\circ} < \text{P.E.}$
Number of stations	0	0	0	0
Lowest [º]	N/A	N/A	N/A	N/A
Highest [º]	N/A	N/A	N/A	N/A
Average [º]	N/A	N/A	N/A	N/A

Table 6-6: Breakdown of R^2 values for 150 tidal stations.

	333K mesh	95K mesh	60K mesh	53K mesh
Interval	$0.98 \leq R^2 \leq 1$	$0.98 \leq R^2 \leq 1$	$0.98 \leq R^2 \leq 1$	$0.98 \leq R^2 \leq 1$
Number of stations	45	39	45	41
Lowest [-]	0.98	0.98	0.98	0.98
Highest [-]	1.00	1.00	1.00	1.00
Average [-]	0.99	0.99	0.99	0.99
Interval	$0.95 \leq R^2 < 0.98$	$0.95 \leq R^2 \leq 0.98$	$0.95 \leq R^2 \leq 0.98$	$0.95 \leq R^2 \leq 0.98$
Number of stations	43	47	45	51
Lowest [-]	0.95	0.95	0.95	0.95
Highest [-]	0.97	0.97	0.97	0.97
Average [-]	0.97	0.97	0.97	0.97

	333K mesh	95K mesh	60K mesh	53K mesh
Interval	$0.90 \le R^2 < 0.95$	$0.90 \le R^2 \le 0.95$	$0.90 \le R^2 \le 0.95$	$0.90 \le R^2 \le 0.95$
Number of stations	37	32	33	33
Lowest [-]	0.90	0.90	0.90	0.90
Highest [-]	0.94	0.94	0.94	0.94
Average [-]	0.93	0.93	0.93	0.92
Interval	$0.80 \le R^2 < 0.90$	$0.80 \le R^2 \le 0.90$	$0.80 \le R^2 \le 0.90$	$0.80 \le R^2 \le 0.90$
Number of stations	18	21	18	19
Lowest [-]	0.80	0.80	0.82	0.80
Highest [-]	0.89	0.89	0.89	0.89
Average [-]	0.85	0.85	0.86	0.85
Interval	$0.70 \le R^2 < 0.80$	$0.70 \le R^2 \le 0.80$	$0.70 \le R^2 \le 0.80$	$0.70 \le R^2 \le 0.80$
Number of stations	3	5	5	1
Lowest [-]	0.72	0.74	0.72	0.76
Highest [-]	0.77	0.79	0.79	0.76
Average [-]	0.75	0.76	0.77	0.76
Interval	$0.50 \le R^2 < 0.70$	$0.50 \le R^2 \le 0.70$	$0.50 \le R^2 \le 0.70$	$0.50 \le R^2 \le 0.70$
Number of stations	4	6	4	5
Lowest [-]	0.58	0.55	0.58	0.58
Highest [-]	0.68	0.65	0.65	0.66
Average [-]	0.63	0.58	0.62	0.62
Interval	$R^2 < 0.50$	$R^2 < 0.50$	$R^2 < 0.50$	$R^2 < 0.50$
Number of stations	0	0	0	0
Lowest [-]	N/A	N/A	N/A	N/A
Highest [-]	N/A	N/A	N/A	N/A
Average [-]	N/A	N/A	N/A	N/A

Most numerical modelers would agree that any solution exhibiting a goodness of fit between historical and model elevations of 0.98 or higher to be a superior solution. However, in order for that superior fit to be a useful solution, it must be relatively in phase. Therefore, the number of tidal stations with R^2 values of 0.98 or higher while being within 10.0 degree of phase are counted. The 333K model did the best with 34 stations attaining R^2 values of 0.98 or higher while being within 10.0 degrees of phase, i.e., 11 stations exhibited a goodness of fit between historical and modeled elevations of 0.98 or higher, yet were outside of 10.0 degree phase error requirement. The 95K and 53K LTEA-based finite element meshes had 12 stations meeting these criteria with the 60K mesh containing 13 stations that satisfy these guidelines. As a result, following the 333K mesh with its 34 stations would be the 60K mesh with 32, the 53K mesh with 29, and the 95K mesh with 27.

Table 6-7 presents a regional assessment of the phase errors and R^2 values, e.g. stations that fall along the East Coast of North America (62 historical tidal stations), within the Gulf of Mexico (44 historical tidal stations), along the Central and South American coasts (9 historical tidal stations), in or around the Caribbean Sea islands (20 historical tidal stations), and in the deep Atlantic Ocean and near Bermuda (15 historical tidal stations). Excellent performance in the deep Atlantic Ocean is translated to the East Coast stations. However, for the Gulf of Mexico region and along the Central and South American coastlines, clearly less favorable results are exhibited.

Table 6-7: Regional phase errors and R^2 values for 150 tidal stations.

	East Coast of North America (62 Tidal Stations)			
	333K mesh	95K mesh	60K mesh	53K mesh
Phase error [°]	10.6	12.2	11.1	11.2
R^2 value [-]	0.98	0.98	0.98	0.98

	Gulf of Mexico (44 Tidal Stations)			
	333K mesh	95K mesh	60K mesh	53K mesh
Phase error [°]	10.9	10.2	10.8	10.4
R^2 value [-]	0.90	0.89	0.91	0.91

	Central and South American Coasts (9 Tidal Stations)			
	333K mesh	95K mesh	60K mesh	53K mesh
Phase error [°]	10.2	9.7	10.4	10.1
R^2 value [-]	0.91	0.89	0.91	0.90

	Caribbean Sea Islands (20 Tidal Stations)			
	333K mesh	95K mesh	60K mesh	53K mesh
Phase error [°]	10.5	10.7	10.7	10.4
R^2 value [-]	0.95	0.95	0.95	0.95

	Atlantic Ocean and Bermuda (15 Tidal Stations)			
	333K mesh	95K mesh	60K mesh	53K mesh
Phase error [°]	4.6	4.8	4.8	4.8
R^2 value [-]	0.99	0.99	0.99	0.99

6.2 Computational Performance

All tidal simulations presented herein are performed in the Compaq Water Resources Simulations Laboratory, at the University of Central Florida, Orlando, Florida (http://cwrsl.cecs.ucf.edu/). This laboratory is equipped with a twelve-node Compaq-ALPHA cluster, which can serve as a parallel super computer. The cluster contains a master node (DS10) and twelve separate processors (12-DS10L), where each 600 MHz Compaq-ALPHA unit is equipped with 1 gigabyte of RAM and a 30 gigabyte hard drive operating at 7200 rpm. These high-performance machines can be run in serial or as a high-speed parallel system with the latest in Myrinet networking technology. Table 6-8 represents the computational performance corresponding to each of the four finite element mesh applications.

Figure 6-5: A twelve-node Compaq-ALPHA cluster (CWRS Laboratory)

Table 6-8: The computational performance corresponding to the four finite element mesh applications.

FEM	Total number of computational nodes	Total number of triangular elements	Time step (s)	Runtime for 90-day simulation
333K	332,582	647,018	4	319.4 hr
95K	95,062	182,941	5	53.5 hr
60K	60,487	108,987	5	29.7 hr
53K	52,774	98,365	5	27.8 hr

It should be noted that the 333K finite element mesh application requires a 4 second time step in order to maintain numerical stability (i.e., numerical overflow results from applying a 5 second time step). More specific information regarding numerical stability is described in Chapter 7.

CHAPTER 7

OPTIMIZATION OF THE 53K FINITE ELEMENT MESH

Chapter 7 includes optimization of the 53K finite element mesh. Four subsections are entitled: 1) Manual Editing Procedures, 2) Model Parameterizations and Boundary Condition Specifications, 3) Computational Performance, and 4) Verification of the Optimized 53K Finite Element Mesh (Qualitative and Quantitative Comparisons).

7.1 Manual Editing Procedures

The main purpose for optimizing the 53K finite element mesh (herein the optimized 53K finite element mesh is referred to as the 48K finite element mesh) is to reduce computational time to run one complete 90-day simulation with virtually the same or better accuracy as the 53K finite element mesh. In order to generate the most efficient finite element mesh, two procedures are applied in this study. One is to decrease the amount of computational nodes within certain regions near the coastline boundary, where the computational nodes are denser than necessary, through manual editing. The second is to increase the applied time step from 5 seconds to 30 seconds. In order to increase the time step, an evaluation of the Courant Number criterion is employed.

7.1.1 Decreased Computational Nodes Procedure

There are two types of computational node reduction: 1) elimination of a number of computational nodes in the ocean without changing of the node spacing on the boundary and 2) elimination of a number of computational nodes in the ocean with changing of the node spacing on the boundary.

Areas A, B, and C, as shown in Figure 7-1, are example locations, where computational nodes are reduced without inducing a boundary change. Figures 7-2, 7-3, and 7-4 correspond to the

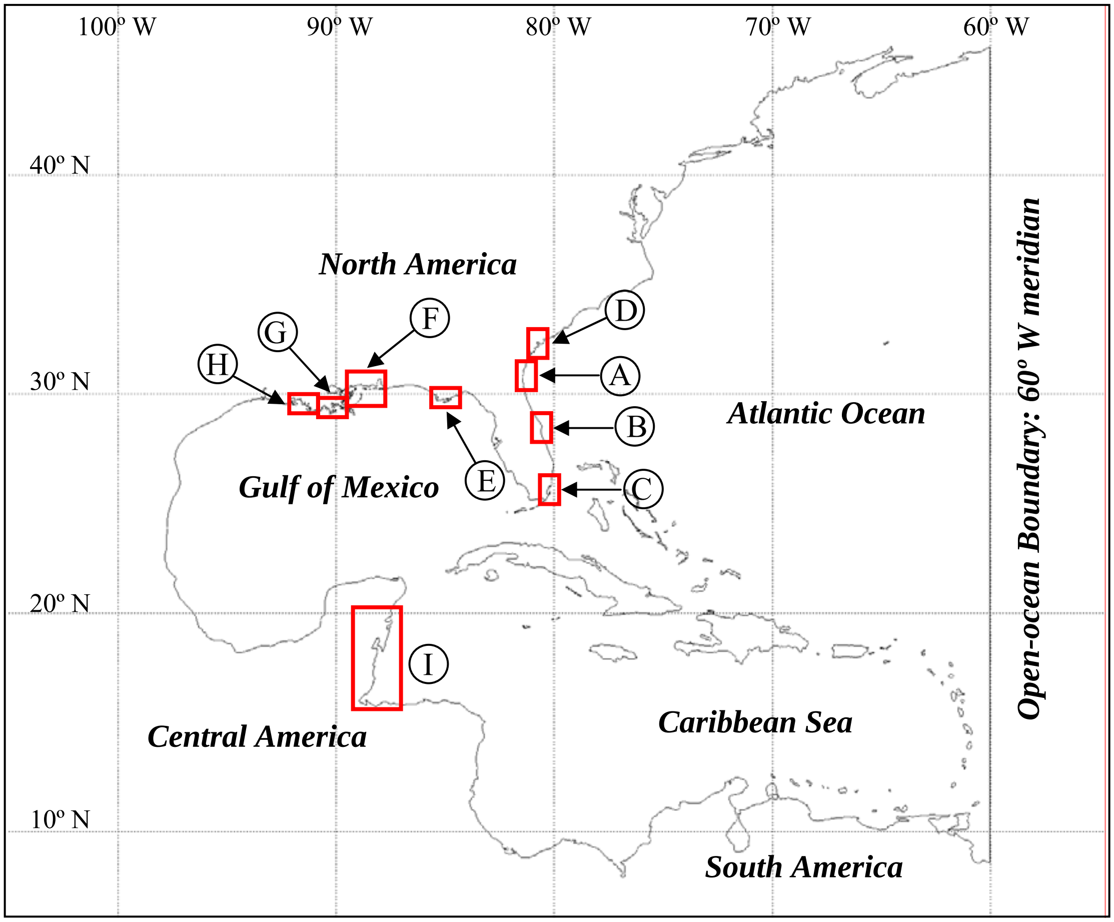

Figure 7-1: WNAT model domain with boundary.

areas A, B, and C. The 53K finite element mesh is represented on the left side, and the 48K finite element mesh is illustrated on the right side. Areas D through I are other example locations (also shown in Figure 7-1), where computational nodes are decreased with changing of the node spacing on the boundary. These locations include excessive geographic features (small node spacing) in the local area, and such high nodal density is deemed unnecessary for a large-scale tidal model simulation. Figures 7-5 through 7-10 correspond to the areas D through I. The 53K finite element mesh is shown on the left or upper side, and the 48K finite element mesh is represented on the right or lower side.

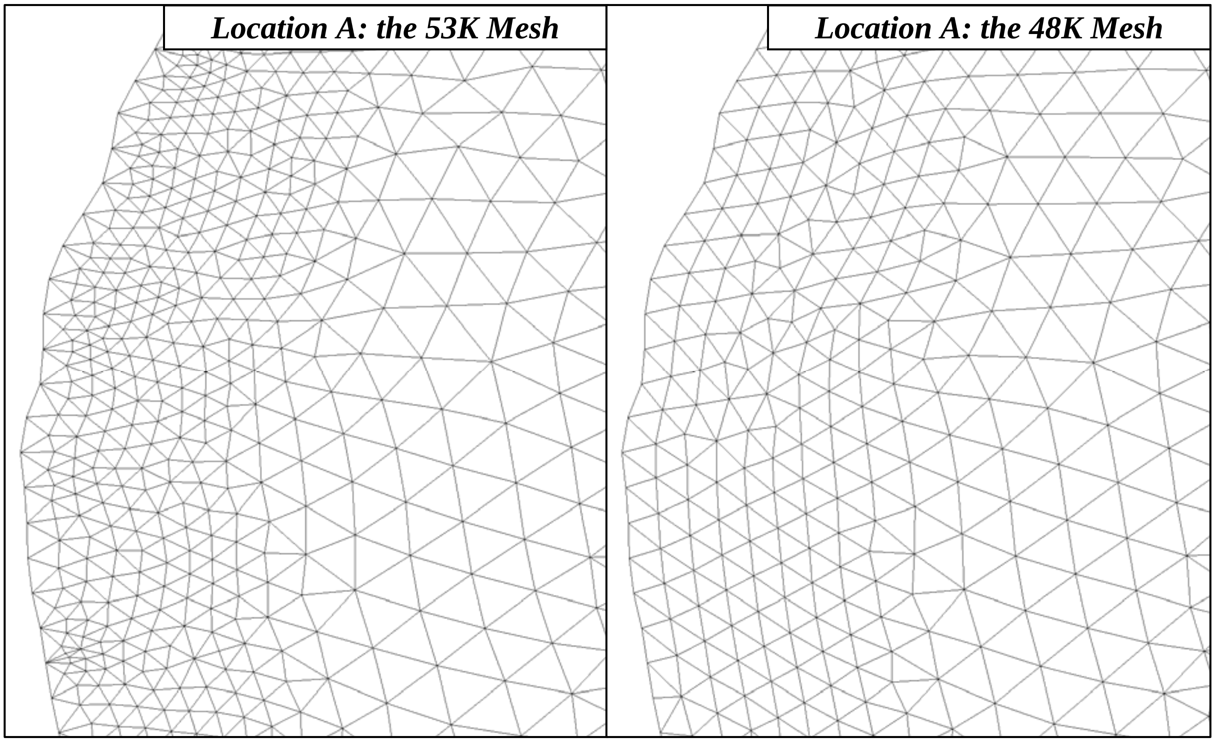

Figure 7-2: The finite element mesh near Fernandina Beach, Amelia River, FL.

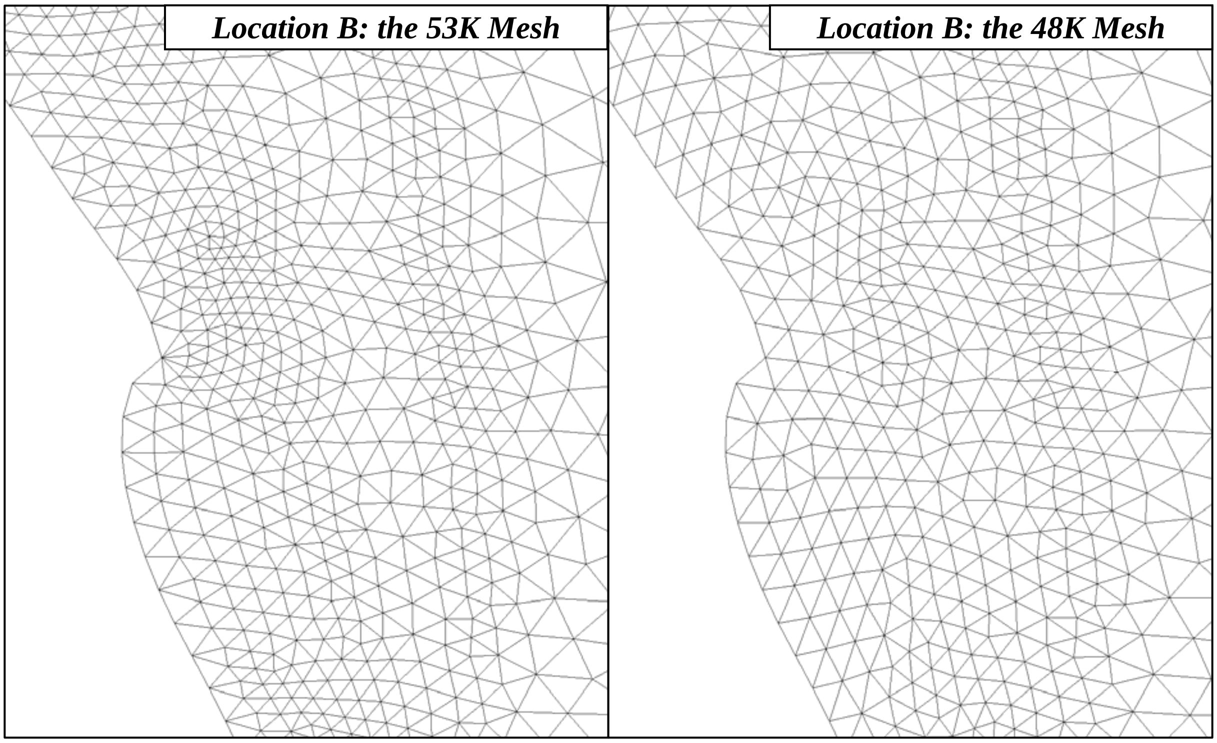

Figure 7-3: The finite element mesh near Trident Pier, Port Canaveral, FL.

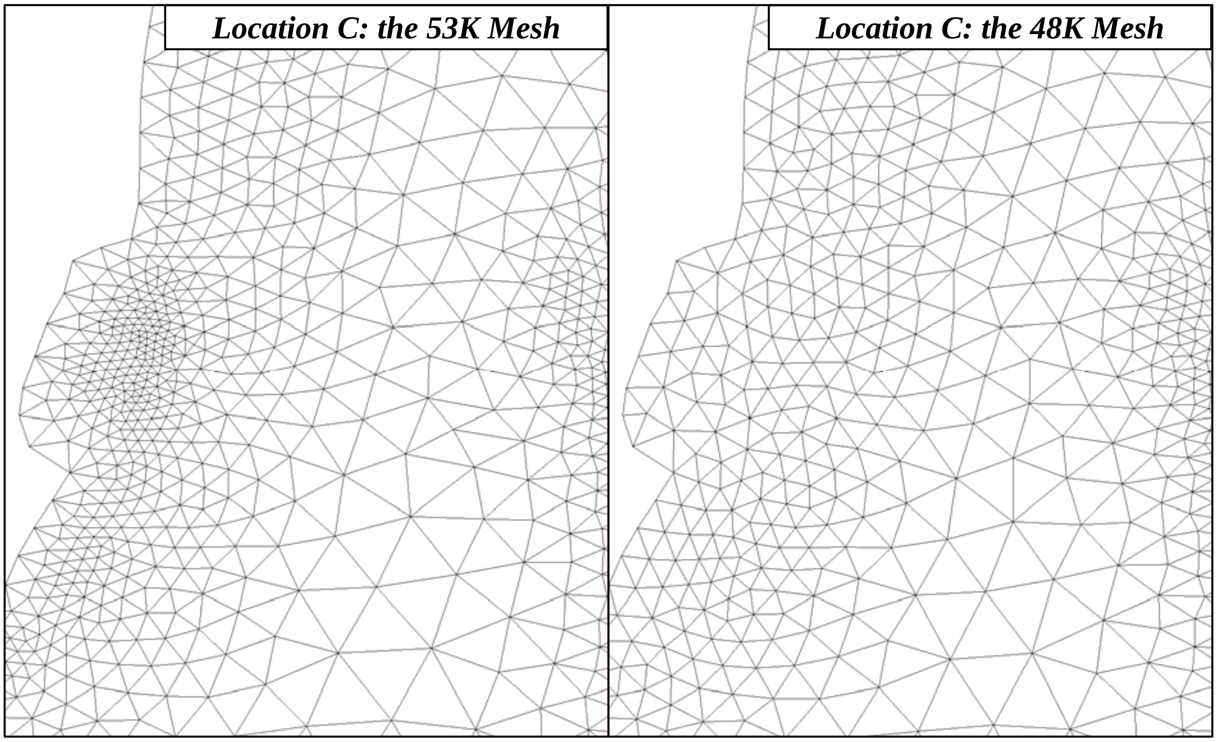

Figure 7-4: The finite element mesh near Virginia Key, Biscayne Bay, FL.

In order to do this mesh reduction procedure, the two-dimensional Surface-water Modeling System (SMS) software package was utilized. The following methodology is employed to reduce the number of computational nodes.

Task 1: Find the location where the finite element mesh is not generated well and/or computational nodes are assumed to be more than necessary inside of the boundary; however, node spacing on the boundary is neat.

Task 2: Eliminate computational nodes and triangular elements around there (not computational nodes on the boundary).

Task 3: Regenerate finite element mesh in this certain location by using the existing computational nodes and the paving technique in the SMS software.

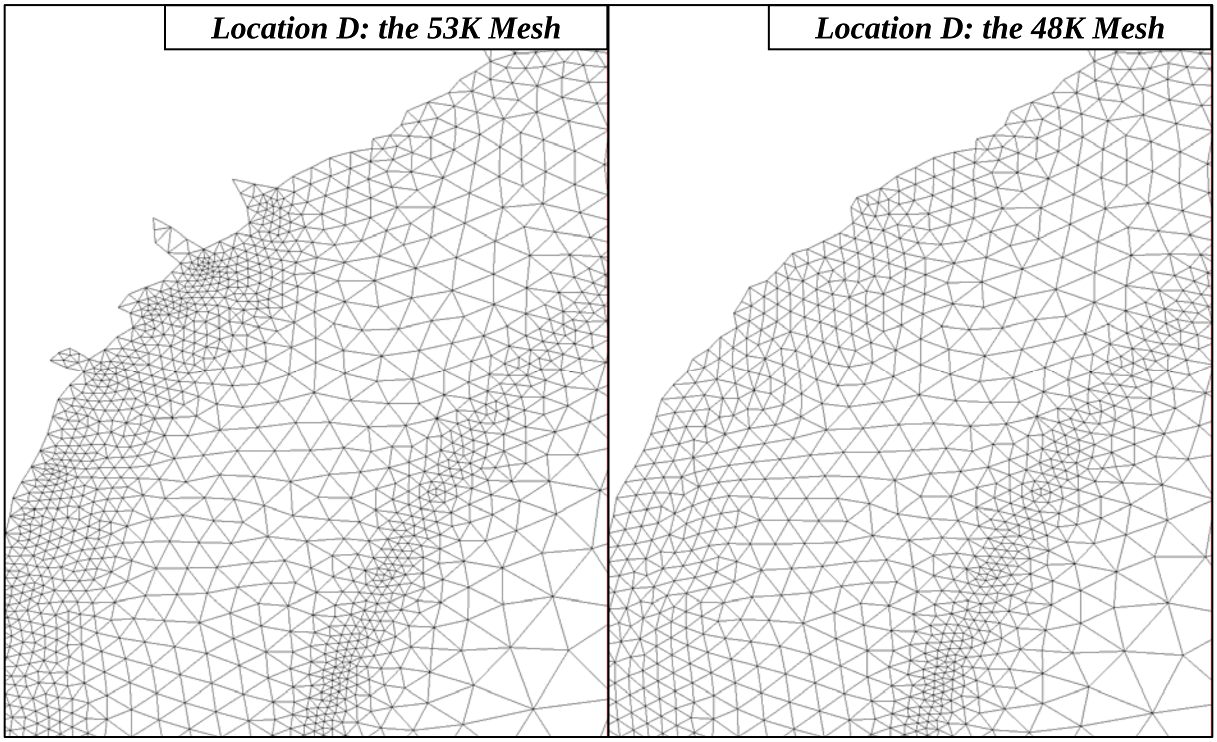

Figure 7-5: The finite element mesh near Fort Pulaski, Savannah River, GA.

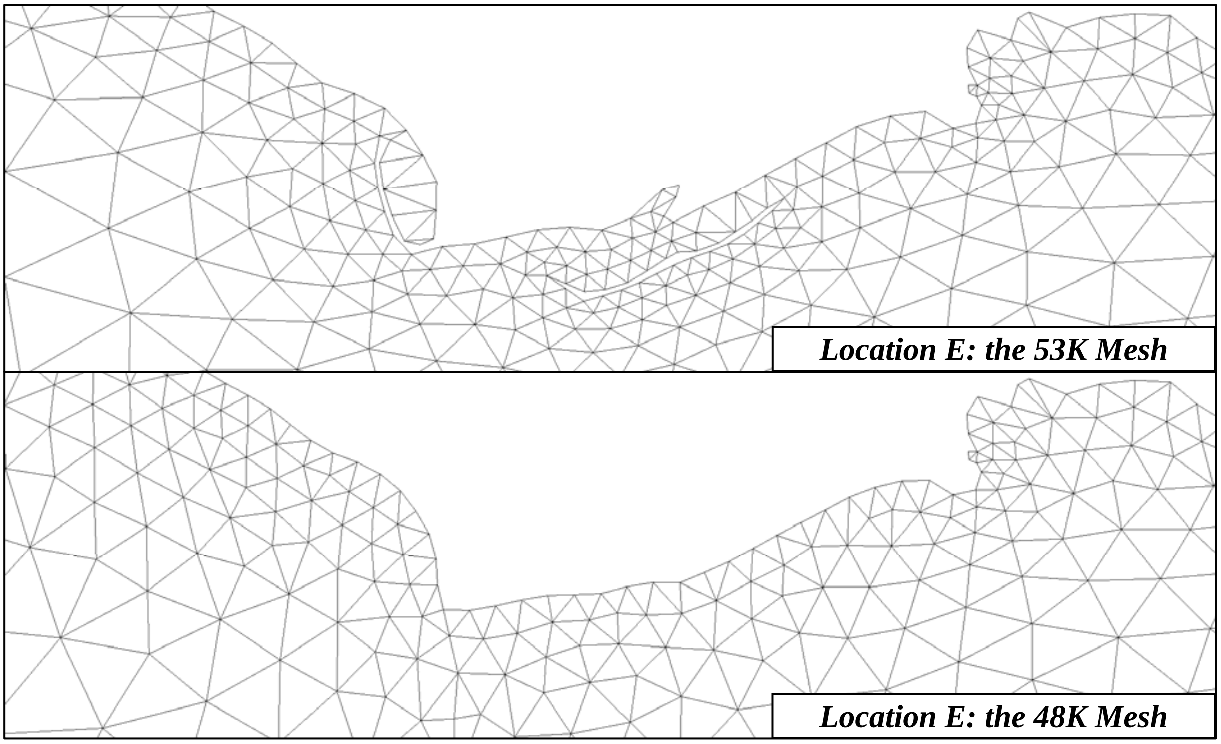

Figure 7-6: The finite element mesh near Apalachicola, Apalachicola River, FL.

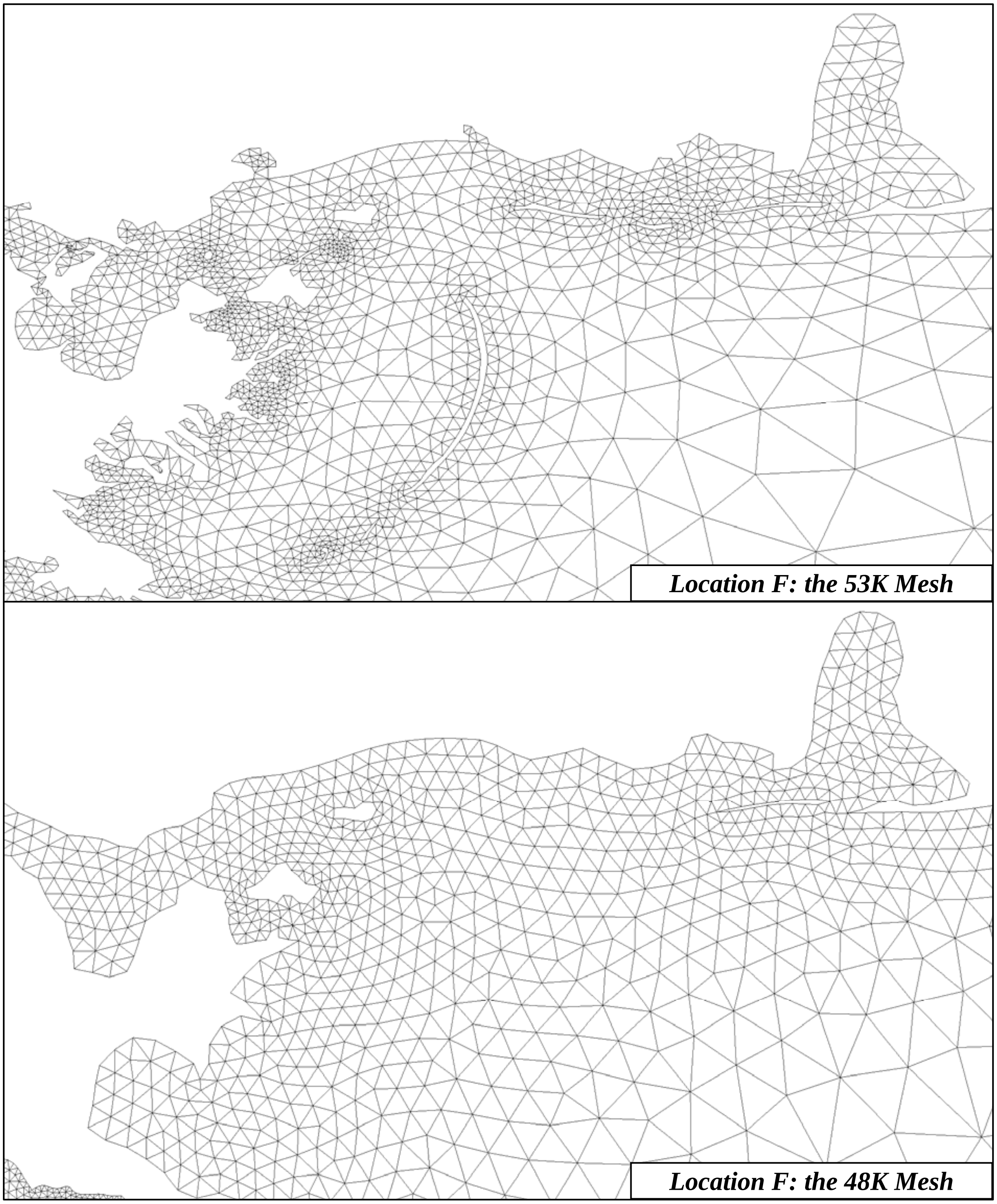

Figure 7-7: The finite element mesh near Chandeleur Sound Area.

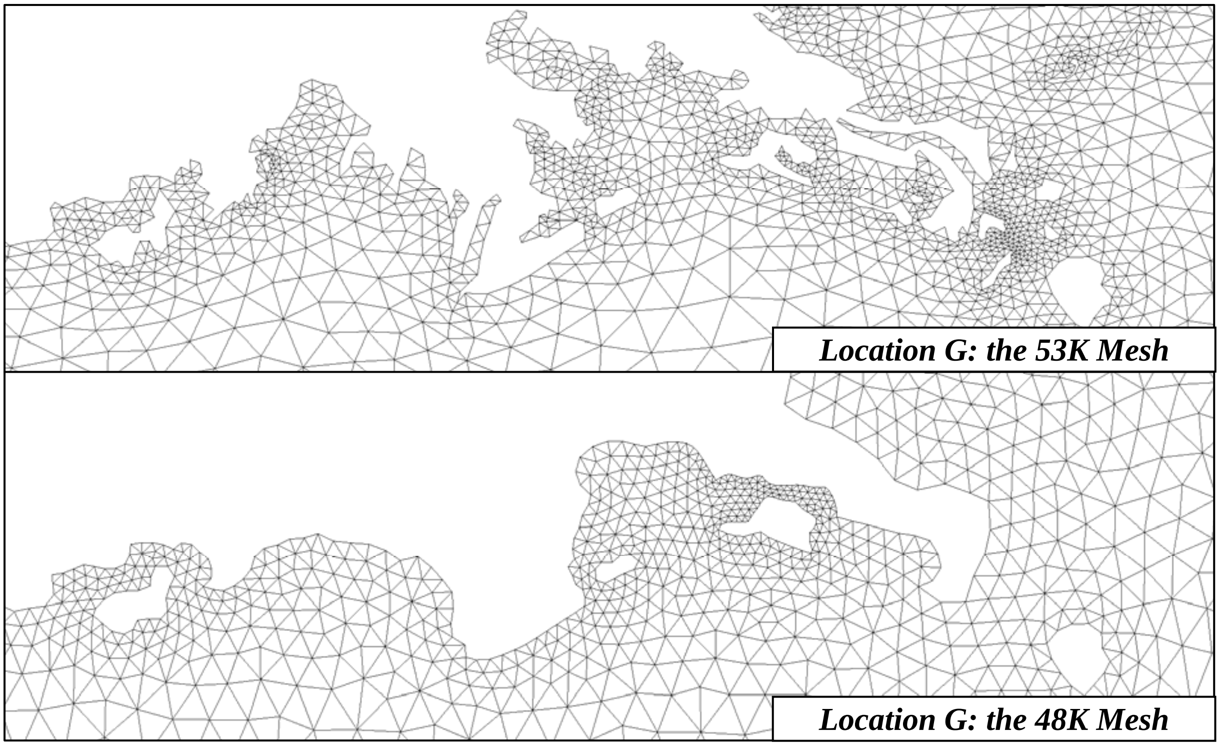

Figure 7-8: The finite element mesh near Port Fourchon, Belle Pass, LA.

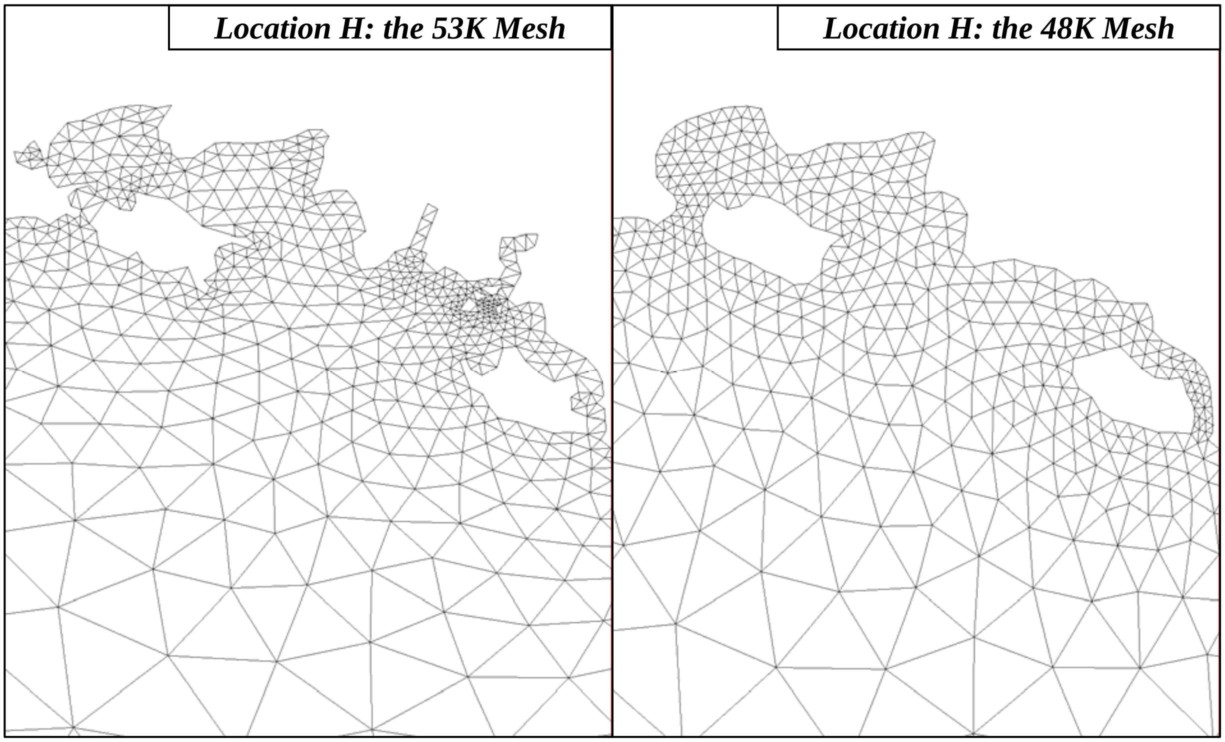

Figure 7-9: The finite element mesh near the Point au Fer, LA.

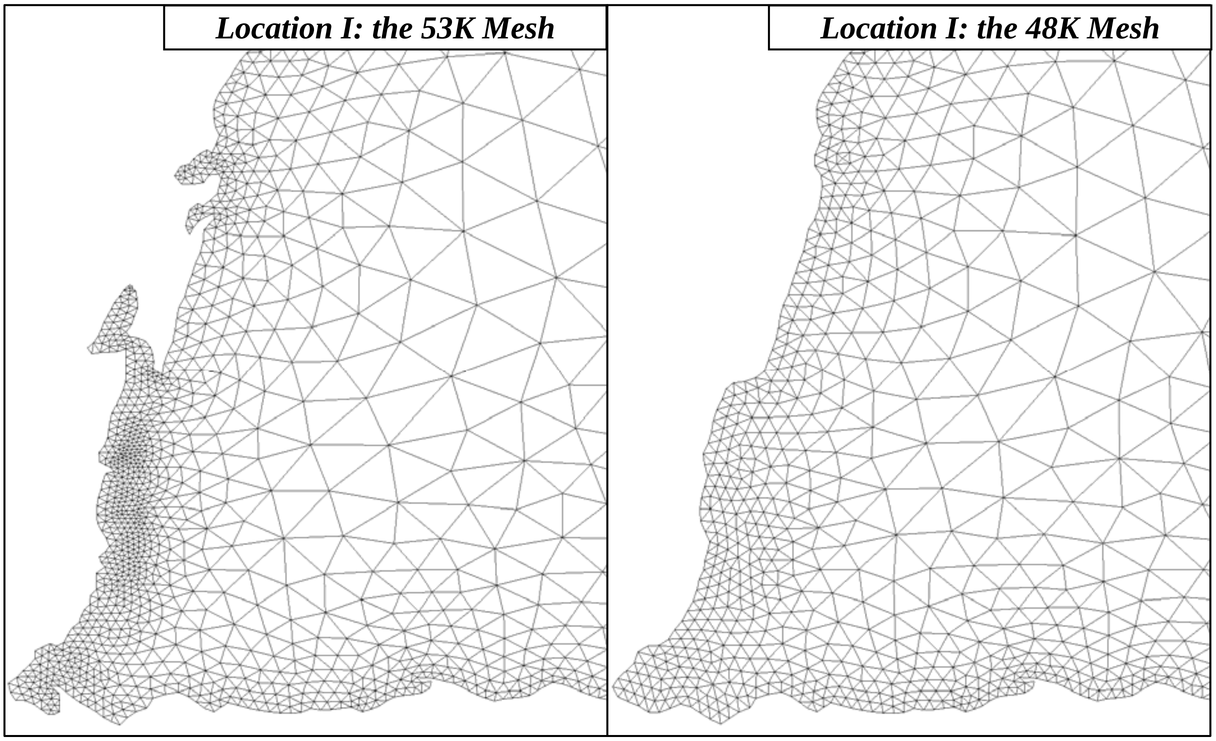

Figure 7-10: The finite element mesh near Puerto Cortes.

The following are procedures to reduce computational nodes while changing boundary node spacing. SMS is utilized again for this method.

Task 1: Find the location where the finite element mesh is assumed to be generated poorly and/or computational nodes exist more than necessary inside of the boundary. In addition, the location includes too much geographic feature in the local area by putting many computational nodes on the boundary.

Task 2: Eliminate computational nodes and triangular elements around these areas (include computational nodes on the boundary).

Task 3: Regenerate the boundary with new node spacing, which is approximately 6 km. This new boundary has to be accorded the same as the 53K finite element mesh boundary as much as possible.

Task 4: Regenerate finite element mesh in this certain location by using new computational nodes on the boundary and original computational nodes in the deep ocean. The paving technique in the SMS software is applied for this process.

7.1.2 Increased Time Step Procedure

This is another procedure to reduce computational run-time to complete a 90-day simulation. In order to generate a much more computationally efficient finite element mesh, the time step for the large-scale tidal model simulation is considered. Since the computational time is a linear trend, it is decreased approximately half if the time step is increased twice. The goal of this procedure is to increase the time step from five seconds to 30 seconds. In consequence, the total amount of the computational time is expected to be approximately one-sixth as when employing a five second time step.

The Courant Number condition, which has a relationship with flow velocity, node spacing, and time step, is applied. The Courant Number is a dimensionless parameter commonly used in computational fluid dynamics, and it is very important to apply this algorithm in order to evaluate numerical stability. The equation of the Courant Number is given by:

$$C_{\#} = \frac{Vt}{L} \qquad (7.1)$$

where $C_{\#}$ is the Courant Number, V is velocity, t is time, *and* L is length. For a finite element application to shallow water flow, the Courant Number condition for numerical stability can be expressed as:

$$C_{\#} = \frac{V\Delta t}{\Delta x} \cong \frac{\sqrt{gh}\Delta t}{\Delta x} \leq 1 \quad (7.2)$$

where Δt = time step, Δx = node spacing, g = acceleration due to gravity, and h = bathymetric depth.

Equation 7.2 indicates that the Courant Number value has to be less than or equal to one in order to maintain numerical stability during the tidal simulation. If the Courant Number value exceeds 1.0 at a computational node somewhere within tidal model domain, instability will develop leading to numerical overflow. Again, the goal of this procedure is to employ a 30 second time step for tidal simulations using the WNAT tidal model domain. However, a 30 second time step can not be applied directory to the 53K finite element mesh because in that case, the Courant Number value exceeds 1.0 at 646 computational nodes. Therefore, the node spacing has to be relaxed in these locations (see Figure 7-11) by using a manual editing procedure in order to reduce the Courant Number value.

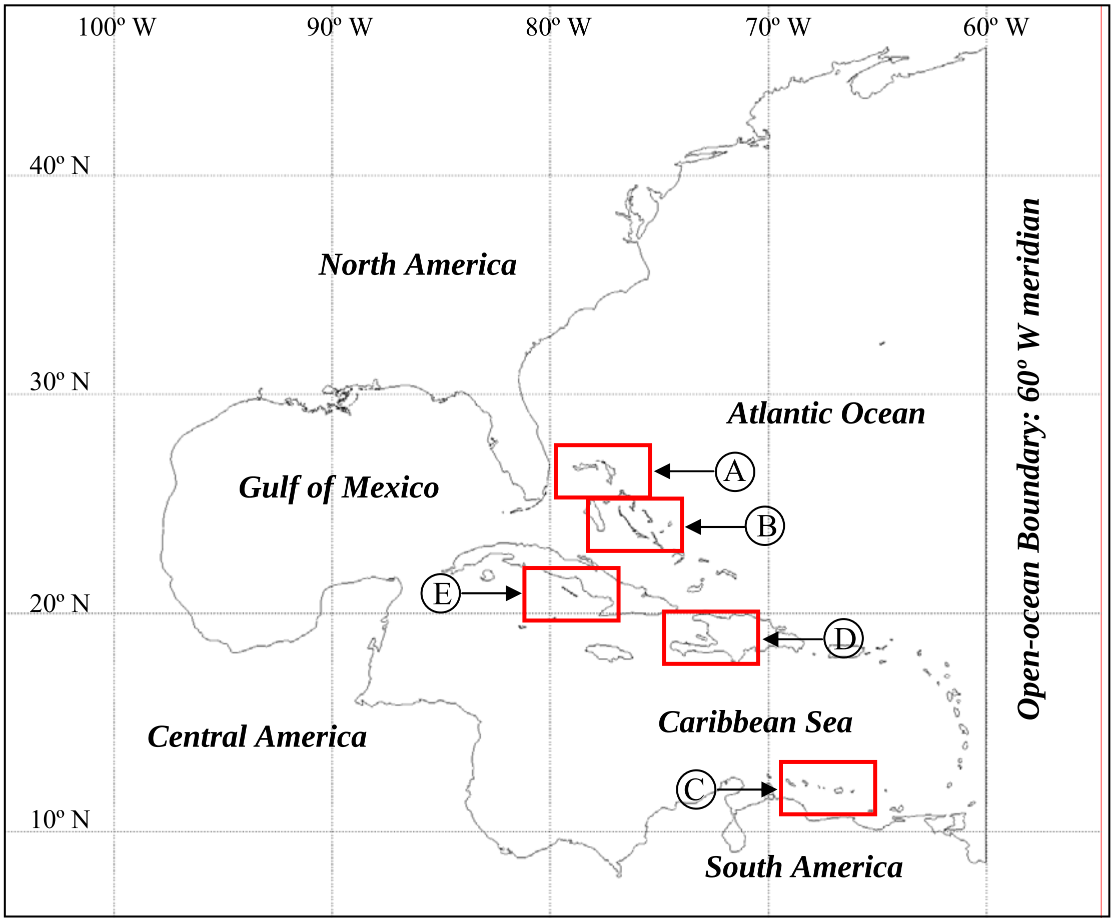

Figure 7-11: WNAT model domain with boundary.

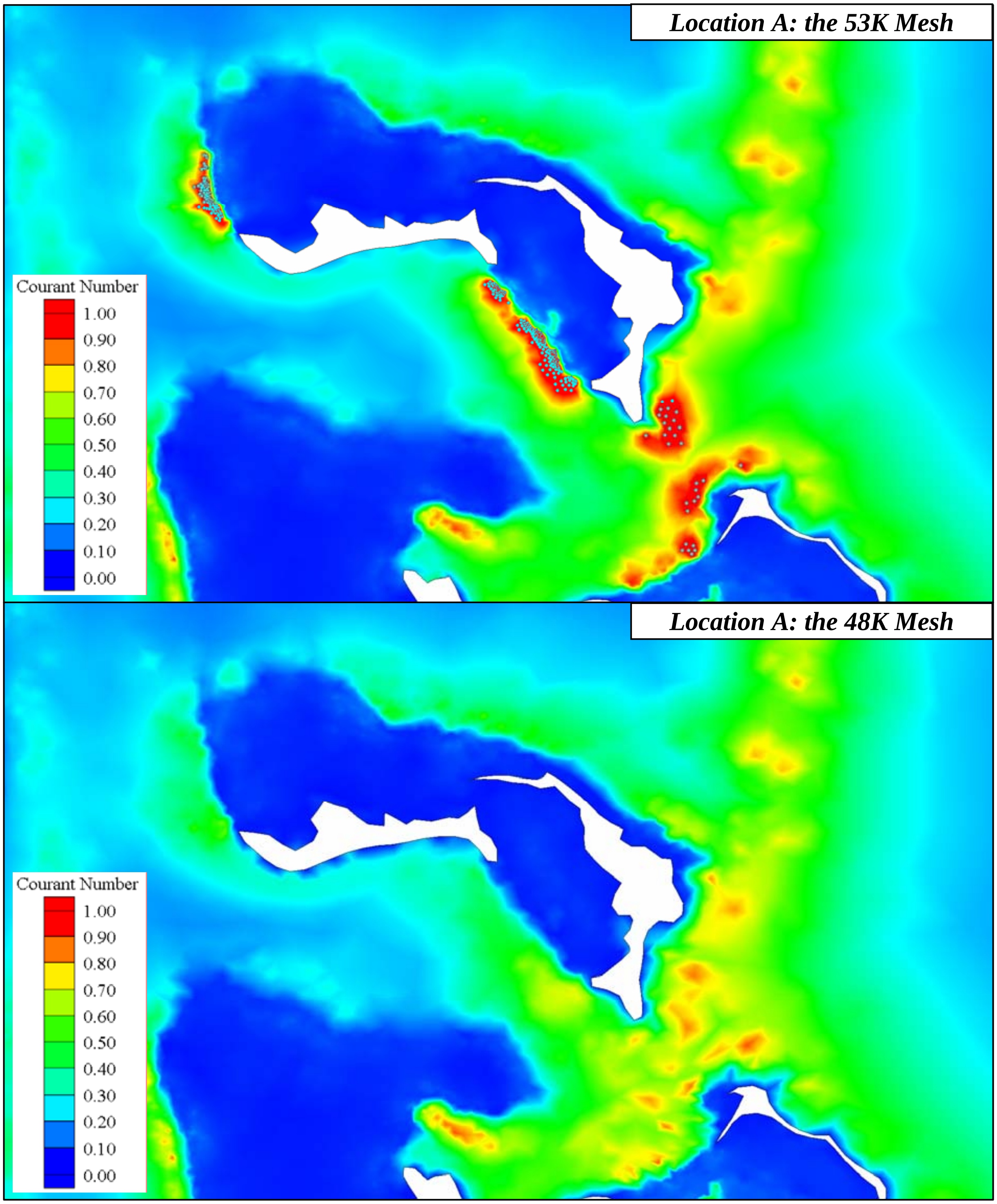

Figure 7-12: Contours of the Courant Number near Settlement Point, Grand Bahamas for the 53K (top) and 48K finite element meshes (bottom).

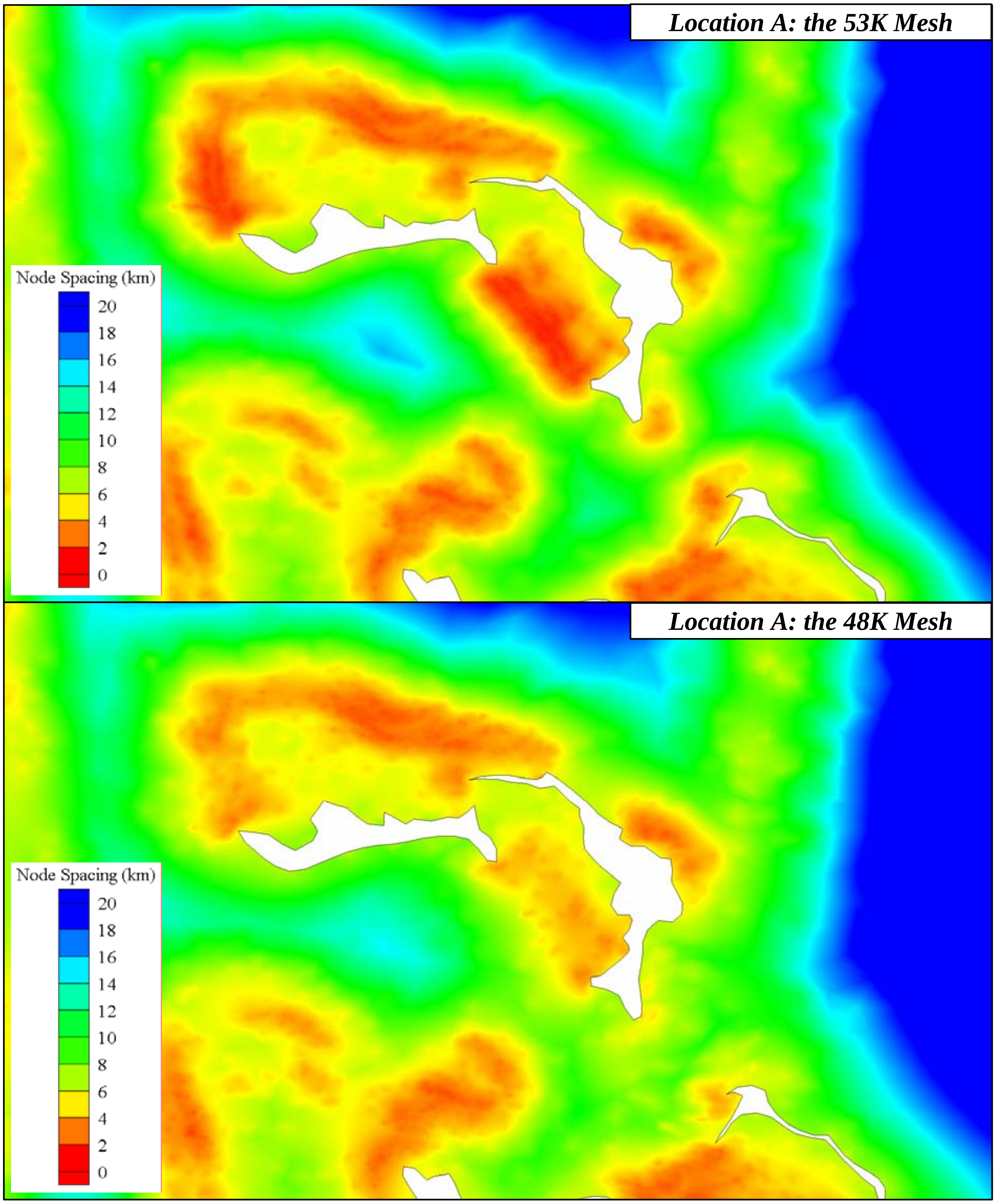

Figure 7-13: Contours of the node spacing near Settlement Point, Grand Bahamas for the 53K (top) and 48K finite element meshes (bottom).

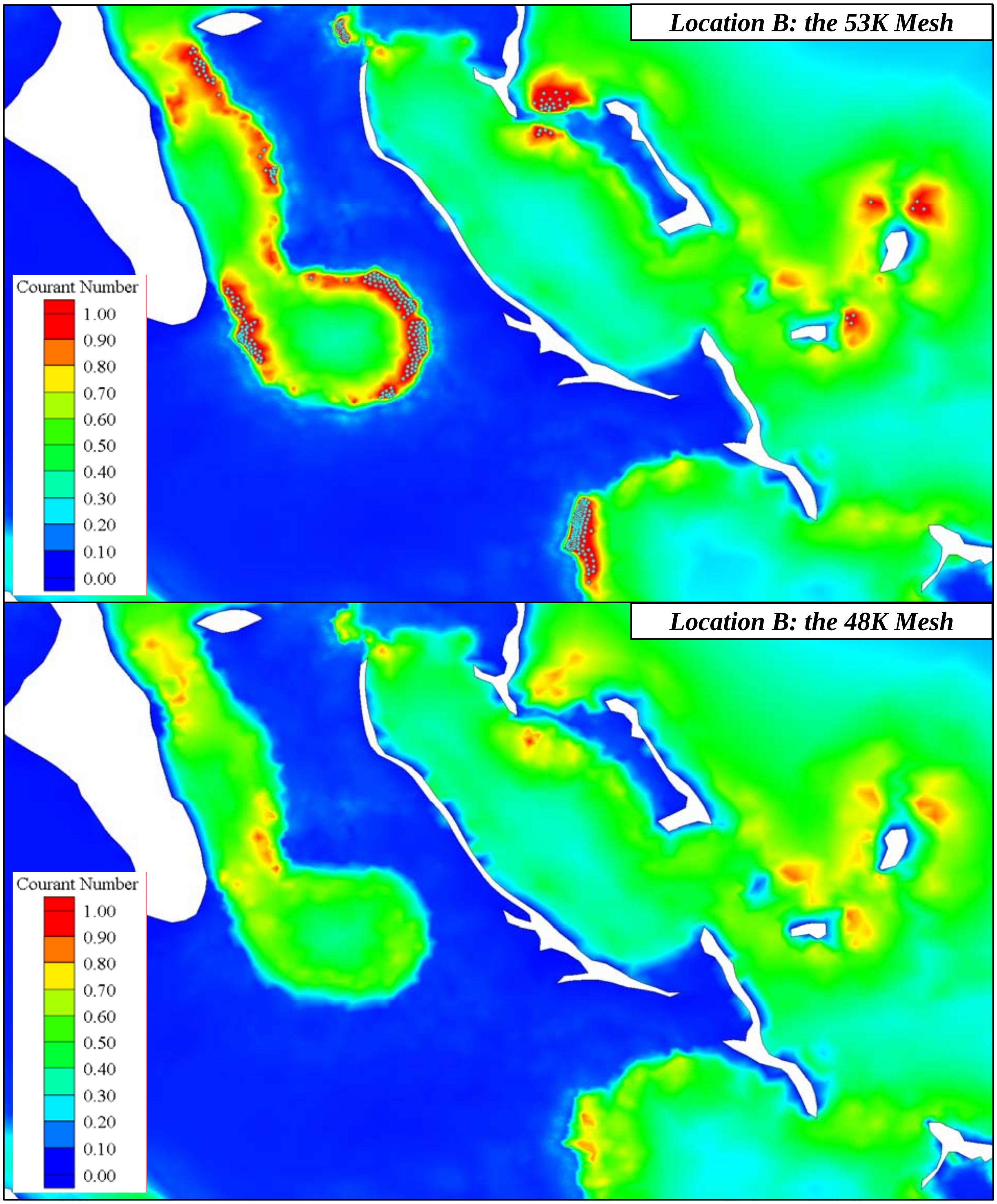

Figure 7-14: Contours of the Courant Number near Andros Island
for the 53K (top) and 48K finite element meshes (bottom).

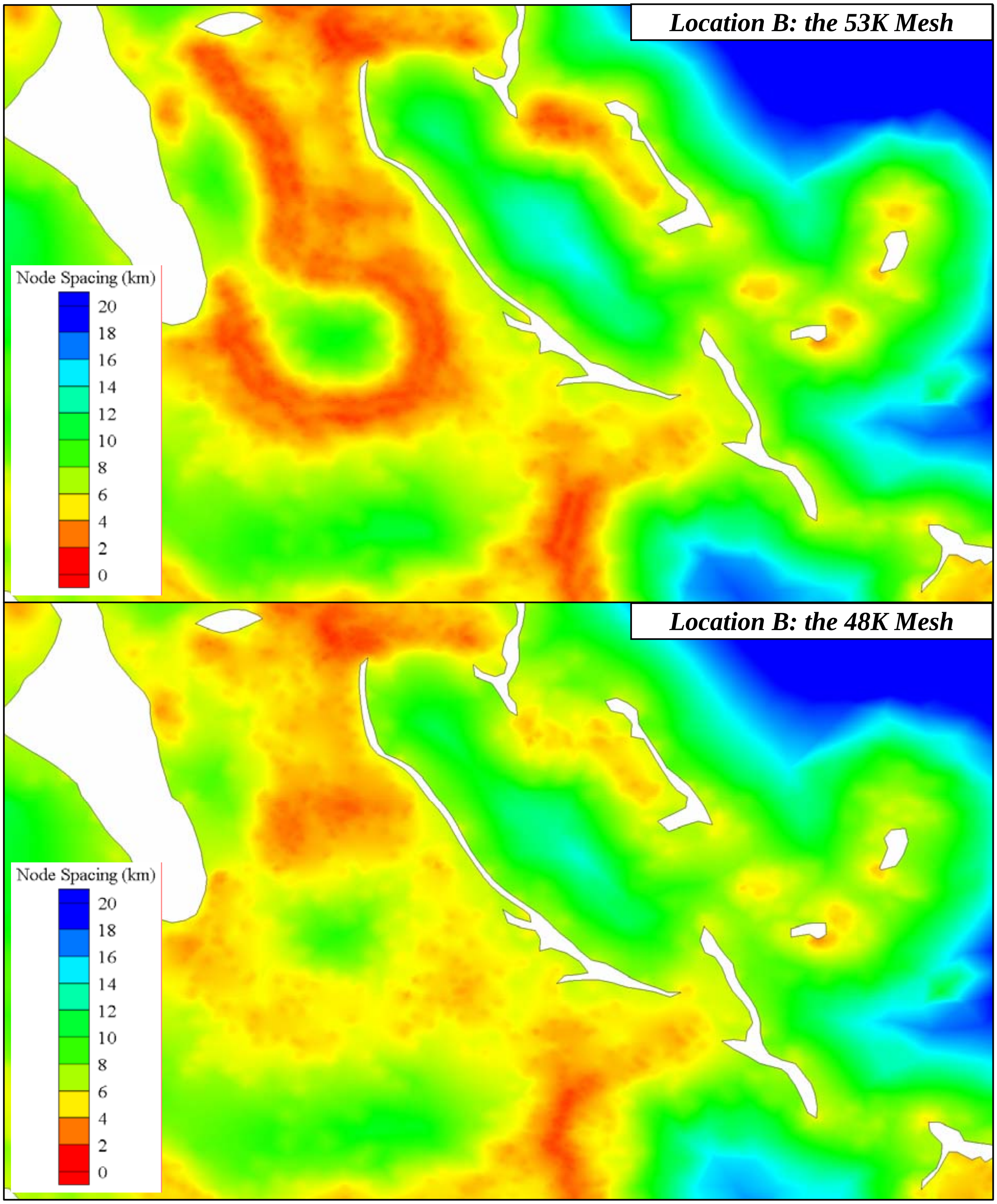

Figure 7-15: Contours of the node spacing near Andros Island for the 53K (top) and 48K finite element meshes (bottom).

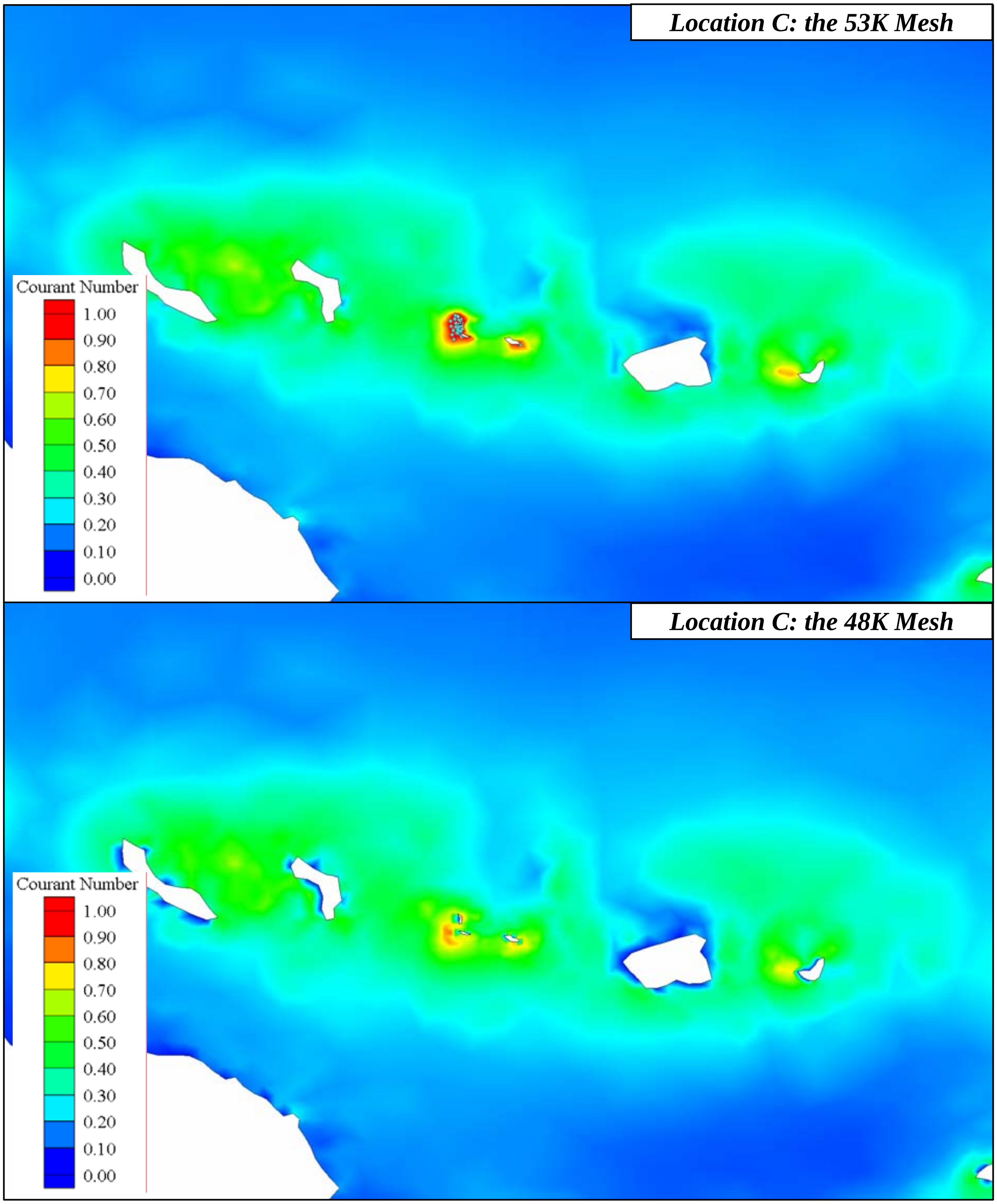

Figure 7-16: Contours of the Courant Number near Willemstad, Curacao Antilles for the 53K (top) and 48K finite element meshes (bottom).

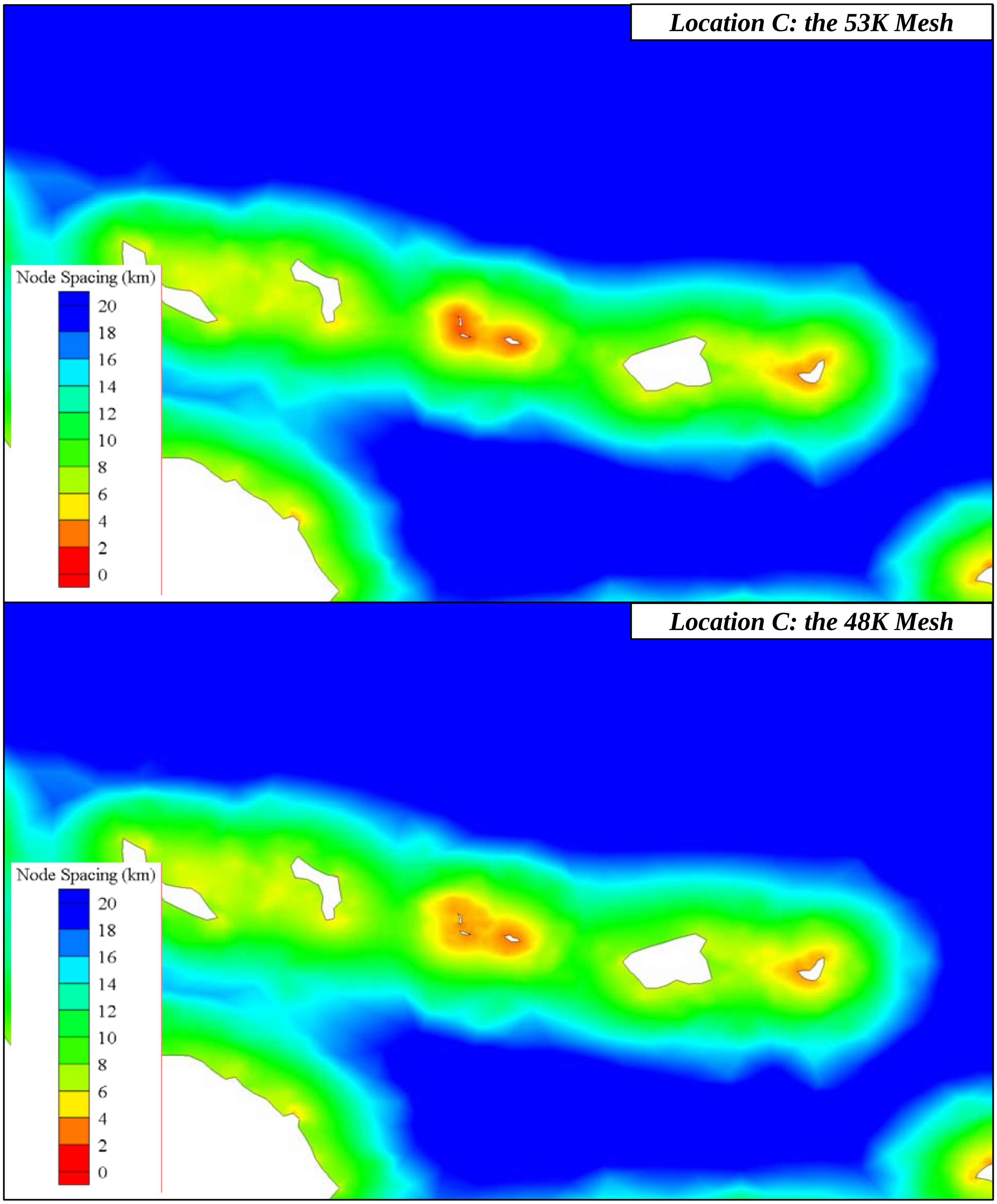

Figure 7-17: Contours of the node spacing near Willemstad, Curacao Antilles for the 53K (top) and 48K finite element meshes (bottom).

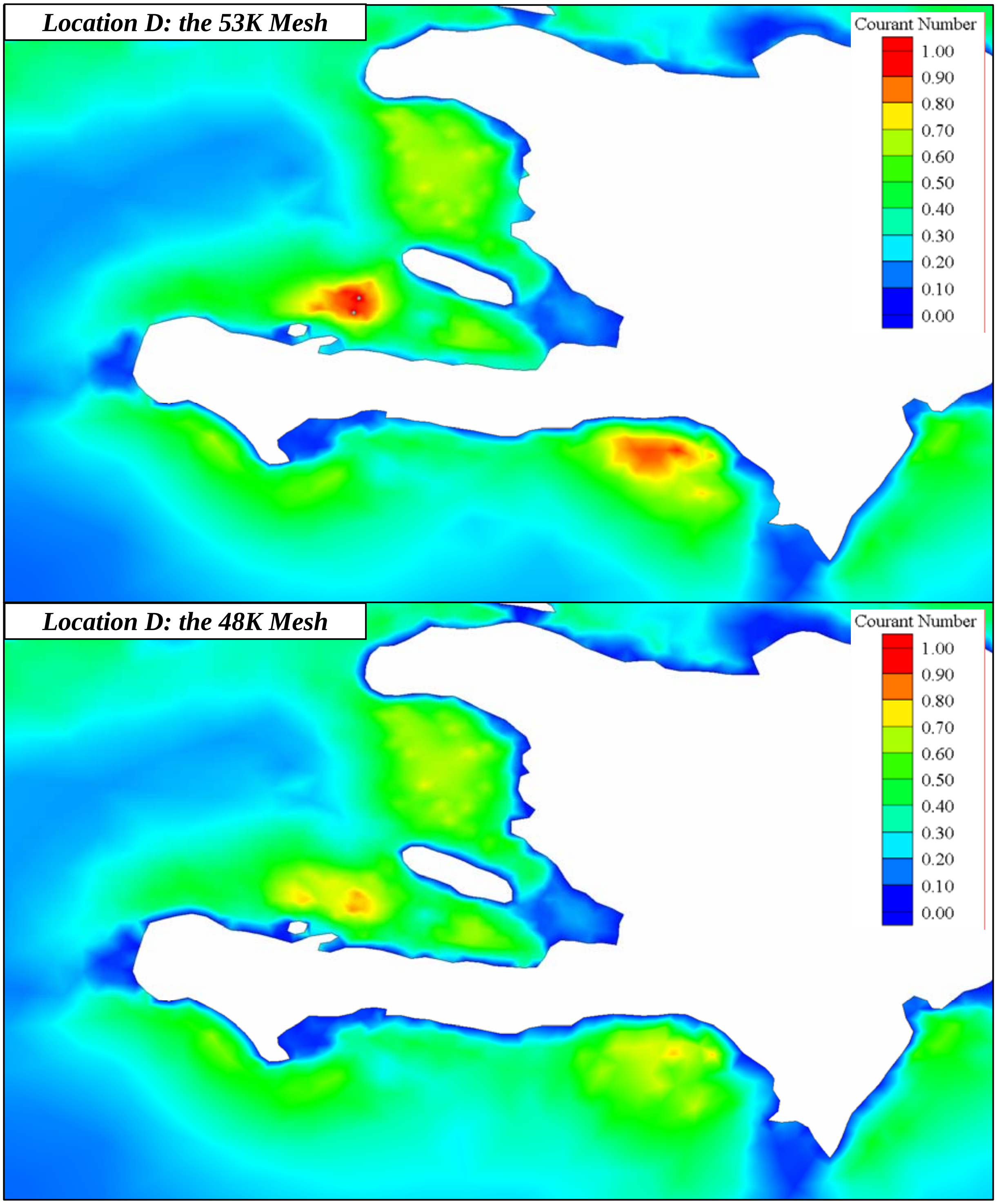

Figure 7-18: Contours of the Courant Number near Port-au-Prince, Haiti for the 53K (top) and 48K finite element meshes (bottom).

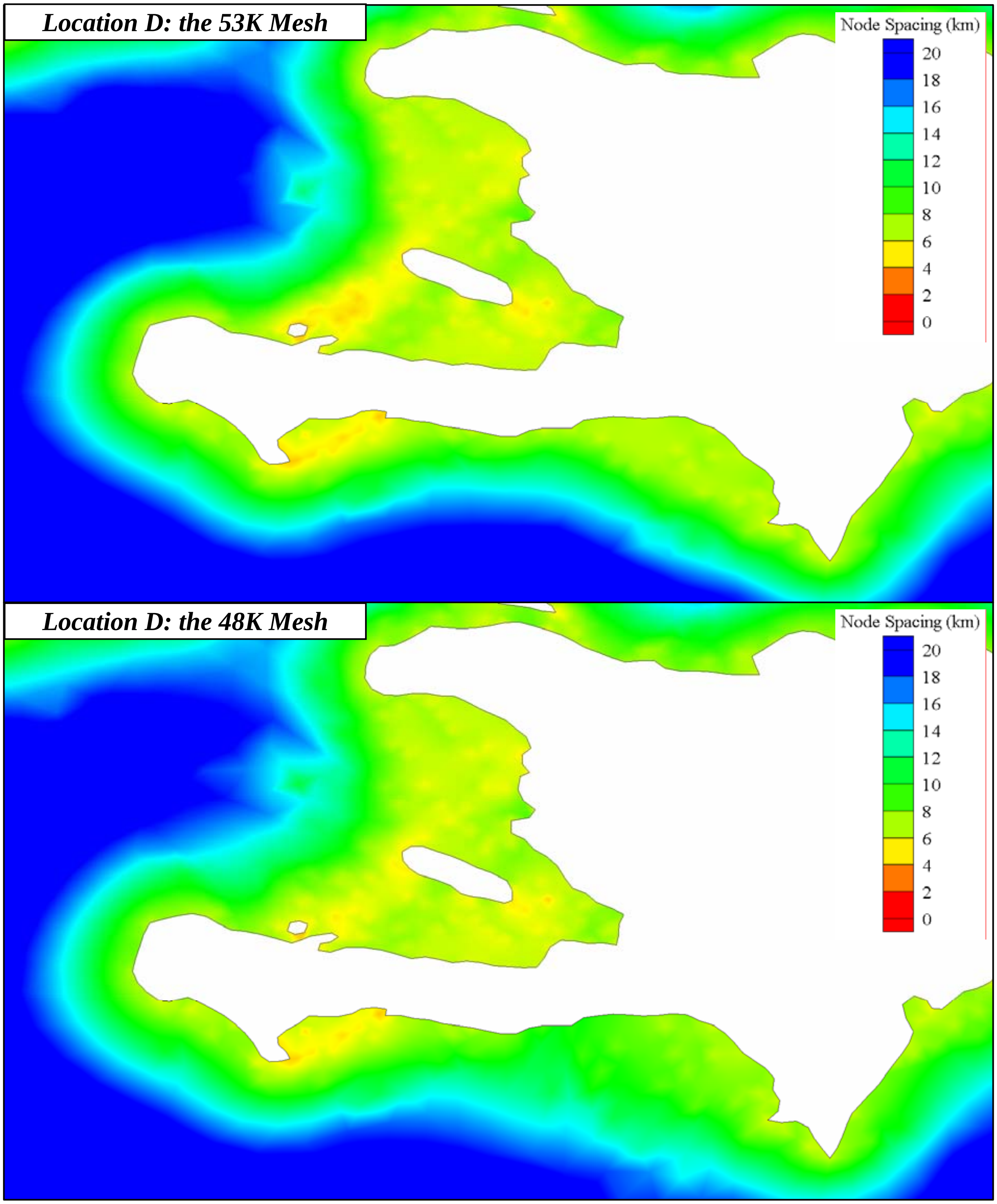

Figure 7-19: Contours of the node spacing near Port-au-Prince, Haiti for the 53K (top) and 48K finite element meshes (bottom).

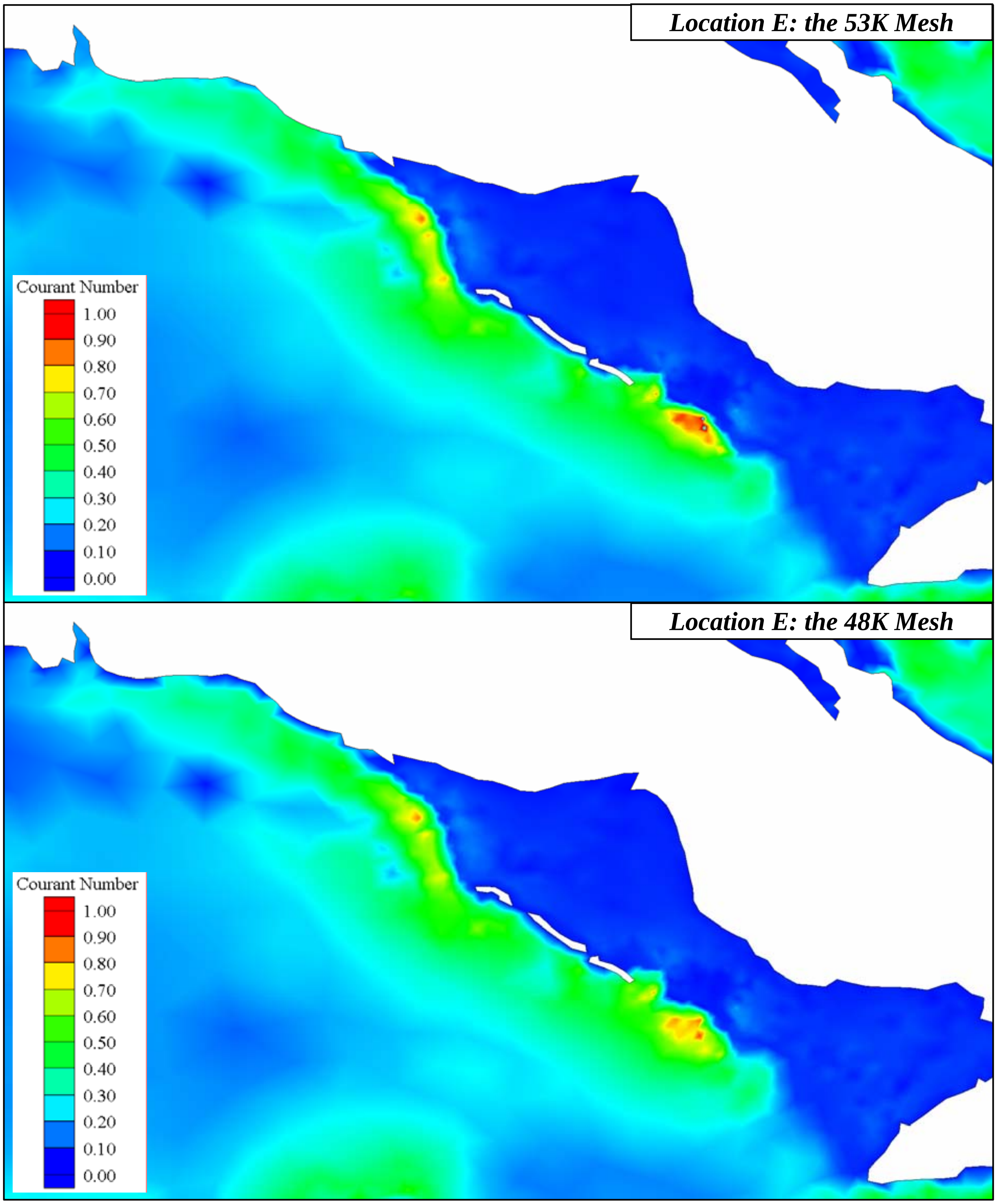

Figure 7-20: Contours of the Courant Number near Casilda, Cuba for the 53K (top) and 48K finite element meshes (bottom).

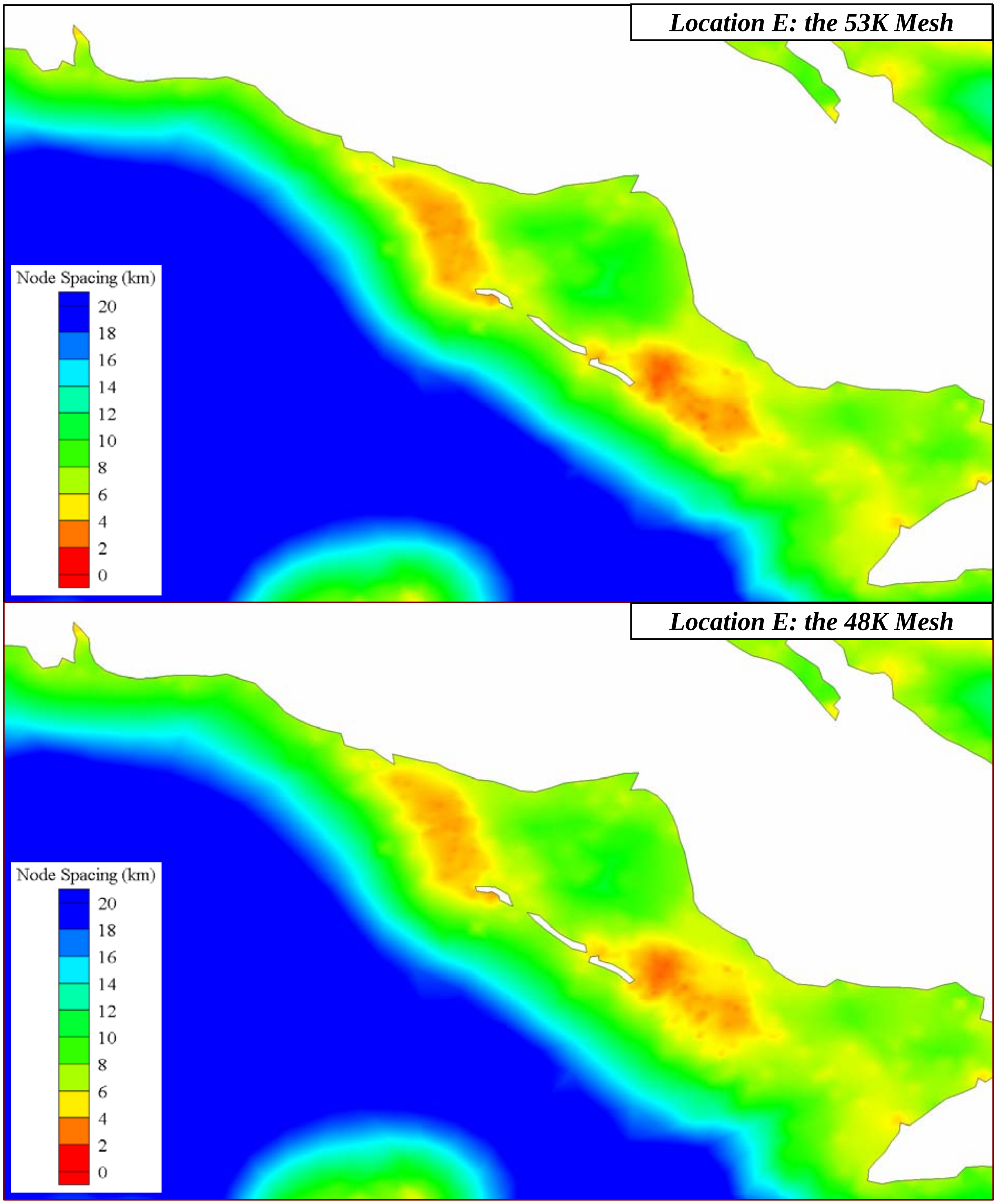

Figure 7-21: Contours of the node spacing near Casilda, Cuba for the 53K (top) and 48K finite element meshes (bottom).

Figures 7-12, 7-14, 7-16, 7-18, and 7-20 represent contours of the Courant Number for the 53K and 48K finite element meshes. The contours in these figures are changed as the Courant Number value is varied. Red areas correspond to regions of high Courant Number values and blue areas are associated with regions of low Courant Number values. Additionally, there are small dots inside of the regions of high Courant Number values in the 53K finite element mesh. These small dots symbolize that the Courant Number value at this computational node exceeds 1.0. Therefore, the finite element mesh around these areas must be relaxed.

Figures 7-13, 7-15, 7-17, 7-19, and 7-21 show contours of the node spacing for the 53K and 48K finite element meshes. When node spacing is changed from a smaller value to a larger value, the contours in these figures are also varied from red to blue. These figures are very useful to understand how the node spacing of the 53K finite element mesh is transformed to arrive at the 48K finite element mesh node spacing in order to relax the finite element mesh at certain location of the 53K mesh.

The location of Figure 7-12 is near Settlement Point, Grand Bahamas. There are many computational nodes that have high Courant Number values in the 53K finite element mesh. In order to reduce these high Courant Number values, some computational nodes and triangular elements are eliminated and then reorganized through manual editing by using the SMS software. There are no computational nodes on the 48K finite element mesh that have a Courant Number value greater than 1.0. Therefore, the 48K mesh is expected to remain numerically stable during simulation. Figure 7-13 represents node spacing contours in this location. It is easy to understand the difference between the 53K and 48K finite element mesh node spacing. Node spacing of the 48K finite element mesh, where the Courant Number value exceed 1.0 in the 53K finite element mesh, is relaxed when it is compared with the 53K finite element mesh node spacing. The location shown in Figures 7-14 and 7-15 is near Andros Island, and the Courant Number-based node reduction procedure follows exactly as that used for the previous location.

Figure 7-16 represents contours of the Courant Number near Willemstad, Curacao Antilles. The procedure of the reduction for the Courant Number value is different from the previous two locations. Since the computational nodes where the Courant Number value exceeds 1.0 are not so numerous as in the 53K finite element mesh, this location does not require the elimination of computational nodes. Hence, the computational nodes are simply repositioned to the outside of the high Courant Number value layer bit by bit in order to increase node spacing and change the depth at that node. There are no regions of high Courant Number values. Consequently, the 48K finite element mesh should not generate local numerical instability around this location. Figure 7-17 shows contours of the node spacing at this location. It is easy to recognize that the 48K finite element mesh has larger node spacing than the 53K finite element mesh where the Courant Number exceeded 1.0 in the 53K finite element mesh. The location shown in Figures 7-18 and 7-19 is near Port-au-Prince, Haiti, and the location shown in Figures 7-20 and 7-21 is near Casilda, Cuba. These two locations have two computational nodes, which have the Courant Number problem. However, it can be solved by applying the same procedure as was done near the Willemstad, Curacao Antilles region.

The following should be noted about the 48K finite element mesh. The total tidal model domain surface area is of course the same as other meshes (8.347×10^6 km^2). The minimum node spacing is 0.5 km, and the maximum node spacing is 160 km. The average boundary spacing is 6.0 km. These values are identical to the 53K finite element mesh. However, the number of computational nodes and triangular elements is different from the 53K finite element mesh. The 48K finite element mesh includes 47,860 computational nodes and 89,212 triangular elements. The differences of local areas between the 53K and 48K finite element meshes have been described (see Figures 7-1 though 7-21).

7.2 Model Parameterizations and Boundary Conditions Specifications

The simulation settings corresponding to the 48K finite element mesh application are presented in this section. The model parameters and the boundary conditions are exactly the same as other the mesh applications (See section 2 of Chapter 3), except for the applied time step. The 48K finite element mesh is applied using a 30 second time step due to the manual editing procedure performed on the 53K finite element mesh. The remaining model parameterizations and boundary conditions specifications can be referenced in section 2 of Chapter 3.

7.3 Computational Performance

Table 7-1 presents the computational performance corresponding to the 48K finite element mesh application.

Table 7-1: The computational performance of the 53K and 48K finite element mesh applications.

FEM	Total number of computational nodes	Total number of triangular elements	Time step (s)	Run time for 90-day simulation	Run time for 5-day simulation
53K	52,774	98,365	5	27.8 hr	92.7 min
48K	47,860	89,212	30	4.1 hr	13.7 min

It should be noted that the run time for a 5-day simulation is an estimate based on the 90-day simulation. The purpose of presenting this 5-day run time is to appreciate the improvements made to the 53K finite element mesh (i.e., the optimization procedure employed here generated a finite element mesh that is capable of producing accurate tidal simulation results on a real-time basis). The run time for a five days simulation requires only 13.7 minutes. Hence, we expect that this finite element mesh can forecast hurricane storm surge, including tides, before landfall occurs.

7.4 Verification of the Optimized 53K Finite Element Mesh

The 48K finite element mesh described above is employed in fully nonlinear simulation of the astronomical tides, as detailed in Chapter 3. This section evaluates a resynthesis of the 48K finite element mesh harmonic constituents (23 harmonic constituents) (see Table 6-1) derived from the model results by applying historical harmonic constituents (maximum 37 harmonic constituents) (see Table 5-2) obtained from 150 tidal stations. Both harmonic constituents from the 48K finite element mesh application and 150 historical tidal stations are only the astronomical tides and do not include other factors (e.g., freshwater inflow). In order to evaluate the 48K finite element mesh results, qualitative, based on visual sense by applying resynthesized plots, and quantitative, premised on statistics, are utilized within the entire tidal model domain. Figure 7-22 represents the WNAT model domain with nine selected tidal stations. The qualitative comparison includes historical data and the 48K finite element mesh results by using resynthesized plots (Figures 7-23 through 7-25), and the quantitative comparison, includes the 53K and 48K finite element mesh results by examining phase and amplitude performance (Table 7-2), for these nine tidal stations are described in this section. Since there is no significant difference between the 53K and 48K finite element mesh results, the resynthesized plots do not contain curves of the 53K finite

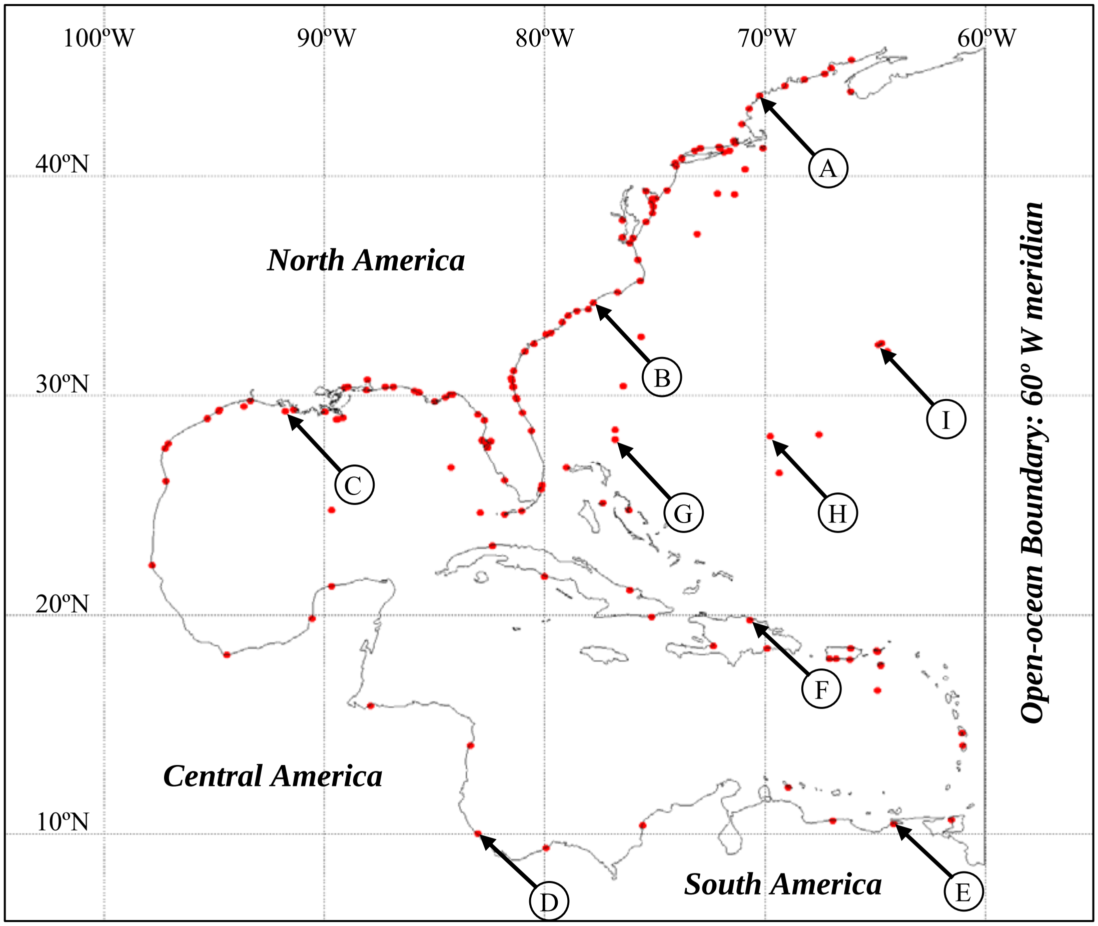

Figure 7-22: Location of 150 historical tidal stations
throughout the WNAT model domain
and identification of nine selected stations (A-I) for resynthesized plots.

element mesh results. Additionally, the quantitative comparison corresponding to both the 53K and 48K finite element mesh results, for the entire WNAT model domain is also presented (Tables 7-3 through 7-5). It should be noted that the qualitative and quantitative comparison results at each single tidal station is illustrated in Appendix E, along with other information. Although the resynthesized plots consist of only historical data and the best simulation results of the 333K, 95K, 60K, 53K and 48K finite element meshes, it gives an indication of the 48K finite element mesh performance since there is not a significant difference between each simulation results.

Figures 7-23 through 7-25 display plots of the resythesized tides for nine separate stations, the locations of which are shown in Figure 7-22. All plots include a blue thick solid curve to represent resynthesized historical harmonic data and a red thin solid curve that is characteristic of the 48K finite element mesh simulation result. Again, there is no curve for the 53K finite element mesh results because it is difficult to see the difference with the 48K finite element mesh results on resynthesized plots. More specific information for the resynthesized plots has been described in Chapter 6.

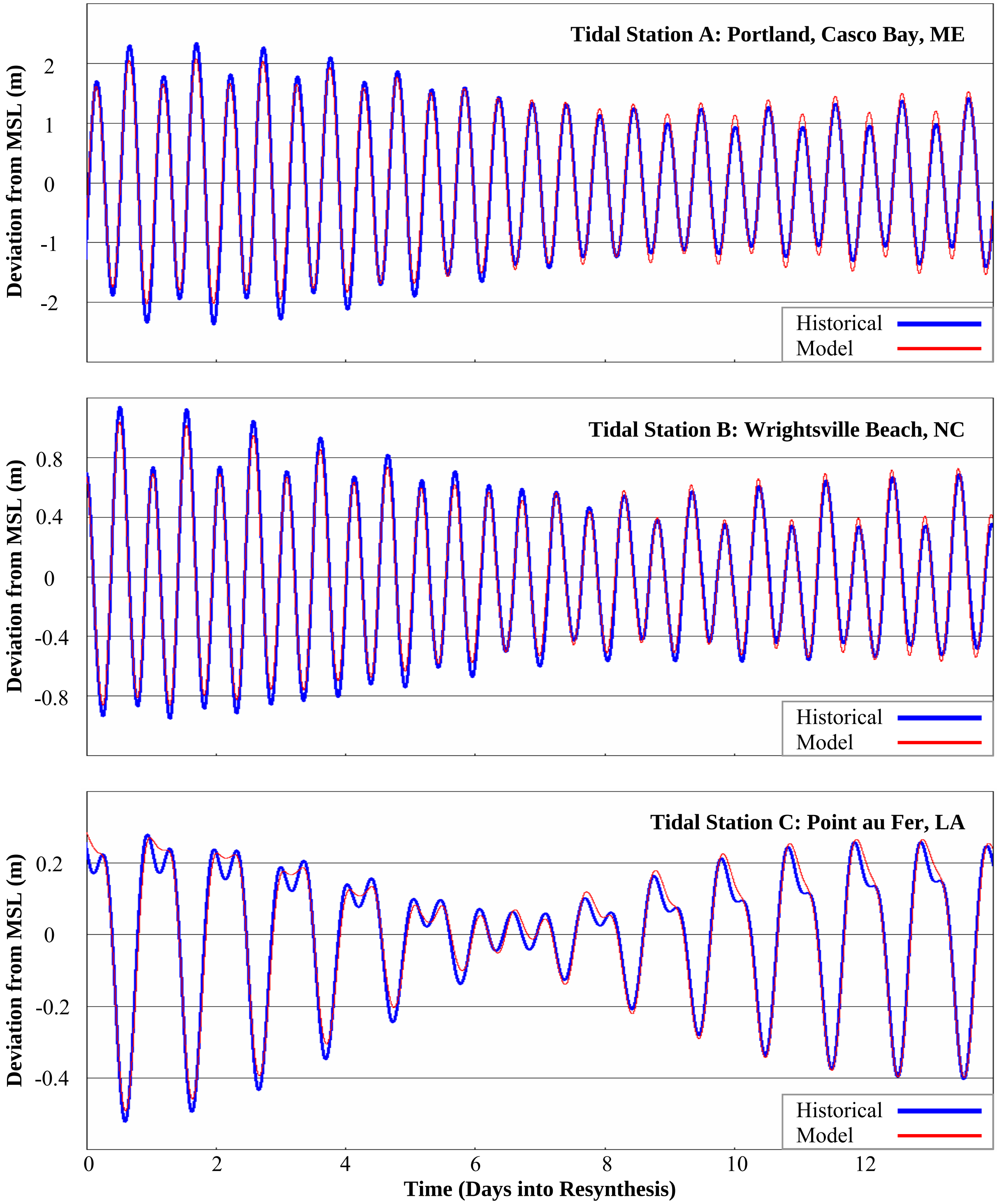

Figure 7-23: A resynthesis of historical and modeled tidal constituents for a complete spring and neap tidal cycle at selected stations A, B, and C (see Figure 7-22 for station locations).

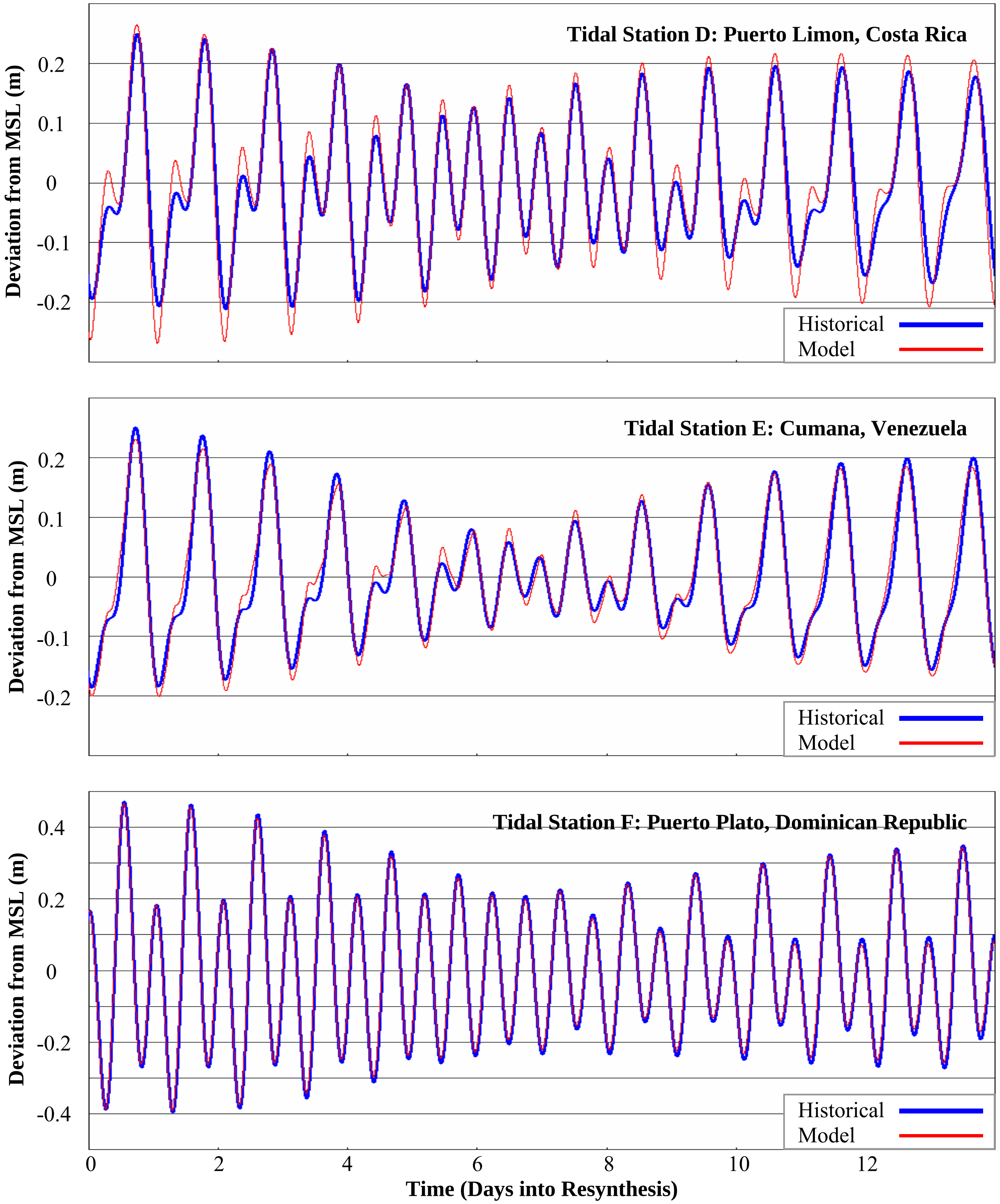

Figure 7-24: A resynthesis of historical and modeled tidal constituents for a complete spring and neap tidal cycle at selected stations D, E, and F (see Figure 7-22 for station locations).

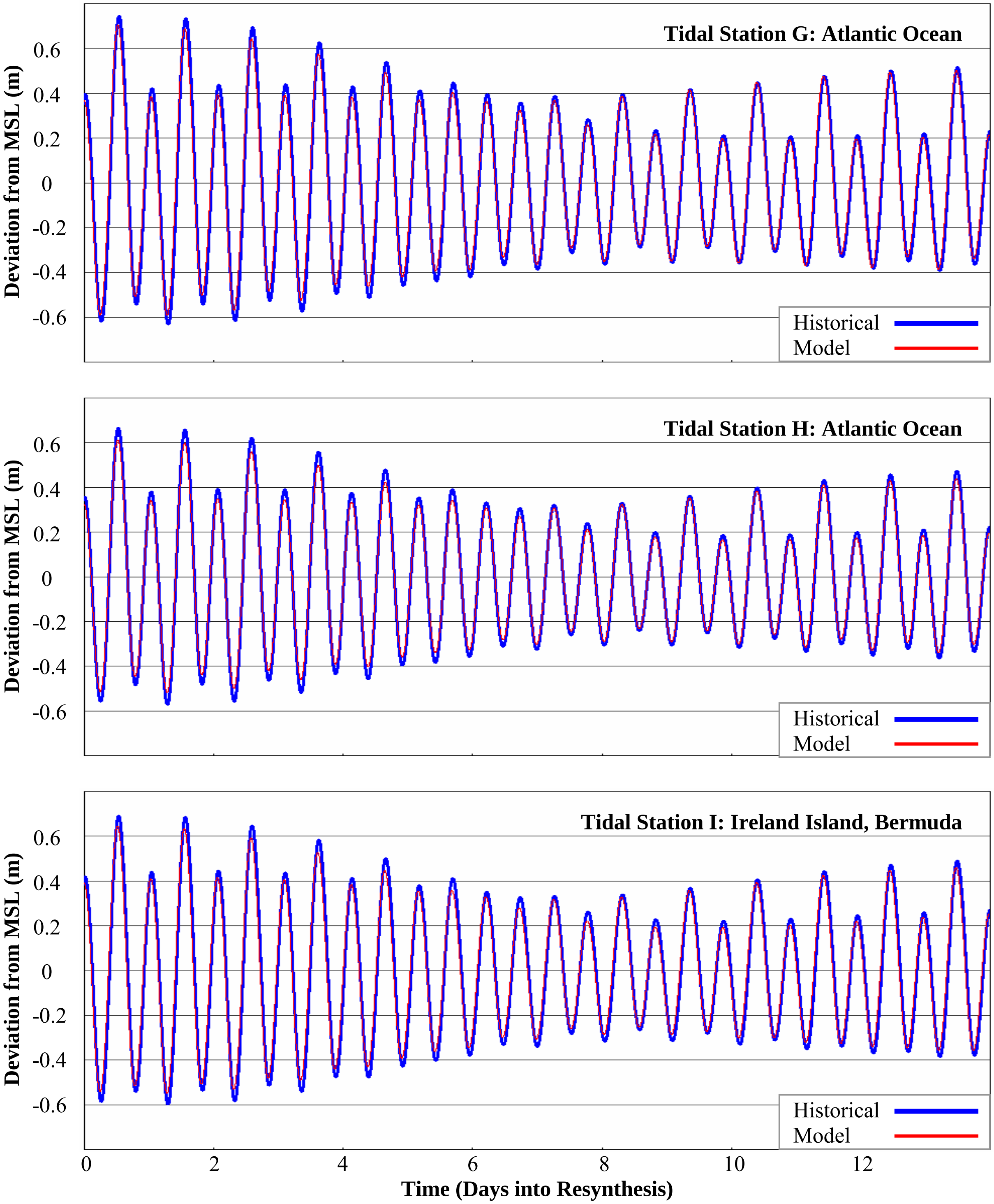

Figure 7-25: A resynthesis of historical and modeled tidal constituents for a complete spring and neap tidal cycle at selected stations G, H, and I (see Figure 7-22 for station locations).

Tables 7-2 through 7-5 indicate quantitative comparisons, which include phase error and the Coefficient of Determination. Since a description for the phase error and the Coefficient of Determination has been given in Chapter 6, only the 53K and 48K finite element mesh results are pointed out.

Table 7-2 presents the phase errors and R^2 values at each of the nine tidal stations identified in Figure 7-22. From Table 7-2, the poorest phasing for the 48K finite element mesh is exhibited at Station C. However, since the model response is only approximately 25 minutes (12.3 degree) out of phase with the historical resynthesized tidal signal, it is difficult to distinguish poor phasing over the 14-day period by using any of the nine stations. Additionally, the maximum difference between the 53K and 48K finite element mesh results for nine tidal stations (the 53K finite element mesh result is better than the 48K finite element mesh result) is only about 8 minutes (4.0 degree) over the 14-day period at the same tidal station. Therefore, the 48K finite element mesh is shown to perform very well. Conversely, the poorest amplitude performance that is recorded in Table 7-2 for Station D is recognized as such in the resynthesized plot shown in Figure 7-23. Furthermore, amplitude performance of the 48K finite element mesh matches or exceeds that of the 53K finite element mesh performance for these nine tidal stations.

Table 7-2: Phase errors and R^2 values for resynthesized plots shown in Figures 7-23 through 7-25.

		53K finite element mesh	48K finite element mesh
Station A	Phase error [º]	4.2	5.0
	R^2 value [-]	0.99	0.99
Station B	Phase error [º]	3.2	4.3
	R^2 value [-]	0.98	0.99
Station C	Phase error [º]	8.3	12.3
	R^2 value [-]	0.98	0.98
Station D	Phase error [º]	1.9	1.7
	R^2 value [-]	0.93	0.93
Station E	Phase error [º]	3.5	3.6
	R^2 value [-]	0.95	0.95
Station F	Phase error [º]	5.7	6.3
	R^2 value [-]	1.00	1.00
Station G	Phase error [º]	11.6	11.7
	R^2 value [-]	0.99	0.99
Station H	Phase error [º]	3.5	3.5
	R^2 value [-]	0.99	0.99
Station I	Phase error [º]	11.4	11.1
	R^2 value [-]	0.99	0.99

Table 7-3 provides overall model performance for the 53K and 48K finite element meshes with respect to phase error and the Coefficient of Determination. For all 150 tidal stations, the average phase error is 10.2 degrees for the 53K finite element mesh and 10.5 degrees for the 48K finite element mesh. There is 0.3 degree difference between these two results. However, the R^2 value for the 48K finite element mesh corresponds to an excellent result (average 0.97 Coefficient of Determination), which is exactly the same as the 53K finite element mesh performance. Overall, the 48K finite element mesh produces almost the same accuracy of the 53K finite element mesh in both phase and amplitude.

Table 7-3: Phase errors and R^2 values for 150 tidal stations.

	53K mesh	48K mesh
Lowest phase error [º]	0.2	0.0
Highest phase error [º]	35.9	34.5
Average phase error [º]	10.2	10.5

	53K mesh	48K mesh
Lowest R^2 value [-]	0.58	0.58
Highest R^2 value [-]	1.00	1.00
Average R^2 value [-]	0.97	0.97

Table 7-4 is included to differentiate the distribution of phase errors and R^2 values in an attempt to further distinguish the 53K and 48K finite element mesh performances. Both phase errors and R^2 values are sorted into seven categories that represent superior (0º ≤ phase error ≤ 2º and 0.98 ≤ R^2 value ≤ 1) to unacceptable results (50º < phase error and R^2 value < 0.50). Neither the 53K and 48K finite element mesh results exhibit unacceptable results as previously defined. 86 tidal stations yielded less than 10 degree phase errors, and 125 tidal stations produced more than 0.90 R^2 values from the 48K finite element mesh application. From the 53K finite element mesh application, there are 87 tidal stations, which is less than 10 degree phase error, and 125 tidal stations, which have more than 0.90 R^2 values. There is no significant difference between both simulations in this evaluation procedure, too.

Table 7-4: Breakdown of phase errors (P.E.) and R^2 value for 150 tidal stations.

	53K mesh	48K mesh
Interval	$0^{\circ} \leq$ P.E. $\leq 2^{\circ}$	
Number of tidal stations	18	19
Lowest phase error	0.2	0.0
Highest phase error	1.9	1.8
Average phase error	1.1	0.8
Interval	$2^{\circ} <$ P.E. $\leq 5^{\circ}$	
Number of tidal stations	36	34
Lowest phase error	2.1	2.1
Highest phase error	4.9	5.0
Average phase error	3.5	3.8
Interval	$5^{\circ} <$ P.E. $\leq 10^{\circ}$	
Number of tidal stations	33	33
Lowest phase error	5.2	5.1
Highest phase error	9.9	9.9
Average phase error	7.5	7.7
Interval	$10^{\circ} <$ P.E. $\leq 20^{\circ}$	
Number of tidal stations	41	42
Lowest phase error	10.2	10.3
Highest phase error	19.1	19.5
Average phase error	14.0	14.5
Interval	$20^{\circ} <$ P.E. $\leq 30^{\circ}$	
Number of tidal stations	19	17
Lowest phase error	20.1	20.3
Highest phase error	29.9	29.5
Average phase error	23.8	23.7
Interval	$30^{\circ} <$ P.E. $\leq 50^{\circ}$	
Number of tidal stations	3	5
Lowest phase error	31.5	30.3
Highest phase error	35.9	34.5
Average phase error	33.6	32.4
Interval	$50^{\circ} <$ P.E.	
Number of tidal stations	0	0
Lowest phase error	N/A	N/A
Highest phase error	N/A	N/A
Average phase error	N/A	N/A

	53K mesh	48K mesh
Interval	$0.98 \leq R^2 \leq 1$	
Number of tidal stations	41	41
Lowest R^2 value	0.98	0.98
Highest R^2 value	1.00	1.00
Average R^2 value	0.99	0.99
Interval	$0.95 \leq R^2 < 0.98$	
Number of tidal stations	51	46
Lowest R^2 value	0.95	0.95
Highest R^2 value	0.97	0.97
Average R^2 value	0.97	0.97
Interval	$0.90 \leq R^2 < 0.95$	
Number of tidal stations	33	38
Lowest R^2 value	0.90	0.90
Highest R^2 value	0.94	0.94
Average R^2 value	0.92	0.92
Interval	$0.80 \leq R^2 < 0.90$	
Number of tidal stations	19	18
Lowest R^2 value	0.80	0.80
Highest R^2 value	0.89	0.89
Average R^2 value	0.85	0.85
Interval	$0.70 \leq R^2 < 0.80$	
Number of tidal stations	1	2
Lowest R^2 value	0.76	0.76
Highest R^2 value	0.76	0.79
Average R^2 value	0.76	0.78
Interval	$0.50 \leq R^2 < 0.70$	
Number of tidal stations	5	5
Lowest R^2 value	0.58	0.58
Highest R^2 value	0.66	0.66
Average R^2 value	0.62	0.63
Interval	$R^2 < 0.50$	
Number of tidal stations	0	0
Lowest R^2 value	N/A	N/A
Highest R^2 value	N/A	N/A
Average R^2 value	N/A	N/A

The number of tidal stations with R^2 values of 0.98 or higher while being within 10.0 degree of phase is counted. The 48K finite element mesh led to 29 tidal stations attaining R^2 values of 0.98 or higher while being within 10.0 degree phase errors and 12 tidal stations reaching more than 0.98 goodness of amplitude fit while being within more than 10.0 degree phase errors. These numbers are exactly the same as the 53K finite element mesh application.

Table 7-5 presents a regional assessment of the phase errors and R^2 values. The separated regions are along the East Coast of the North America, within the Gulf of Mexico, along the Central and South American coasts, in or around the Caribbean Sea islands, and in the deep Atlantic Ocean and near Bermuda. The 48K finite element mesh also performs excellent in the deep Atlantic Ocean, and these results are translated to the tidal stations of the East Coast. However, for the Gulf of Mexico region and along the Central and South American coastlines, clearly less favorable results are exhibited. Finally, there is a little difference, which is maximum 0.7 degree in five regions, between the 53K and 48K finite element mesh results in phase (the 53K finite element mesh results are better than the 48K finite element mesh results). Additionally, there is no difference in the Coefficient of Determination within these five regions.

Table 7-5: Regional phase errors and R^2 values for 150 tidal stations.

		53K mesh		48K mesh	
Region	Number of tidal stations	Phase error [º]	R^2 value [-]	Phase error [º]	R^2 value [-]
East Coast of North America	62	11.2	0.98	11.4	0.98
Gulf of Mexico	44	10.4	0.91	11.1	0.91
Central and South American coasts	9	10.1	0.90	9.2	0.90
Caribbean Sea islands	20	10.4	0.95	10.9	0.95
Atlantic Ocean and Bermuda	15	4.8	0.99	5.0	0.99

CHAPTER 8

CONCLUSIONS AND FUTURE WORK

Chapter 8 presents conclusions and future work for this research. The goal of this study was to generate a computationally efficient finite element mesh for the WNAT model domain with the same level of accuracy as a standard computational grid (the 333K finite element mesh). In order to obtain a more optimal finite element mesh for this large domain, a LTEA was utilized to produce three coarser computational grids (the 95K, 60K, and 53K finite element meshes). Furthermore, optimization of the 53K finite element mesh was implemented in efforts to arrive at an optimal computational grid (the 48K finite element mesh) for the WNAT model domain.

8.1 Conclusions

Four computational grids (the 333K, 95K, 60K, and 53K finite element meshes) produced highly accurate solutions when they were compared with historical data. Although the 333K finite element mesh produced the best results, there is not a significant difference with the other three coarser finite element meshes. From these three coarser finite element mesh results, it was realized that the 6 km spaced boundary was more compatible with the LTEA-generated node spacing guidelines with the 53K finite element mesh as the target element sizes. Therefore, the element size transitions were most consistent for the 53K finite element mesh. The 60K finite element mesh, which uses 5 km node spacing along the boundary, applied too many nodes along the coastline with no extra geometric detail added that might enhance the solution. However, these coastal nodes did enhance local phase and amplitude performance since transition constraints resulted in more nearshore computational points. While the 95K finite element mesh included the most interior computational nodes of all the LTEA-based finite element meshes, the additional nodes were under-utilized because of the specified element size transition requirements.

One of the outcomes of coarsening the mesh is to smooth out the bathymetry (see Figures 4-10 and 4-11). The fact that such a loss of bathymetric resolution (e.g. when reducing from the 333K to the 53K finite element mesh) does not spoil the relative results indicates that the bathymetric data set may contain significant features that are unimportant to the tidal physics described. Further, consider that the Gulf of Mexico and Caribbean Sea are separate basins. In order to describe flow into and out of these basins, the inflow and outflow pathways must be well resolved, e.g. flow through the Strait of Florida around the southern tip of Florida (see Figure 3-2). Poorer results in these basins must be directly related to inaccurate descriptions of local inflow and outflow topographies. As a result, the methodology presented herein has potential for assessing the importance and accuracy of bathymetric data.

Optimization of the 53K finite element mesh was implemented to generate an optimal computational grid (the 48K finite element mesh) for the WNAT model domain. The main purpose of this procedure included a reduction in the number of computational nodes and an increase in the applied time step without sacrificing computational accuracy. It is important to note that these two grid parameters are interrelated between the relationship provided by the

Courant number criterion (i.e., nodal density relaxation results in an increased applied time step). Although the 48K finite element mesh produced a little bit worse results than the 53K finite element mesh, it is still assessed the best finite element mesh to simulate astronomical tide in the Western North Atlantic Ocean because of the significant increase in computational efficiency. The 48K finite element mesh succeeded in reducing computational run times by approximately one-seventh of the 53K finite element mesh run time. Again, this computational speedup is realized by reducing the number of computational nodes in order to drive up the applied time step based on the Courant number criterion. As a result, a revolutionary finite element mesh was developed for hydrodynamic calculations in a large domain. Clearly the research presented herein can aid other hydrodynamic studies where unstructured meshes are employed.

8.2 Future Work

This section describes future work related to this research, which can be separated into the following categories:

Future Work 1:	The 48K finite element mesh will be applied to simulate historical storm tides in the WNAT model domain.
Future Work 2:	The model will be tested with the inclusion of short wave actions in order to obtain more accurate results for storm tides.
Future Work 3:	The 48K finite element mesh will be used to forecast real-time storm tides in the WNAT model domain.

Future Work 4: In addition, the 48K finite element mesh will be utilized for local area studies by incorporating more specific geographic features, e.g. rivers, floodplains, and estuaries, into the computational domain.

Future Work 5: Mesh generation as described in this study can be used as a basis for three-dimensional grid development.

APPENDIX A

ADCIRC-2DDI INPUT FILE: MESH DESCRIPTION (333K MESH)

```
333K finite element mesh for WNAT model domain
647018  332582
1  -60.0400000000    8.5596800000    6.2721881866
2  -60.0400000000    8.5858220000    6.2725310326
3  -60.0400000000    8.6119650000    9.5620222092
```

Input file of this portion is abbreviated.

```
332580  -90.2890130000  30.0088940000    0.0870342106
332581  -90.2858920000  30.0167570000    0.0810440034
332582  -90.2858920000  30.0121580000    0.0633030310
1    3      1     2   293
2    3   293     2   294
3    3      2     3   294
```

Input file of this portion is abbreviated.

```
647016    3 332578 332581 332579
647017    3 332582 332581 332578
647018    3 332580 332582 332578
1 = Number of open boundaries
292 = Total number of open boundary nodes
292 = Number of nodes for open boundary 1
1
2
3
```

Input file of this portion is abbreviated.

```
290
291
292
116 = Number of land boundaries
18094 = Total number of land boundary nodes
11341 1 = Number of nodes for land boundary 1
303827
304996
304995
```

Input file of this portion is abbreviated.

```
41441
41440
42221
```

APPENDIX B

ADCIRC-2DDI INPUT FILE: PARAMETERS (333K MESH)

```
90-day simulation with 333K ! 32 CHARACTER ALPHANUMERIC RUN DESCRIPTION
No.1:  ! 24 CHARACTER ALPANUMERIC RUN IDENTIFICATION
1      ! NFOVER - NONFATAL ERROR OVERRIDE OPTION
0      ! NABOUT - ABREVIATED OUTPUT OPTION PARAMETER
0      ! NSCREEN - UNIT 6 OUTPUT OPTION PARAMETER
0      ! IHOT - HOT START PARAMETER
2      ! ICS - COORDINATE SYSTEM SELECTION PARAMETER
0      ! IM - MODEL SELECTION PARAMETER
2      ! NOLIBF - BOTTOM FRICTION TERM SELECTION PARAMETER
2      ! NOLIFA - FINITE AMPLITUDE TERM SELECTION PARAMETER
0      ! NOLICA - SPATIAL DERIVATIVE CONVECTIVE SELECTION PARAMETER
0      ! NOLICAT - TIME DERIVATIVE CONVECTIVE TERM SELECTION PARA.
0      ! NWP – VAR. BOTTOM FRICTION & LATERAL VISCOSITY OPTION PARA.
1      ! NCOR - VARIABLE CORIOLIS IN SPACE OPTION PARAMETER
1      ! NTIP - TIDAL POTENTIAL OPTION PARAMETER
0      ! NWS - WIND STRESS AND BAROMETRIC PRESSURE OPTION PARAMETER
1      ! NRAMP - RAMP FUNCTION OPTION
9.81   ! G - ACCELERATION DUE TO GRAVITY - DETERMINES UNITS
-0.01  ! TAU0 - WEIGHTING FACTOR IN GWCE
4.0    ! DT - TIME STEP (IN SECONDS)
0.00   ! STATIM - STARTING TIME (IN DAYS)
0.00   ! REFTIM - REFERENCE TIME (IN DAYS)
90.0   ! RNDAY - TOTAL LENGTH OF SIMULATION (IN DAYS)
20.0   ! DRAMP - DURATION OF RAMP FUNCTION (IN DAYS)
0.35   0.30   0.35       ! TIME WEIGHTING FACTORS FOR THE GWCE EQUATION
0.1   2   1   0.05       ! H0, NODEDRYMIN, NODEWETRMP, VELMIN
-79.0   35.0             ! SLAM0, SFEA0 - CENTER OF CPP PROJECTION
0.0025   1.0   10.0   0.33333  ! FFACTOR, HBREAK, FTHETA, FGAMMA
5.00   ! ESL - LATERAL EDDY VISCOSITY COEFFICIENT; IGNORED IF NWP=1
0.0    ! CORI - CORIOLIS PARAMETER - IGNORED IF NCOR = 1
7      ! NTIF - TOTAL NUMBER OF TIDAL POTENTIAL CONSTITUENTS
K1     ! ALPHANUMERIC DESCRIPTION OF TIDAL POTENTIAL FORCING DATA
0.141565   0.000072921158358   0.736   1.000   0.000
O1     ! ALPHANUMERIC DESCRIPTION OF TIDAL POTENTIAL FORCING DATA
0.100514   0.000067597744151   0.695   1.000   0.000
M2     ! ALPHANUMERIC DESCRIPTION OF TIDAL POTENTIAL FORCING DATA
0.242334   0.000140518902509   0.693   1.000   0.000
S2     ! ALPHANUMERIC DESCRIPTION OF TIDAL POTENTIAL FORCING DATA
0.112841   0.000145444104333   0.693   1.000   0.000
N2     ! ALPHANUMERIC DESCRIPTION OF TIDAL POTENTIAL FORCING DATA
0.046398   0.000137879699487   0.693   1.000   0.000
K2     ! ALPHANUMERIC DESCRIPYION OF TIDAL POTENTIAL FORCING DATA
0.030704   0.000145842317201   0.693   1.000   0.000
Q1     ! ALPHANUMERIC DESCRIPTION OF TIDAL POTENTIAL FORCING DATA
```

```
0.019256   0.000064958541129   0.695   1.000   0.000
7        ! NBFR - TOTAL NUMBER OF FORCING FREQUENCIES ON OPEN BOUNDARY
K1       ! ALPHANUMERIC DESCRIPTION OF OPEN BOUNDARY FORCING DATA
0.000072921158358   1.000   0.000
O1       ! ALPHANUMERIC DESCRIPTION OF OPEN BOUNDARY FORCING DATA
0.000067597744151   1.000   0.000
M2       ! ALPHANUMERIC DESCRIPTION OF OPEN BOUNDARY FORCING DATA
0.000140518902509   1.000   0.000
S2       ! ALPHANUMERIC DESCRIPTION OF OPEN BOUNDARY FORCING DATA
0.000145444104333   1.000   0.000
N2       ! ALPHANUMERIC DESCRIPTION OF OPEN BOUNDARY FORCING DATA
0.000137879699487   1.000   0.000
K2       ! ALPHANUMERIC DESCRIPTION OF OPEN BOUNDARY FORCING DATA
0.000145842317201   1.000   0.000
Q1       ! ALPHANUMERIC DESCRIPTION OF OPEN BOUNDARY FORCING DATA
0.000064958541129   1.000   0.000
K1       ! ALPHA NUMERIC DESCRIPTION OF ELEVATION BOUNDARY FORCING
   0.1013   243.05   207   0
   0.1010   242.96   208   0
   0.1008   242.88   232   0
```

Input file of this portion is abbreviated.

```
   0.0925   79.57   254525   0
   0.0933   78.67   254543   0
   0.0944   77.34   254562   0
O1
   0.0860   231.62   207   0
   0.0858   231.58   208   0
   0.0857   231.55   232   0
```

Input file of this portion is abbreviated.

```
   0.0713   331.01   254525   0
   0.0728   330.93   254543   0
   0.0751   330.81   254562   0
M2
   0.5396   223.40   207   0
   0.5364   223.29   208   0
   0.5331   223.17   232   0
```

Input file of this portion is abbreviated.

```
   0.4997   344.95   254525   0
```

```
   0.4993   344.90   254543   0
   0.4988   344.81   254562   0
 S2
   0.1875   275.64   207   0
   0.1865   275.26   208   0
   0.1854   274.87   232   0
```

Input file of this portion is abbreviated.

```
   0.1359   17.26   254525   0
   0.1359   17.18   254543   0
   0.1358   17.07   254562   0
 N2
   0.1168   197.46   207   0
   0.1161   197.42   208   0
   0.1154   197.38   232   0
```

Input file of this portion is abbreviated.

```
   0.1172   323.04   254525   0
   0.1172   322.94   254543   0
   0.1172   322.80   254562   0
 K2
   0.0510   237.47   207   0
   0.0507   237.39   208   0
   0.0503   237.31   232   0
```

Input file of this portion is abbreviated.

```
   0.0302   19.77   254525   0
   0.0302   19.77   254543   0
   0.0301   19.77   254562   0
 Q1
   0.0143   210.72   207   0
   0.0143   210.68   208   0
   0.0143   210.63   232   0
```

Input file of this portion is abbreviated.

```
   0.0174   307.15   254525   0
   0.0177   307.26   254543   0
   0.0182   307.42   254562   0
 100.0  ! ANGINN: INNER ANGLE THRESHOLD
 1   0.0   90.0   225      ! NOUTE, TOUTSE, TOUTFE, NSPOOLE: ELE. ST. OUTPUT INFO.
```

```
 203     ! NUMBER OF ELEV. STATIONS
-66.11666       43.83333        589 Yarmouth, Nova Scotia
-66.05000       45.26666        630 St. John, New Brunswick
-66.98500       44.90333        8410140 Eastport, Passamaquoddy Bay, ME
```

Input file of this portion is abbreviated.

```
-64.69500       32.37000        St. Davids Island, Bermuda
-64.83333       32.31666        417 Ireland Island, Bermuda
-64.43333       32.01666        415 Atlantic Ocean near Bermuda
 0   0.0   90.0   90        ! NOUTV, TOUTSV, TOUTFV, NSPOOLV: VEL. ST. OUTPUT INFO.
 0                          ! TOTAL NUMBER OF VELOCITY RECORDING STATIONS
 0  178.0  180.0  360       ! NOUTGE, TOUTSGE, TOUTFGE, NSPOOLGE: GL. ELE. OUT
 0  178.0  180.0  360       ! NOUTGV, TOUTSGV, TOUTFGV, NSPOOLGV: GL. VEL. OUT
 23                         ! NHARFR - NUMBER OF CONSTITUENTS TO BE INCLUDED
 STEADY                     ! HAFNAM - ALPHA DESCRIPTOR FOR CONSTITUENT NAME
 0.000000000000000  1.0  0.0          ! HAFREQ, HAFF, HAFACE
 MN
 0.000002639203022  1.0  0.0
 SM
 0.000004925201824  1.0  0.0
 O1
 0.000067597744151  1.0  0.0
 K1
 0.000072921158358  1.0  0.0
 MNS2
 0.000132954497662  1.0  0.0
 2MS2
 0.000135593700684  1.0  0.0
 N2
 0.000137879699487  1.0  0.0
 M2
 0.000140518902509  1.0  0.0
 2MN2
 0.000143158105531  1.0  0.0
 S2
 0.000145444104333  1.0  0.0
 2SM2
 0.000150369306157  1.0  0.0
 MN4
 0.000278398601995  1.0  0.0
 M4
 0.000281037805017  1.0  0.0
 MS4
```

```
0.000285963006842  1.0  0.0
2MN6
0.000418917504504  1.0  0.0
M6
0.000421556707526  1.0  0.0
MSN6
0.000423842706328  1.0  0.0
M8
0.000562075610035  1.0  0.0
M10
0.000702594512543  1.0  0.0
P1
0.000072522946000  1.0  0.0
K2
0.000145842317201  1.0  0.0
Q1
0.000064958541129  1.0  0.0
45.0  90.0  75  0.0  ! THAS, THAF, NHAINC, FMV – HAR. ANAL. PARA.
1  0  0  0           ! NHASE, NHASV, NHAGE, NHAGV - CONTROL HAR.ANAL.
1  8640              ! NHSTAR, NHSINC - HOT START FILE GENERATION PARA.
1  0  2.98E-5  25  0 ! ITITER, ISLDIA, CONVCR, ITMAX, ILUMP - ALGEBRAIC SOLUT.
12                   ! MNPROC
```

APPENDIX C

INFORMATION OF 203 TIDAL STATIONS

Station number	**Tidal station name**	**Longitude [decimal deg.]**	**Latitude [decimal deg.]**	**Overseeing agency**
1	589 Yarmouth, Nova Scotia	66.11666 W.	43.83333 N.	IHO
2	630 St. John, New Brunswick	66.05000 W.	45.26666 N.	IHO
3	8410140 EASTPORT, PASSAMAQUODDY BAY , ME	66.98500 W.	44.90333 N.	NOS
4	8411250 CUTLER NAVAL BASE, MACHIAS BAY , ME	67.29667 W.	44.64167 N.	NOS
5	8413320 BAR HARBOR, FRENCHMAN BAY , ME	68.20500 W.	44.39167 N.	NOS
6	8415490 ROCKLAND , ME	69.10167 W.	44.10500 N.	NOS
7	8418150 PORTLAND, CASCO BAY , ME	70.24667 W.	43.65667 N.	NOS
8	8419870 SEAVEY ISLAND, PORTSMOUTH HARBOR , ME	70.74167 W.	43.08000 N.	NOS
9	8423898 FORT POINT, NEWCASTLE ISLAND , NH	70.71167 W.	43.07167 N.	NOS
10	8443970 BOSTON, BOSTON HARBOR , MA	71.05167 W.	42.35500 N.	NOS
11	8447270 BUZZARDS BAY (RR BRIDGE), CAPE COD CANAL, MA	70.61667 W.	41.74167 N.	NOS
12	8449130 NANTUCKET ISLAND, NANTUCKET SOUND , MA	70.09667 W.	41.28500 N.	NOS
13	8447930 WOODS HOLE, BUZZARDS BAY , MA	70.67167 W.	41.52333 N.	NOS
14	8447386 FALL RIVER, HOPE BAY , MA	71.16333 W.	41.70500 N.	NOS
15	8452944 CONIMICUT LIGHT, NARRAGANSETT BAY , RI	71.34333 W.	41.71667 N.	NOS
16	8454049 QUONSET POINT , RI	71.40833 W.	41.58500 N.	NOS
17	8452660 NEWPORT, NARRAGANSETT BAY , RI	71.32667 W.	41.50500 N.	NOS
18	8459681 BLOCK ISLAND, SW END, BLOCK ISLAND SOUND, RI	71.61000 W.	41.16333 N.	NOS
19	8510321 MONTAUK POINT LIGHT , NY	71.85667 W.	41.07167 N.	NOS

Station number	Tidal station name	Longitude [decimal deg.]	Latitude [decimal deg.]	Overseeing agency
20	8510560 MONTAUK, FORT POND BAY , NY	71.96000 W.	41.04833 N.	NOS
21	8510719 SILVER EEL POND, FISHERS IS. , NY	72.03000 W.	41.25667 N.	NOS
22	8461490 NEW LONDON, THAMES RIVER , CT	72.08667 W.	41.35500 N.	NOS
23	8465705 NEW HAVEN, NEW HAVEN HARBOR , CT	72.90833 W.	41.28333 N.	NOS
24	8467150 BRIDGEPORT, BRIDGEPORT HARBOR , CT	73.18167 W.	41.17333 N.	NOS
25	8516945 KINGS POINT, LONG ISLAND SOUND , NY	73.76500 W.	40.81000 N.	NOS
26	8516990 WILLETS POINT, LITTLE BAY, EAST RIVER , NY	73.78167 W.	40.79333 N.	NOS
27	8519024 FORT WADSWORTH, STATEN ISLAND , NY	74.05500 W.	40.60667 N.	NOS
28	8531232 SOUTH AMBOY RARITAN RIVER , NJ	74.28167 W.	40.49167 N.	NOS
29	8531680 SANDY HOOK , NJ	74.01000 W.	40.46667 N.	NOS
30	8534720 ATLANTIC CITY, ATLANTIC OCEAN , NJ	74.41833 W.	39.35500 N.	NOS
31	8536110 CAPE MAY, CAPE MAY CANAL, DELAWARE BAY , NJ	74.96000 W.	38.96833 N.	NOS
32	8537121 SHIP JOHN SHOAL, DELAWARE RIVER , NJ	75.37500 W.	39.30500 N.	NOS
33	8555889 BRANDYWINE SHOAL LIGHT, DELAWARE BAY , DE	75.11333 W.	38.98667 N.	NOS
34	8557380 LEWES, FT. MILES , DE	75.12000 W.	38.78167 N.	NOS
35	8558690 INDIAN RIVER INLET , DE	75.07000 W.	38.61000 N.	NOS
36	8570280 OCEAN CITY, FISHING PIER , MD	75.08333 W.	38.32667 N.	NOS
37	8570283 OCEAN CITY INLET , MD	75.09167 W.	38.32833 N.	NOS
38	8630308 CHINCOTEAGUE CHANNEL, SOUTH END , VA	75.40500 W.	37.90667 N.	NOS

Station number	Tidal station name	Longitude [decimal deg.]	Latitude [decimal deg.]	Overseeing agency
39	8632200 KIPTOPEKE, CHESAPEAKE BAY , VA	75.98833 W.	37.16667 N.	NOS
40	8573364 TOLCHESTER BEACH, CHESAPEAKE BAY , MD	76.24500 W.	39.21333 N.	NOS
41	8573927 CHESAPEAKE CITY , MD	75.81000 W.	39.52667 N.	NOS
42	8574070 HAVRE DE GRACE , MD	76.09000 W.	39.53667 N.	NOS
43	8575512 U.S. NAVAL ACADEMY, SEVERN R., CHES. BAY, MD	76.48000 W.	38.98333 N.	NOS
44	8577330 SOLOMONS ISLAND, PATUXENT RIVER , MD	76.45167 W.	38.31667 N.	NOS
45	8635150 COLONIAL BEACH, POTOMAC RIVER , VA	76.96000 W.	38.25167 N.	NOS
46	8635750 LEWISETTA, POTOMAC RIVER , VA	76.46500 W.	37.99500 N.	NOS
47	8636580 WINDMILL POINT, RAPPAHANNOCK RIVER , VA	76.29000 W.	37.61500 N.	NOS
48	8637624 GLOUCESTER POINT, YORK RIVER , VA	76.50000 W.	37.24667 N.	NOS
49	8637689 YORKTOWN USCG TRAINING CENTER, YORK R. , VA	76.47833 W.	37.22667 N.	NOS
50	8638424 KINGSMILL, JAMES RIVER , VA	76.66333 W.	37.22000 N.	NOS
51	8638610 SEWELLS POINT, HAMPTON ROADS , VA	76.33000 W.	36.94667 N.	NOS
52	8638660 PORTSMOUTH,NORFOLK NAVAL SHIPYRD , VA	76.29333 W.	36.82167 N.	NOS
53	8638863 CHESAPEAKE BAY BRIDGE TUNNEL , VA	76.11333 W.	36.96667 N.	NOS
54	8651370 DUCK, FRF PIER , NC	75.74667 W.	36.18333 N.	NOS
55	8652587 OREGON INLET MARINA, PAMLICO SOUND , NC	75.54833 W.	35.79500 N.	NOS
56	8654400 CAPE HATTERAS FISHING PIER , NC	75.63500 W.	35.22333 N.	NOS
57	8654792 OCRACOKE ISLAND , NC	75.98833 W.	35.11500 N.	NOS

Station number	**Tidal station name**	**Longitude [decimal deg.]**	**Latitude [decimal deg.]**	**Overseeing agency**
58	8655875 SEA LEVEL, CORE SOUND , NC	76.34333 W.	34.87500 N.	NOS
59	8656483 BEAUFORT, DUKE MARINE LAB , NC	76.67000 W.	34.72000 N.	NOS
60	8658163 WRIGHTSVILLE BEACH , NC	77.79500 W.	34.21000 N.	NOS
61	428 South Port, NC	78.01666 W.	33.91500 N.	IHO
62	8659897 SUNSET BEACH PIER, ATLANTIC OCEAN , NC	78.50667 W.	33.86500 N.	NOS
63	8661070 SPRINGMAID PIER, ATLANTIC OCEAN , SC	78.91833 W.	33.65500 N.	NOS
64	8662245 OYSTER LANDING, CRAB HAUL CREEK , SC	79.18667 W.	33.35167 N.	NOS
65	8664941 SOUTH CAPERS ISLAND, CAPERS CREEK , SC	79.70667 W.	32.85667 N.	NOS
66	8665530 CHARLESTON, COOPER RIVER ENTRANCE , SC	79.92500 W.	32.78167 N.	NOS
67	8668498 HUNTING ISLAND PIER, FRIPPS INLET , SC	80.46500 W.	32.34000 N.	NOS
68	8670870 FORT PULASKI, SAVANNAH RIVER , GA	80.90167 W.	32.03333 N.	NOS
69	8677344 ST SIMONS LIGHTHOUSE, ST SIMONS ISLAND , GA	81.39667 W.	31.13167 N.	NOS
70	8679511 KINGS BAY , GA	81.51500 W.	30.79667 N.	NOS
71	8720030 FERNANDINA BEACH, AMELIA RIVER , FL	81.46500 W.	30.67167 N.	NOS
72	8720211 WWTD, MAYPORT NAVAL STA., ST JOHNS RIVER, FL	81.41333 W.	30.40000 N.	NOS
73	8720218 BAR PILOTS DOCK, ST JOHNS RIVER , FL	81.43000 W.	30.39667 N.	NOS
74	8720220 MAYPORT , FL	81.43167 W.	30.39333 N.	NOS
75	8720554 VILANO BEACH (ICWW) , FL	81.30000 W.	29.91667 N.	NOS
76	8720582 STATE ROAD 312, MATANZAS RIVER , FL	81.30667 W.	29.86667 N.	NOS

Station number	**Tidal station name**	**Longitude [decimal deg.]**	**Latitude [decimal deg.]**	**Overseeing agency**
77	8720587 ST. AUGUSTINE BEACH, ATLANTIC OCEAN , FL	81.26333 W.	29.85667 N.	NOS
78	8720651 CRESCENT BEACH, MATANZAS RIVER , FL	81.25833 W.	29.76833 N.	NOS
79	8720757 BINGS LANDING, MATANZAS RIVER , FL	81.20500 W.	29.61500 N.	NOS
80	8721020 DAYTONA BEACH (OCEAN) , FL	81.00500 W.	29.22833 N.	NOS
81	8721604 TRIDENT PIER, PORT CANAVERAL , FL	80.59333 W.	28.41500 N.	NOS
82	8721608 CANAVERAL HARBOR ENTRANCE , FL	80.60167 W.	28.40833 N.	NOS
83	8722670 LAKE WORTH PIER, ATLANTIC OCEAN , FL	80.03333 W.	26.61167 N.	NOS
84	8723080 HAULOVER PIER, N. MIAMI BEACH , FL	80.12000 W.	25.90333 N.	NOS
85	8723170 MIAMI BEACH (CITY PIER) , FL	80.13167 W.	25.76833 N.	NOS
86	8723178 MIAMI BEACH, GOVERNMENT CUT , FL	80.13000 W.	25.76333 N.	NOS
87	8723214 VIRGINIA KEY, BISCAYNE BAY , FL	80.16167 W.	25.73167 N.	NOS
88	8723962 KEY COLONY BEACH , FL	81.01667 W.	24.71833 N.	NOS
89	8723970 VACA KEY, FLORIDA BAY , FL	81.10500 W.	24.71167 N.	NOS
90	8724580 KEY WEST , FL	81.80833 W.	24.55333 N.	NOS
91	8724698 LOGGERHEAD KEY, DRY TORTUGAS , FL	82.92000 W.	24.63167 N.	NOS
92	8725110 NAPLES, GULF OF MEXICO , FL	81.80667 W.	26.13000 N.	NOS
93	8726384 PORT MANATEE, TAMPA BAY , FL	82.56333 W.	27.63667 N.	NOS
94	8726667 CSX ROCKPORT, MCKAY BAY ENTRANCE , FL	82.42500 W.	27.91333 N.	NOS
95	8726607 PORT TAMPA, OLD TAMPA BAY , FL	82.55333 W.	27.85833 N.	NOS

Station number	**Tidal station name**	**Longitude [decimal deg.]**	**Latitude [decimal deg.]**	**Overseeing agency**
96	8726520 ST. PETERSBURG, TAMPA BAY , FL	82.62667 W.	27.76000 N.	NOS
97	8726724 CLEARWATER BEACH, GULF OF MEXICO , FL	82.83167 W.	27.97833 N.	NOS
98	8727235 JOHNS ISLAND, CHASSAHOWITZKA BAY , FL	82.63833 W.	28.69167 N.	NOS
99	8727246 CHASSAHOWITZKA RIVER , FL	82.57667 W.	28.71500 N.	NOS
100	8727274 MASON CREEK, HOMOSASSA BAY , FL	82.63833 W.	28.76167 N.	NOS
101	8727277 TUCKERS ISLAND, HOMOSASSA RIVER , FL	82.69500 W.	28.77167 N.	NOS
102	8727293 HALLS RIVER BRIDGE, HALLS RIVER , FL	82.60333 W.	28.80000 N.	NOS
103	8727306 OZELLO , FL	82.65833 W.	28.82500 N.	NOS
104	8727328 OZELLO NORTH , FL	82.66667 W.	28.86333 N.	NOS
105	8727333 SHARK RIVER, CRYSTAL BAY , FL	82.72333 W.	28.87000 N.	NOS
106	8727336 DIXIE BAY , FL	82.63500 W.	28.88167 N.	NOS
107	8727343 CRYSTAL RIVER, KINGS BAY , FL	82.59833 W.	28.89833 N.	NOS
108	8727348 TWIN RIVERS MARINA, CRYSTAL RIVER , FL	82.63833 W.	28.90500 N.	NOS
109	8727359 SHELL ISLAND, CRYSTAL RIVER , FL	82.69167 W.	28.92333 N.	NOS
110	8727520 CEDAR KEY, GULF OF MEXICO , FL	83.03167 W.	29.13500 N.	NOS
111	8728130 ST. MARKS LHTSE., APALACHEE BAY , FL	84.17833 W.	30.07833 N.	NOS
112	8728229 SHELL POINT, WALKER CREEK , FL	84.29000 W.	30.06000 N.	NOS
113	8728360 TURKEY POINT , FL	84.51167 W.	29.91500 N.	NOS
114	8728690 APALACHICOLA, APALACHICOLA RIVER , FL	84.98167 W.	29.72667 N.	NOS

Station number	Tidal station name	Longitude [decimal deg.]	Latitude [decimal deg.]	Overseeing agency
115	8729108 PANAMA CITY, ST. ANDREW BAY , FL	85.66667 W.	30.15167 N.	NOS
116	400 Alligator Bayou, FL	85.75000 W.	30.16666 N.	IHO
117	8729210 PANAMA CITY BEACH, GULF OF MEXICO , FL	85.87833 W.	30.21333 N.	NOS
118	8729678 NAVARRE BEACH , FL	86.86500 W.	30.37667 N.	NOS
119	8729840 PENSACOLA, PENSACOLA BAY , FL	87.21167 W.	30.40333 N.	NOS
120	8735180 DAUPHIN ISLAND, MOBILE BAY , AL	88.07500 W.	30.25000 N.	NOS
121	8737048 MOBILE STATE DOCKS, MOBILE RIVER , AL	88.04333 W.	30.70833 N.	NOS
122	8744117 BILOXI, BAY OF BILOXI , MS	88.90333 W.	30.41167 N.	NOS
123	8745557 GULFPORT HARBOR, MISSISSIPPI SOUND , MS	89.08167 W.	30.36000 N.	NOS
124	8747437 BAY WAVELAND YC, BAY ST. LOUIS , MS	89.32500 W.	30.32500 N.	NOS
125	8747766 WAVELAND, MISSISSIPPI SOUND , MS	89.36667 W.	30.28167 N.	NOS
126	402 Cat Island, MS	89.16666 W.	30.23333 N.	IHO
127	8762372 EAST BANK 1, NORCO, BAYOU LABRANCHE , LA	90.36833 W.	30.05000 N.	NOS
128	8760551 SOUTH PASS , LA	89.14000 W.	28.99000 N.	NOS
129	8760922 PILOTS STATION EAST, SOUTHWEST PASS, LA , LA	89.40667 W.	28.93167 N.	NOS
130	8760943 PILOT STATION, SW PASS , LA	89.41833 W.	28.92500 N.	NOS
131	8761724 GRAND ISLE, EAST POINT , LA	89.95667 W.	29.26333 N.	NOS
132	8761720 GRAND ISLE , LA	89.96833 W.	29.25500 N.	NOS
133	8762075 PORT FOURCHON, BELLE PASS , LA	90.20000 W.	29.11500 N.	NOS

Station number	Tidal station name	Longitude [decimal deg.]	Latitude [decimal deg.]	Overseeing agency
134	8764311 EUGENE ISLAND , LA	91.38500 W.	29.37167 N.	NOS
135	378 Point au Fer, LA	91.75000 W.	29.28666 N.	IHO
136	8768094 CALCASIEU PASS, EAST JETTY , LA	93.34333 W.	29.76500 N.	NOS
137	8771081 SABINE OFFSHORE , TX	93.64000 W.	29.49833 N.	NOS
138	8770570 SABINE PASS NORTH , TX	93.87000 W.	29.73000 N.	NOS
139	8770971 ROLLOVER PASS , TX	94.51333 W.	29.51500 N.	NOS
140	8771341 GALVESTON BAY ENTRANCE, NORTH JETTY , TX	94.72500 W.	29.35833 N.	NOS
141	8771328 PORT BOLIVAR, BOLIVAR ROADS , TX	94.78000 W.	29.36500 N.	NOS
142	8771450 GALVESTON PIER 21, GALVESTON CHANNEL , TX	94.79333 W.	29.31000 N.	NOS
143	8771510 GALVESTON PLEASURE PIER, GULF OF MEXICO , TX	94.78833 W.	29.28500 N.	NOS
144	8772440 FREEPORT, DOW BARGE CANAL , TX	95.30833 W.	28.94833 N.	NOS
145	8773701 PORT OCONNOR, MATAGORDA BAY , TX	96.38833 W.	28.45167 N.	NOS
146	8775237 PORT ARANSAS , TX	97.06000 W.	27.83833 N.	NOS
147	8775270 PORT ARANSAS, H. CALDWELL PIER , TX	97.05000 W.	27.82667 N.	NOS
148	8775792 PACKERY CHANNEL , TX	97.23667 W.	27.63333 N.	NOS
149	8775870 CORPUS CHRISTI, GULF OF MEXICO , TX	97.21667 W.	27.58000 N.	NOS
150	8779748 SOUTH PADRE ISLAND C.G. STATION , TX	97.17667 W.	26.07667 N.	NOS
151	8779750 PADRE ISLAND, BRAZOS SANTIAGO PASS , TX	97.15667 W.	26.06833 N.	NOS
152	8779770 PORT ISABEL, LAGUNA MADRE , TX	97.21500 W.	26.06000 N.	NOS

Station number	**Tidal station name**	**Longitude [decimal deg.]**	**Latitude [decimal deg.]**	**Overseeing agency**
153	9500966 MADERO, TAMPICO HARBOR , MT	97.79500 W.	22.26167 N.	NOS
154	14 Ciudad Madero, Mexico	97.85833 W.	22.21666 N.	GOM
155	276 Coatracoalcos, Mexico	94.41166 W.	18.14833 N.	IHO
156	289 Campeche, Mexico	90.53333 W.	19.83333 N.	IHO
157	295 Progreso, Yucatan, Mexico	89.65000 W.	21.30000 N.	IHO
158	9650593 PUERTO CORTES	87.87000 W.	15.83500 N.	NOS
159	257 Puerto Cabezas, Nicaragua	83.36666 W.	14.01666 N.	IHO
160	187 Puerto Limon, Costa Rica	83.03333 W.	10.00000 N.	IHO
161	184 Cristobal, Panama	79.91666 W.	9.35000 N.	IHO
162	196 Cartagena, Colombia	75.53333 W.	10.38333 N.	IHO
163	236 Willemstad, Curacao Antilles	68.93333 W.	12.10000 N.	IHO
164	200 La Guaira, Venezuela	66.93333 W.	10.61666 N.	IHO
165	198 Cumana, Venezuela	64.16666 W.	10.45000 N.	IHO
166	202 Port of Spain Trinidad and Tobago	61.51666 W.	10.65000 N.	IHO
167	256 Castries, St. Lucia, B.W.I.	61.00000 W.	14.01666 N.	IHO
168	259 Fort-de-France, Martinique	61.05000 W.	14.58333 N.	IHO
169	269 East Caribbean Sea	64.88333 W.	16.53333 N.	IHO
170	9751401 LIME TREE BAY, ST CROIX , VI	64.75333 W.	17.69667 N.	NOS
171	9751567 BENNER BAY	64.87000 W.	18.32000 N.	NOS

Station number	**Tidal station name**	**Longitude [decimal deg.]**	**Latitude [decimal deg.]**	**Overseeing agency**
172	9751639 CHARLOTTE AMALIE, ST. THOMAS , VI	64.92000 W.	18.33500 N.	NOS
173	9755371 SAN JUAN, LA PUNTILLA, SAN JUAN BAY , PR	66.11667 W.	18.45833 N.	NOS
174	9755679 LAS MAREAS , PR	66.15833 W.	17.92833 N.	NOS
175	9758053 PUNTA GUAYANILLA , PR	66.76167 W.	17.97667 N.	NOS
176	9759110 MAGUEYES ISLAND, CARIBBEAN SEA , PR	67.04667 W.	17.97167 N.	NOS
177	283 Ciudad, Dominican Republic	69.88333 W.	18.46666 N.	IHO
178	288 Puerto Plato, Dominican Republic	70.68333 W.	19.75000 N.	IHO
179	284 Port-au-Prince, Haiti	72.35000 W.	18.55000 N.	IHO
180	290 Guantanomo Bay, Cuba	75.15000 W.	19.90000 N.	IHO
181	294 Gibara, Cuba	76.11666 W.	21.10000 N.	IHO
182	298 Casilda, Cuba	79.98333 W.	21.75000 N.	IHO
183	303 Havana, Cuba	82.36666 W.	23.13333 N.	IHO
184	9710441 SETTLEMENT POINT, GRAND BAHAMAS , BA	78.99667 W.	26.71000 N.	NOS
185	315 Nassau, Bahamas	77.35000 W.	25.08333 N.	IHO
186	313 Eleuthera, Bahamas	76.15000 W.	24.76666 N.	IHO
187	527 Atlantic Ocean	70.90000 W.	40.30000 N.	IHO
188	509 Atlantic Ocean	71.36666 W.	39.16666 N.	IHO
189	510 Atlantic Ocean	72.16666 W.	39.21666 N.	IHO
190	464 Atlantic Ocean	73.08333 W.	37.36666 N.	IHO

Station number	**Tidal station name**	**Longitude [decimal deg.]**	**Latitude [decimal deg.]**	**Overseeing agency**
191	422 Atlantic Ocean	75.61666 W.	32.68333 N.	IHO
192	41 Atlantic Ocean	76.41666 W.	30.43333 N.	IHO
193	360 Atlantic Ocean	76.80000 W.	28.45000 N.	IHO
194	355 Atlantic Ocean	76.78333 W.	28.01666 N.	IHO
195	338 Atlantic Ocean	69.33333 W.	26.46666 N.	IHO
196	359 Atlantic Ocean	67.53333 W.	28.23333 N.	IHO
197	357 Atlantic Ocean	69.75000 W.	28.13333 N.	IHO
198	348 Florida Bank	84.25000 W.	26.70000 N.	IHO
199	312 Middle of GOM	89.65000 W.	24.76666 N.	IHO
200	2695540 BERMUDA ESSO PIER, ST. GEORGES ISLAND	64.70333 W.	32.37333 N.	NOS
201	St. Davids Island, Bermuda	64.69500 W.	32.37000 N.	IHO
202	417 Ireland Island, Bermuda	64.83333 W.	32.31666 N.	IHO
203	415 Atlantic Ocean near Bermuda	64.43333 W.	32.01666 N.	IHO

[NOTE]

First row shows continuous tidal stations number, second row represents tidal stations name, third row indicates longitude in decimal degree, fourth row is latitude in decimal degree, and fifth row explains overseeing agency.

APPENDIX D

ELIMINATED 53 TIDAL STATIONS

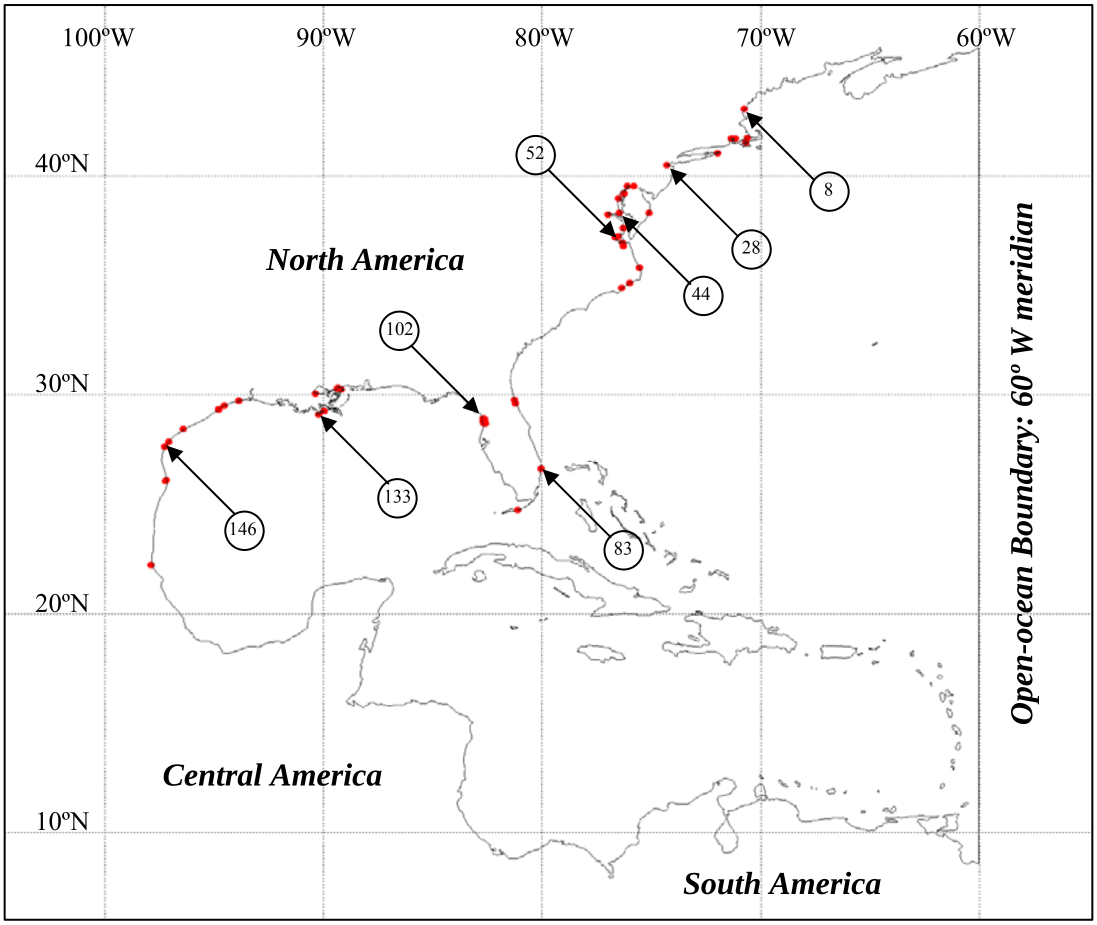

WNAT tidal model domain with eliminated 53 tidal stations.

[NOTE]

The continuous tidal station number starts from Yarmouth, Nova Scotia, Canada. Then, it goes though East coast of North America, shoreline of Gulf of Mexico, and along the Central and South American coasts. Finally, the continuous tidal station number passes through in or around the Caribbean Sea islands and in the deep Atlantic Ocean and near Bermuda. The tidal station numbers in the above figure are indicated rough location.

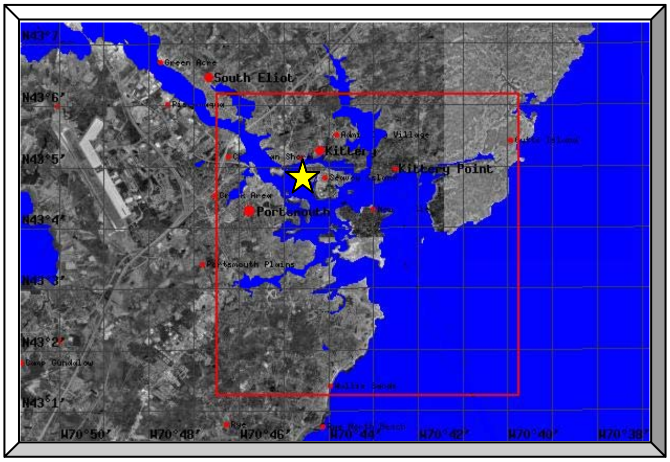

Seavey Island, Portsmouth Harbor, ME	
Continuous station number	8
Overseeing agency	NOS
Longitude [decimal deg.]	70.74 W.
Latitude [decimal deg.]	43.08 N.
Reason for elimination	Near the river

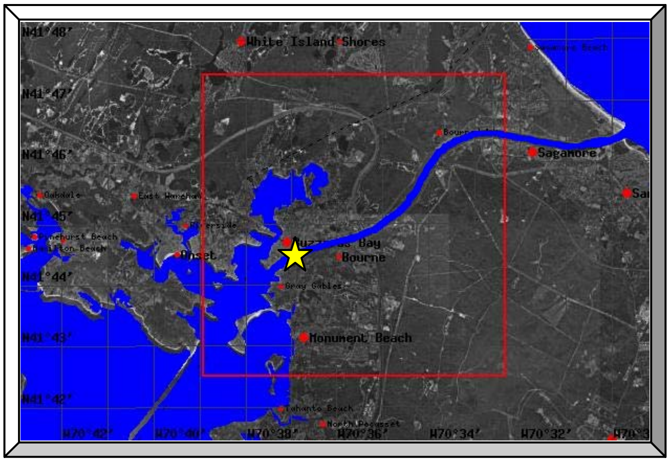

Buzzards Bay (RR Bridge), Cape Cod Canal, MA	
Continuous station number	11
Overseeing agency	NOS
Longitude [decimal deg.]	70.62 W.
Latitude [decimal deg.]	41.74 N.
Reason for elimination	In the canal

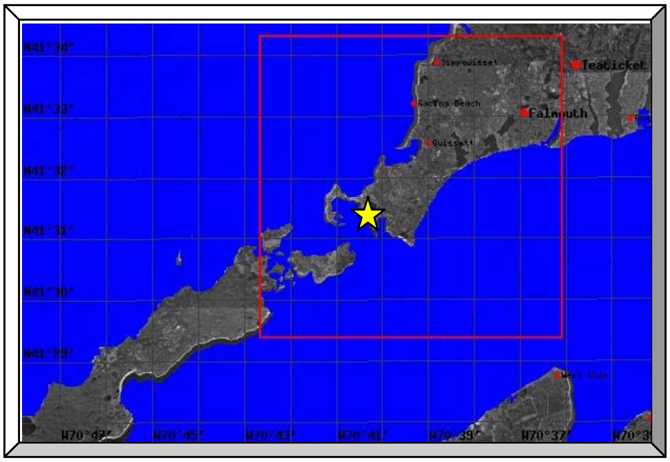

Woods Hole, Buzzards Bay, MA	
Continuous station number	13
Overseeing agency	NOS
Longitude [decimal deg.]	70.67 W.
Latitude [decimal deg.]	41.52 N.
Reason for elimination	In the bay

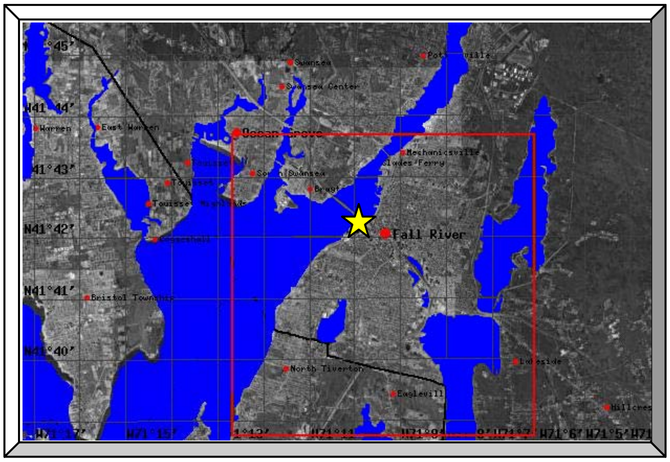

Fall River, Hope Bay, MA	
Continuous station number	14
Overseeing agency	NOS
Longitude [decimal deg.]	71.16 W.
Latitude [decimal deg.]	41.71 N.
Reason for elimination	In the bay

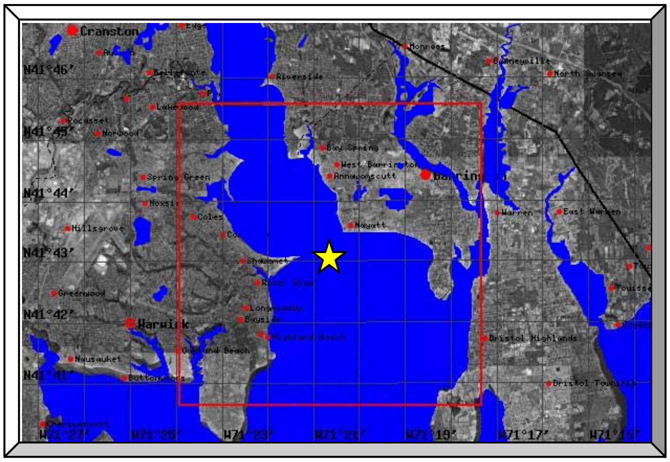

Conimicut Light, Narragansett Bay, RI	
Continuous station number	15
Overseeing agency	NOS
Longitude [decimal deg.]	71.34 W.
Latitude [decimal deg.]	41.72 N.
Reason for elimination	In the bay

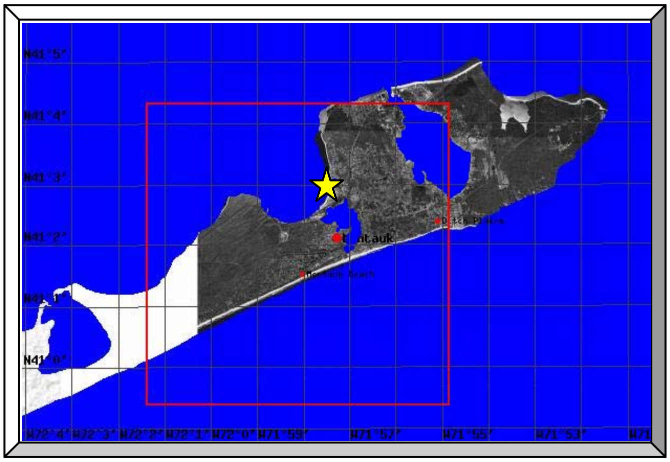

Montauk, Fort Pond Bay, NY	
Continuous station number	20
Overseeing agency	NOS
Longitude [decimal deg.]	71.96 W.
Latitude [decimal deg.]	41.05 N.
Reason for elimination	In the bay

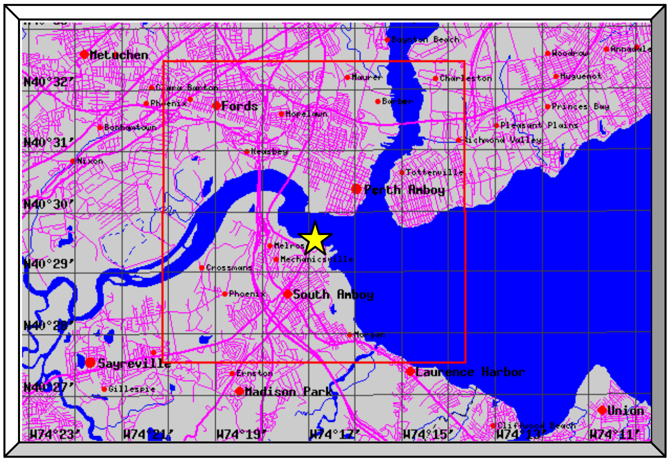

South Amboy Raritan River, NJ	
Continuous station number	28
Overseeing agency	NOS
Longitude [decimal deg.]	74.28 W.
Latitude [decimal deg.]	40.49 N.
Reason for elimination	In the river

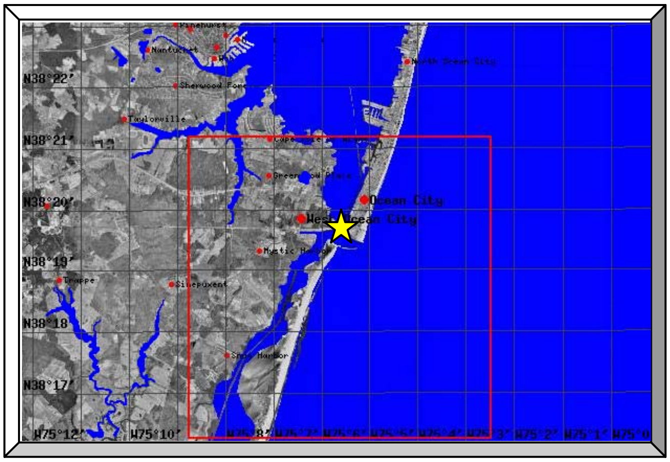

Ocean City Inlet, MD	
Continuous station number	37
Overseeing agency	NOS
Longitude [decimal deg.]	75.09 W.
Latitude [decimal deg.]	38.33 N.
Reason for elimination	In the inlet

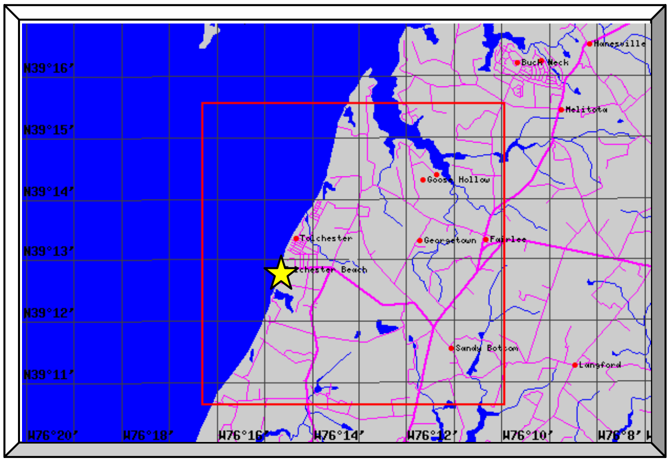

Tolchester Beach, Chesapeake Bay, MD	
Continuous station number	40
Overseeing agency	NOS
Longitude [decimal deg.]	76.25 W.
Latitude [decimal deg.]	39.21 N.
Reason for elimination	In the bay

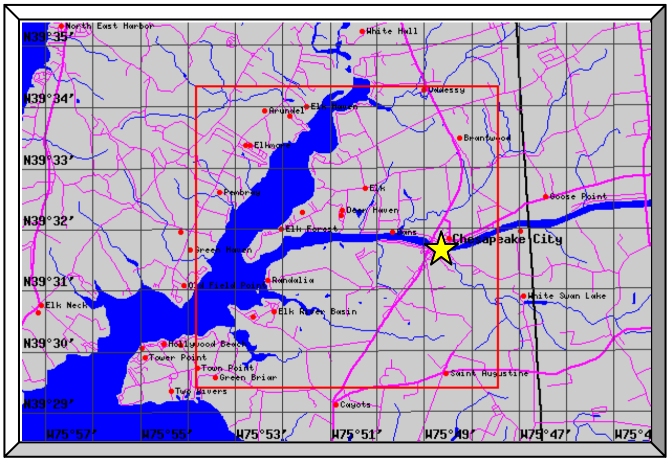

Chesapeake City, MD	
Continuous station number	41
Overseeing agency	NOS
Longitude [decimal deg.]	75.81 W.
Latitude [decimal deg.]	39.53 N.
Reason for elimination	In the river

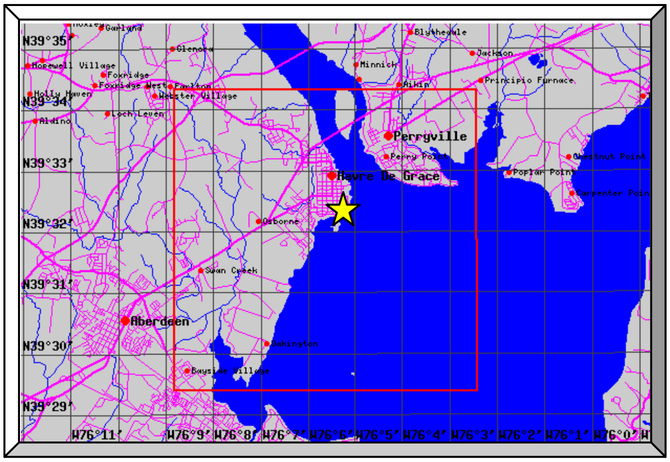

Havre de Grace, MD	
Continuous station number	42
Overseeing agency	NOS
Longitude [decimal deg.]	76.09 W.
Latitude [decimal deg.]	39.54 N.
Reason for elimination	Near the mouth of the river

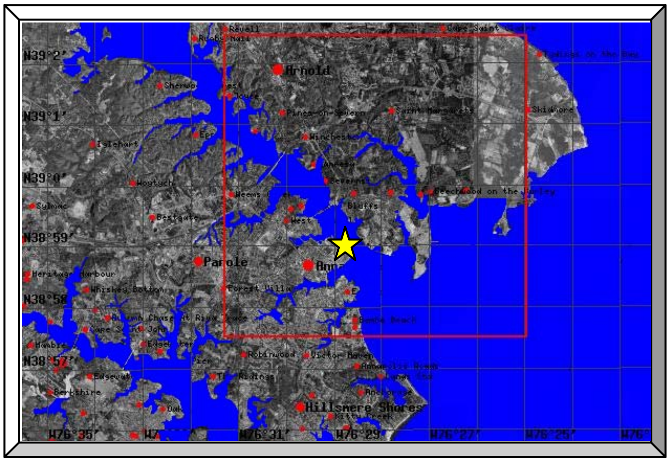

U.S. Navel Academy, Severn R., Ches. Bay, MD	
Continuous station number	43
Overseeing agency	NOS
Longitude [decimal deg.]	76.48 W.
Latitude [decimal deg.]	38.98 N.
Reason for elimination	In the bay

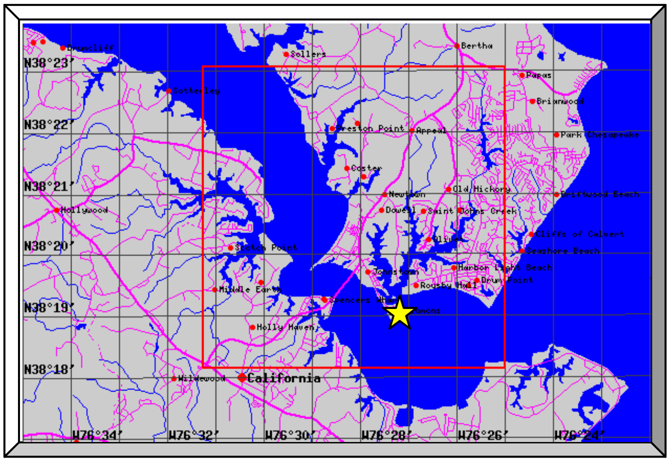

Solomons Island, Patuxent River, MD	
Continuous station number	44
Overseeing agency	NOS
Longitude [decimal deg.]	76.45 W.
Latitude [decimal deg.]	38.32 N.
Reason for elimination	In the river

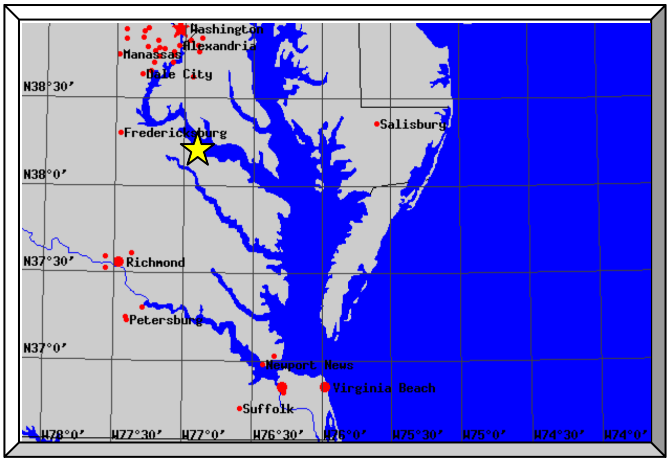

Colonial Beach, Potomac River, VA	
Continuous station number	45
Overseeing agency	NOS
Longitude [decimal deg.]	76.96 W.
Latitude [decimal deg.]	38.25 N.
Reason for elimination	In the river

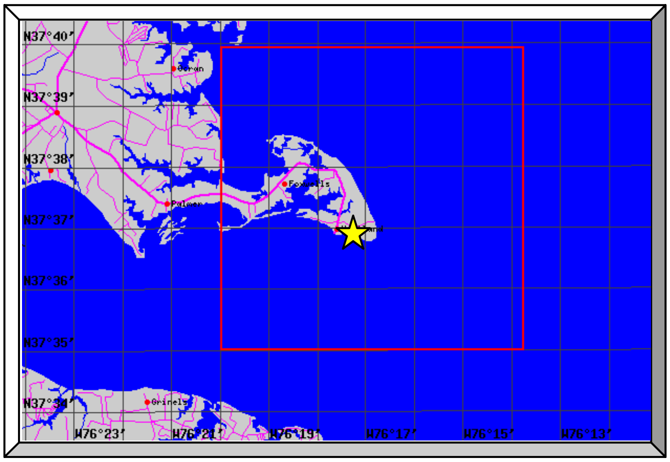

Windmill Point, Rappahannock River, VA	
Continuous station number	47
Overseeing agency	NOS
Longitude [decimal deg.]	76.29 W.
Latitude [decimal deg.]	37.62 N.
Reason for elimination	In the mouth of the river

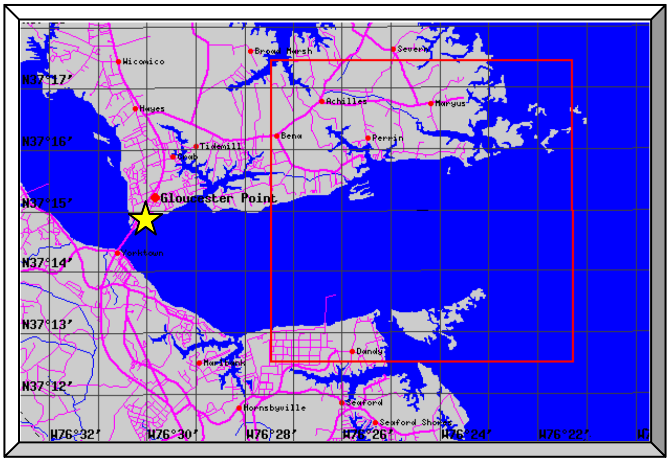

Gloucester Point, York River, VA	
Continuous station number	48
Overseeing agency	NOS
Longitude [decimal deg.]	76.50 W.
Latitude [decimal deg.]	37.25 N.
Reason for elimination	In the river

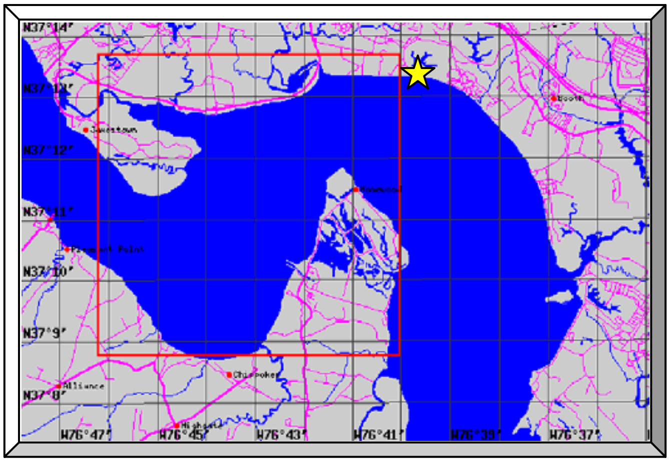

Kingsmill, James River, VA	
Continuous station number	50
Overseeing agency	NOS
Longitude [decimal deg.]	76.66 W.
Latitude [decimal deg.]	37.22 N.
Reason for elimination	In the river

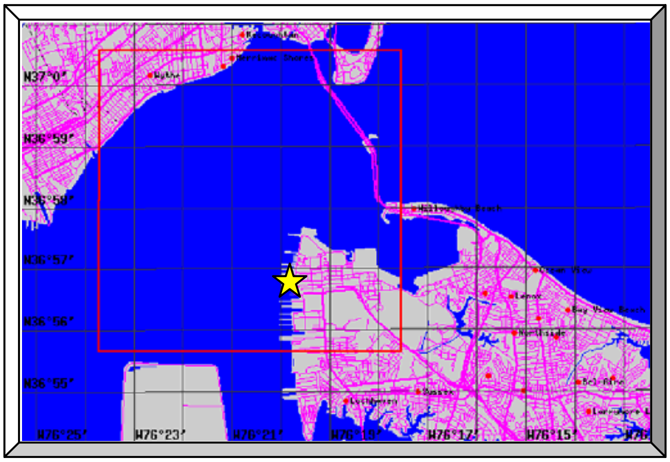

Sewells Point, Hampton Roads, VA	
Continuous station number	51
Overseeing agency	NOS
Longitude [decimal deg.]	76.33 W.
Latitude [decimal deg.]	36.95 N.
Reason for elimination	In the mouth of the river

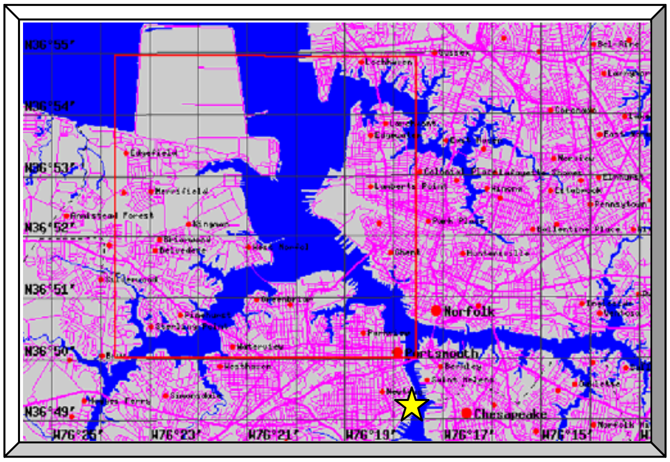

Portsmouth, Norfolk Naval Shipyrd, VA	
Continuous station number	52
Overseeing agency	NOS
Longitude [decimal deg.]	76.29 W.
Latitude [decimal deg.]	36.82 N.
Reason for elimination	In the river

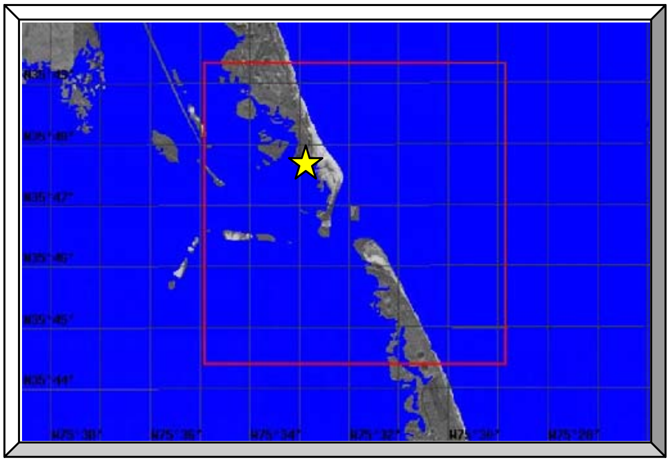

Oregon Inlet Marina, Pamlico Sound, NC	
Continuous station number	55
Overseeing agency	NOS
Longitude [decimal deg.]	75.55 W.
Latitude [decimal deg.]	35.80 N.
Reason for elimination	In the inlet

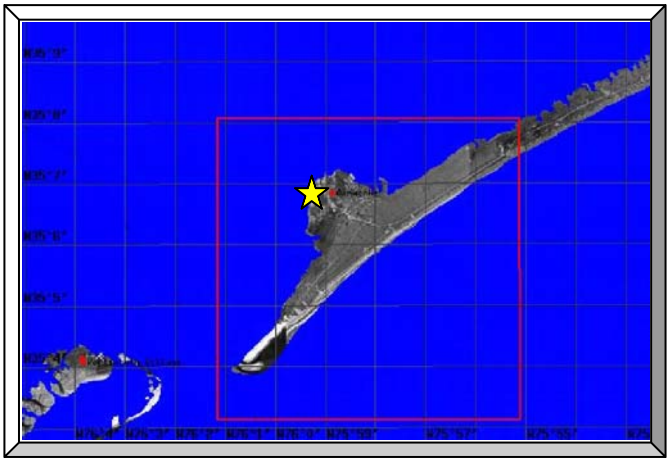

Ocracoke Island, NC	
Continuous station number	57
Overseeing agency	NOS
Longitude [decimal deg.]	75.99 W.
Latitude [decimal deg.]	35.12 N.
Reason for elimination	In the inlet

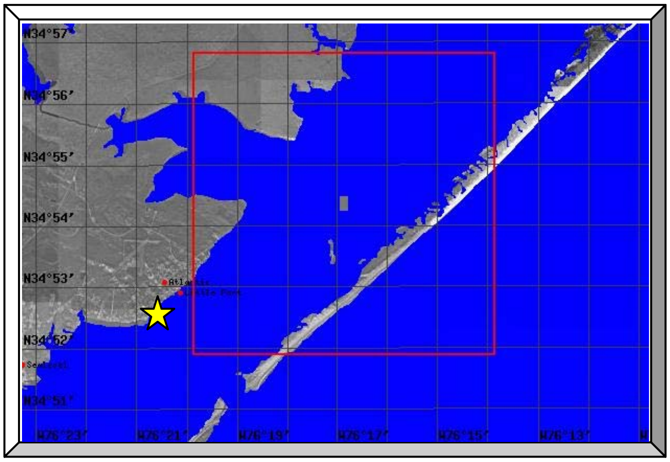

Sea Level, Core Sound, NC	
Continuous station number	58
Overseeing agency	NOS
Longitude [decimal deg.]	76.34 W.
Latitude [decimal deg.]	34.88 N.
Reason for elimination	In the inlet

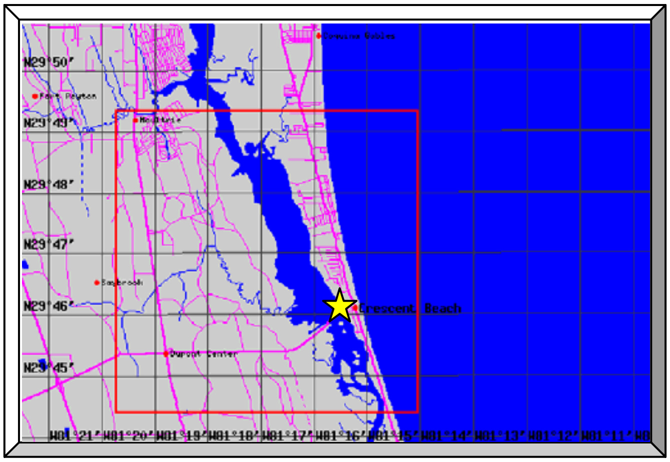

Crescent Beach, Matanzas River, FL	
Continuous station number	78
Overseeing agency	NOS
Longitude [decimal deg.]	81.26 W.
Latitude [decimal deg.]	29.77 N.
Reason for elimination	In the river

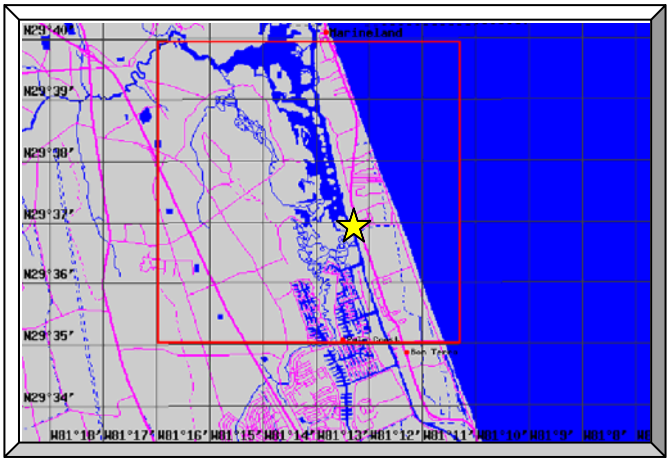

Bings Landing, Matanzas River, FL	
Continuous station number	79
Overseeing agency	NOS
Longitude [decimal deg.]	81.21 W.
Latitude [decimal deg.]	29.62 N.
Reason for elimination	In the river

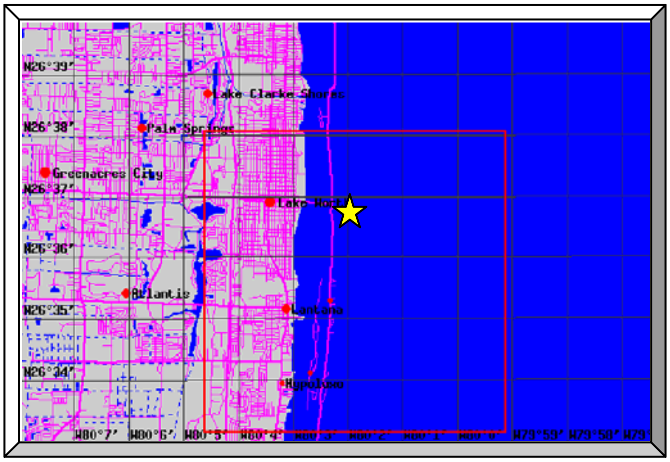

Lake Worth Pier, Atlantic Ocean, FL	
Continuous station number	83
Overseeing agency	NOS
Longitude [decimal deg.]	80.03 W.
Latitude [decimal deg.]	26.61 N.
Reason for elimination	Drying out

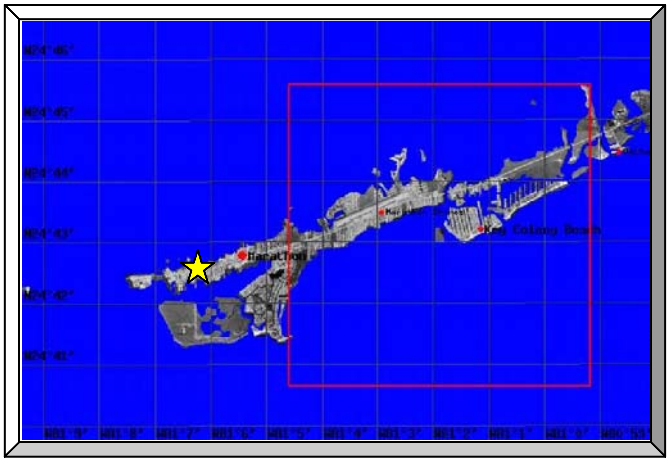

Vaca Key, Florida Bay, FL	
Continuous station number	89
Overseeing agency	NOS
Longitude [decimal deg.]	81.11 W.
Latitude [decimal deg.]	24.71 N.
Reason for elimination	In the bay

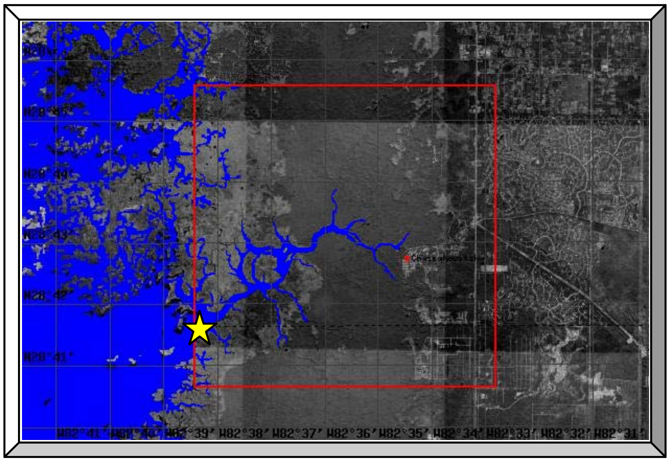

Johns Island, Chassahowitzka Bay, FL	
Continuous station number	98
Overseeing agency	NOS
Longitude [decimal deg.]	82.64 W.
Latitude [decimal deg.]	28.69 N.
Reason for elimination	Complicated location

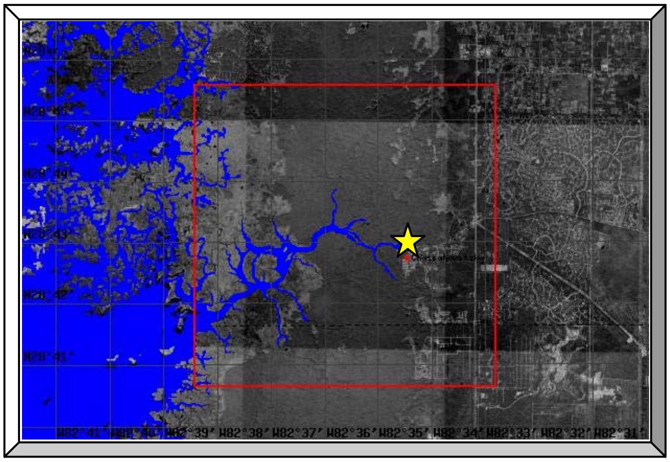

Chassahowitzka River, FL	
Continuous station number	99
Overseeing agency	NOS
Longitude [decimal deg.]	82.58 W.
Latitude [decimal deg.]	28.72 N.
Reason for elimination	Complicated location

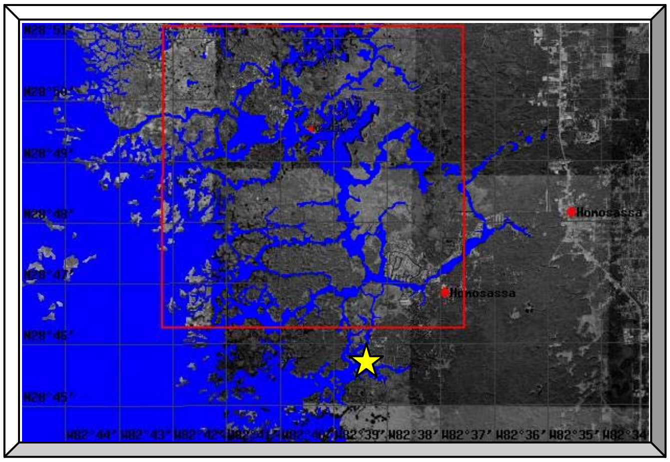

Mason Creek, Homosassa Bay	
Continuous station number	100
Overseeing agency	NOS
Longitude [decimal deg.]	82.64 W.
Latitude [decimal deg.]	28.76 N.
Reason for elimination	Complicated location

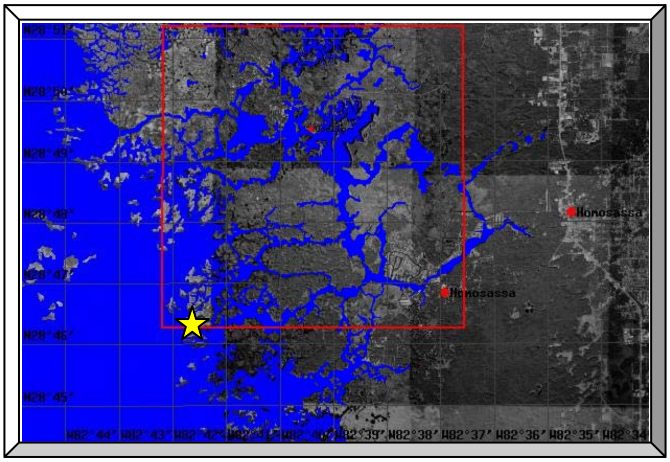

Tuckers Island, Homosassa River, FL	
Continuous station number	101
Overseeing agency	NOS
Longitude [decimal deg.]	82.70 W.
Latitude [decimal deg.]	28.77 N.
Reason for elimination	Complicated location

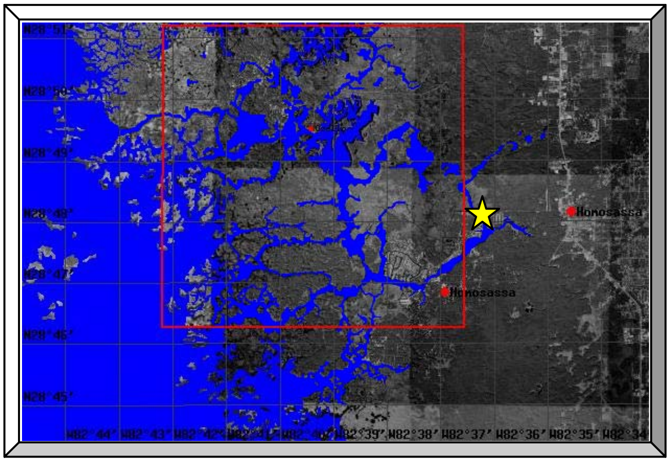

Halls River Bridge, Halls River, FL	
Continuous station number	102
Overseeing agency	NOS
Longitude [decimal deg.]	82.60 W.
Latitude [decimal deg.]	28.80 N.
Reason for elimination	Complicated location

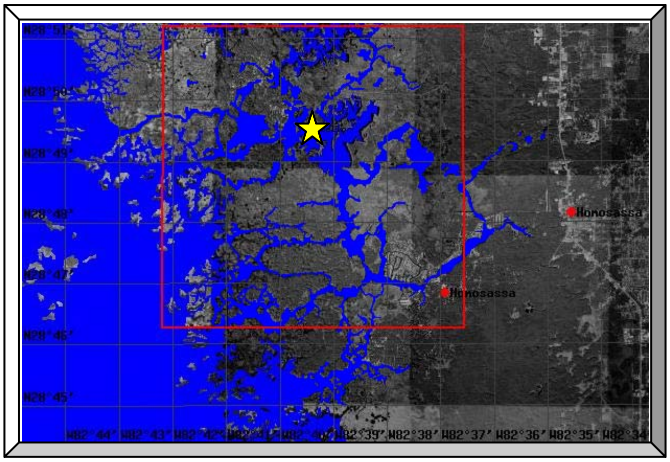

Ozello, FL	
Continuous station number	103
Overseeing agency	NOS
Longitude [decimal deg.]	82.66 W.
Latitude [decimal deg.]	28.83 N.
Reason for elimination	Complicated location

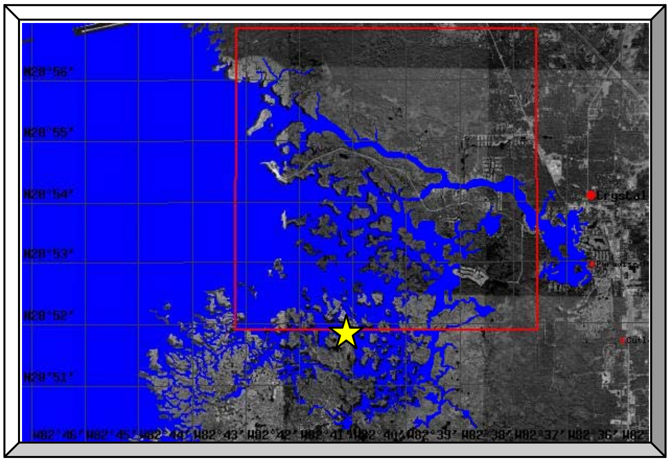

Ozello North, FL	
Continuous station number	104
Overseeing agency	NOS
Longitude [decimal deg.]	82.67 W.
Latitude [decimal deg.]	28.86 N.
Reason for elimination	Complicated location

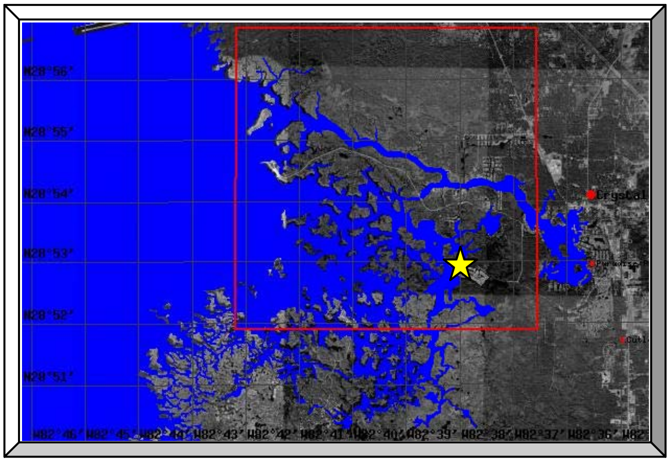

Dixie Bay, FL	
Continuous station number	106
Overseeing agency	NOS
Longitude [decimal deg.]	82.64 W.
Latitude [decimal deg.]	28.88 N.
Reason for elimination	Complicated location

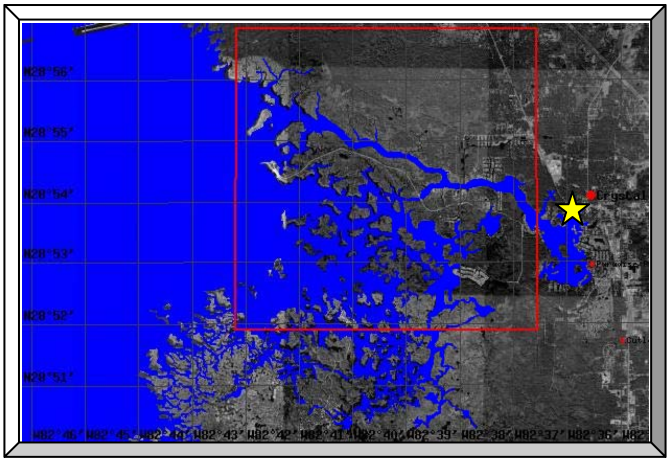

Crystal River, Kings Bay, FL	
Continuous station number	107
Overseeing agency	NOS
Longitude [decimal deg.]	82.60 W.
Latitude [decimal deg.]	28.90 N.
Reason for elimination	Complicated location

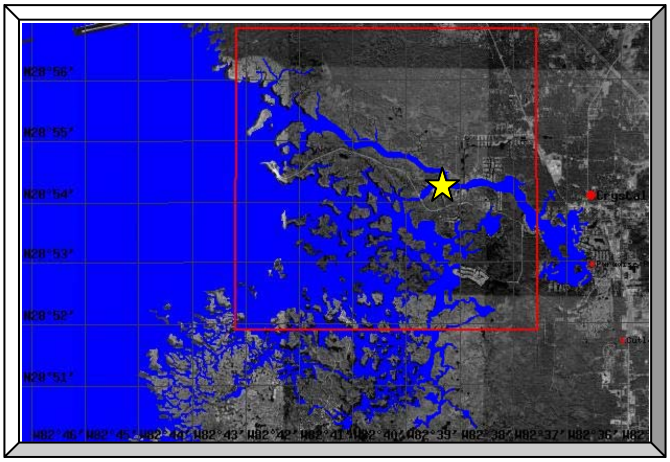

Twin Rivers Marina, Crystal River, FL	
Continuous station number	108
Overseeing agency	NOS
Longitude [decimal deg.]	82.64 W.
Latitude [decimal deg.]	28.91 N.
Reason for elimination	Complicated location

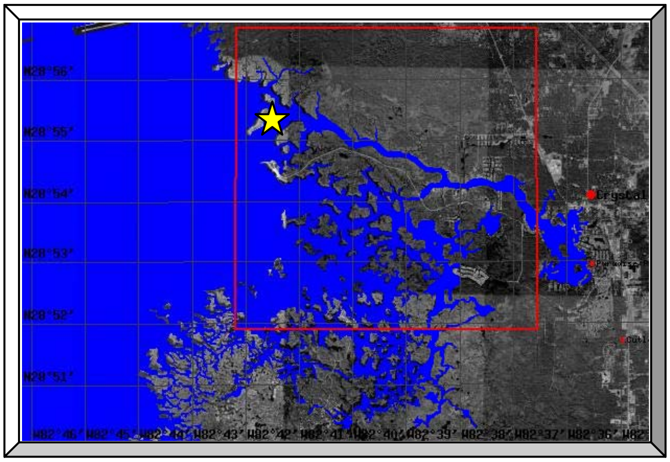

Shell Island, Crystal River, FL	
Continuous station number	109
Overseeing agency	NOS
Longitude [decimal deg.]	82.69 W.
Latitude [decimal deg.]	28.92 N.
Reason for elimination	Complicated location

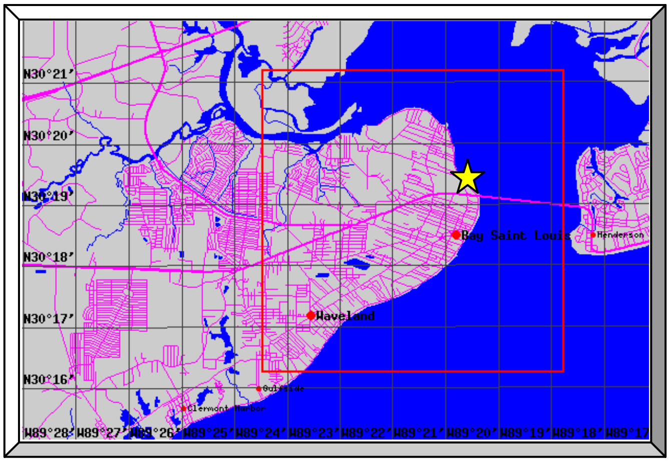

Bay Waveland YC, Bay St. Louis, MS	
Continuous station number	124
Overseeing agency	NOS
Longitude [decimal deg.]	89.33 W.
Latitude [decimal deg.]	30.33 N.
Reason for elimination	Effect of drying out at station 125

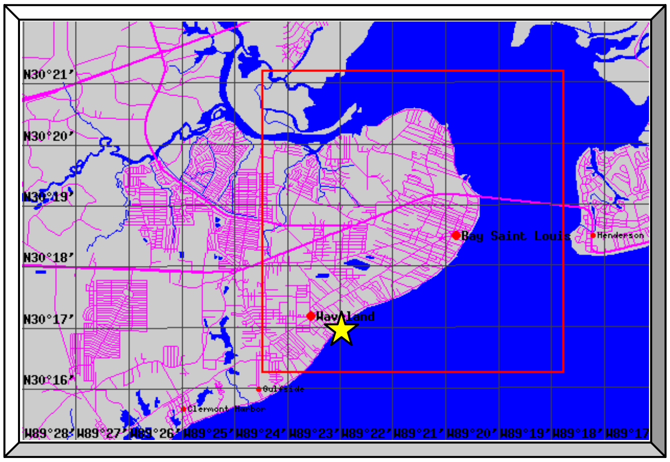

Waveland, Mississippi Sound, MS	
Continuous station number	125
Overseeing agency	NOS
Longitude [decimal deg.]	89.37 W.
Latitude [decimal deg.]	30.28 N.
Reason for elimination	Drying out

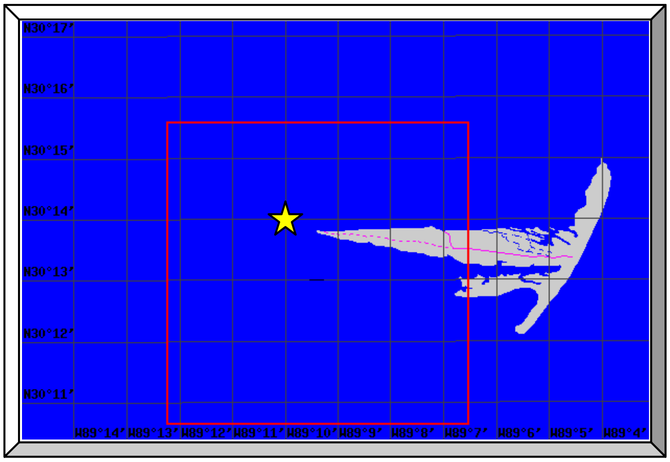

Cat Island, MS	
Continuous station number	126
Overseeing agency	IHO
Longitude [decimal deg.]	89.17 W.
Latitude [decimal deg.]	30.23 N.
Reason for elimination	Drying out

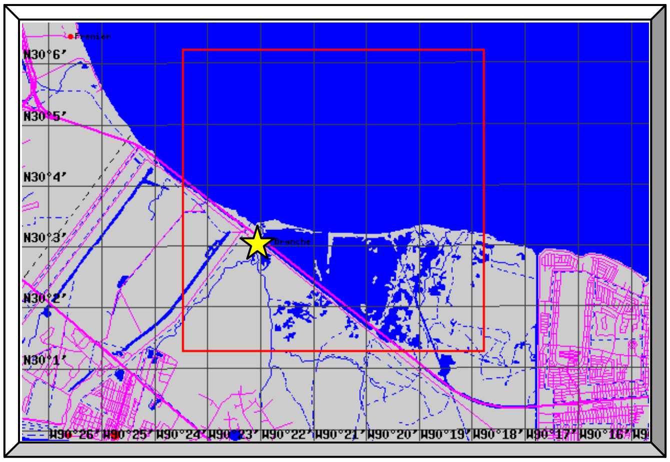

East Bank 1, Norco, Bayou Labranche, LA	
Continuous station number	127
Overseeing agency	NOS
Longitude [decimal deg.]	90.37 W.
Latitude [decimal deg.]	30.05 N.
Reason for elimination	In the inlet

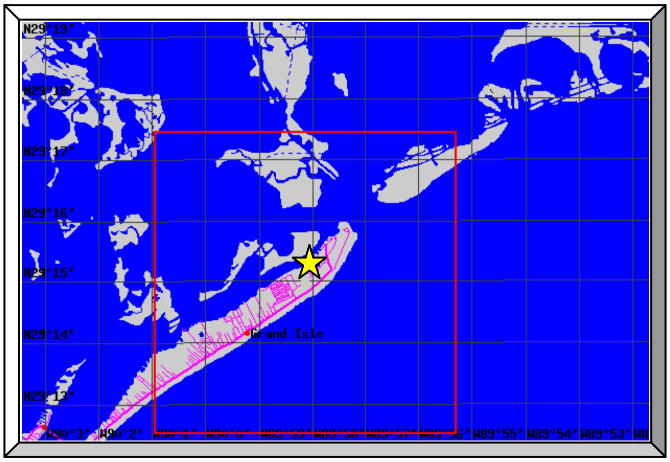

Grand Isle, LA	
Continuous station number	132
Overseeing agency	NOS
Longitude [decimal deg.]	89.97 W.
Latitude [decimal deg.]	29.26 N.
Reason for elimination	In the inlet

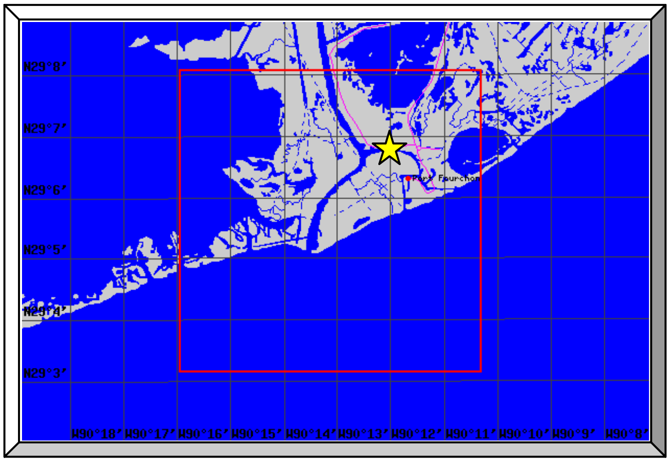

Port Fourchon, Belle Pass, LA	
Continuous station number	133
Overseeing agency	NOS
Longitude [decimal deg.]	90.20 W.
Latitude [decimal deg.]	29.12 N.
Reason for elimination	In the river

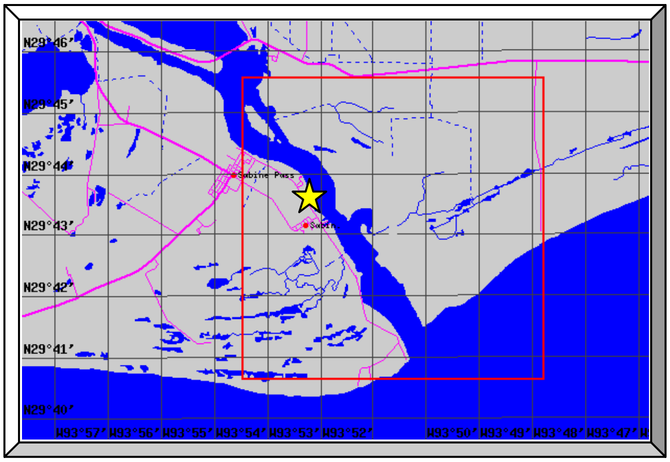

Sabine Pass North, TX	
Continuous station number	138
Overseeing agency	NOS
Longitude [decimal deg.]	93.87 W.
Latitude [decimal deg.]	29.73 N.
Reason for elimination	In the river

Rollover Pass, TX	
Continuous station number	139
Overseeing agency	NOS
Longitude [decimal deg.]	94.51 W.
Latitude [decimal deg.]	29.52 N.
Reason for elimination	In the inlet

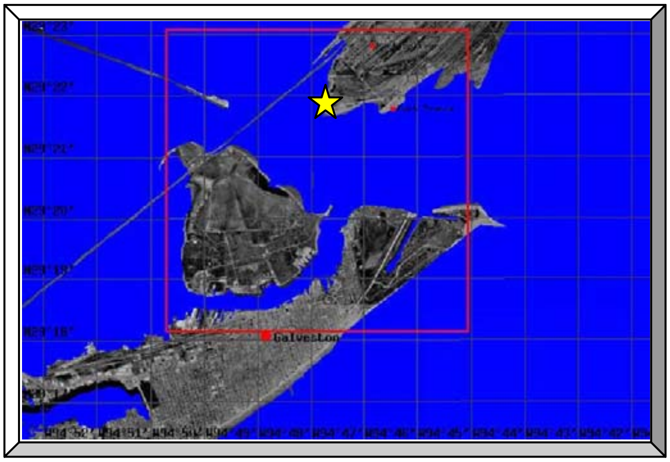

Port Bolivar, Bolivar Roads, TX	
Continuous station number	141
Overseeing agency	NOS
Longitude [decimal deg.]	94.78 W.
Latitude [decimal deg.]	29.37 N.
Reason for elimination	In the inlet

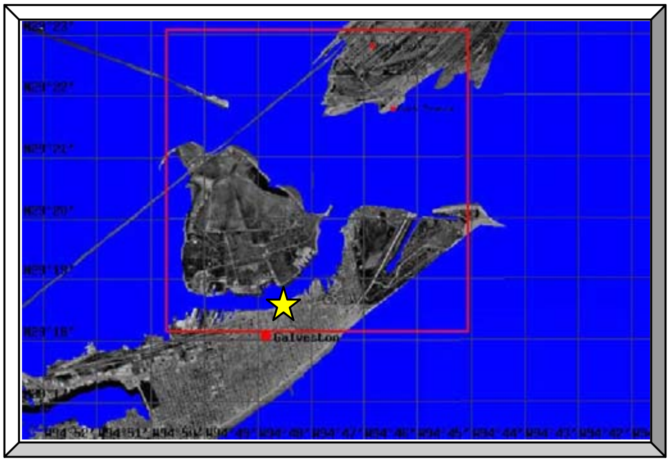

Galveston Pier 21, Galveston Channel, TX	
Continuous station number	142
Overseeing agency	NOS
Longitude [decimal deg.]	94.79 W.
Latitude [decimal deg.]	29.31 N.
Reason for elimination	In the channel

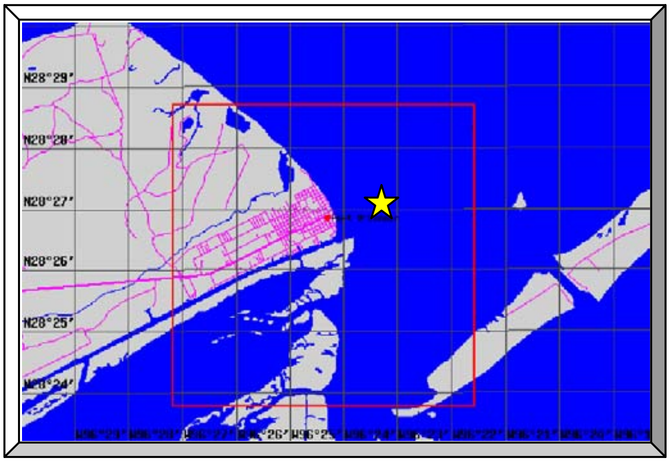

Port Oconnor, Matagorda Bay, TX	
Continuous station number	145
Overseeing agency	NOS
Longitude [decimal deg.]	96.39 W.
Latitude [decimal deg.]	28.45 N.
Reason for elimination	In the bay

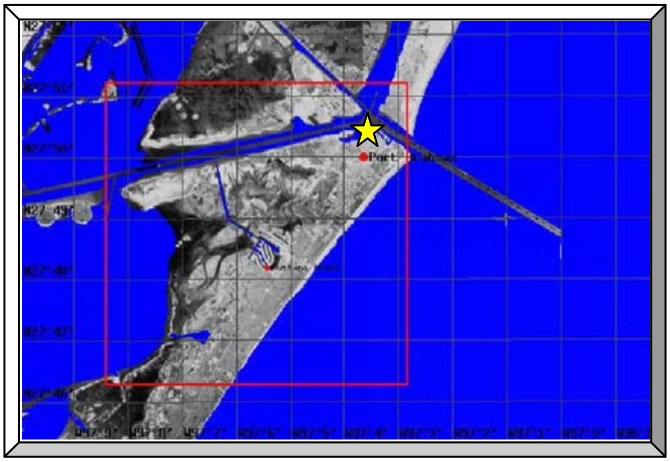

Port Aransas, TX	
Continuous station number	146
Overseeing agency	NOS
Longitude [decimal deg.]	97.06 W.
Latitude [decimal deg.]	27.84 N.
Reason for elimination	In the river

Packery Channel, TX	
Continuous station number	148
Overseeing agency	NOS
Longitude [decimal deg.]	97.24 W.
Latitude [decimal deg.]	27.63 N.
Reason for elimination	In the channel

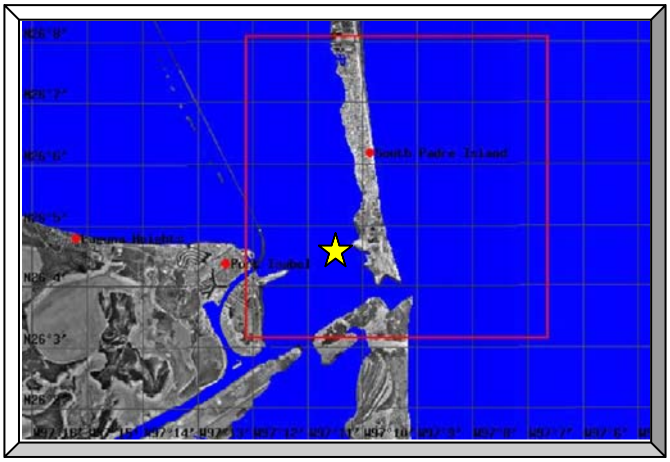

South Padre Island C.G. Station, TX	
Continuous station number	150
Overseeing agency	NOS
Longitude [decimal deg.]	97.18 W.
Latitude [decimal deg.]	26.08 N.
Reason for elimination	In the inlet

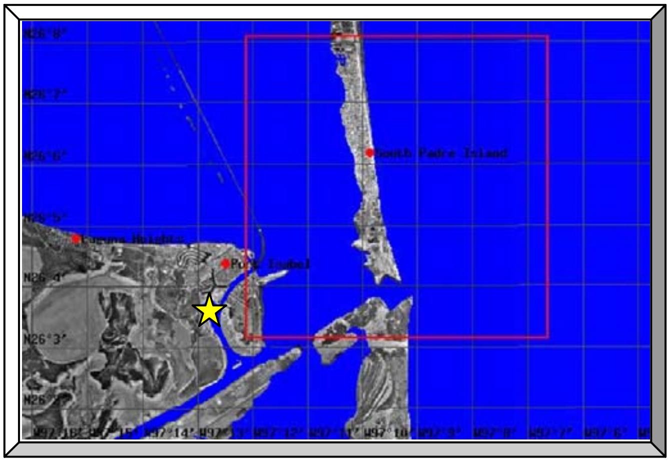

Port Isabel, Laguna Madre, TX	
Continuous station number	152
Overseeing agency	NOS
Longitude [decimal deg.]	97.22 W.
Latitude [decimal deg.]	26.06 N.
Reason for elimination	In the river

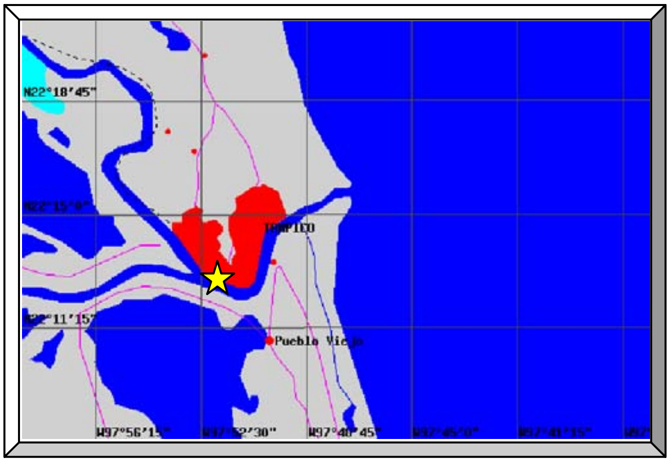

Ciudad Madero, Mexico	
Continuous station number	154
Overseeing agency	GOM
Longitude [decimal deg.]	97.86 W.
Latitude [decimal deg.]	22.22 N.
Reason for elimination	In the river

APPENDIX E

150 TIDAL STATIONS

WITH QUALITATIVE AND QUANTITATIVE COMPARISON

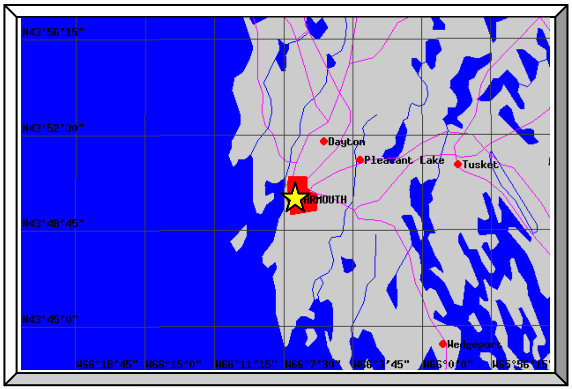

St. 1: Yarmouth, Nova Scotia					
Observer			IHO		
Longitude			66.12 W		
Latitude			43.83 N		
Simulation Results					
	333K	95K	60K	53K	48K
Ph [º]	0.8	0.9	2.3	0.4	1.7
R^2 [-]	1.00	1.00	1.00	1.00	1.00

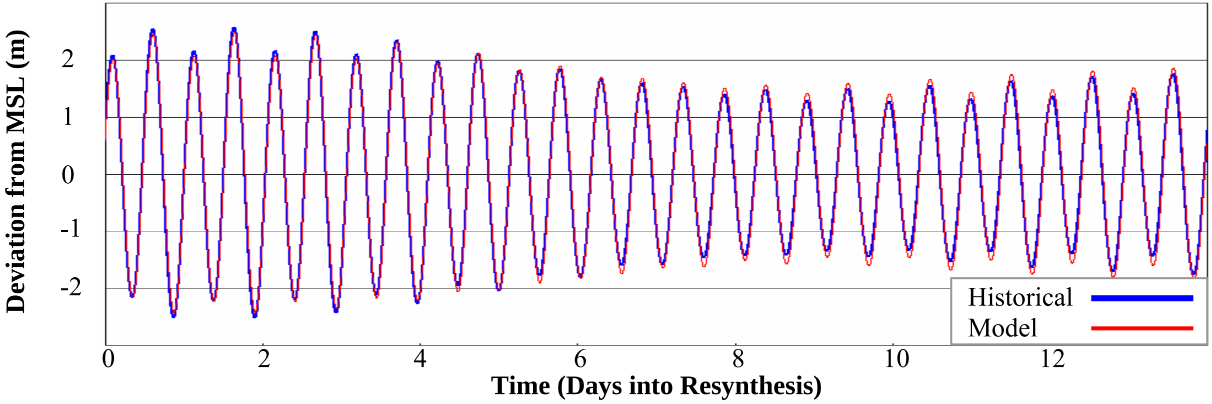

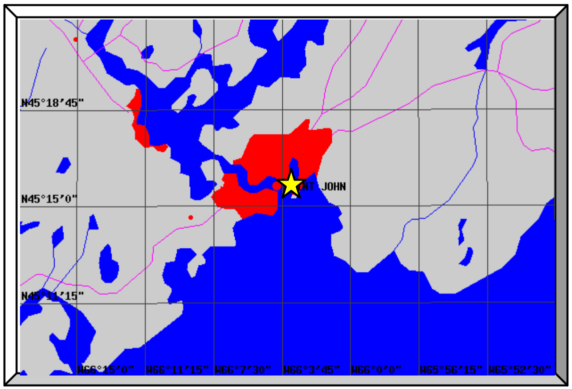

St. 2: St. John, New Brunswick					
Observer			IHO		
Longitude			66.05 W		
Latitude			45.27 N		
Simulation Results					
	333K	95K	60K	53K	48K
Ph [º]	0.8	0.8	2.7	3.6	4.6
R^2 [-]	1.00	1.00	1.00	1.00	1.00

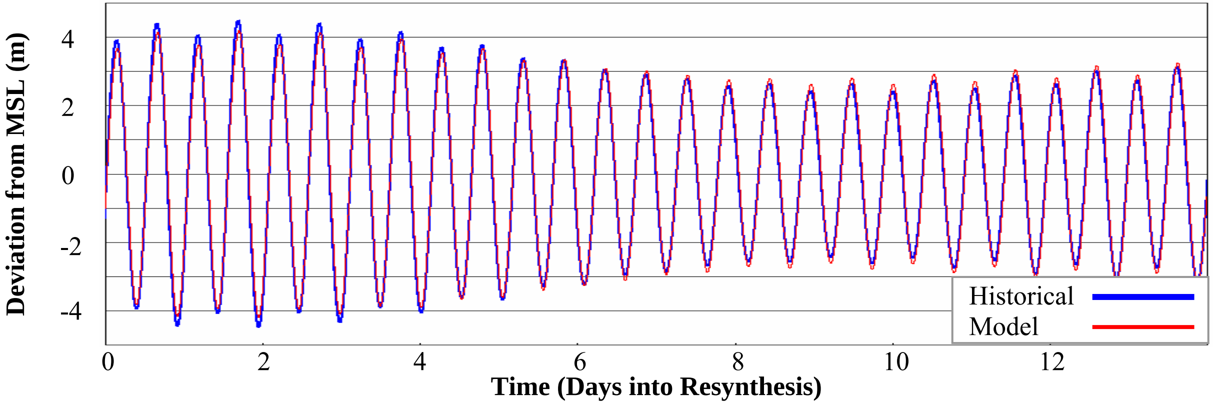

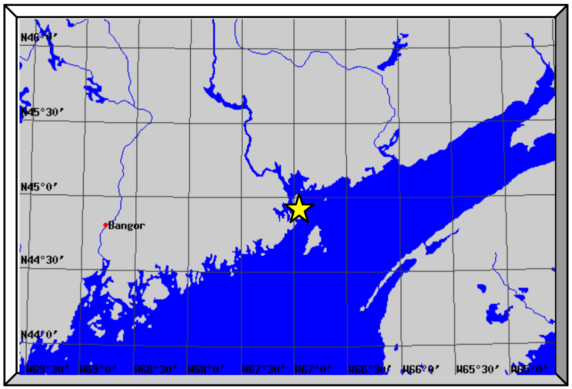

<table>
<tr><th colspan="6">St. 3: Eastport, Passamaquoddy Bay, ME</th></tr>
<tr><td colspan="2">Observer</td><td colspan="4">NOS</td></tr>
<tr><td colspan="2">Longitude</td><td colspan="4">66.99 W</td></tr>
<tr><td colspan="2">Latitude</td><td colspan="4">44.90 N</td></tr>
<tr><td colspan="6">Simulation Results</td></tr>
<tr><td></td><td>333K</td><td>95K</td><td>60K</td><td>53K</td><td>48K</td></tr>
<tr><td>Ph [º]</td><td>1.2</td><td>2.3</td><td>5.2</td><td>5.8</td><td>6.4</td></tr>
<tr><td>R^2 [-]</td><td>0.97</td><td>0.98</td><td>0.97</td><td>0.97</td><td>0.97</td></tr>
</table>

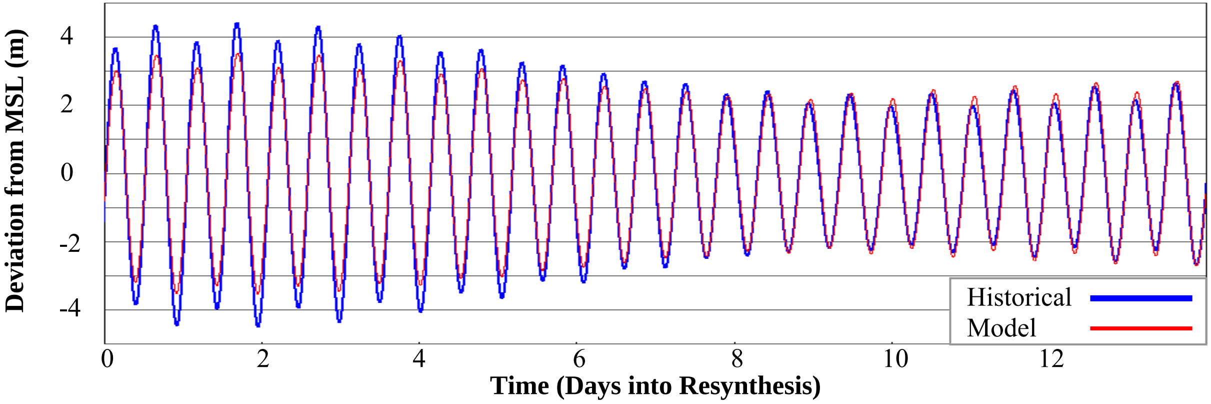

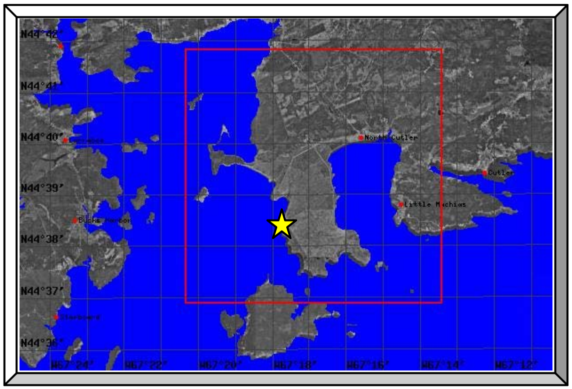

<table>
<tr><th colspan="6">St. 4: Cutler Naval Base, Machias Bay, ME</th></tr>
<tr><td colspan="2">Observer</td><td colspan="4">NOS</td></tr>
<tr><td colspan="2">Longitude</td><td colspan="4">67.30 W</td></tr>
<tr><td colspan="2">Latitude</td><td colspan="4">44.64 N</td></tr>
<tr><td colspan="6">Simulation Results</td></tr>
<tr><td></td><td>333K</td><td>95K</td><td>60K</td><td>53K</td><td>48K</td></tr>
<tr><td>Ph [º]</td><td>0.9</td><td>0.4</td><td>4.2</td><td>3.0</td><td>4.8</td></tr>
<tr><td>R^2 [-]</td><td>0.98</td><td>0.99</td><td>0.99</td><td>0.99</td><td>0.99</td></tr>
</table>

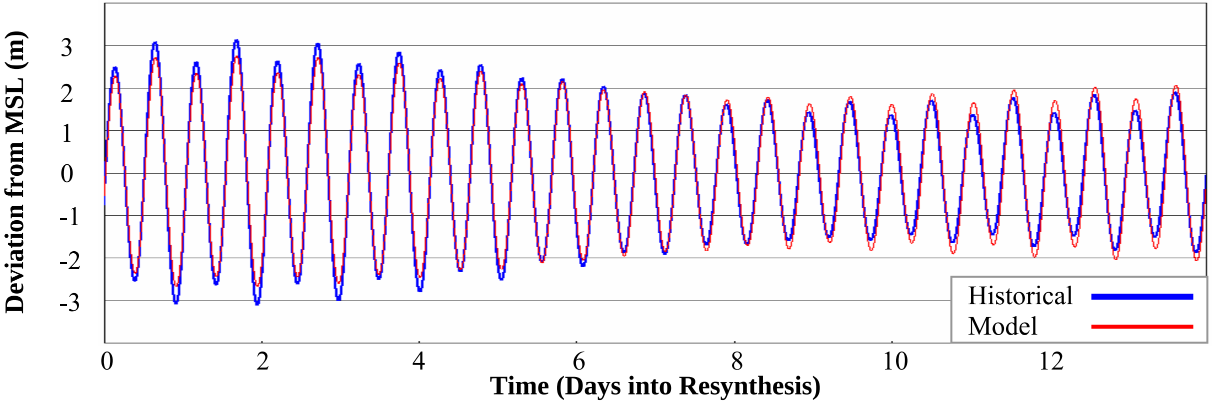

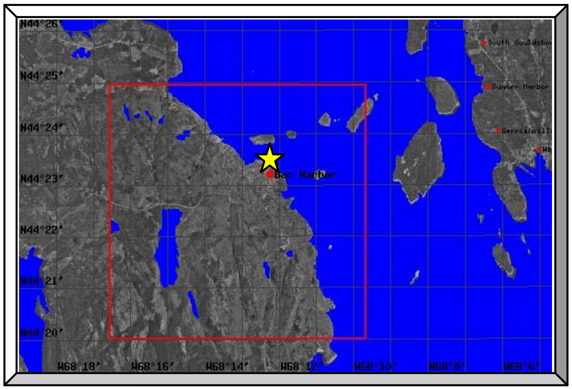

<table>
<tr><th colspan="6">St. 5: Bar Harbor, Frenchman Bay, ME</th></tr>
<tr><td colspan="2">Observer</td><td colspan="4">NOS</td></tr>
<tr><td colspan="2">Longitude</td><td colspan="4">68.21 W</td></tr>
<tr><td colspan="2">Latitude</td><td colspan="4">44.39 N</td></tr>
<tr><td colspan="6">Simulation Results</td></tr>
<tr><td></td><td>333K</td><td>95K</td><td>60K</td><td>53K</td><td>48K</td></tr>
<tr><td>*Ph* [º]</td><td>3.0</td><td>1.1</td><td>6.6</td><td>2.8</td><td>4.6</td></tr>
<tr><td>R^2 [-]</td><td>0.98</td><td>0.98</td><td>0.98</td><td>0.98</td><td>0.98</td></tr>
</table>

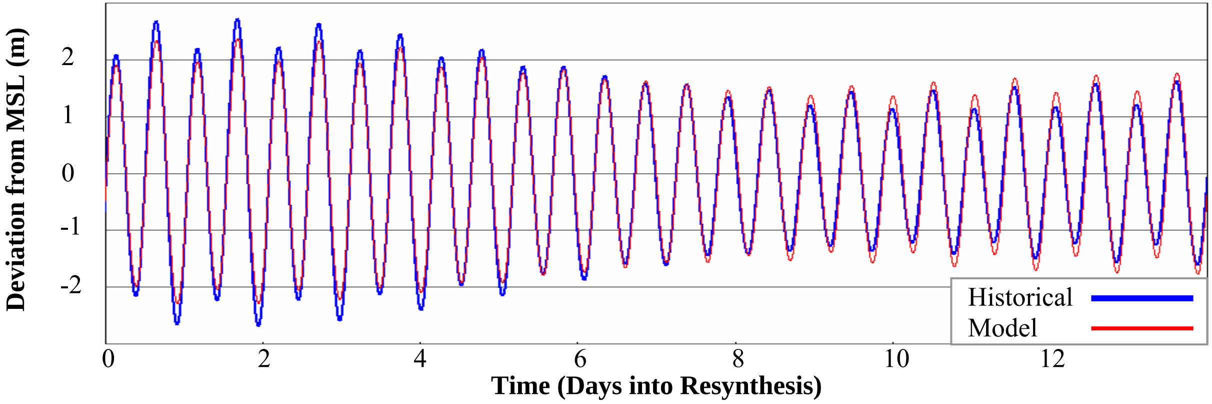

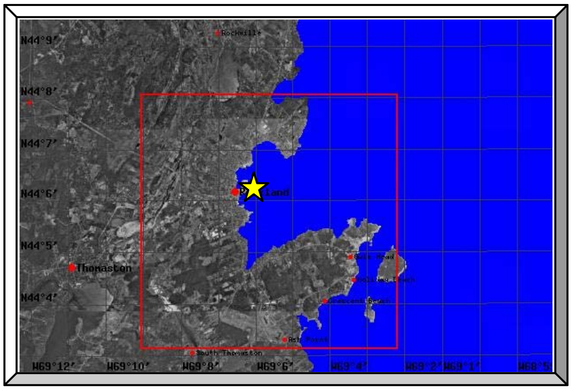

<table>
<tr><th colspan="6">St. 6: Rockland ME</th></tr>
<tr><td colspan="2">Observer</td><td colspan="4">NOS</td></tr>
<tr><td colspan="2">Longitude</td><td colspan="4">69.10 W</td></tr>
<tr><td colspan="2">Latitude</td><td colspan="4">44.11 N</td></tr>
<tr><td colspan="6">Simulation Results</td></tr>
<tr><td></td><td>333K</td><td>95K</td><td>60K</td><td>53K</td><td>48K</td></tr>
<tr><td>*Ph* [º]</td><td>6.4</td><td>8.4</td><td>5.3</td><td>4.5</td><td>5.7</td></tr>
<tr><td>R^2 [-]</td><td>0.98</td><td>0.98</td><td>0.99</td><td>0.99</td><td>0.99</td></tr>
</table>

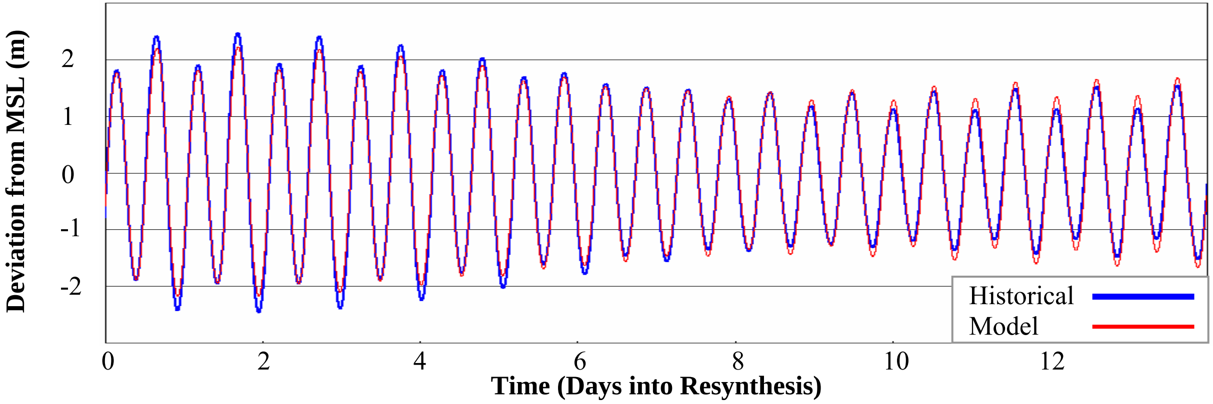

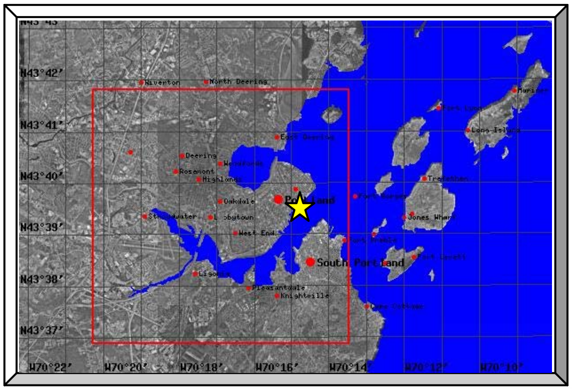

St. 7: Portland, Casco Bay, ME					
Observer	NOS				
Longitude	70.25 W				
Latitude	43.66 N				
Simulation Results					
	333K	95K	60K	53K	48K
Ph [°]	3.2	3.5	5.2	4.2	5.0
R^2 [-]	0.98	0.98	0.98	0.99	0.99

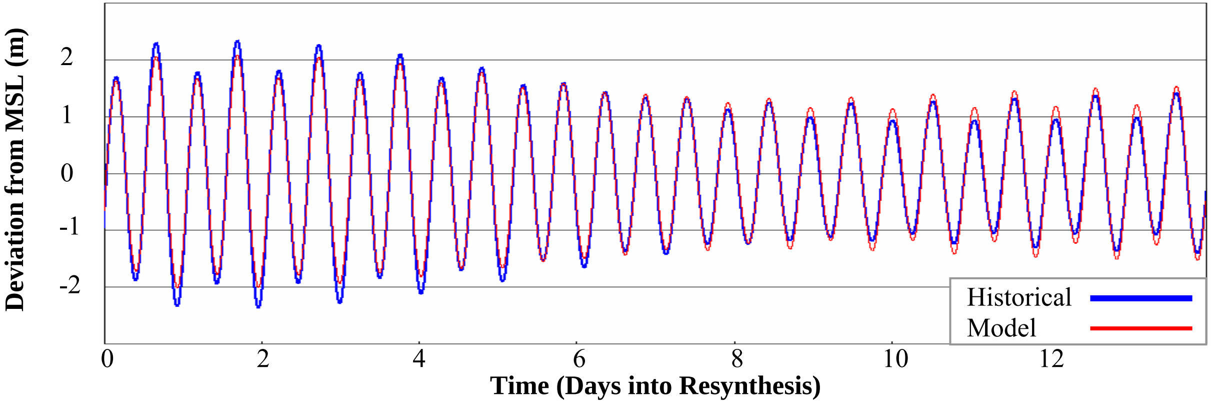

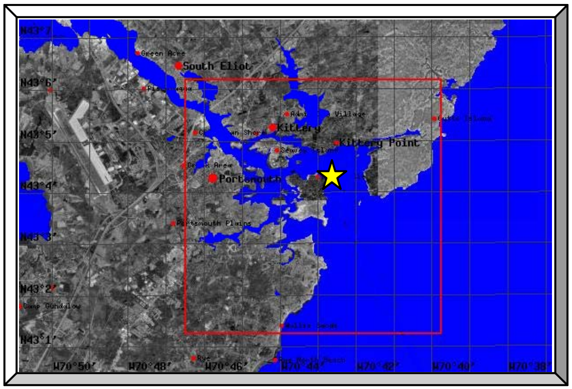

St. 9: Fort Point, Newcastle Island, NH					
Observer	NOS				
Longitude	70.71 W				
Latitude	43.07 N				
Simulation Results					
	333K	95K	60K	53K	48K
Ph [°]	4.8	3.2	7.4	5.9	6.6
R^2 [-]	0.98	0.99	0.99	0.99	0.99

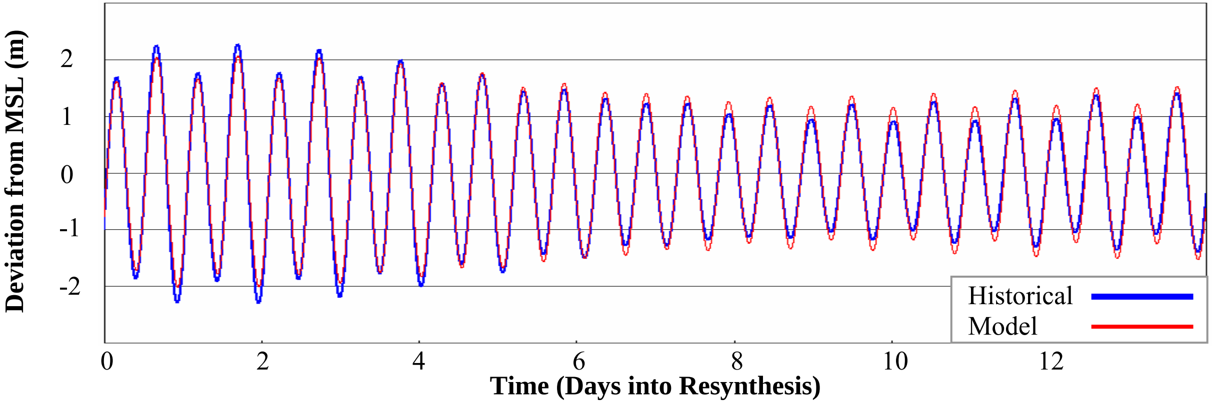

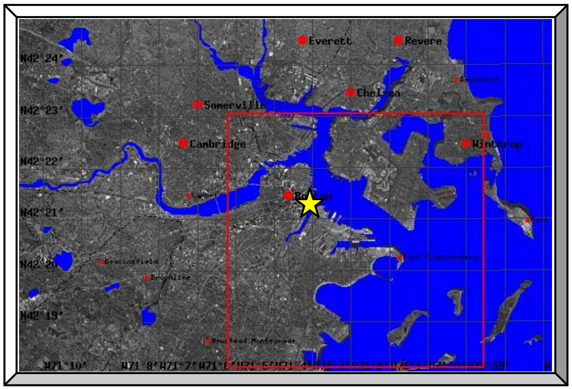

St. 10: Boston, Boston Harbor, MA					
Observer			NOS		
Longitude			71.05 W		
Latitude			42.36 N		
Simulation Results					
	333K	95K	60K	53K	48K
Ph [º]	0.9	4.3	5.4	4.3	4.0
R^2 [-]	0.98	0.97	0.98	0.98	0.98

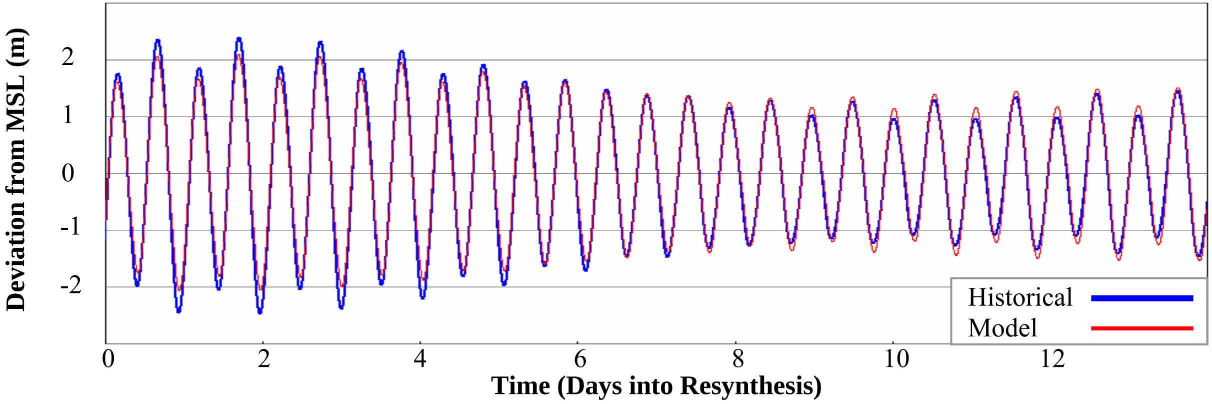

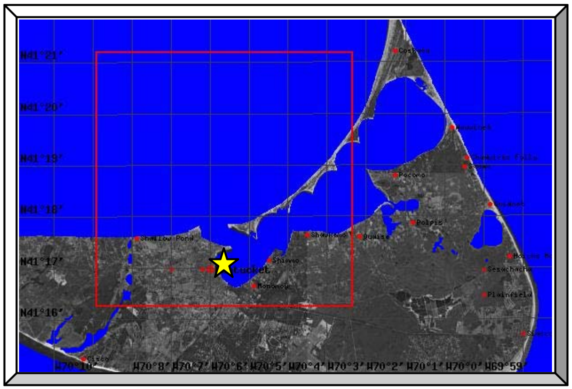

St. 12: Nantucket Island, Nantucket Sound, MA					
Observer			NOS		
Longitude			70.10 W		
Latitude			41.29 N		
Simulation Results					
	333K	95K	60K	53K	48K
Ph [º]	17.8	10.5	29.7	8.8	21.3
R^2 [-]	0.94	0.83	0.96	0.92	0.94

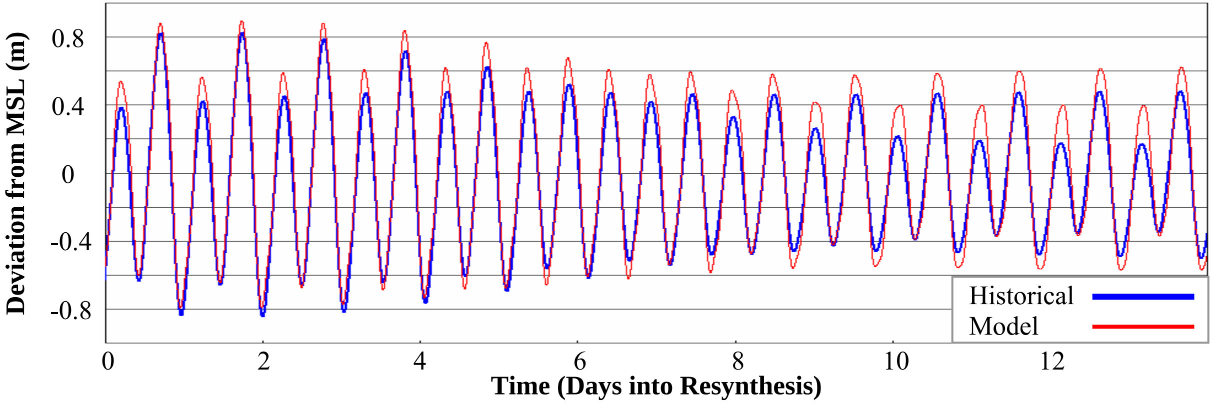

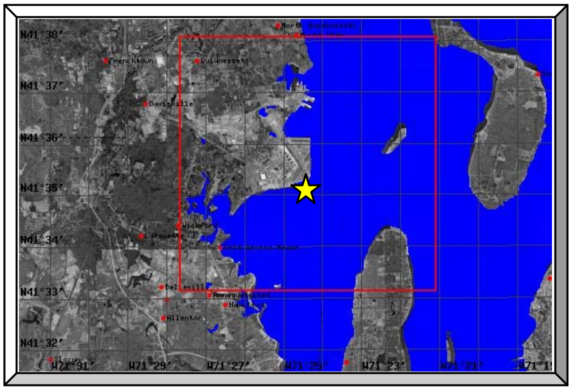

St. 16: Quonset Point, RI					
Observer	NOS				
Longitude	71.41 W				
Latitude	41.59 N				
Simulation Results					
	333K	95K	60K	53K	48K
Ph [º]	11.5	19.1	4.7	4.6	8.0
R^2 [-]	0.92	0.95	0.94	0.95	0.95

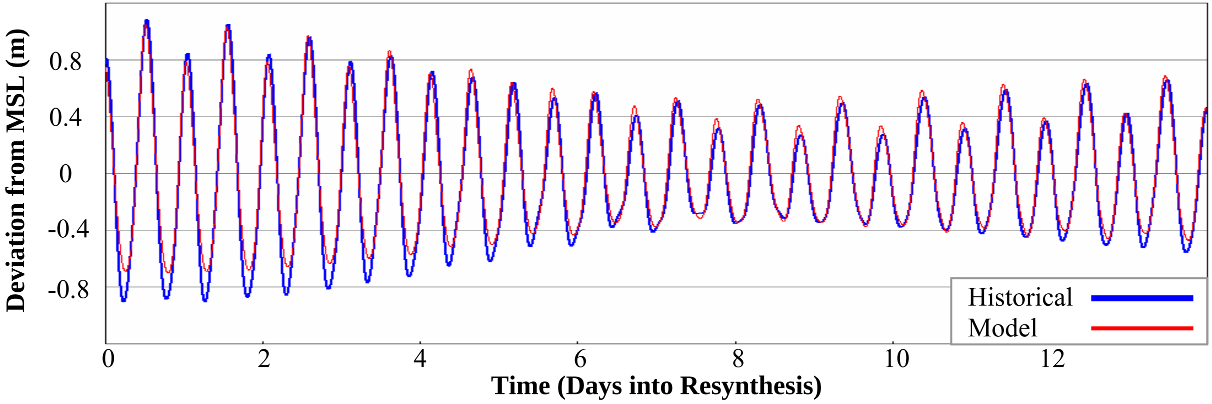

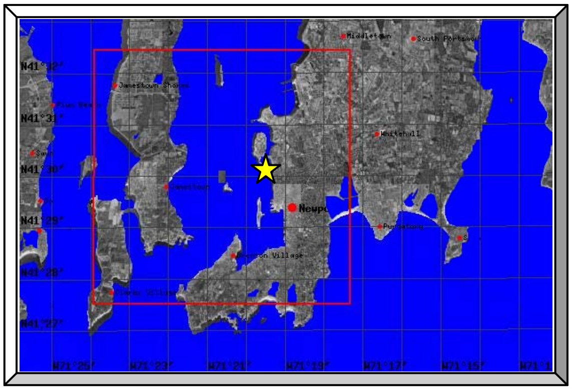

St. 17: Newport, Narragansett Bay, RI					
Observer	NOS				
Longitude	71.33 W				
Latitude	41.51 N				
Simulation Results					
	333K	95K	60K	53K	48K
Ph [º]	4.2	5.6	4.8	6.6	8.0
R^2 [-]	0.94	0.98	0.96	0.97	0.96

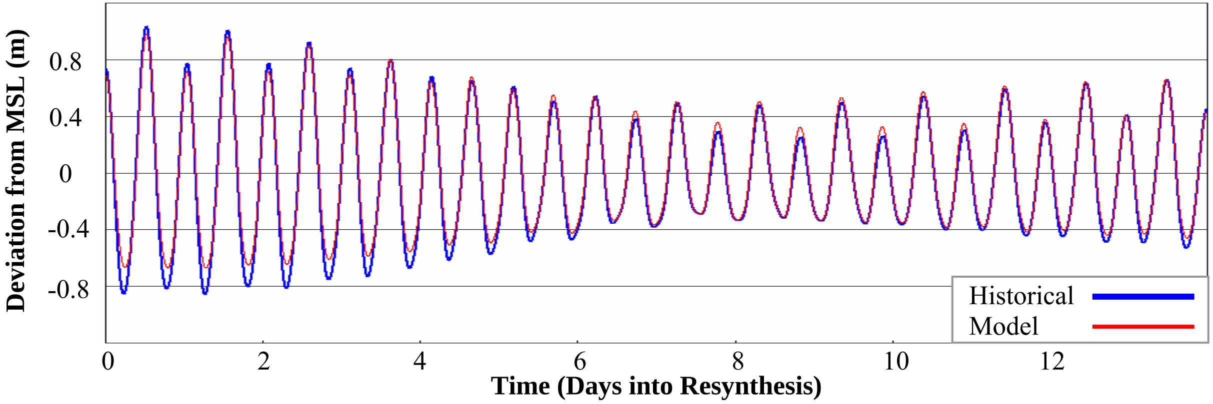

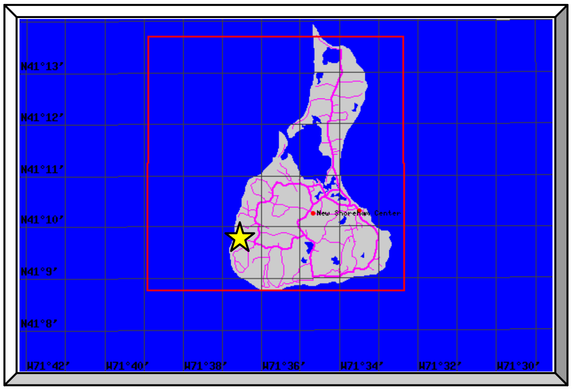

St. 18: Block Island, SW End, Block Is. Sound, RI	
Observer	NOS
Longitude	71.61 W
Latitude	41.16 N
Simulation Results	

	333K	95K	60K	53K	48K
Ph [º]	6.0	11.6	9.5	9.5	8.5
R^2 [-]	0.97	0.97	0.97	0.97	0.97

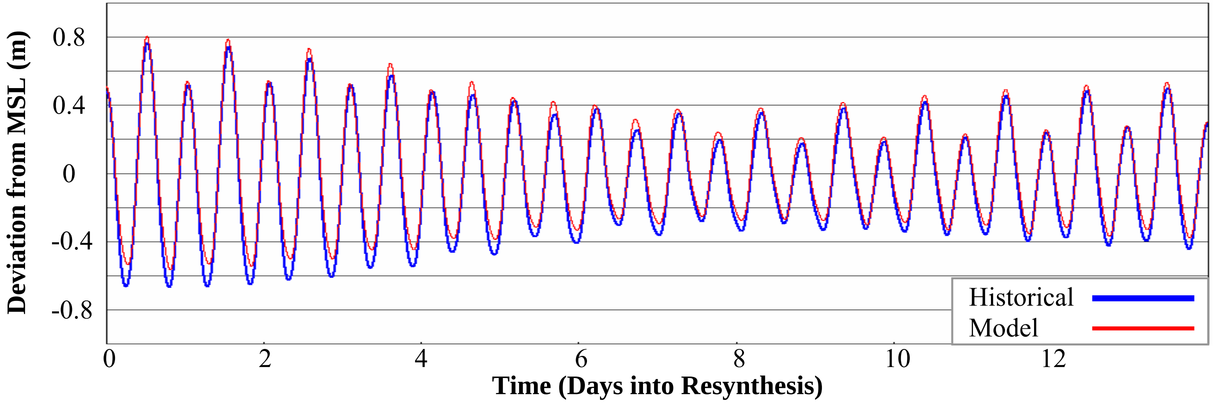

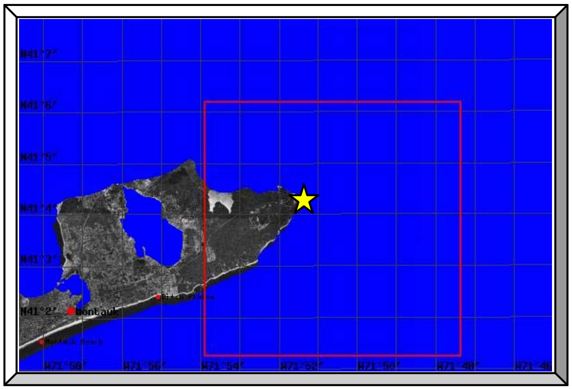

St. 19: Montauk Point Light, NY	
Observer	NOS
Longitude	71.86 W
Latitude	41.07 N
Simulation Results	

	333K	95K	60K	53K	48K
Ph [º]	0.3	0.6	1.3	1.2	0.5
R^2 [-]	0.93	0.95	0.95	0.95	0.95

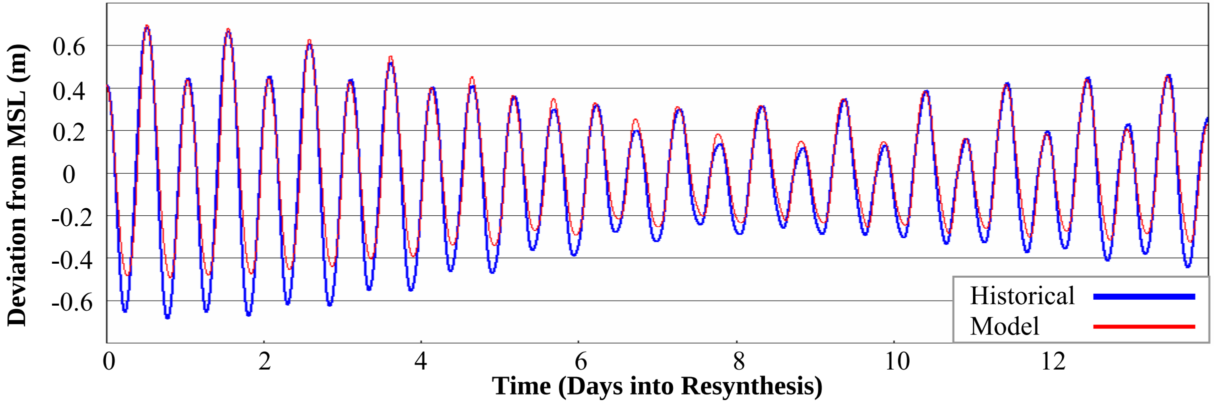

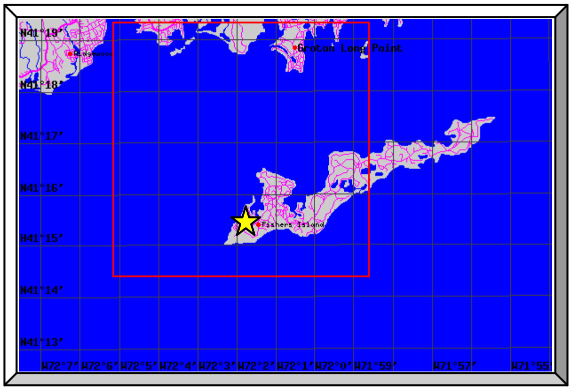

St. 21: Silver EEL Pond, Fishers Is., NY					
Observer			NOS		
Longitude			72.03 W		
Latitude			41.26 N		
Simulation Results					
	333K	95K	60K	53K	48K
Ph [º]	14.1	16.7	13.2	17.0	14.7
R^2 [-]	0.94	0.87	0.93	0.90	0.91

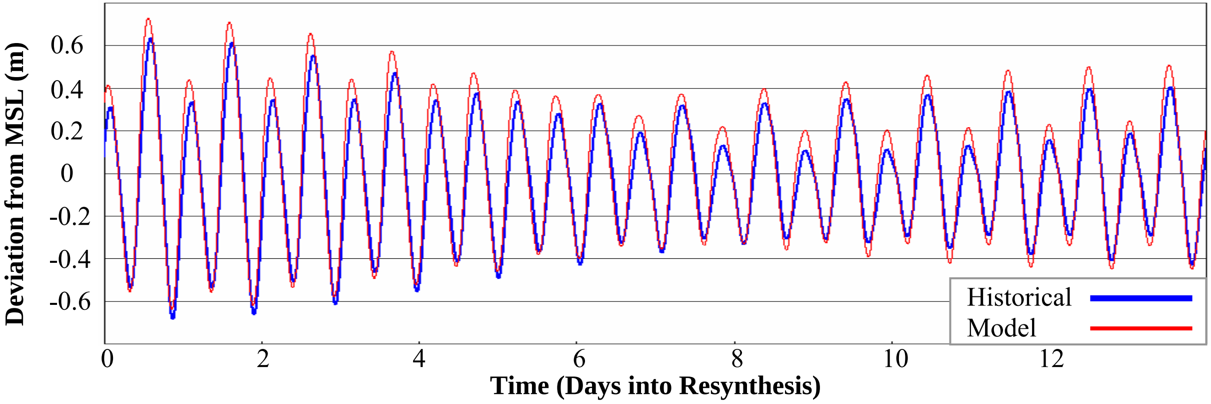

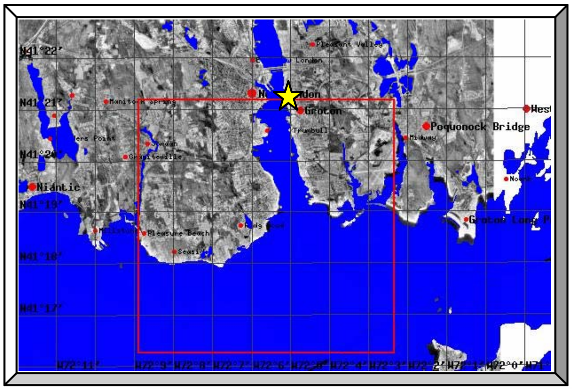

St. 22: New London, Thames River, CT					
Observer			NOS		
Longitude			72.09 W		
Latitude			41.36 N		
Simulation Results					
	333K	95K	60K	53K	48K
Ph [º]	14.0	15.8	14.5	16.4	15.7
R^2 [-]	0.95	0.91	0.93	0.93	0.91

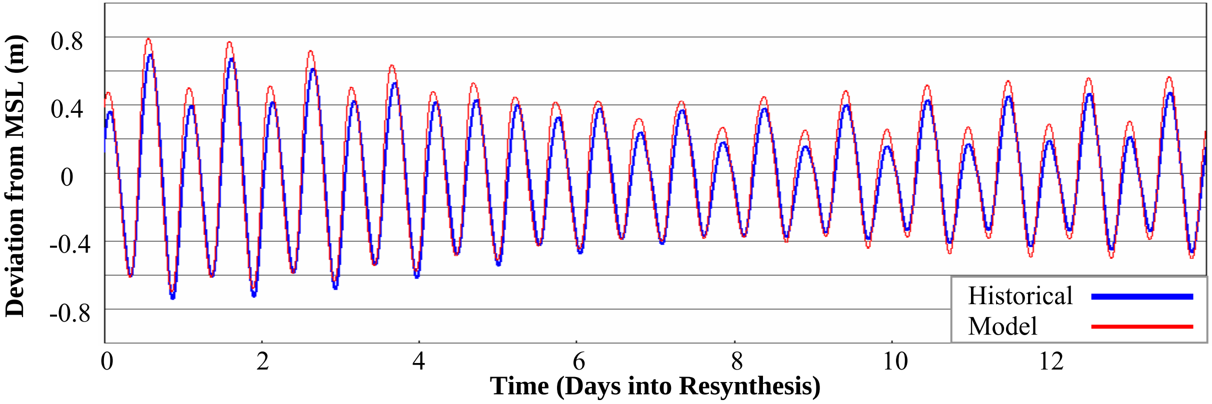

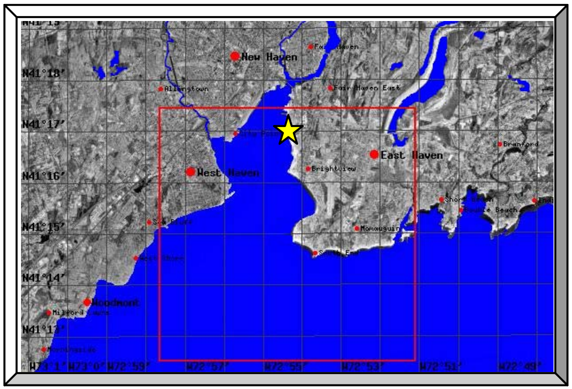

<table>
<tr><td colspan="6">St. 23: New Haven, New Haven Harbor, CT</td></tr>
<tr><td colspan="3">Observer</td><td colspan="3">NOS</td></tr>
<tr><td colspan="3">Longitude</td><td colspan="3">72.91 W</td></tr>
<tr><td colspan="3">Latitude</td><td colspan="3">41.28 N</td></tr>
<tr><td colspan="6">Simulation Results</td></tr>
<tr><td></td><td>333K</td><td>95K</td><td>60K</td><td>53K</td><td>48K</td></tr>
<tr><td>*Ph* [º]</td><td>5.7</td><td>11.2</td><td>5.2</td><td>10.3</td><td>8.7</td></tr>
<tr><td>R^2 [-]</td><td>0.97</td><td>0.98</td><td>0.98</td><td>0.98</td><td>0.98</td></tr>
</table>

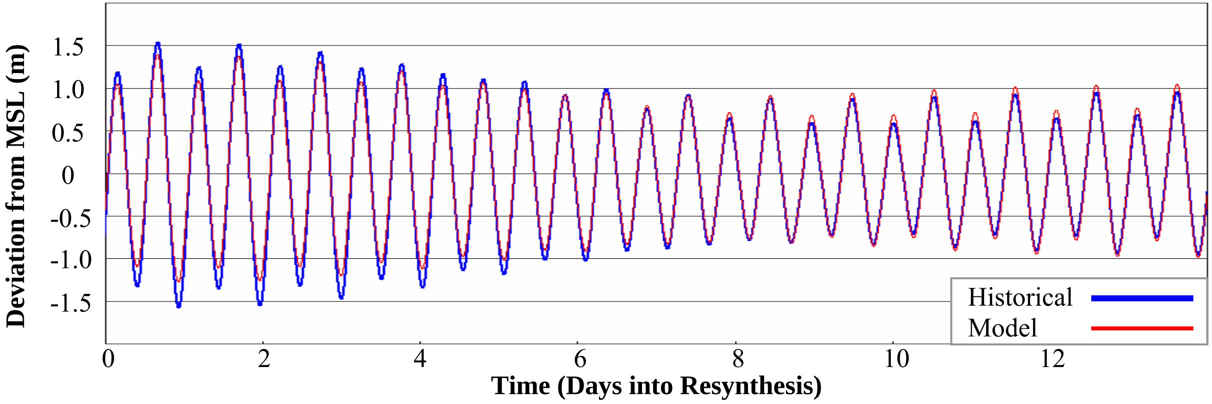

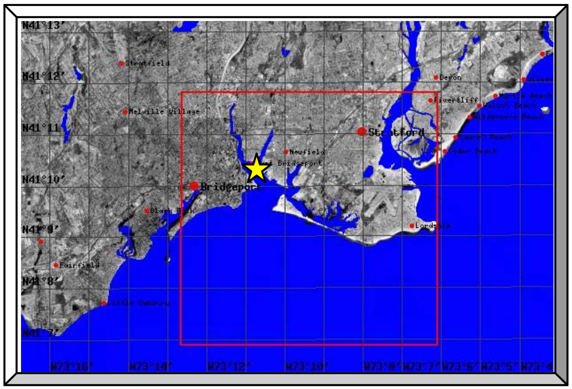

<table>
<tr><td colspan="6">St. 24: Bridgeport, Bridgeport Harbor, CT</td></tr>
<tr><td colspan="3">Observer</td><td colspan="3">NOS</td></tr>
<tr><td colspan="3">Longitude</td><td colspan="3">73.18 W</td></tr>
<tr><td colspan="3">Latitude</td><td colspan="3">41.17 N</td></tr>
<tr><td colspan="6">Simulation Results</td></tr>
<tr><td></td><td>333K</td><td>95K</td><td>60K</td><td>53K</td><td>48K</td></tr>
<tr><td>*Ph* [º]</td><td>4.0</td><td>10.2</td><td>4.6</td><td>8.9</td><td>8.1</td></tr>
<tr><td>R^2 [-]</td><td>0.98</td><td>0.98</td><td>0.98</td><td>0.99</td><td>0.99</td></tr>
</table>

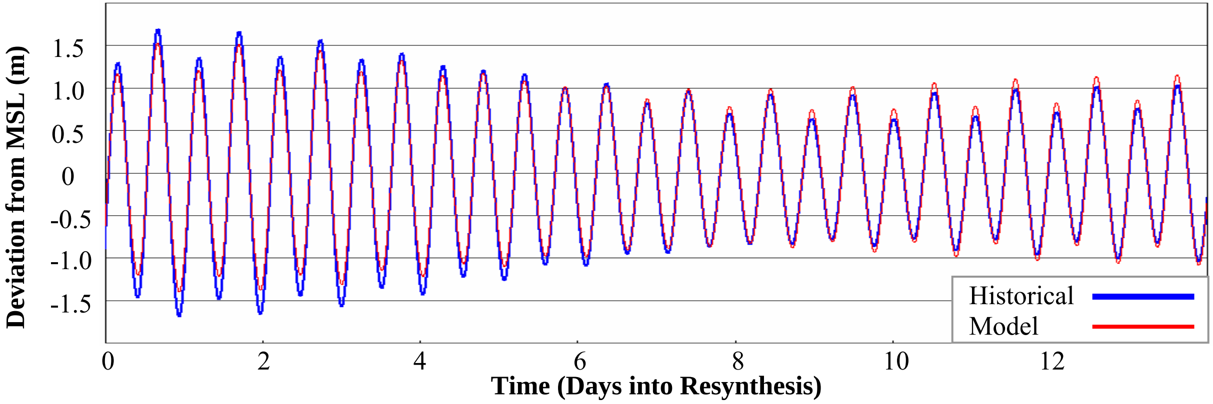

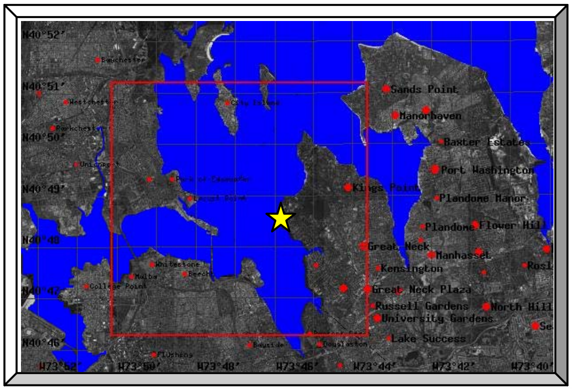

St. 25: Kings Point, Long Island Sound, NY	
Observer	NOS
Longitude	73.77 W
Latitude	40.81 N

Simulation Results					
	333K	95K	60K	53K	48K
Ph [º]	8.1	17.9	11.6	13.3	14.4
R^2 [-]	0.98	0.97	0.98	0.98	0.98

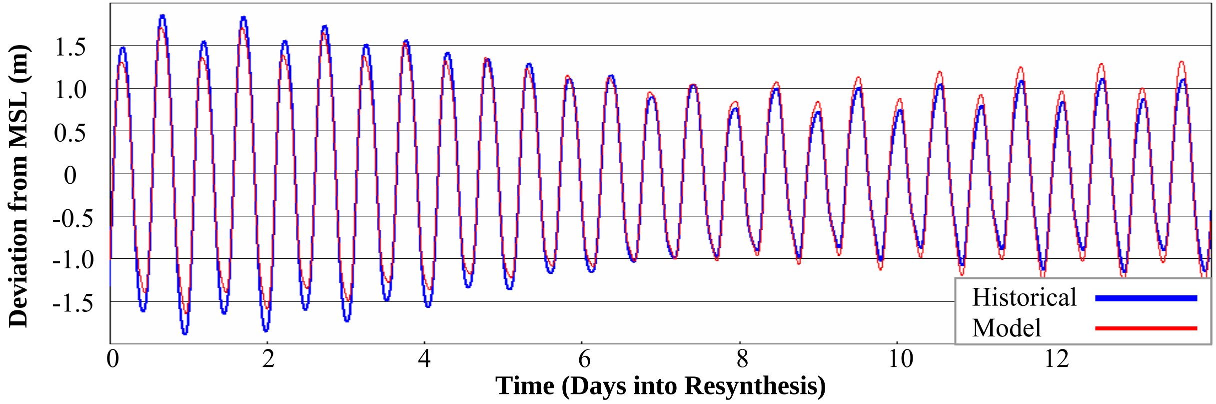

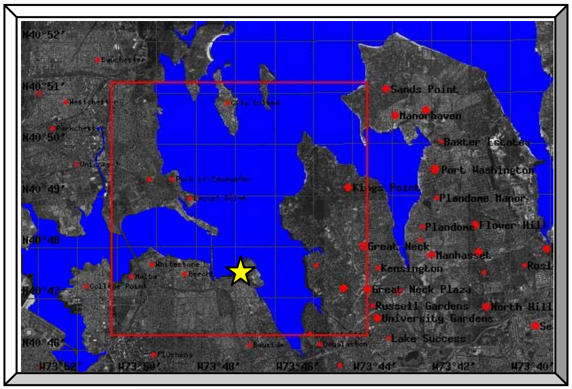

St. 26: Willets Point, Little Bay, East River, NY	
Observer	NOS
Longitude	73.78 W
Latitude	40.79 N

Simulation Results					
	333K	95K	60K	53K	48K
Ph [º]	9.6	19.0	12.4	14.4	15.4
R^2 [-]	0.98	0.96	0.98	0.98	0.98

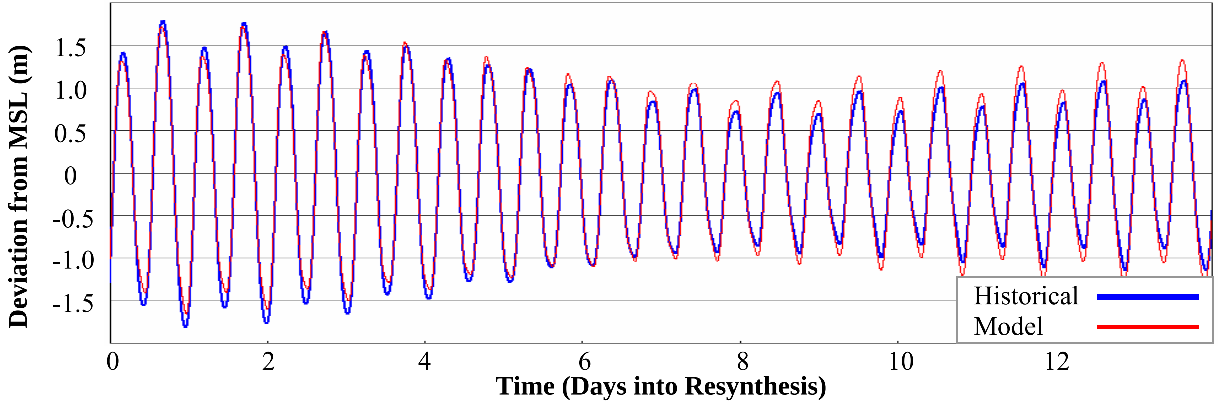

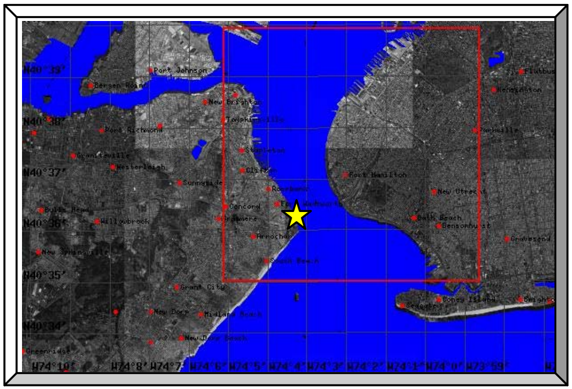

St. 27: Fort Wadsworth, Staten Island, NY					
Observer			NOS		
Longitude			74.06 W		
Latitude			40.61 N		
Simulation Results					
	333K	95K	60K	53K	48K
Ph [º]	13.1	9.7	11.2	9.5	10.9
R^2 [-]	0.96	0.96	0.96	0.95	0.96

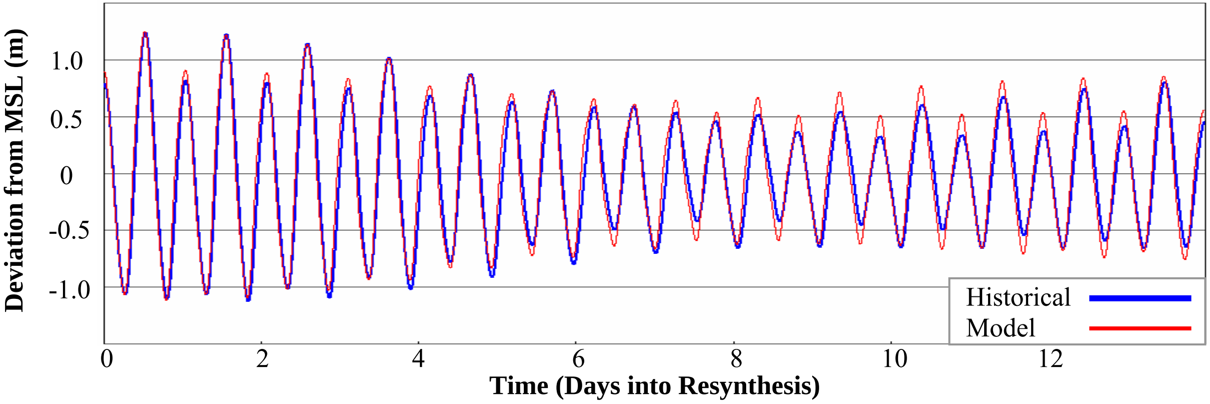

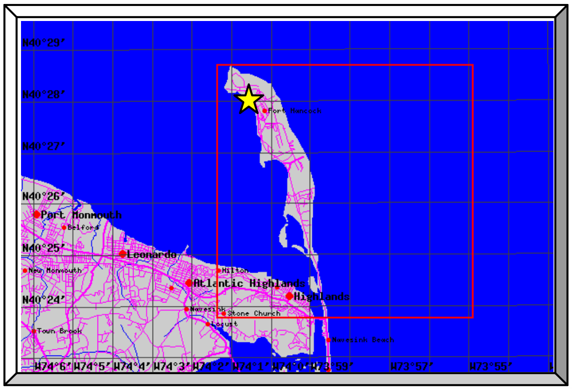

St. 29: Sandy Hook, NJ					
Observer			NOS		
Longitude			74.01 W		
Latitude			40.47 N		
Simulation Results					
	333K	95K	60K	53K	48K
Ph [º]	2.8	2.7	2.1	1.0	0.0
R^2 [-]	0.97	0.96	0.96	0.96	0.96

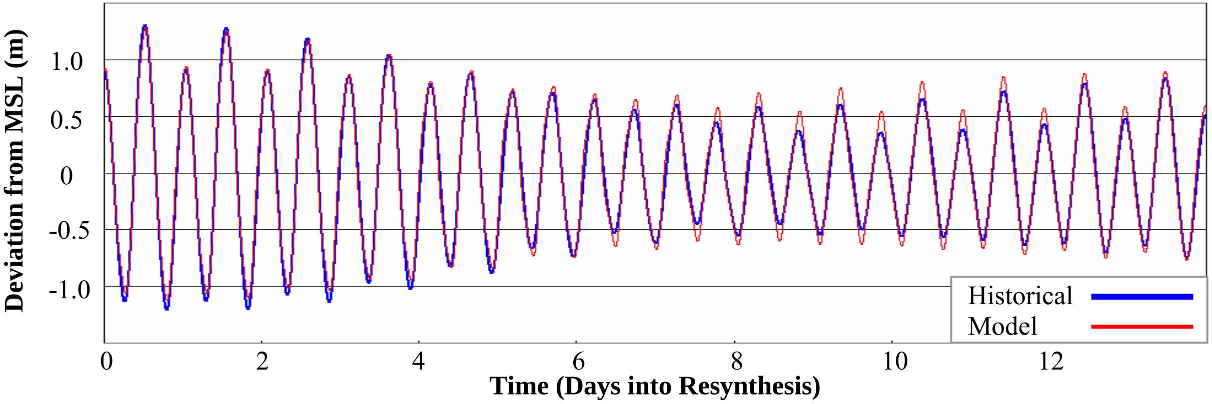

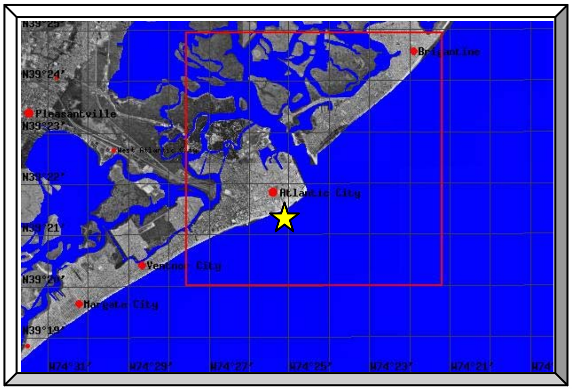

St. 30: Atlantic City, Atlantic Ocean, NJ					
Observer			NOS		
Longitude			74.42 W		
Latitude			39.36 N		
Simulation Results					
	333K	95K	60K	53K	48K
Ph [º]	4.6	4.7	3.7	3.5	3.5
R^2 [-]	0.97	0.97	0.98	0.97	0.97

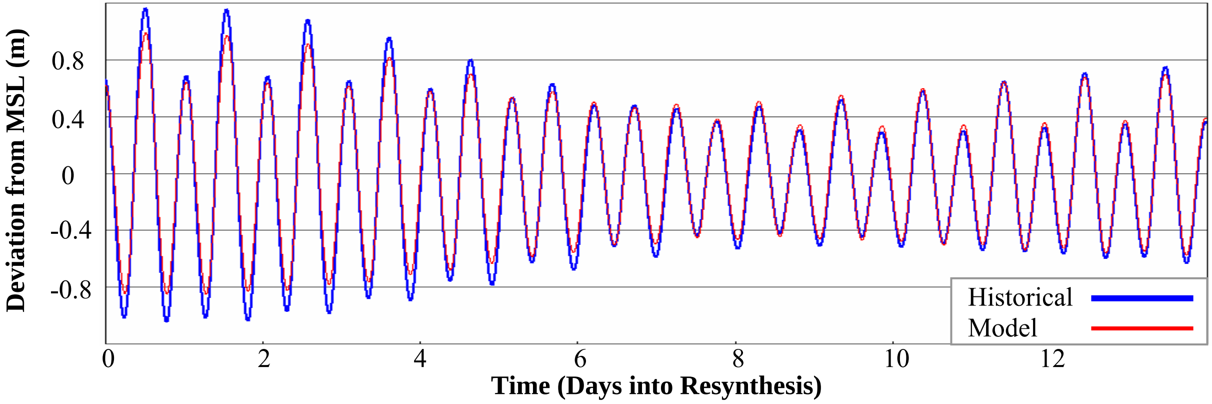

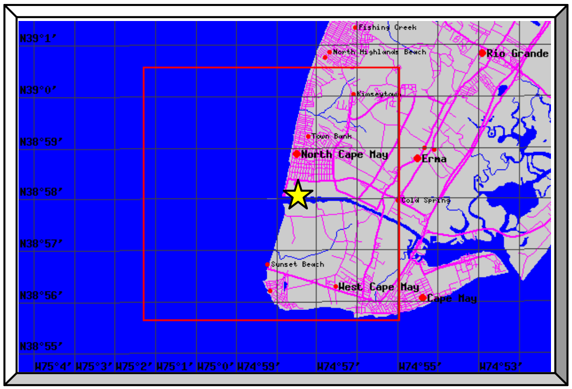

St. 31: Cape May Canal, Delaware Bay, NJ					
Observer			NOS		
Longitude			74.96 W		
Latitude			38.97 N		
Simulation Results					
	333K	95K	60K	53K	48K
Ph [º]	4.5	9.5	3.3	8.2	0.2
R^2 [-]	0.97	0.96	0.97	0.96	0.97

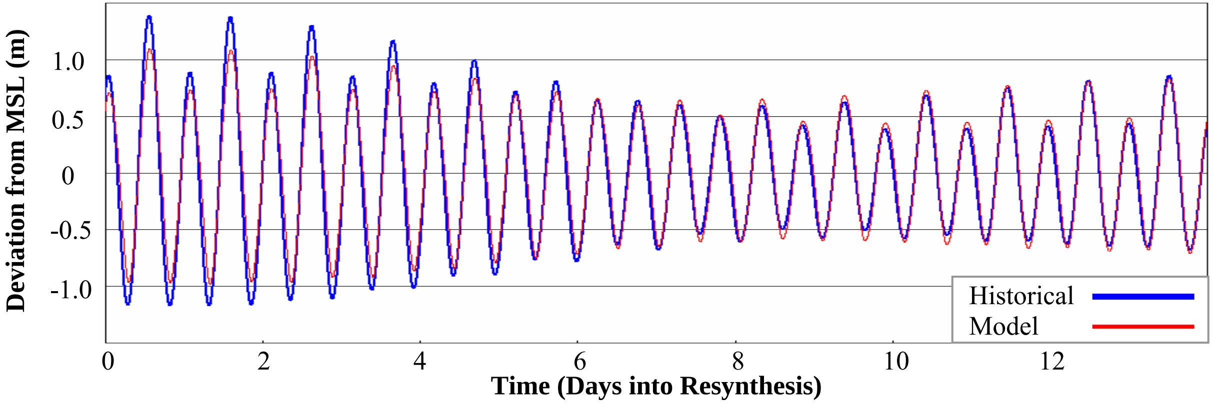

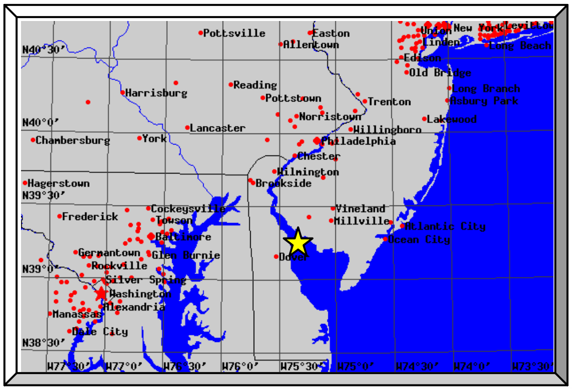

St. 32: Ship John Shoal, Delaware River, NJ					
Observer	NOS				
Longitude	75.38 W				
Latitude	39.31 N				
Simulation Results					
	333K	95K	60K	53K	48K
Ph [º]	1.2	11.1	3.5	9.9	1.4
R^2 [-]	0.95	0.97	0.96	0.97	0.96

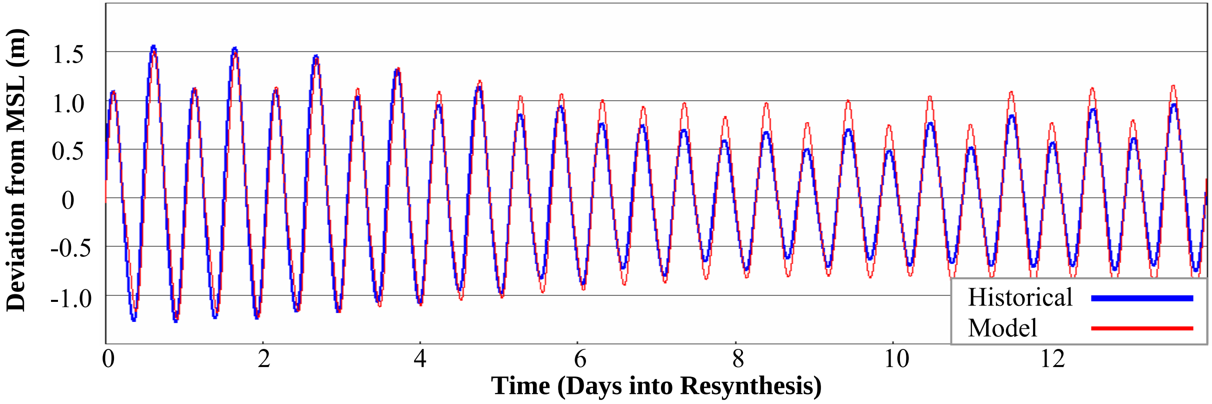

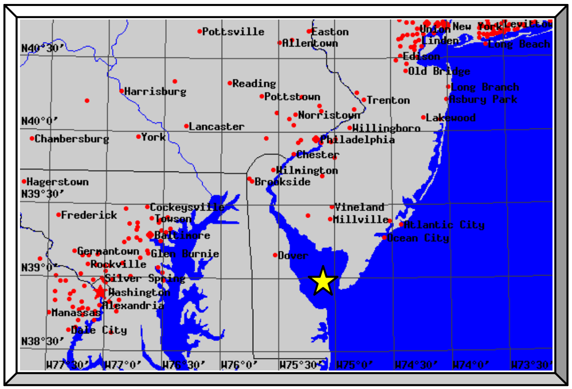

St. 33: Brandywine Shoal Light, Delaware Bay, DE					
Observer	NOS				
Longitude	75.11 W				
Latitude	38.99 N				
Simulation Results					
	333K	95K	60K	53K	48K
Ph [º]	1.3	12.5	0.0	5.9	0.3
R^2 [-]	0.98	0.96	0.97	0.96	0.97

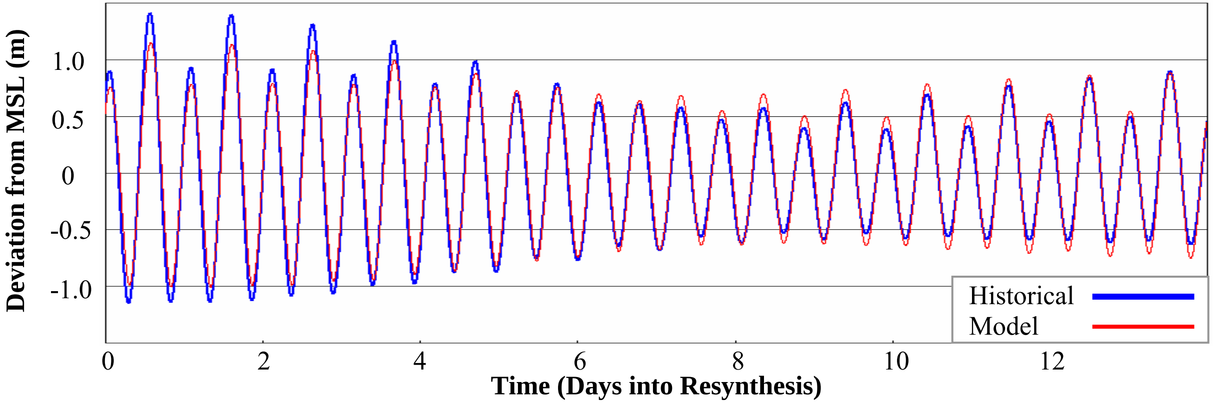

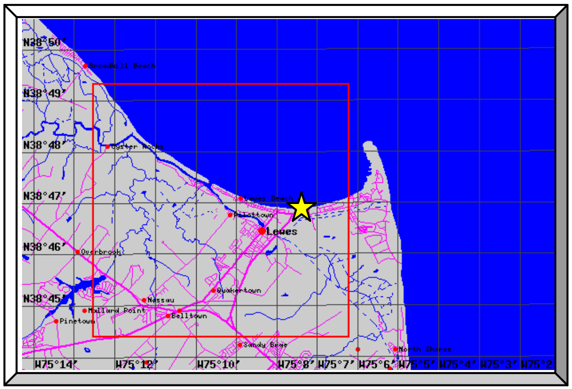

St. 34: Lewes, Ft. Miles, DE					
Observer			NOS		
Longitude			75.12 W		
Latitude			38.78 N		
Simulation Results					
	333K	95K	60K	53K	48K
Ph [º]	6.5	9.3	6.1	3.0	6.0
R^2 [-]	0.98	0.96	0.97	0.97	0.97

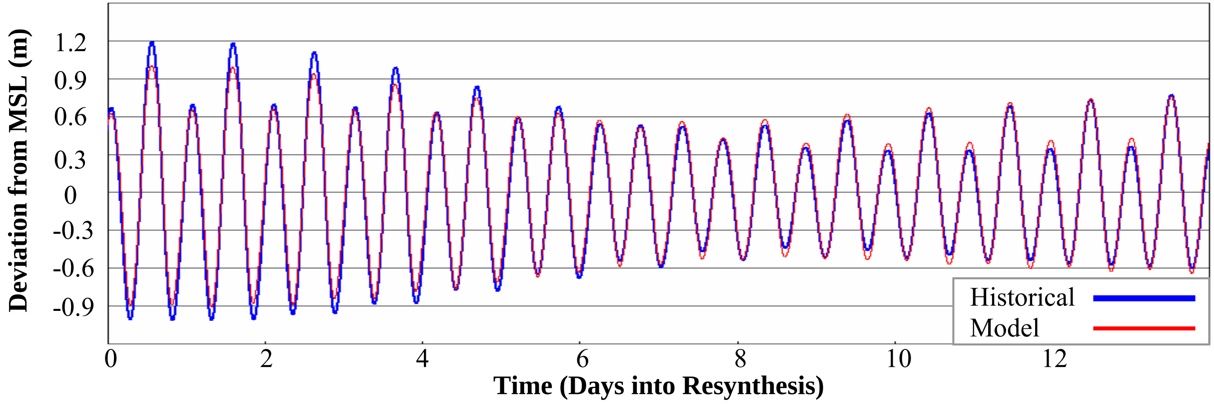

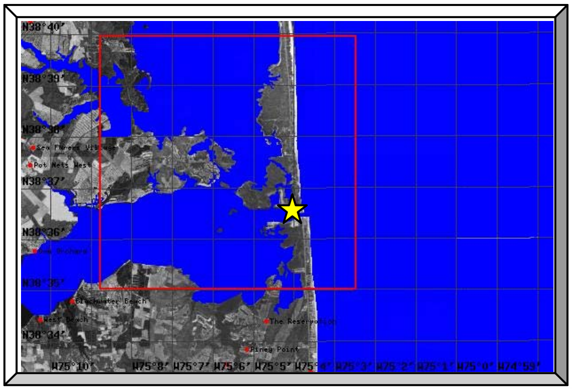

St. 35: Indian River Inlet, DE					
Observer			NOS		
Longitude			75.07 W		
Latitude			38.61 N		
Simulation Results					
	333K	95K	60K	53K	48K
Ph [º]	25.6	29.7	27.0	27.9	29.5
R^2 [-]	0.82	0.83	0.83	0.84	0.81

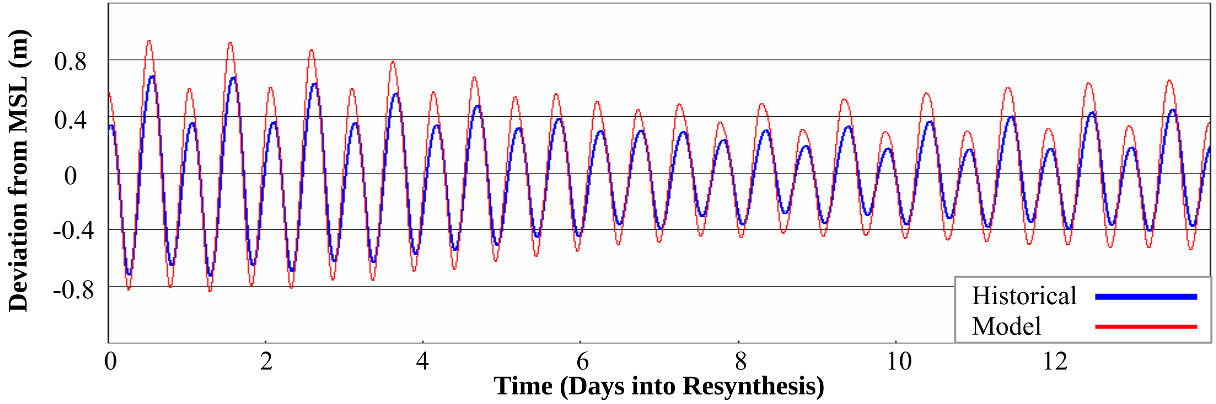

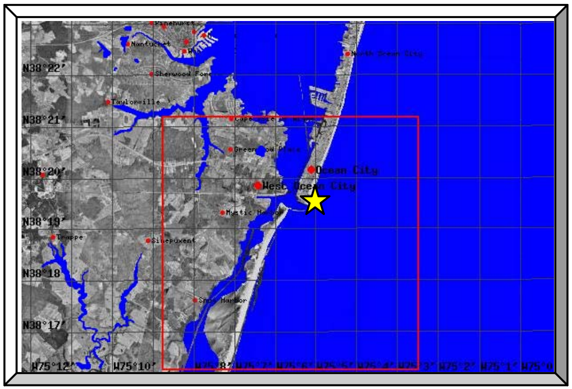

St. 36: Ocean City, Fishing Pier, MD					
Observer			NOS		
Longitude			75.08 W		
Latitude			38.33 N		
Simulation Results					
	333K	95K	60K	53K	48K
Ph [º]	4.3	4.7	5.8	4.8	7.6
R^2 [-]	0.96	0.96	0.97	0.96	0.96

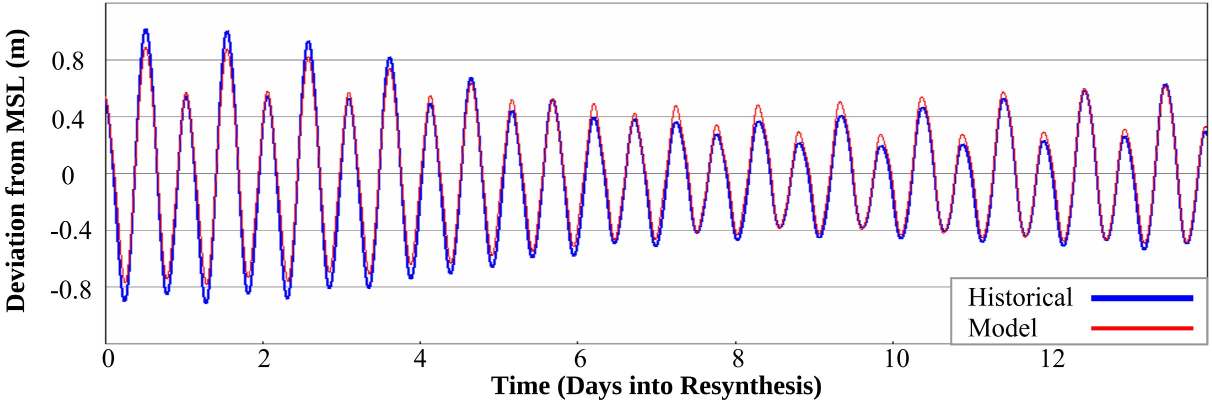

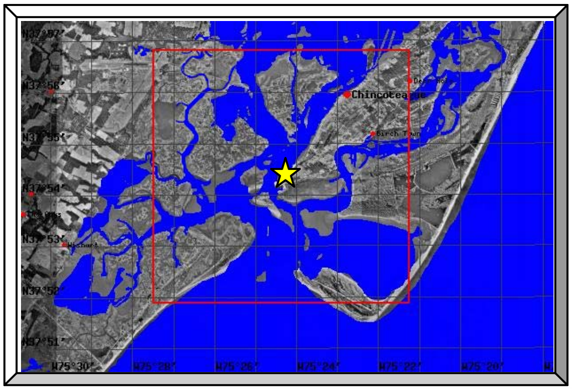

St. 38: Chincoteague Channel, South End, VA					
Observer			NOS		
Longitude			75.41 W		
Latitude			37.91 N		
Simulation Results					
	333K	95K	60K	53K	48K
Ph [º]	24.5	15.0	26.4	20.7	24.6
R^2 [-]	0.72	0.55	0.72	0.61	0.62

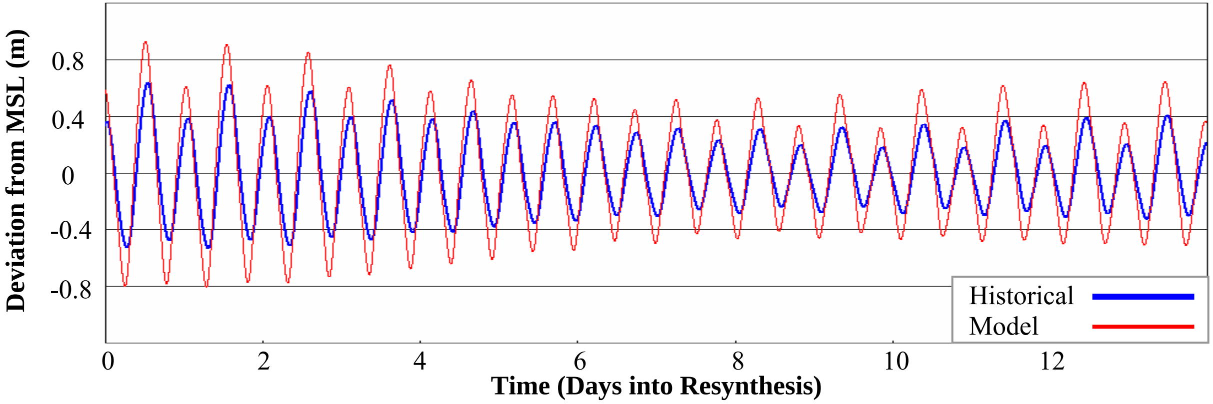

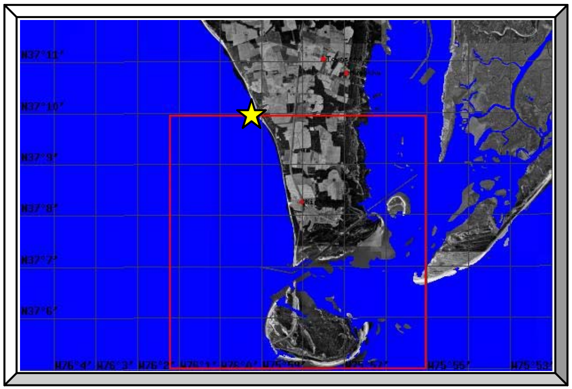

St. 39: Kiptopeke, Chesapeake Bay, VA					
Observer			NOS		
Longitude			75.99 W		
Latitude			37.17 N		
Simulation Results					
	333K	95K	60K	53K	48K
Ph [º]	9.5	16.3	10.1	11.0	9.8
R^2 [-]	0.97	0.98	0.98	0.98	0.97

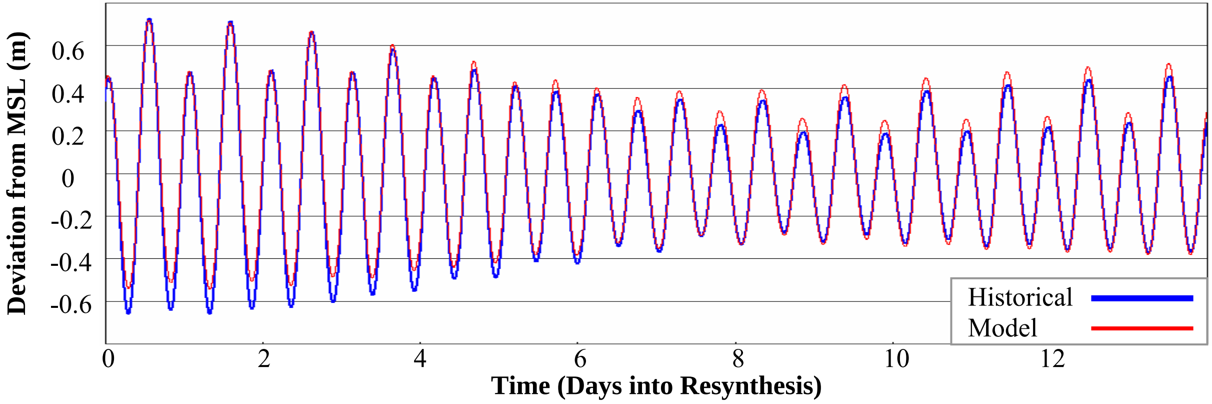

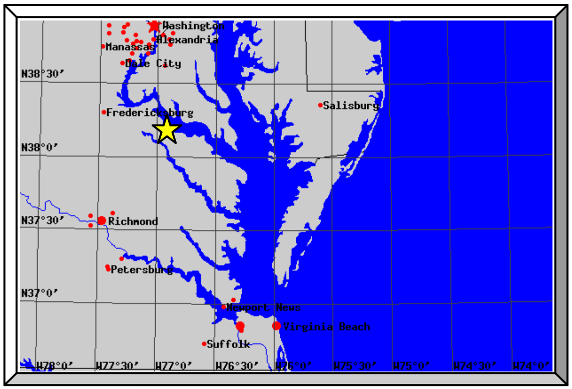

St. 46: Lewisetta, Potomac River, VA					
Observer			NOS		
Longitude			76.47 W		
Latitude			38.00 N		
Simulation Results					
	333K	95K	60K	53K	48K
Ph [º]	8.9	4.4	4.3	7.2	9.6
R^2 [-]	0.86	0.86	0.85	0.87	0.84

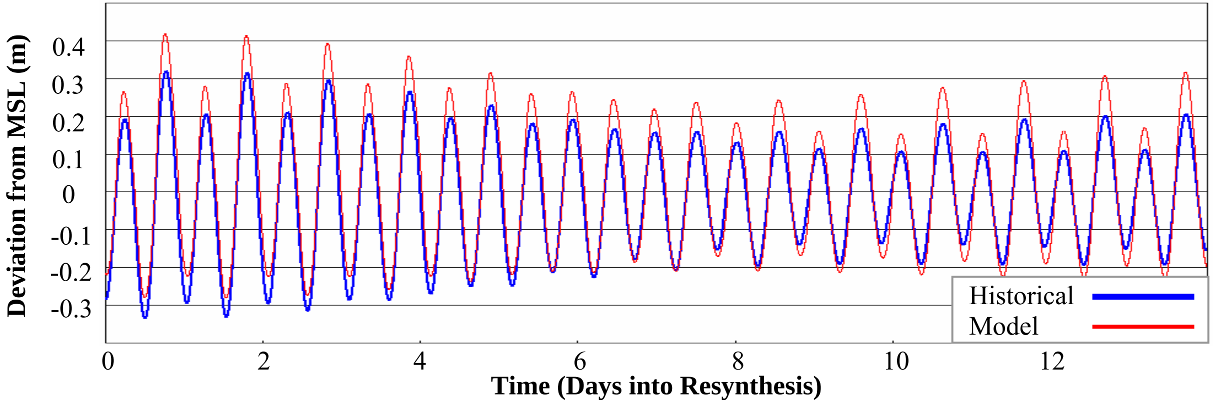

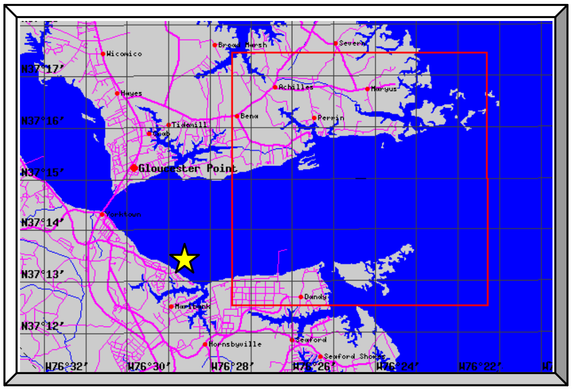

St. 49: York River, VA					
Observer	NOS				
Longitude	76.48 W				
Latitude	37.23 N				
Simulation Results					
	333K	95K	60K	53K	48K
Ph [º]	22.6	45.5	26.4	31.5	31.6
R^2 [-]	0.93	0.79	0.89	0.95	0.93

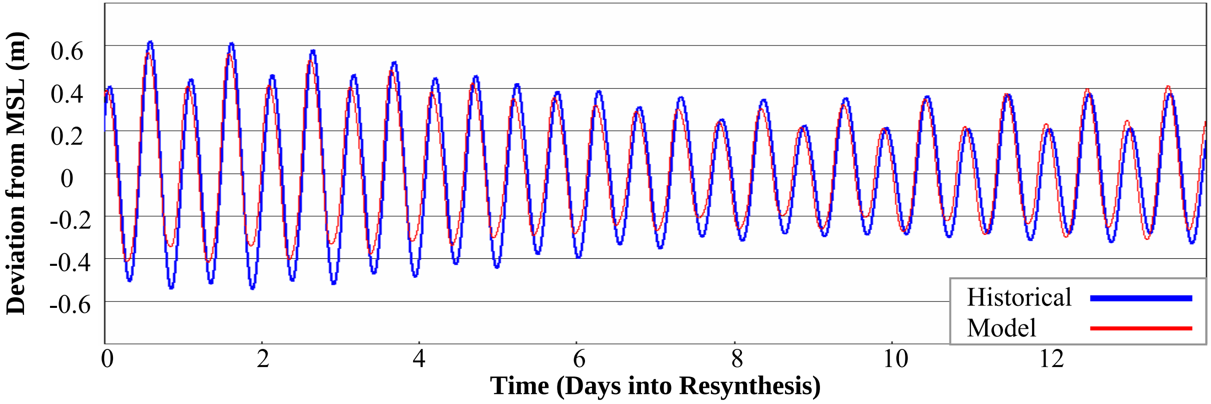

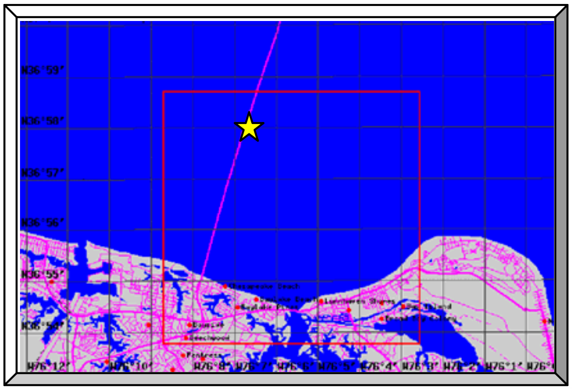

St. 53: Chesapeake Bay Bridge Tunnel, VA					
Observer	NOS				
Longitude	76.11 W				
Latitude	36.97 N				
Simulation Results					
	333K	95K	60K	53K	48K
Ph [º]	6.7	15.0	6.4	9.1	7.6
R^2 [-]	0.98	0.98	0.98	0.98	0.97

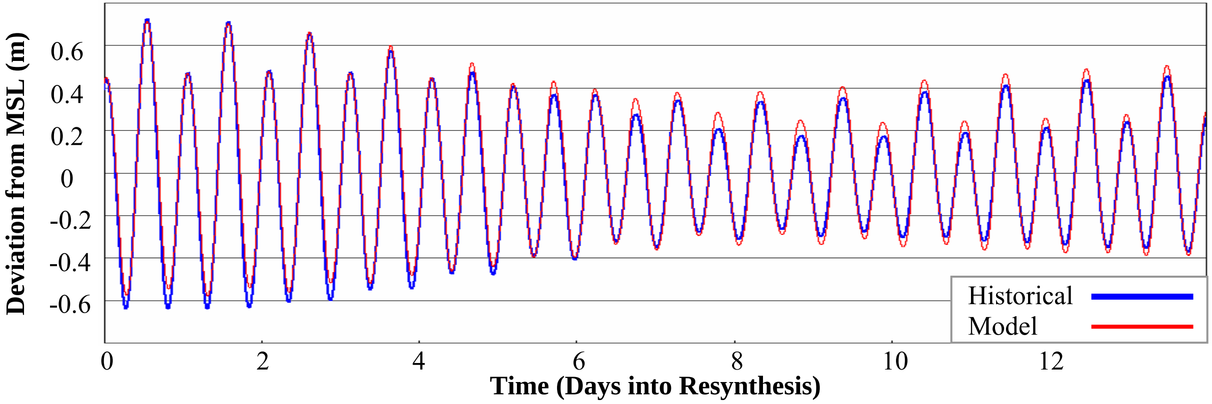

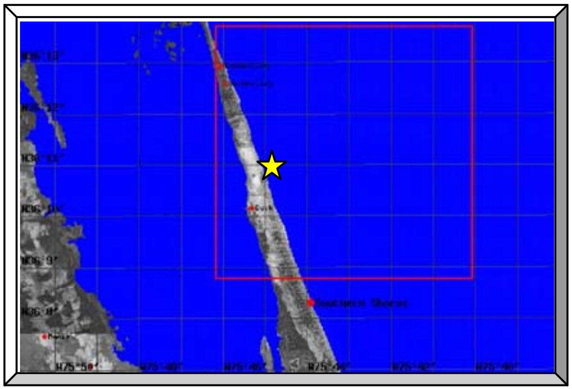

<table>
<tr><th colspan="6">St. 54: Duck, FRF Pier, NC</th></tr>
<tr><td colspan="2">Observer</td><td colspan="4">NOS</td></tr>
<tr><td colspan="2">Longitude</td><td colspan="4">75.75 W</td></tr>
<tr><td colspan="2">Latitude</td><td colspan="4">36.18 N</td></tr>
<tr><td colspan="6">Simulation Results</td></tr>
<tr><td></td><td>333K</td><td>95K</td><td>60K</td><td>53K</td><td>48K</td></tr>
<tr><td><i>Ph</i> [º]</td><td>6.3</td><td>15.9</td><td>5.6</td><td>12.9</td><td>5.0</td></tr>
<tr><td>R^2 [-]</td><td>0.98</td><td>0.94</td><td>0.98</td><td>0.95</td><td>0.98</td></tr>
</table>

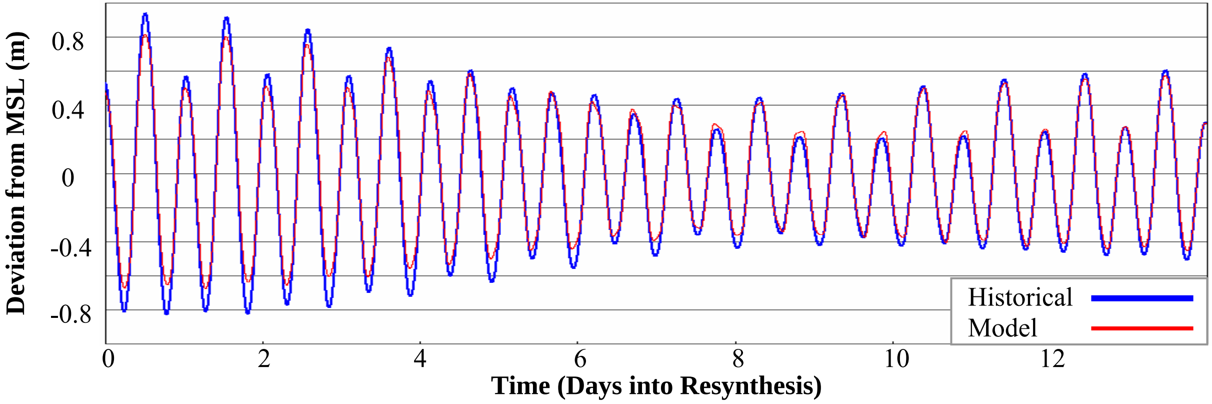

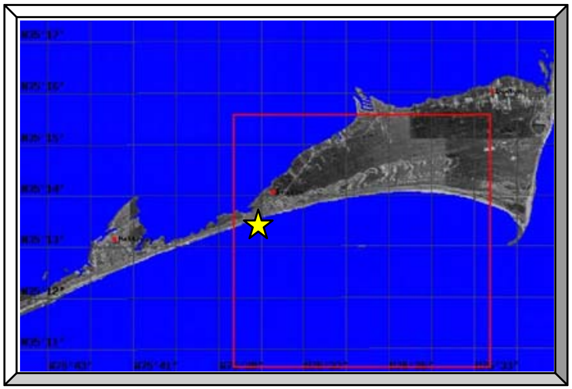

<table>
<tr><th colspan="6">St. 56: Cape Hatteras Fishing Pier, NC</th></tr>
<tr><td colspan="2">Observer</td><td colspan="4">NOS</td></tr>
<tr><td colspan="2">Longitude</td><td colspan="4">75.64 W</td></tr>
<tr><td colspan="2">Latitude</td><td colspan="4">35.22 N</td></tr>
<tr><td colspan="6">Simulation Results</td></tr>
<tr><td></td><td>333K</td><td>95K</td><td>60K</td><td>53K</td><td>48K</td></tr>
<tr><td><i>Ph</i> [º]</td><td>5.0</td><td>5.9</td><td>4.7</td><td>7.1</td><td>4.9</td></tr>
<tr><td>R^2 [-]</td><td>0.97</td><td>0.97</td><td>0.97</td><td>0.97</td><td>0.97</td></tr>
</table>

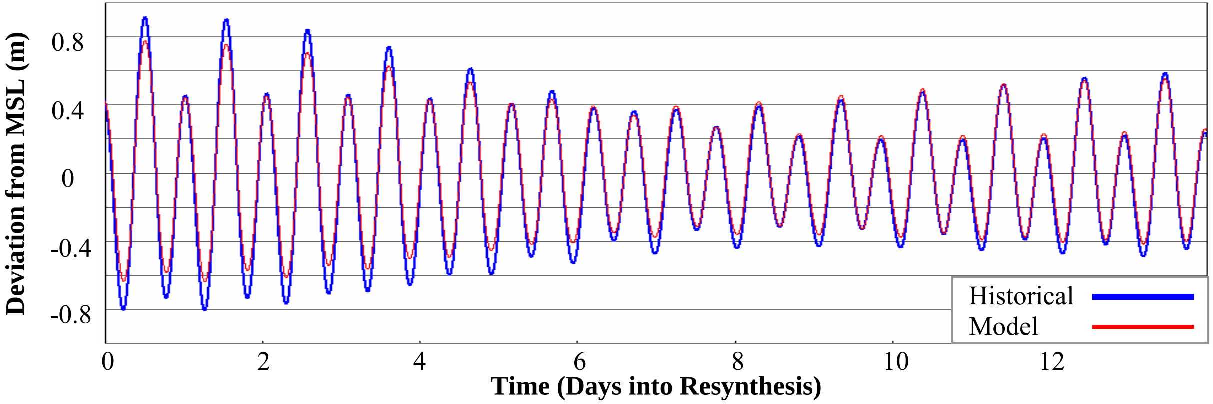

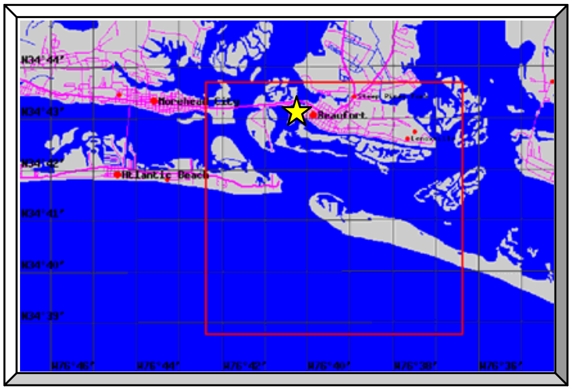

St. 59: Beaufort, Duke Marine Lab, NC					
Observer			NOS		
Longitude			76.67 W		
Latitude			34.72 N		
Simulation Results					
	333K	95K	60K	53K	48K
Ph [º]	25.2	26.7	24.0	26.5	28.5
R^2 [-]	0.96	0.96	0.95	0.97	0.96

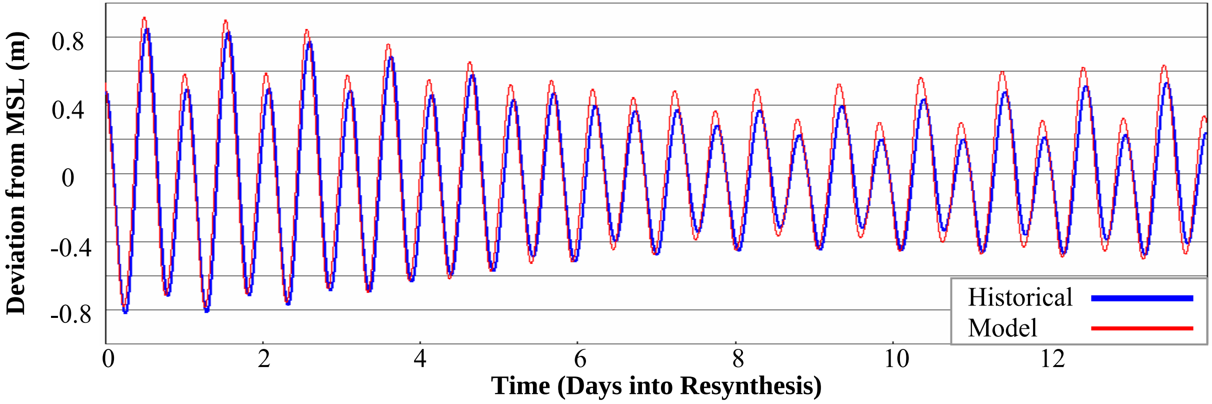

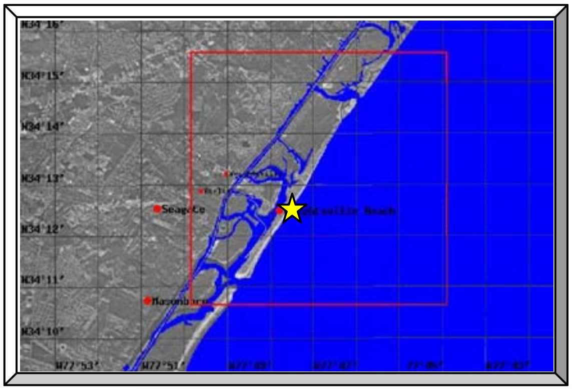

St. 60: Wrightsville Beach, NC					
Observer			NOS		
Longitude			77.80 W		
Latitude			34.21 N		
Simulation Results					
	333K	95K	60K	53K	48K
Ph [º]	5.5	3.2	4.6	3.2	4.3
R^2 [-]	0.99	0.99	0.99	0.98	0.99

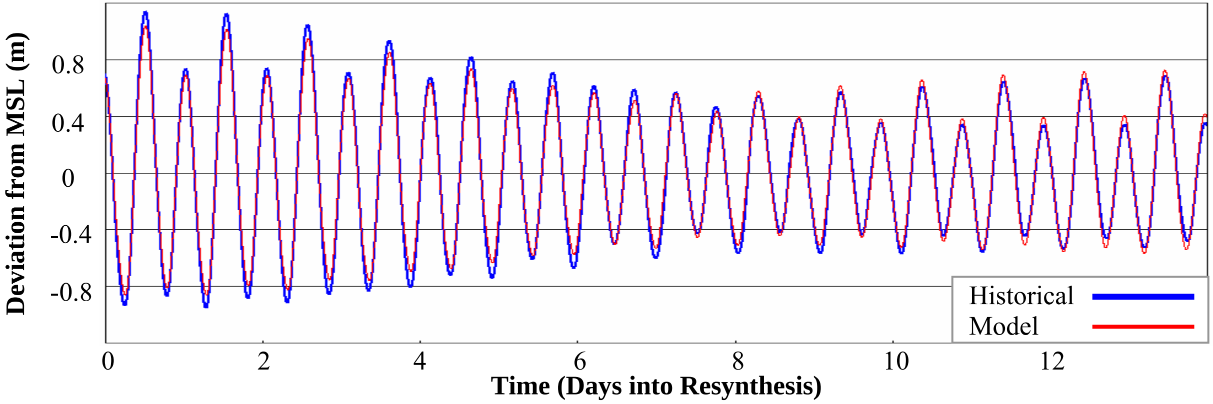

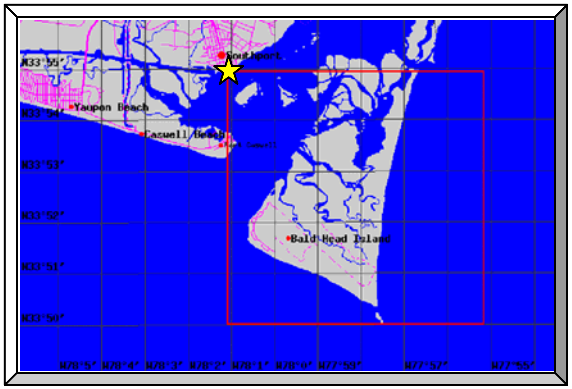

St. 61: South Port, NC					
Observer	IHO				
Longitude	78.02 W				
Latitude	33.92 N				
Simulation Results					
	333K	95K	60K	53K	48K
Ph [º]	16.4	15.0	16.3	15.7	12.9
R^2 [-]	0.98	0.98	0.98	0.98	0.97

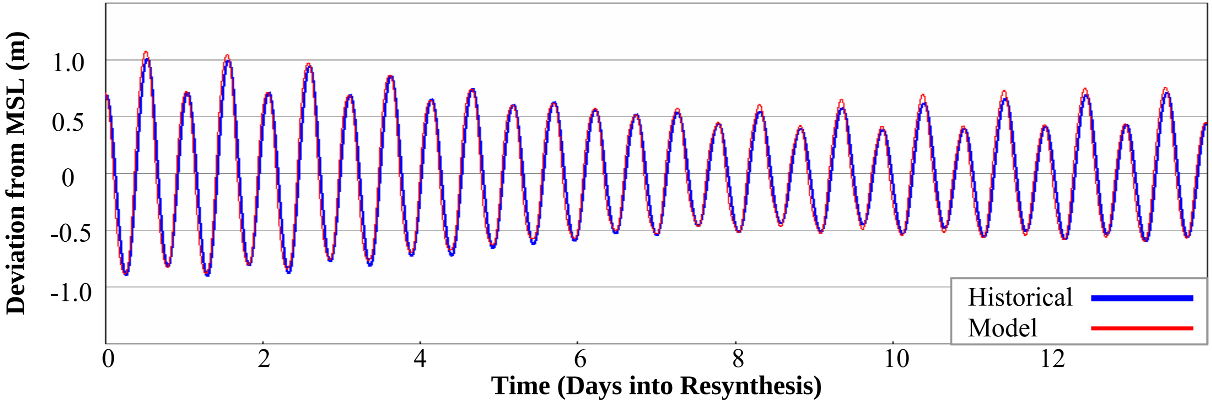

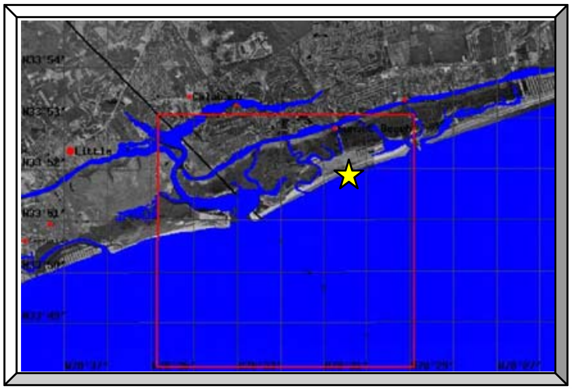

St. 62: Sunset Beach Pier, Atlantic Ocean, NC					
Observer	NOS				
Longitude	78.51 W				
Latitude	33.87 N				
Simulation Results					
	333K	95K	60K	53K	48K
Ph [º]	2.1	2.7	2.0	2.5	0.2
R^2 [-]	0.99	0.98	0.98	0.98	0.98

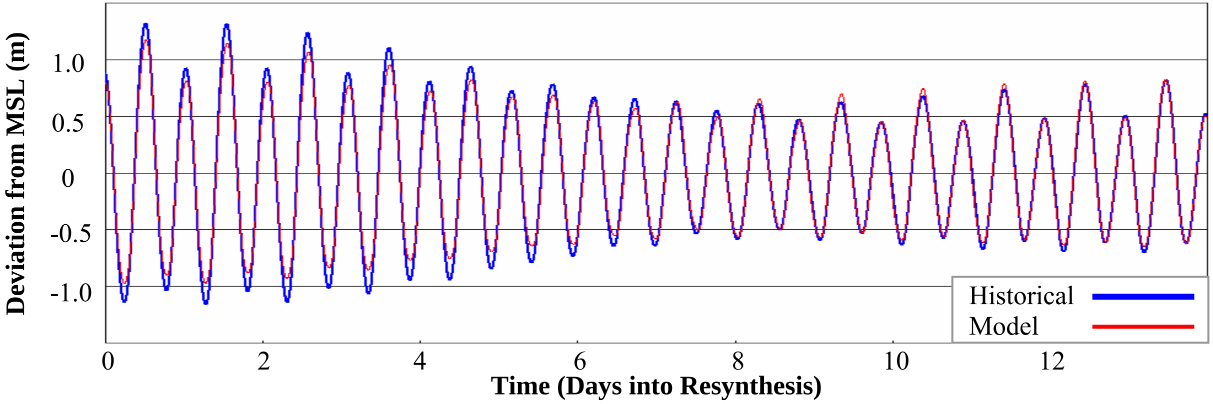

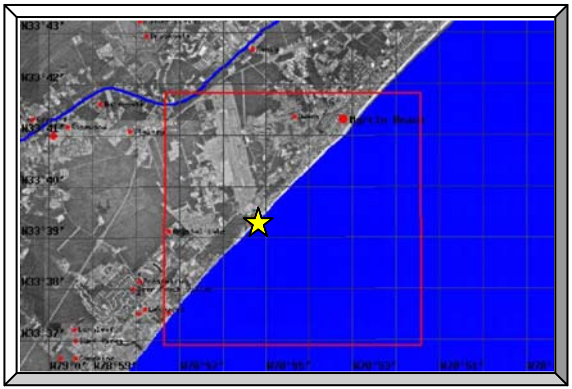

St. 63: Springmaid Pier, Atlantic Ocean, SC					
Observer	NOS				
Longitude	78.92 W				
Latitude	33.66 N				
Simulation Results					
	333K	95K	60K	53K	48K
Ph [º]	5.3	5.9	5.2	4.6	5.4
R^2 [-]	0.97	0.97	0.97	0.97	0.97

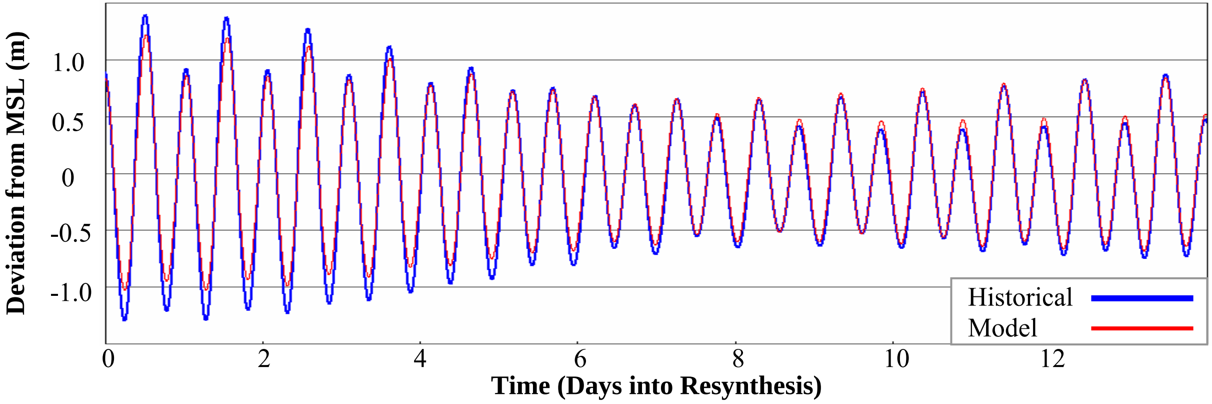

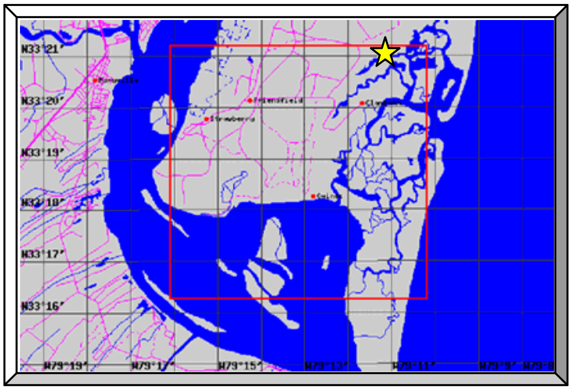

St. 64: Oyster Landing, Crab Haul Creek, SC					
Observer	NOS				
Longitude	79.19 W				
Latitude	33.35 N				
Simulation Results					
	333K	95K	60K	53K	48K
Ph [º]	31.1	29.6	30.9	29.9	32.4
R^2 [-]	0.96	0.96	0.96	0.96	0.96

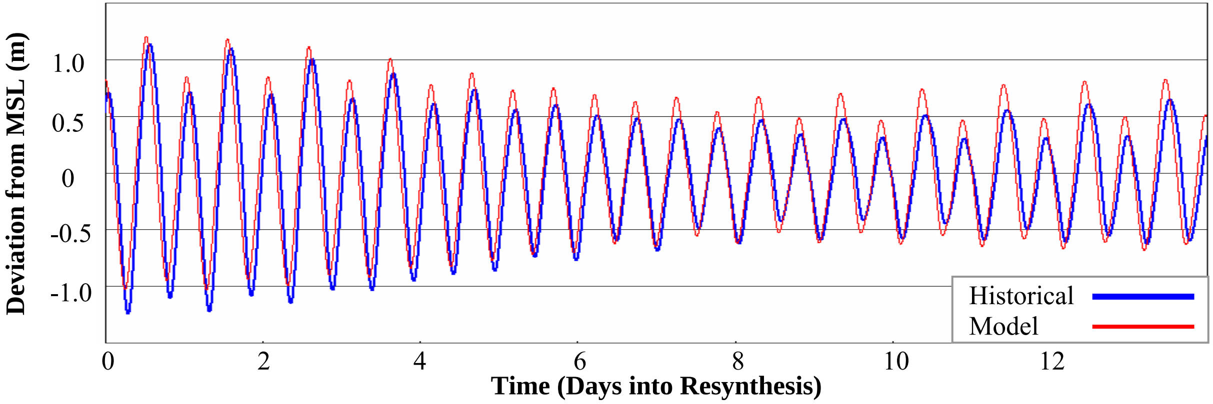

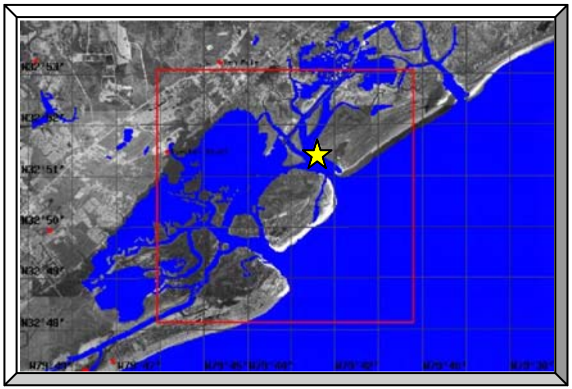

St. 65: South Capers Island, Capers Creek, SC

Observer	NOS
Longitude	79.71 W
Latitude	32.86 N

Simulation Results

	333K	95K	60K	53K	48K
Ph [º]	17.2	15.8	15.5	15.2	17.1
R^2 [-]	0.97	0.97	0.97	0.96	0.97

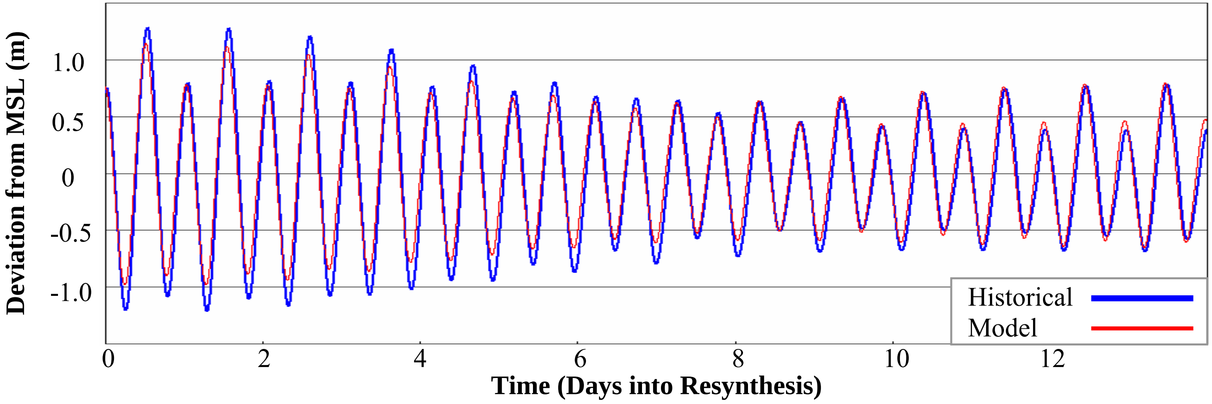

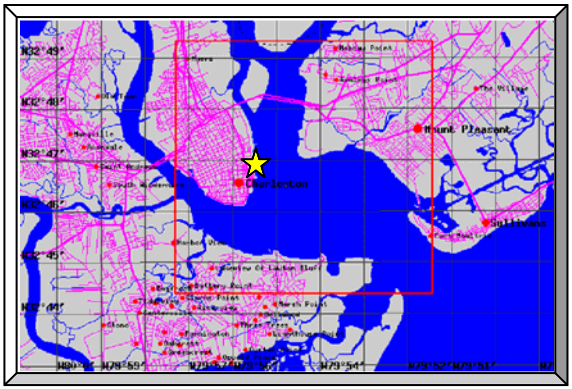

St. 66: Charleston, Cooper River Entrance, SC

Observer	NOS
Longitude	79.93 W
Latitude	32.78 N

Simulation Results

	333K	95K	60K	53K	48K
Ph [º]	19.2	17.0	17.3	18.7	18.6
R^2 [-]	0.96	0.96	0.96	0.96	0.96

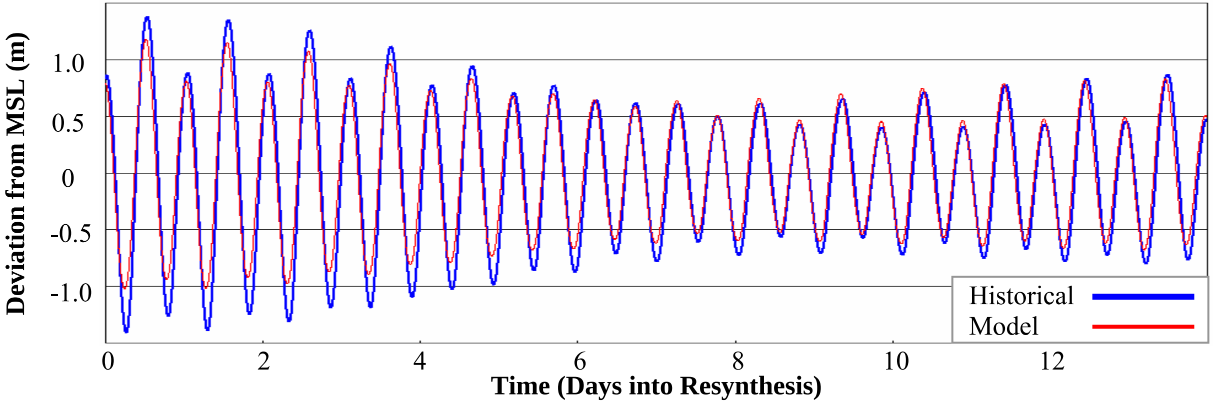

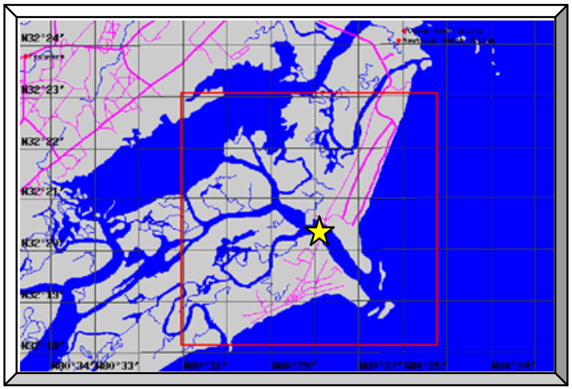

St. 67: Hunting Island Pier, Fripps Inlet, SC	
Observer	NOS
Longitude	80.47 W
Latitude	32.34 N

Simulation Results

	333K	95K	60K	53K	48K
Ph [º]	14.6	15.6	14.0	15.4	14.0
R^2 [-]	0.97	0.97	0.97	0.97	0.97

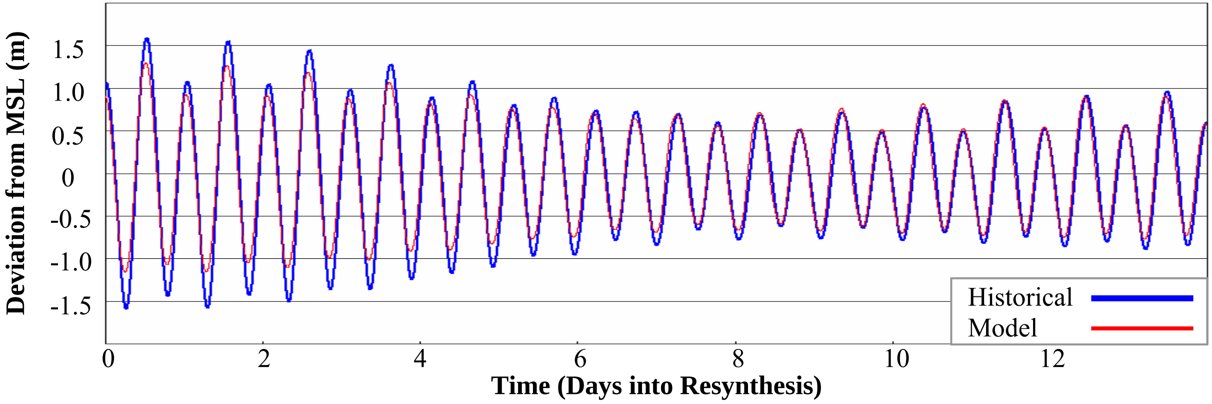

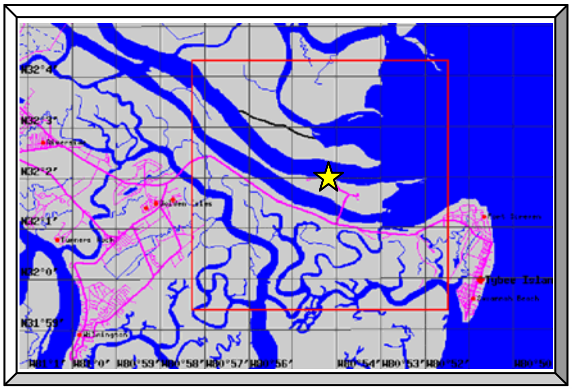

St. 68: Fort Pulaski, Savannah River, GA	
Observer	NOS
Longitude	80.90 W
Latitude	32.03 N

Simulation Results

	333K	95K	60K	53K	48K
Ph [º]	17.2	10.3	15.9	14.4	18.5
R^2 [-]	0.97	0.97	0.97	0.97	0.96

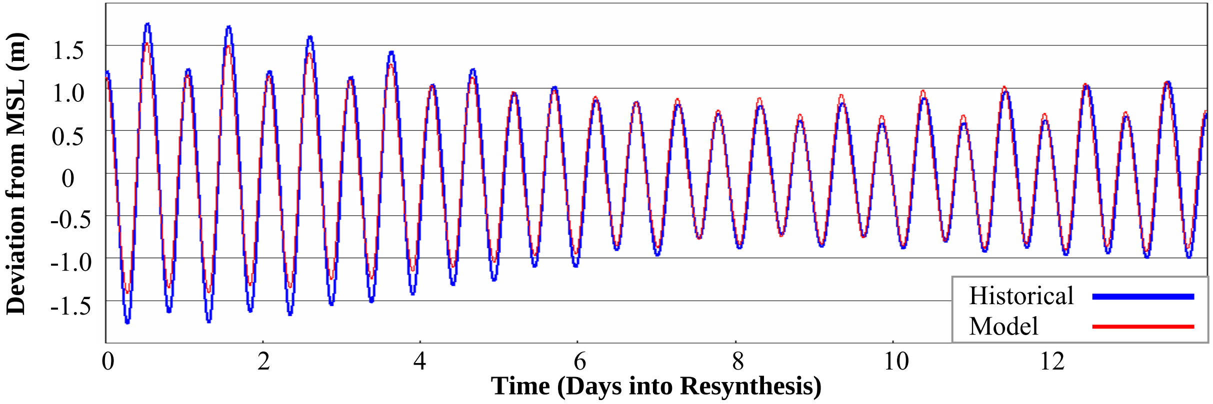

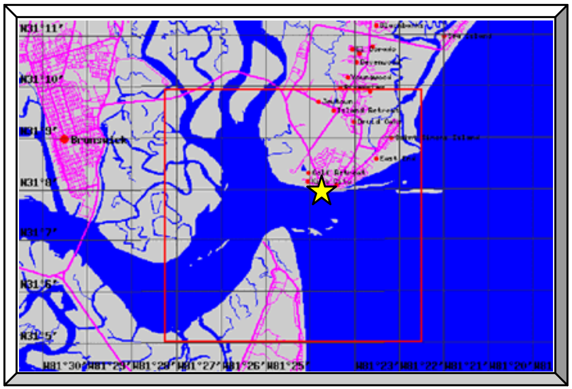

St. 69: St. Simons Lighthouse, St. Simons Is., GA					
Observer	NOS				
Longitude	81.40 W				
Latitude	31.13 N				
Simulation Results					
	333K	95K	60K	53K	48K
Ph [º]	17.4	19.8	19.4	21.6	19.4
R^2 [-]	0.98	0.97	0.97	0.97	0.98

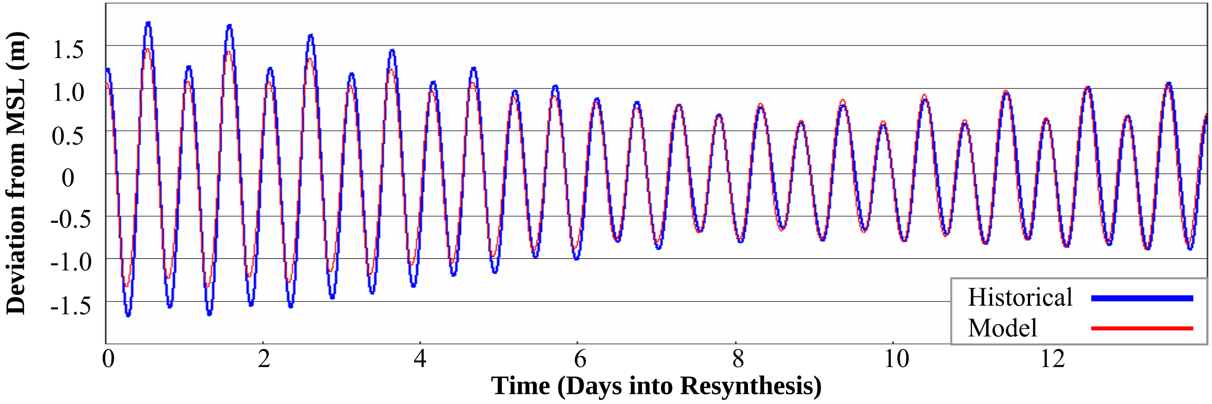

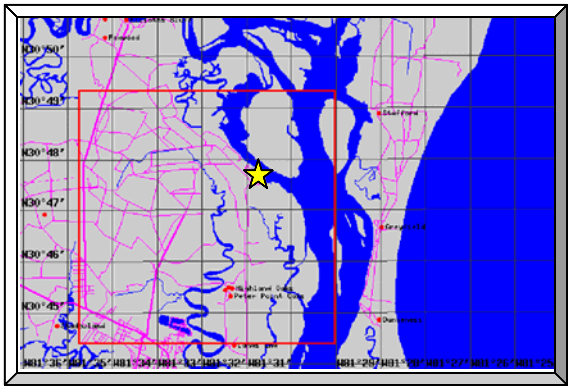

St. 70: Kings Bay, GA					
Observer	NOS				
Longitude	81.52 W				
Latitude	30.80 N				
Simulation Results					
	333K	95K	60K	53K	48K
Ph [º]	25.9	27.9	26.3	29.1	26.6
R^2 [-]	0.97	0.97	0.97	0.97	0.97

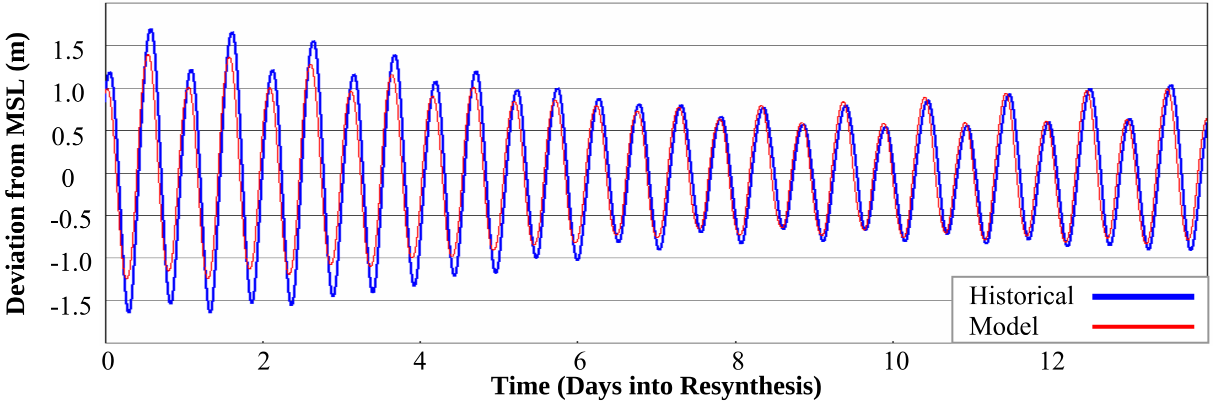

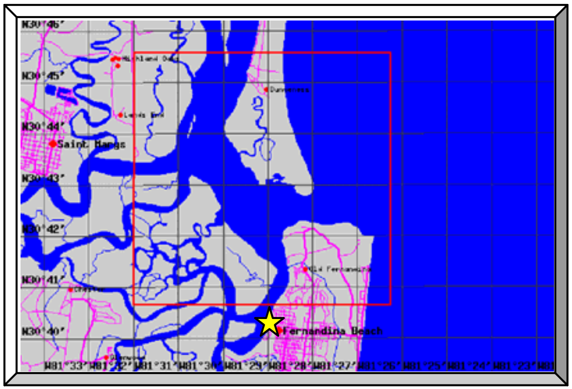

St. 71: Fernandina Beach, Amelia River, FL					
Observer			NOS		
Longitude			81.47 W		
Latitude			30.67 N		
Simulation Results					
	333K	95K	60K	53K	48K
Ph [º]	20.5	22.0	20.2	22.0	20.9
R^2 [-]	0.98	0.98	0.98	0.98	0.98

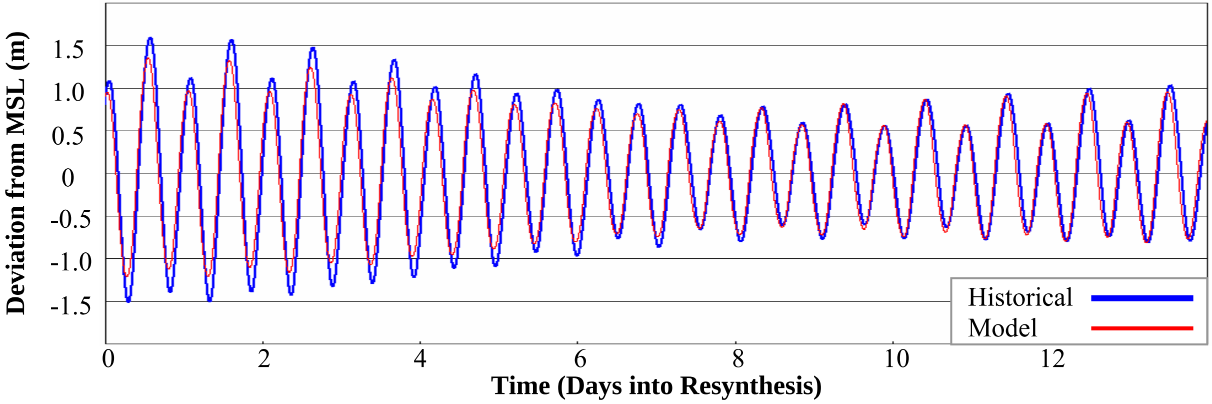

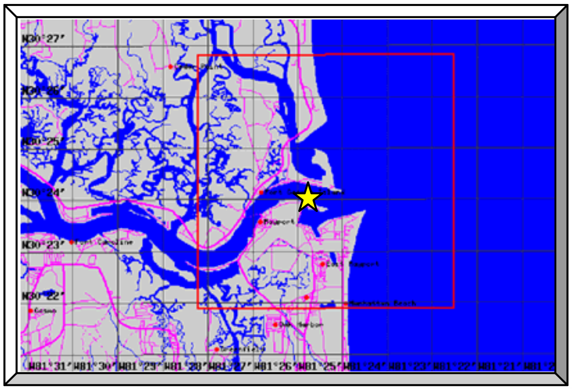

St. 72: WWTD, Mayport Naval St., St. Johns R., FL					
Observer			NOS		
Longitude			81.41 W		
Latitude			30.40 N		
Simulation Results					
	333K	95K	60K	53K	48K
Ph [º]	12.9	12.3	11.9	11.5	12.1
R^2 [-]	0.98	0.98	0.98	0.98	0.98

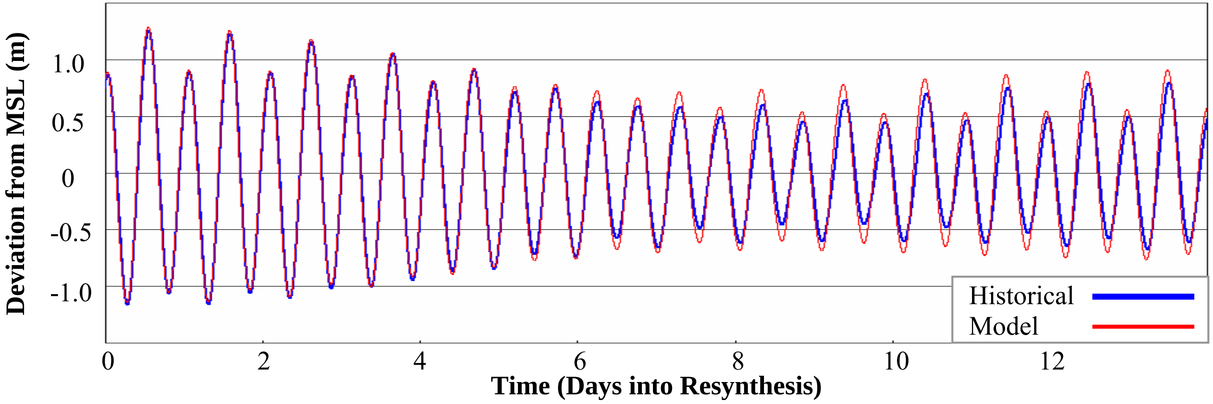

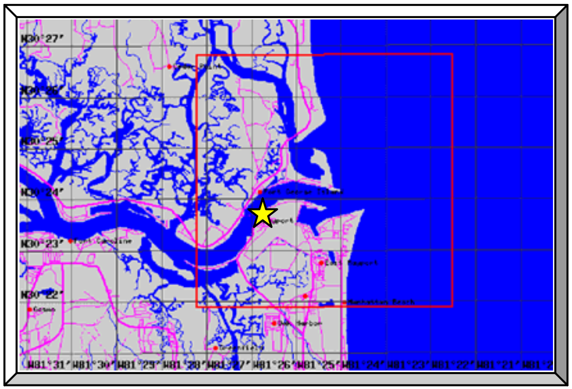

St. 73: Bar Pilots Dock, St. Johns River, FL					
Observer			NOS		
Longitude			81.43 W		
Latitude			30.40 N		
Simulation Results					
	333K	95K	60K	53K	48K
Ph [º]	15.3	14.4	14.0	13.5	14.2
R^2 [-]	0.96	0.96	0.96	0.96	0.96

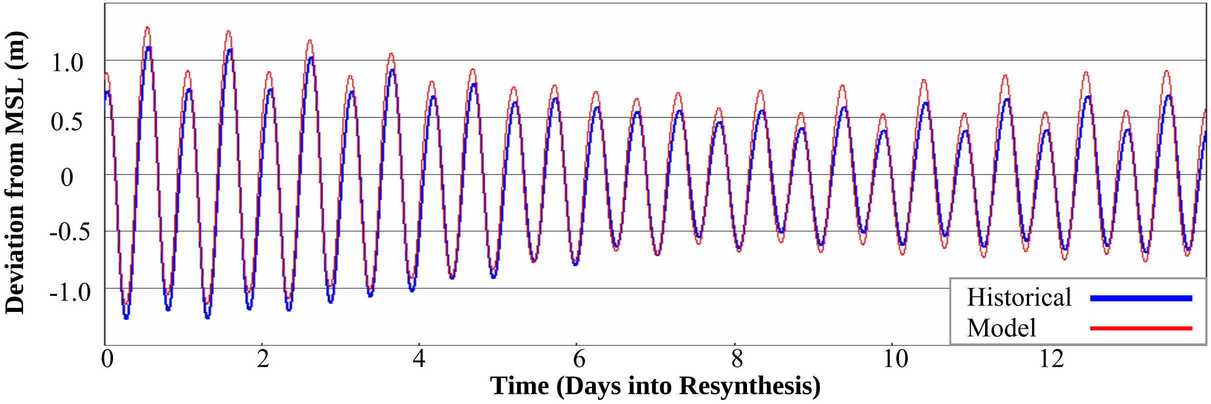

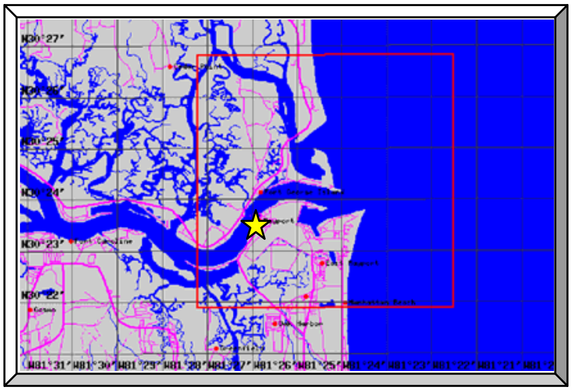

St. 74: Mayport, FL					
Observer			NOS		
Longitude			81.43 W		
Latitude			30.39 N		
Simulation Results					
	333K	95K	60K	53K	48K
Ph [º]	18.2	17.3	16.9	16.5	17.0
R^2 [-]	0.95	0.95	0.95	0.95	0.95

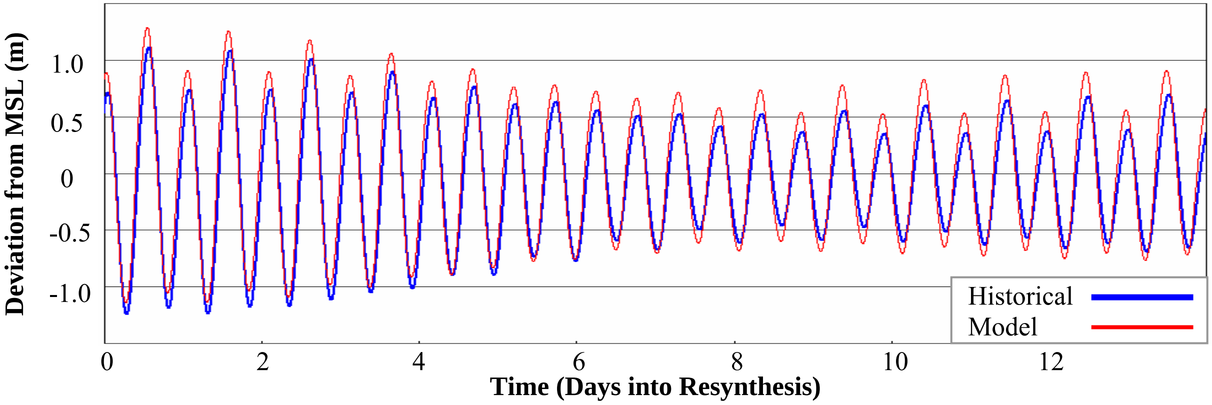

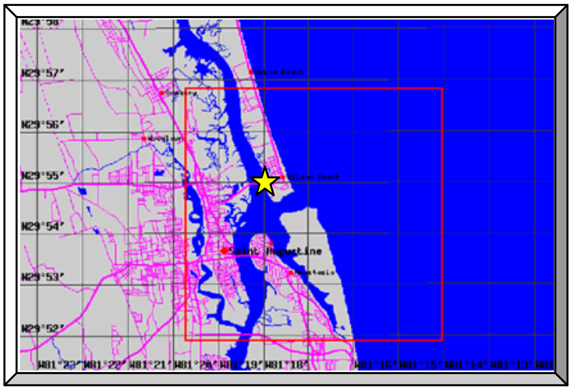

St. 75: Vilano Beach (ICWW), FL					
Observer			NOS		
Longitude			81.30 W		
Latitude			29.92 N		
Simulation Results					
	333K	95K	60K	53K	48K
Ph [º]	19.3	16.7	17.5	15.0	17.5
R^2 [-]	0.98	0.97	0.98	0.97	0.98

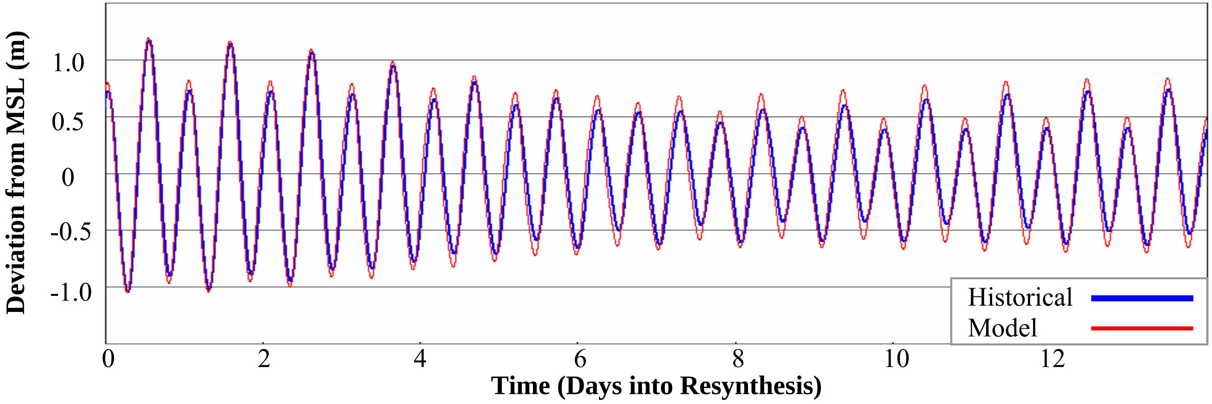

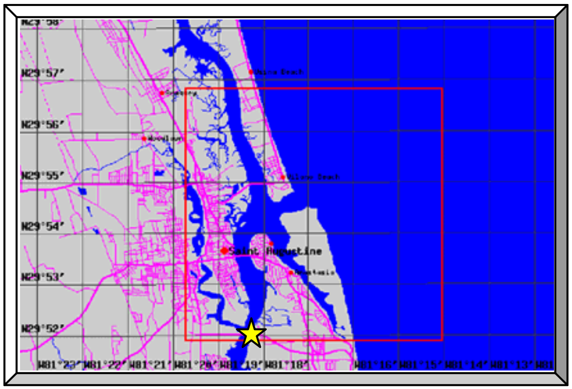

St. 76: State Road 312, Matanzas River, FL					
Observer			NOS		
Longitude			81.31 W		
Latitude			29.87 N		
Simulation Results					
	333K	95K	60K	53K	48K
Ph [º]	25.0	22.2	23.2	20.5	22.9
R^2 [-]	0.98	0.97	0.98	0.97	0.98

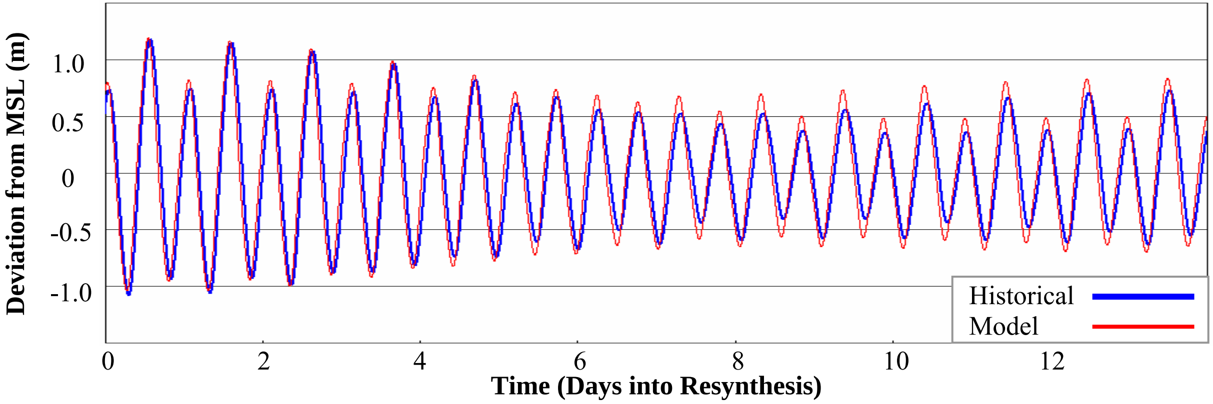

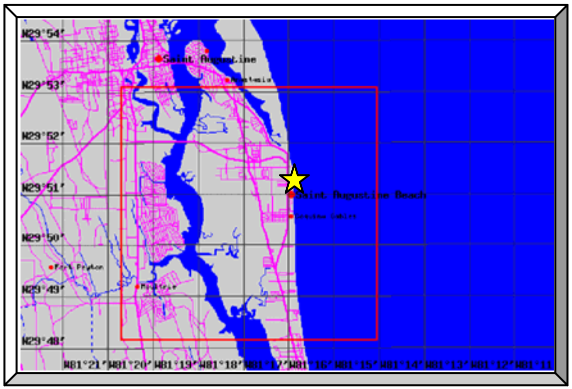

St. 77: At. Augustine Beach, Atlantic Ocean, FL					
Observer	NOS				
Longitude	81.26 W				
Latitude	29.86 N				
Simulation Results					
	333K	95K	60K	53K	48K
Ph [º]	5.4	2.6	3.7	1.1	3.8
R^2 [-]	0.98	0.97	0.97	0.97	0.97

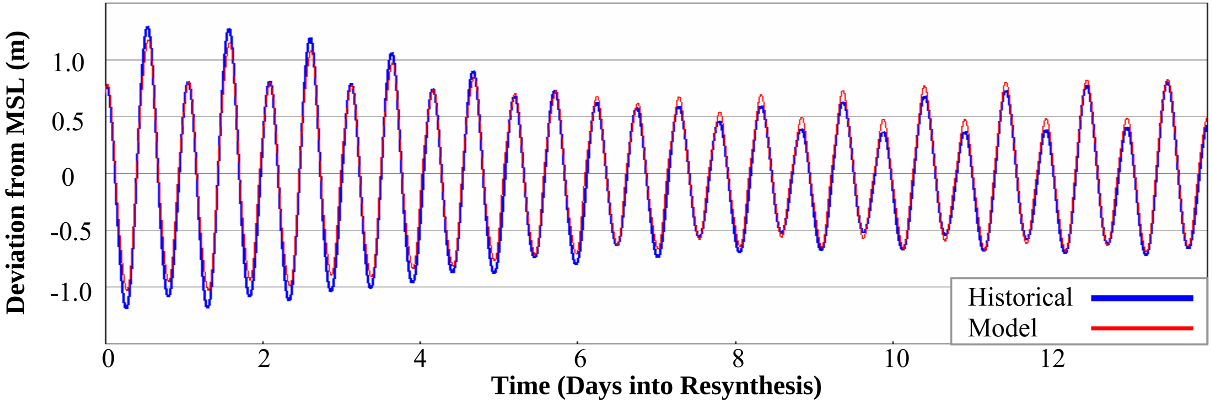

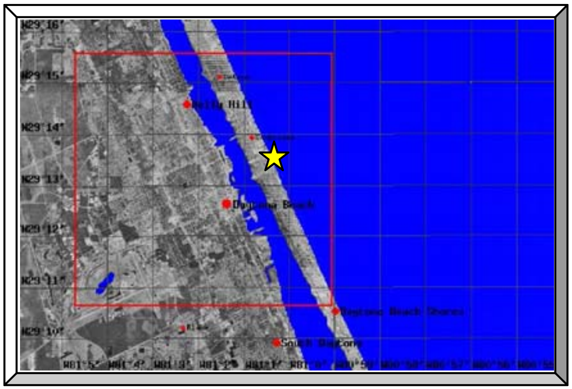

St. 80: Daytona Beach (Ocean), FL					
Observer	NOS				
Longitude	81.01 W				
Latitude	29.23 N				
Simulation Results					
	333K	95K	60K	53K	48K
Ph [º]	6.2	3.4	5.0	2.1	4.2
R^2 [-]	0.97	0.97	0.97	0.97	0.97

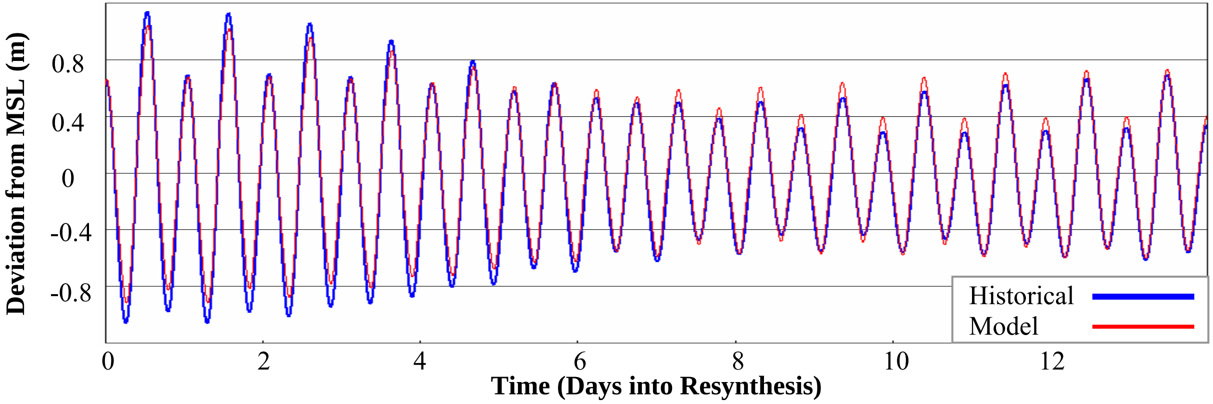

St. 81: Trident Pier, Port Canaveral, FL	
Observer	NOS
Longitude	80.59 W
Latitude	28.42 N

Simulation Results					
	333K	95K	60K	53K	48K
Ph [º]	11.5	13.2	13.4	11.7	12.7
R^2 [-]	0.96	0.96	0.95	0.96	0.96

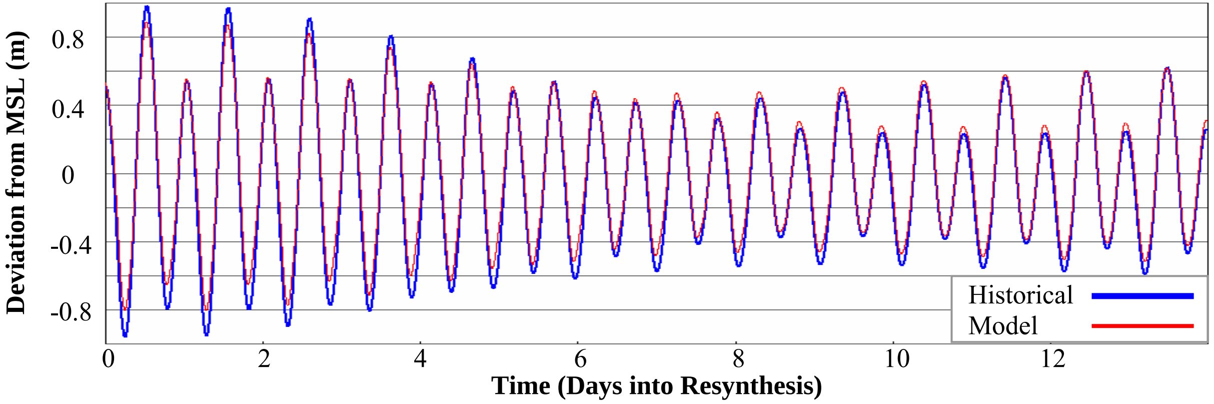

St. 82: Canaveral Harbor Entrance, FL	
Observer	NOS
Longitude	80.60 W
Latitude	28.41 N

Simulation Results					
	333K	95K	60K	53K	48K
Ph [º]	9.9	11.6	11.9	10.2	11.1
R^2 [-]	0.97	0.96	0.96	0.96	0.96

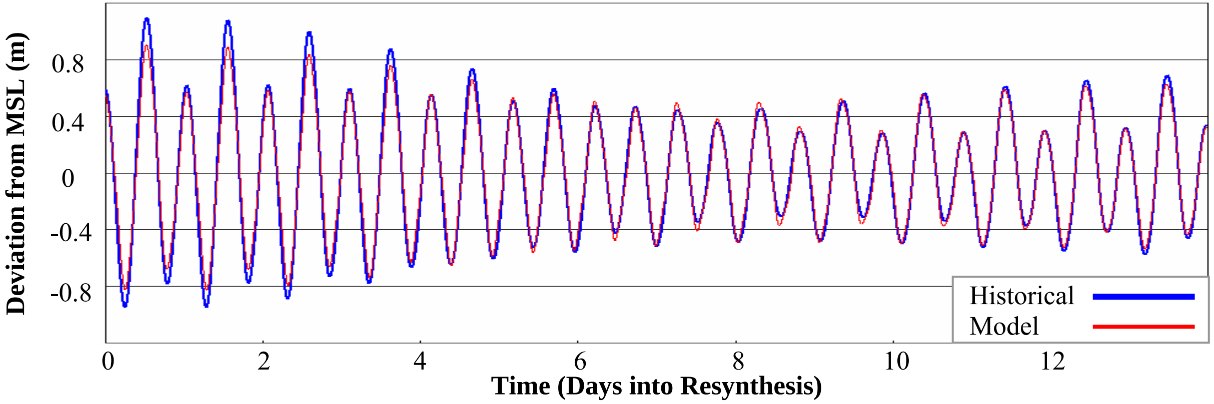

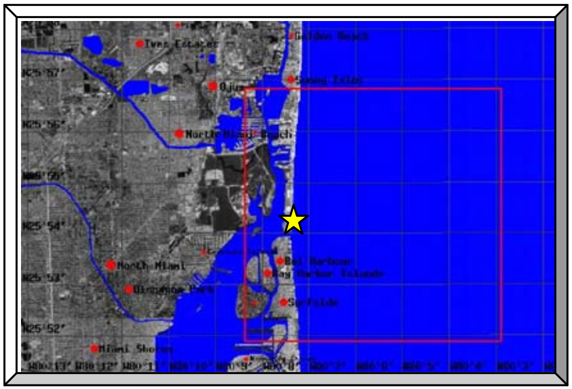

St. 84: Haulover Pier, N. Miami Beach, FL	
Observer	NOS
Longitude	80.12 W
Latitude	25.90 N

Simulation Results

	333K	95K	60K	53K	48K
Ph [°]	7.5	7.8	7.9	7.5	7.8
R^2 [-]	0.98	0.98	0.98	0.98	0.98

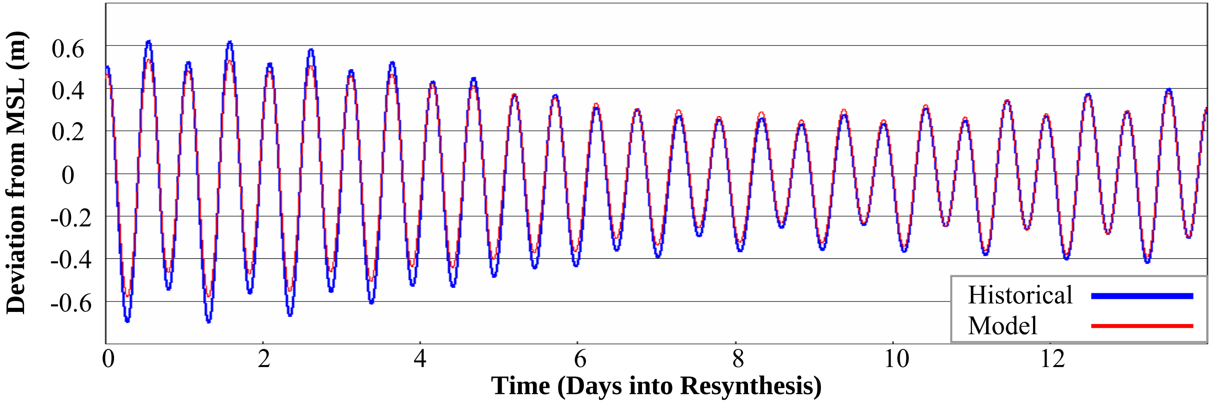

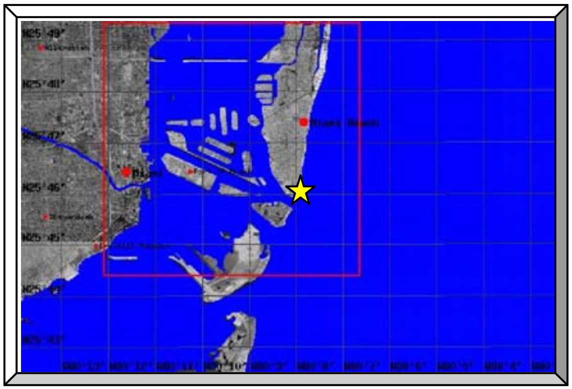

St. 85: Miami Beach (City Pier), FL	
Observer	NOS
Longitude	80.13 W
Latitude	25.77 N

Simulation Results

	333K	95K	60K	53K	48K
Ph [°]	7.7	8.0	8.1	7.7	7.9
R^2 [-]	0.95	0.95	0.95	0.95	0.95

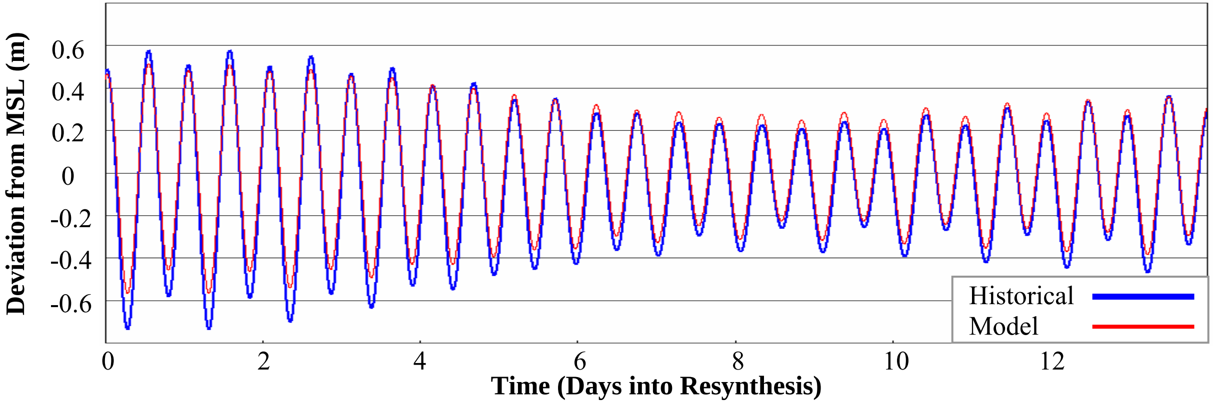

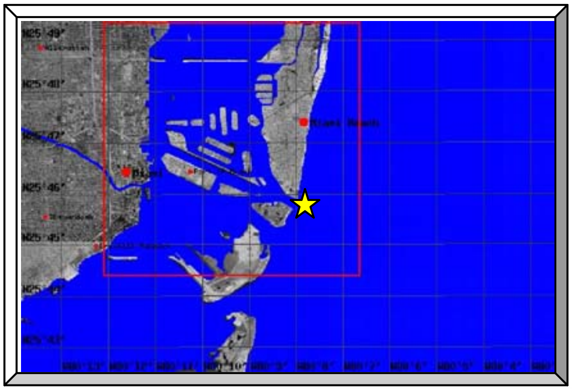

St. 86: Miami Beach, Government Cut, FL					
Observer			NOS		
Longitude			80.13 W		
Latitude			25.76 N		
Simulation Results					
	333K	95K	60K	53K	48K
Ph [º]	13.1	13.4	13.5	13.1	13.3
R^2 [-]	0.96	0.96	0.96	0.96	0.96

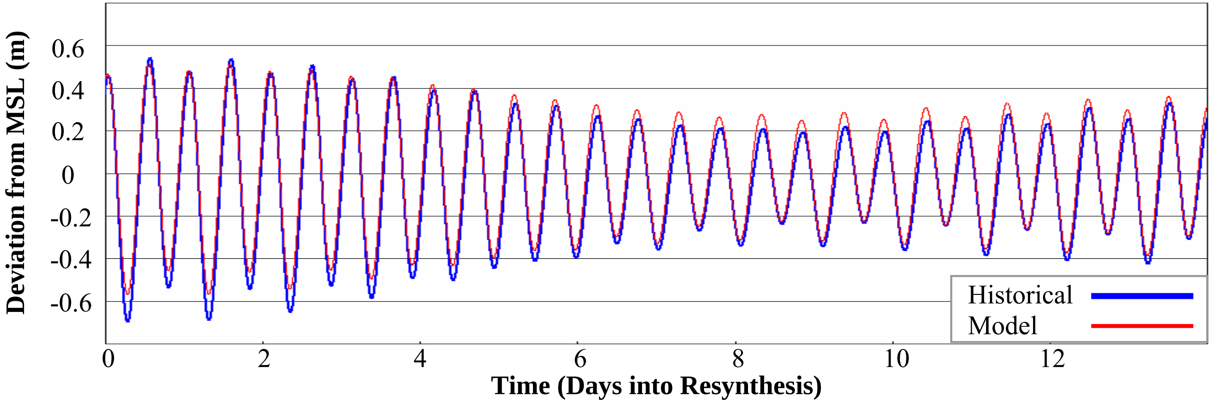

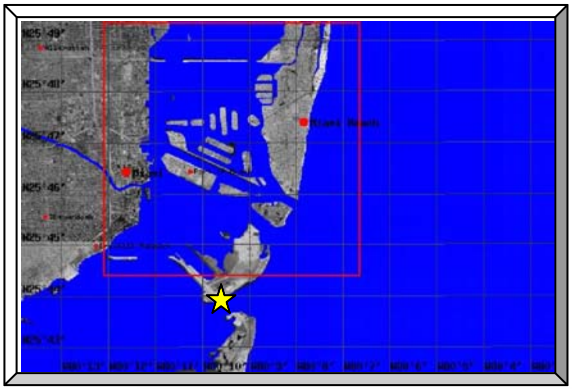

St. 87: Virginia Key, Biscayne Bay, FL					
Observer			NOS		
Longitude			80.16 W		
Latitude			25.73 N		
Simulation Results					
	333K	95K	60K	53K	48K
Ph [º]	20.3	26.9	26.0	25.8	27.0
R^2 [-]	0.90	0.93	0.93	0.94	0.94

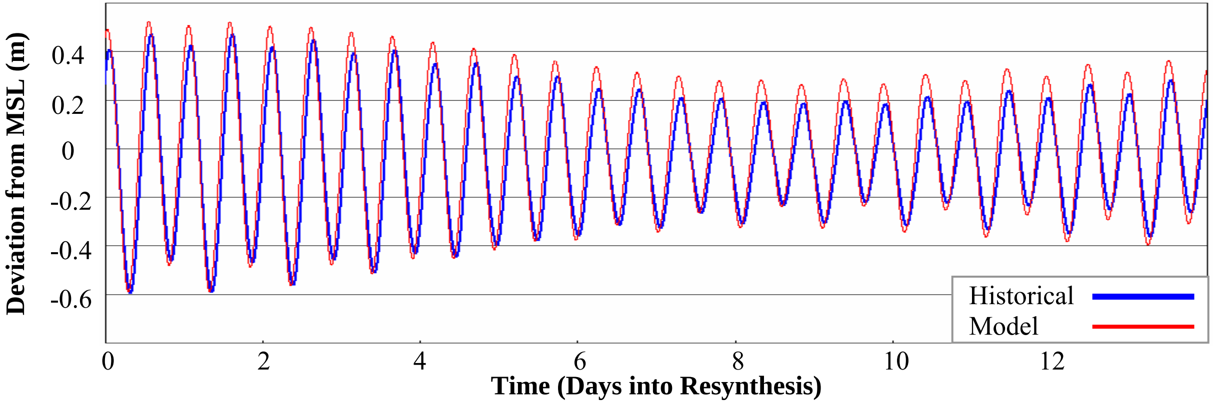

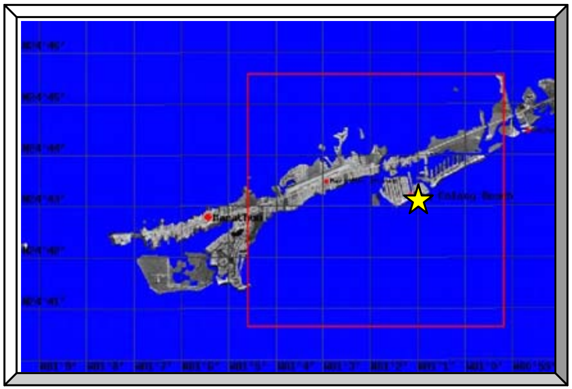

St. 88: Key Colony Beach, FL					
Observer			NOS		
Longitude			81.02 W		
Latitude			24.72 N		
Simulation Results					
	333K	95K	60K	53K	48K
Ph [º]	6.7	5.9	6.9	5.7	7.2
R^2 [-]	0.88	0.89	0.88	0.88	0.88

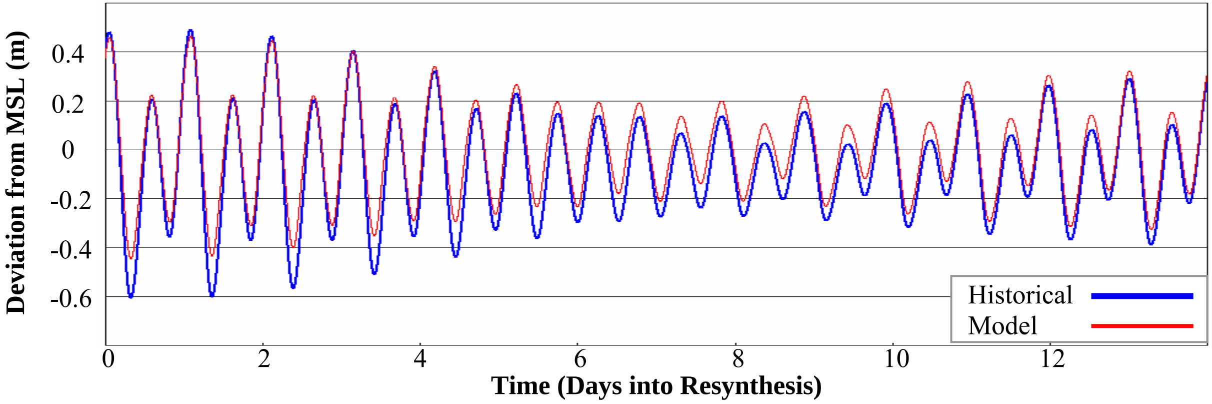

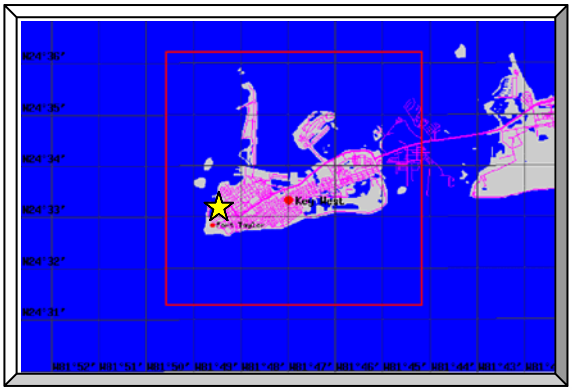

St. 90: Key West, FL					
Observer			NOS		
Longitude			81.81 W		
Latitude			24.55 N		
Simulation Results					
	333K	95K	60K	53K	48K
Ph [º]	20.1	17.2	19.5	15.8	16.6
R^2 [-]	0.88	0.88	0.88	0.89	0.88

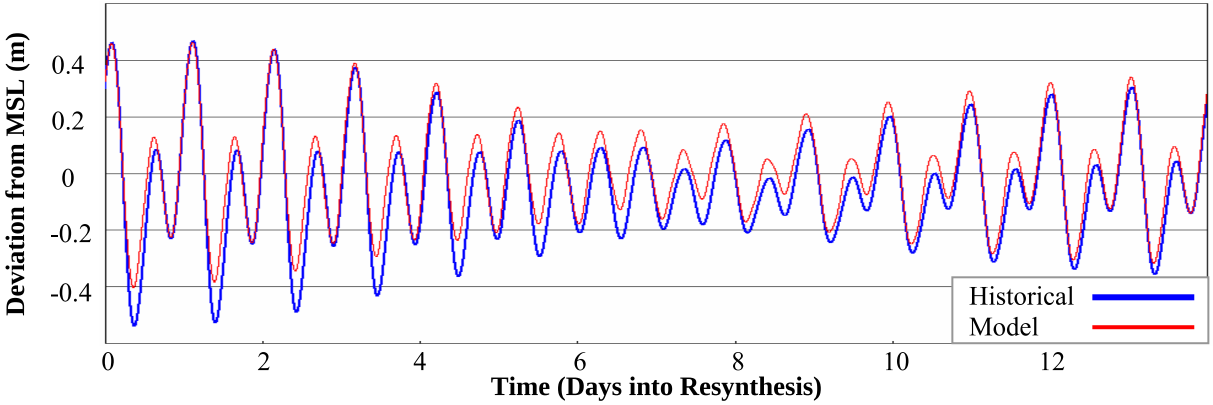

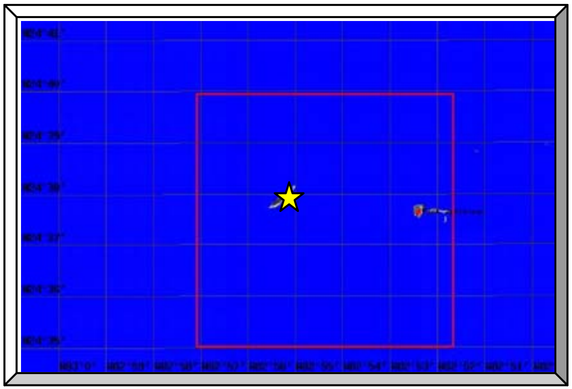

St. 91: Loggerhead Key, Dry Tortugas, FL					
Observer			NOS		
Longitude			82.92 W		
Latitude			24.63 N		
Simulation Results					
	333K	95K	60K	53K	48K
Ph [º]	3.0	3.4	3.8	3.1	2.6
R^2 [-]	0.75	0.76	0.76	0.76	0.76

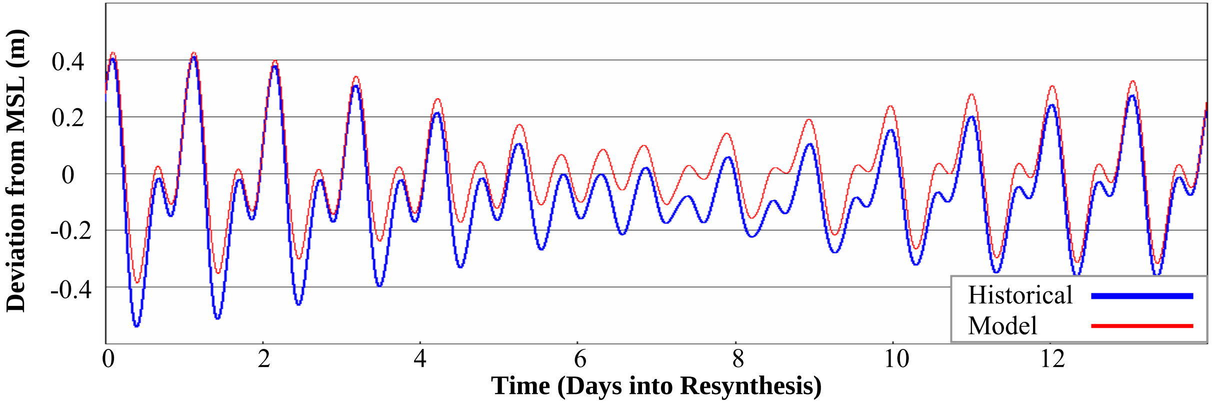

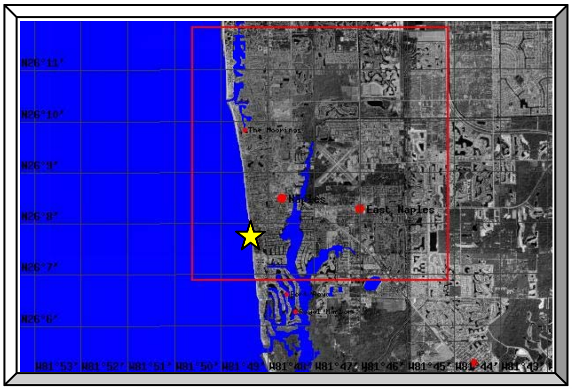

St. 92: Naples, Gulf of Mexico, FL					
Observer			NOS		
Longitude			81.81 W		
Latitude			26.13 N		
Simulation Results					
	333K	95K	60K	53K	48K
Ph [º]	22.4	23.8	22.5	25.6	22.6
R^2 [-]	0.92	0.92	0.92	0.92	0.92

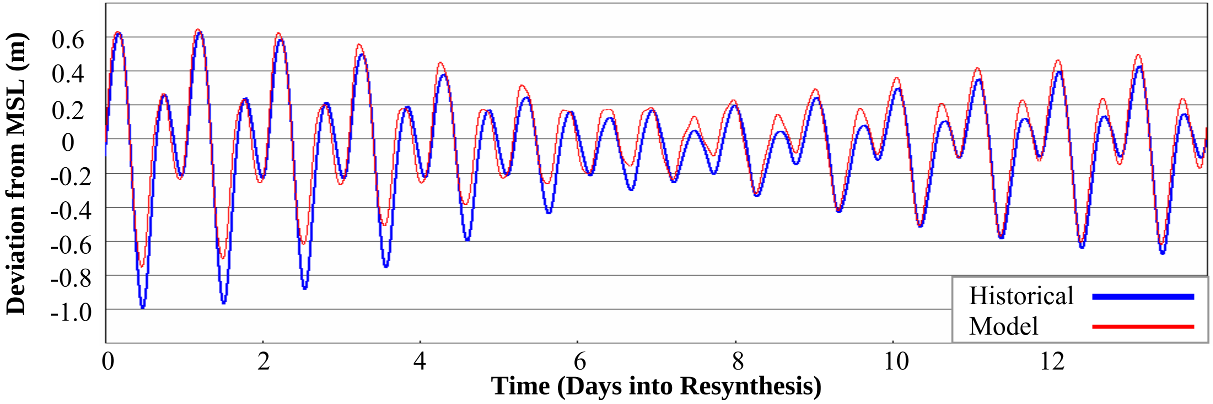

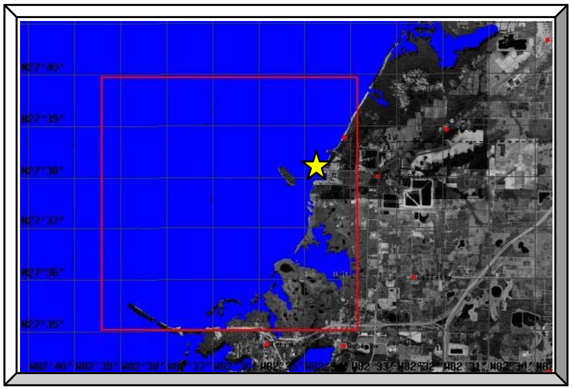

St. 93: Port Manatee, Tampa Bay, FL					
Observer	NOS				
Longitude	82.56 W				
Latitude	27.64 N				
Simulation Results					
	333K	95K	60K	53K	48K
Ph [º]	7.3	14.5	12.0	12.8	11.3
R^2 [-]	0.77	0.74	0.78	0.80	0.80

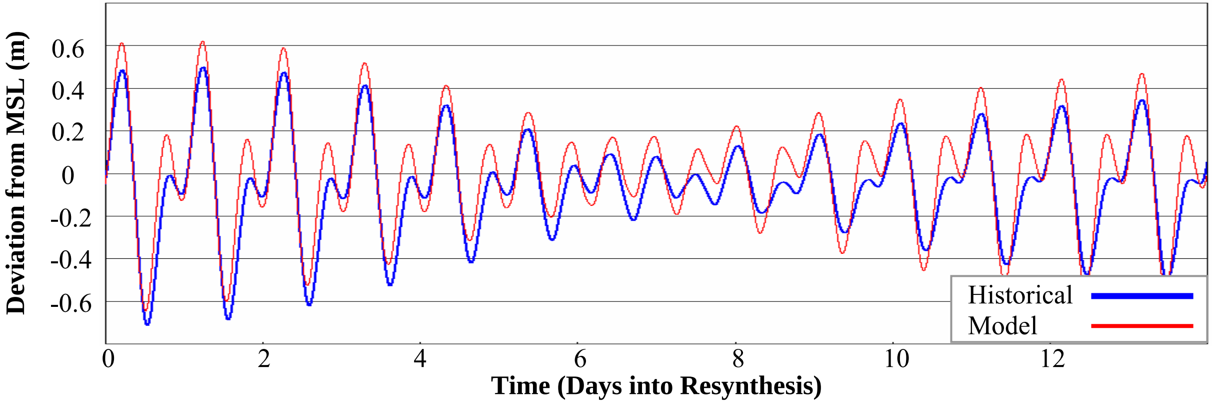

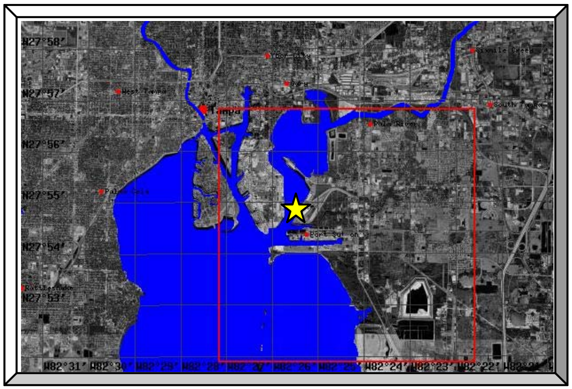

St. 94: CSX Rockport, Mckay Bay Entrance, FL					
Observer	NOS				
Longitude	82.43 W				
Latitude	27.91 N				
Simulation Results					
	333K	95K	60K	53K	48K
Ph [º]	18.4	3.8	20.4	9.8	8.0
R^2 [-]	0.84	0.85	0.85	0.85	0.85

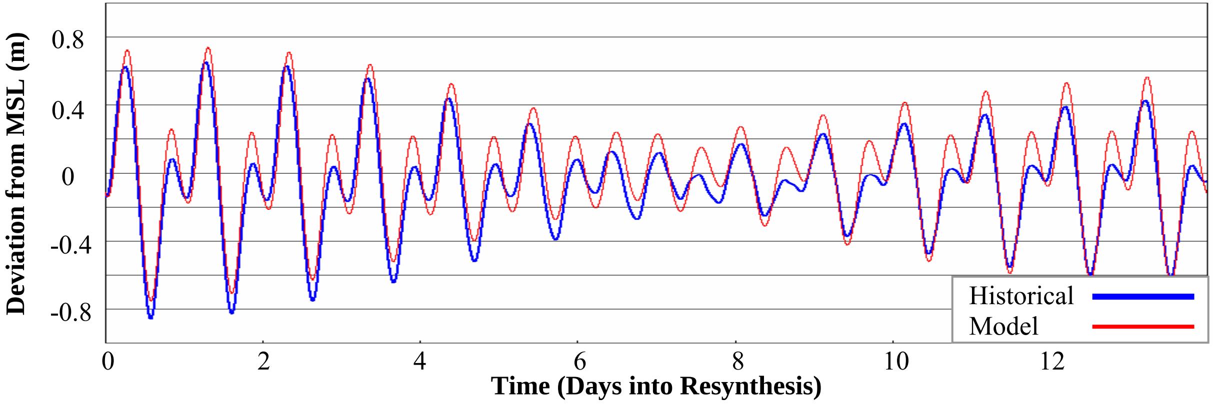

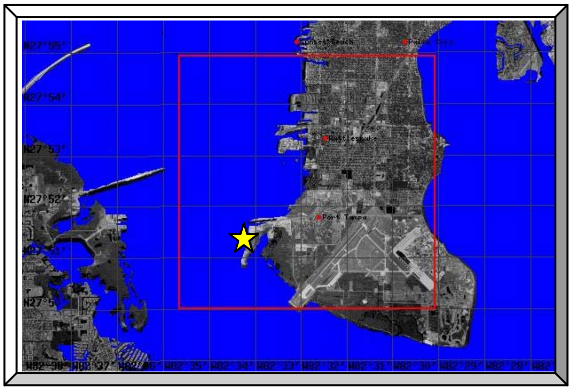

St. 95: Port Tampa, Old Tampa Bay, FL					
Observer			NOS		
Longitude			82.55 W		
Latitude			27.86 N		
Simulation Results					
	333K	95K	60K	53K	48K
Ph [º]	23.3	12.2	23.2	15.7	13.1
R^2 [-]	0.82	0.74	0.85	0.86	0.86

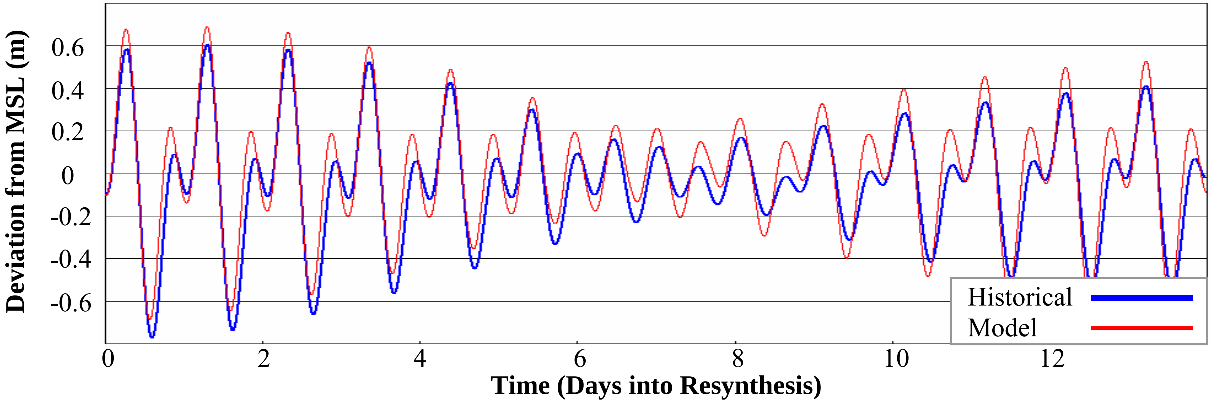

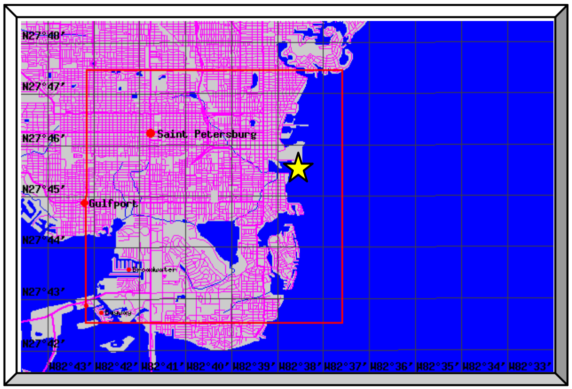

St. 96: St. Petersburg, Tampa Bay, FL					
Observer			NOS		
Longitude			82.63 W		
Latitude			27.76 N		
Simulation Results					
	333K	95K	60K	53K	48K
Ph [º]	16.1	19.8	17.9	16.2	14.5
R^2 [-]	0.80	0.80	0.82	0.83	0.83

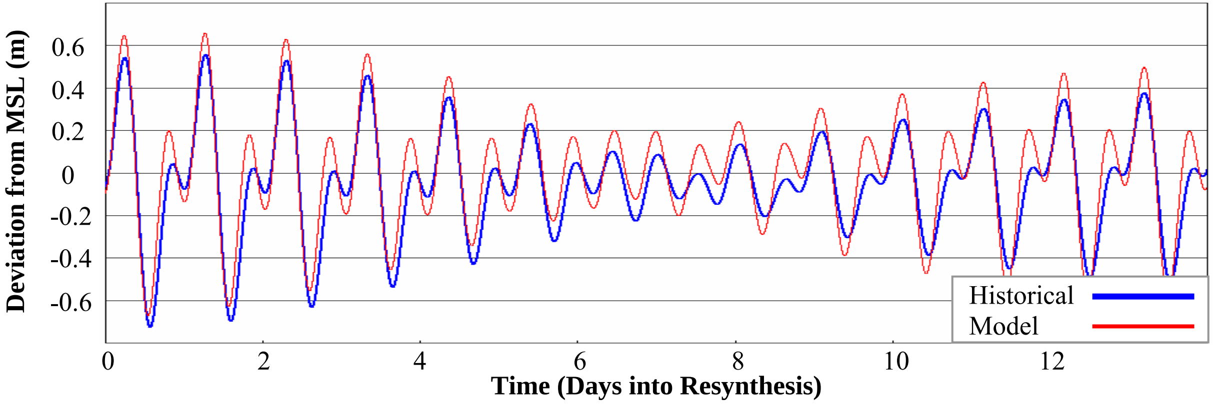

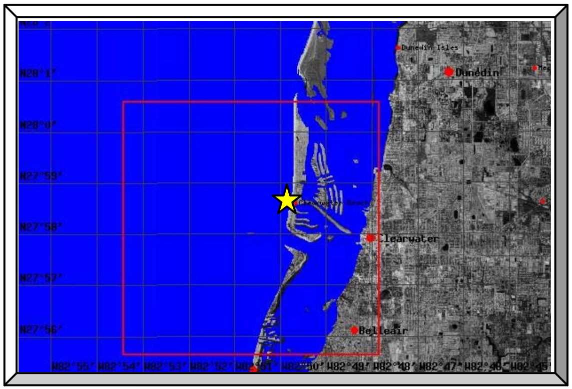

St. 97: Clearwater Beach, Gulf of Mexico, FL					
Observer		NOS			
Longitude		82.83 W			
Latitude		27.98 N			
Simulation Results					
	333K	95K	60K	53K	48K
Ph [º]	5.8	4.6	1.6	4.4	4.6
R^2 [-]	0.93	0.93	0.93	0.93	0.93

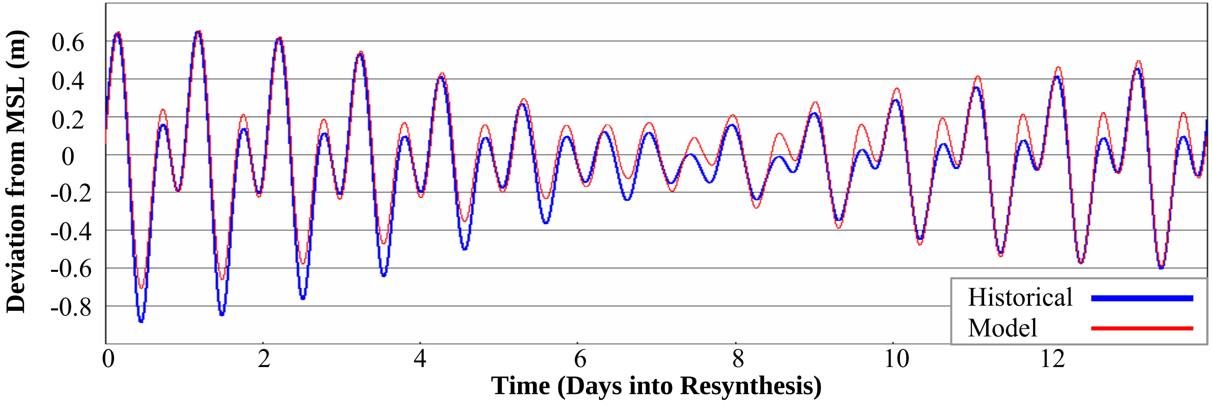

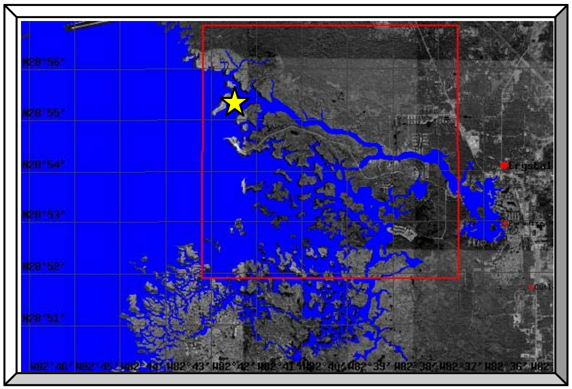

St. 105: Shark River, Crystal Bay, FL					
Observer		NOS			
Longitude		82.72 W			
Latitude		28.87 N			
Simulation Results					
	333K	95K	60K	53K	48K
Ph [º]	17.1	17.7	22.2	13.4	15.5
R^2 [-]	0.88	0.85	0.86	0.85	0.86

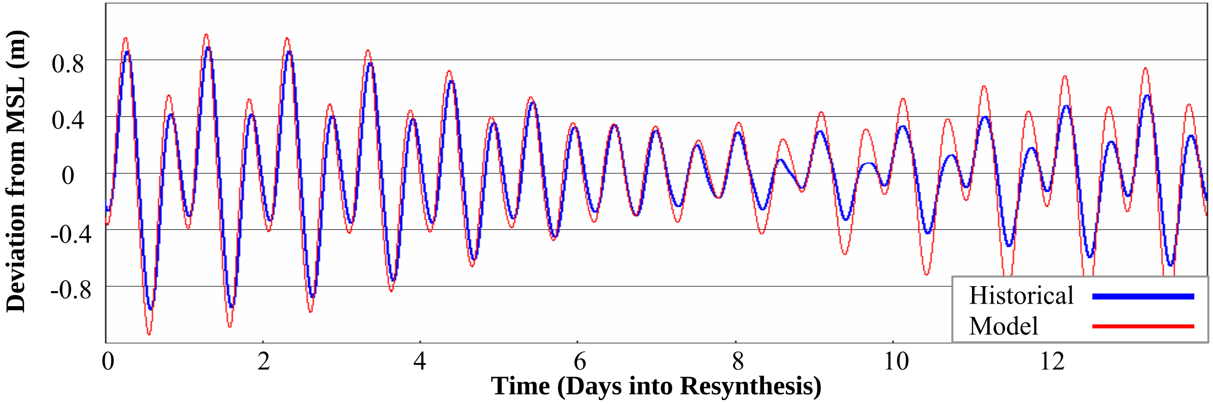

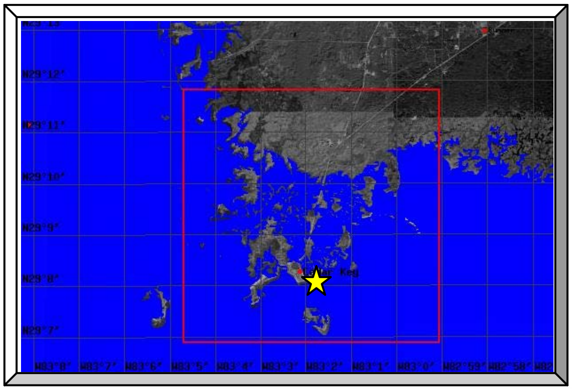

St. 110: Cedar Key, Gulf of Mexico, FL					
Observer			NOS		
Longitude			83.03 W		
Latitude			29.14 N		
Simulation Results					
	333K	95K	60K	53K	48K
Ph [º]	1.8	2.5	4.5	0.8	0.3
R^2 [-]	0.92	0.93	0.93	0.93	0.93

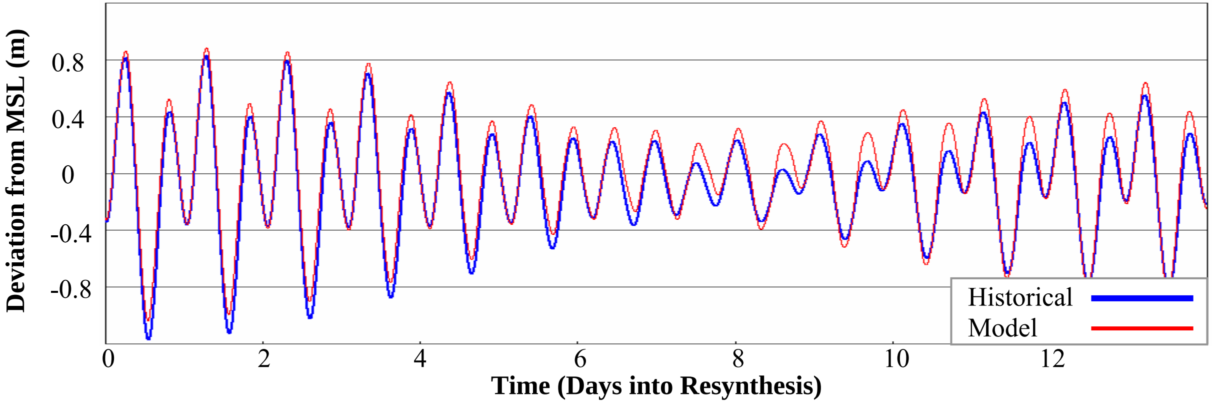

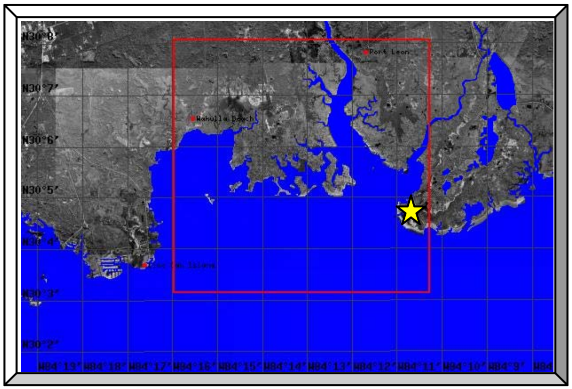

St. 111: St. Marks Lhtse., Apalachee Bay, FL					
Observer			NOS		
Longitude			84.18 W		
Latitude			30.08 N		
Simulation Results					
	333K	95K	60K	53K	48K
Ph [º]	22.2	17.4	15.8	20.2	21.3
R^2 [-]	0.94	0.93	0.93	0.94	0.93

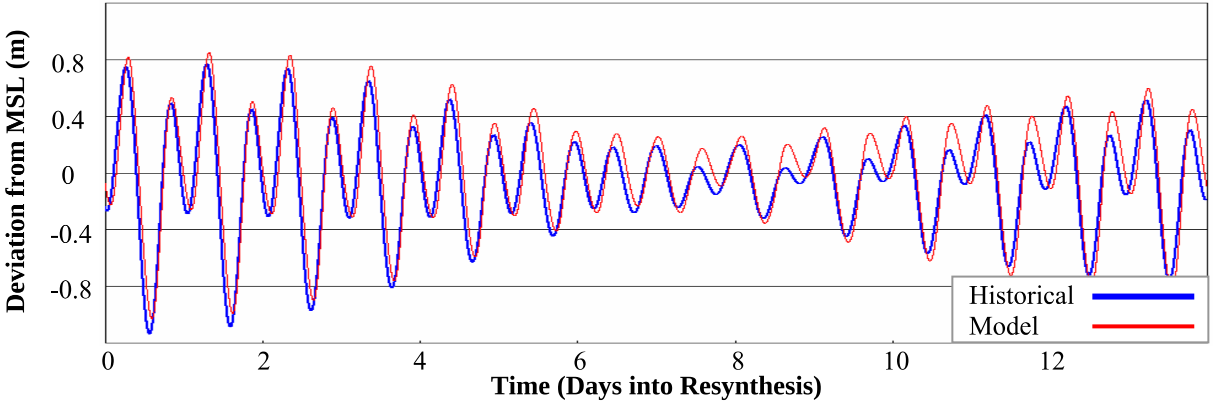

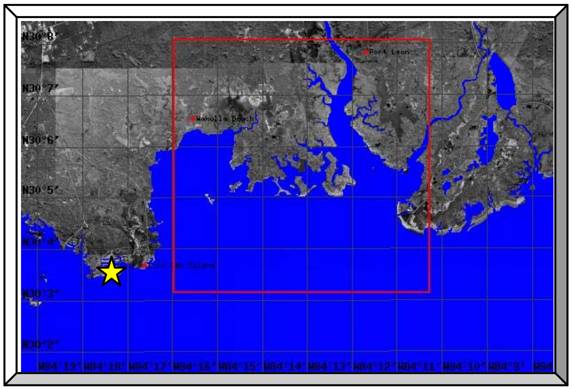

St. 112: Shell Point, Walker Creek, FL					
Observer			NOS		
Longitude			84.29 W		
Latitude			30.06 N		
Simulation Results					
	333K	95K	60K	53K	48K
Ph [º]	11.6	8.8	5.5	9.7	9.9
R^2 [-]	0.95	0.95	0.96	0.96	0.96

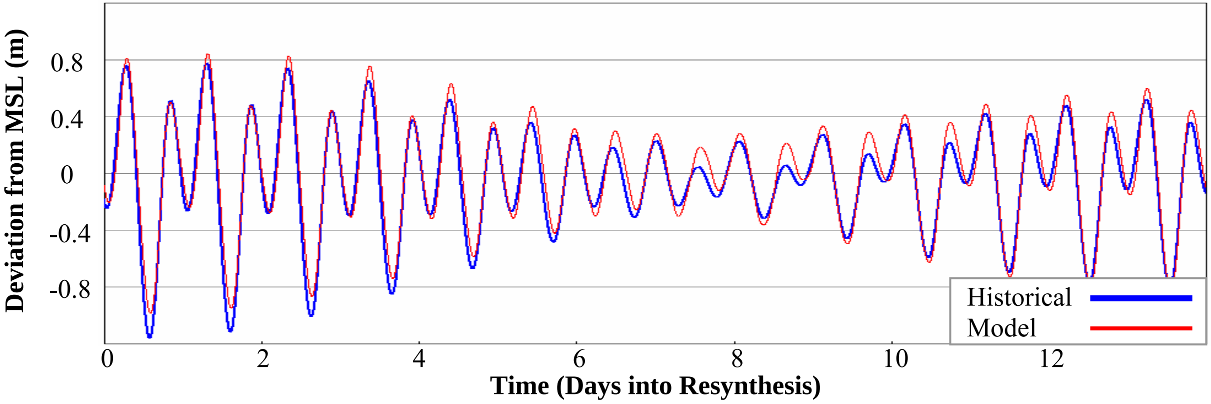

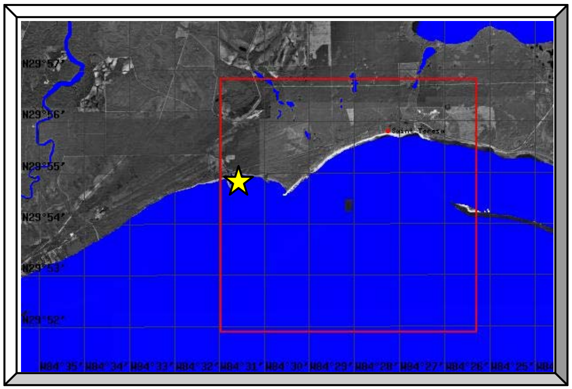

St. 113: Turkey Point, FL					
Observer			NOS		
Longitude			84.51 W		
Latitude			29.92 N		
Simulation Results					
	333K	95K	60K	53K	48K
Ph [º]	10.0	6.8	4.0	7.0	7.6
R^2 [-]	0.94	0.94	0.94	0.95	0.94

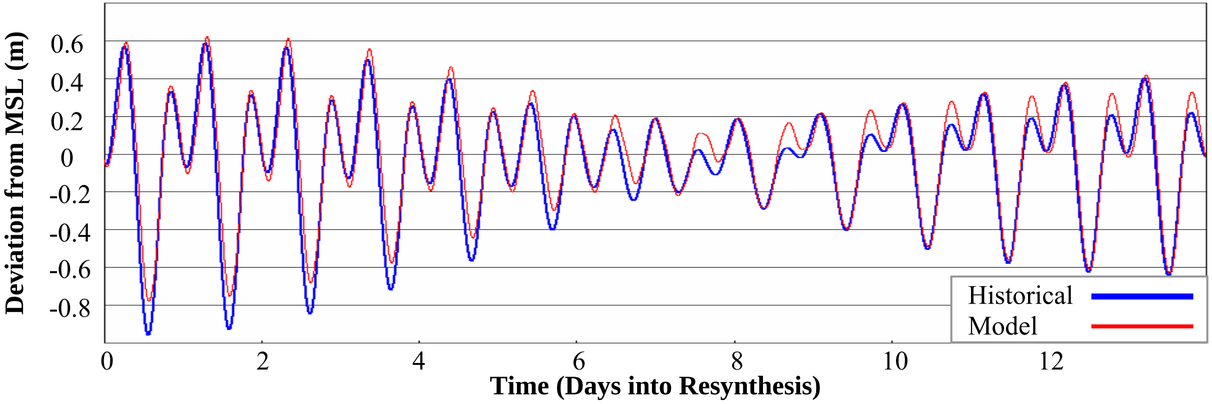

St. 114: Apalachicola, Apalachicola River, FL					
Observer			NOS		
Longitude			84.98 W		
Latitude			29.73 N		
Simulation Results					
	333K	95K	60K	53K	48K
Ph [º]	29.1	22.9	14.5	35.9	34.5
R^2 [-]	0.91	0.60	0.88	0.91	0.90

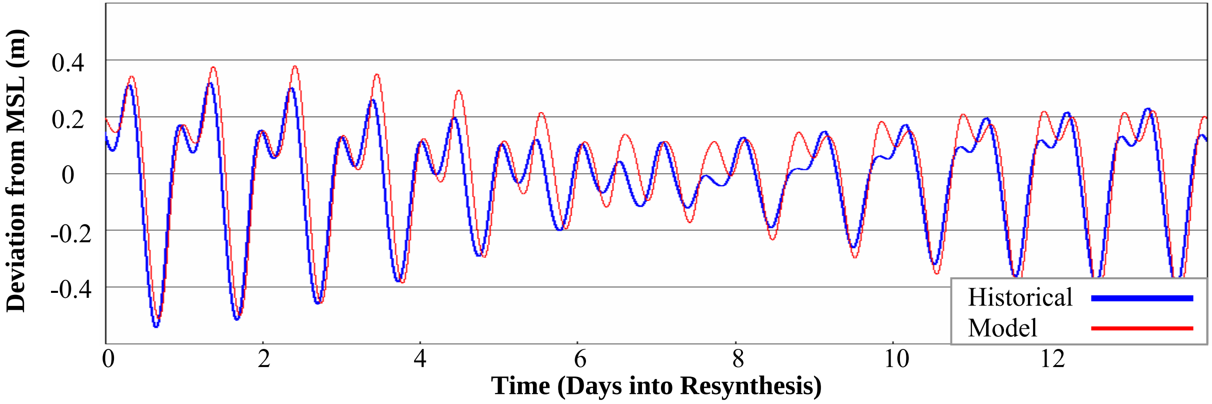

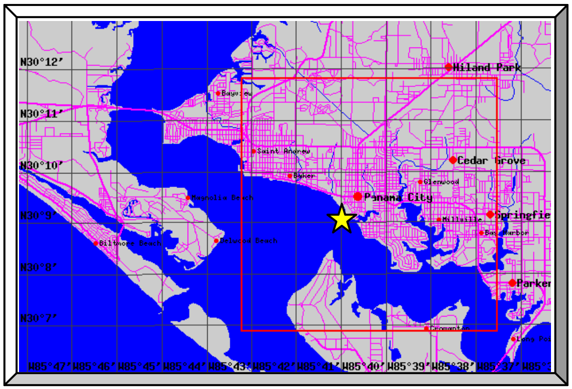

St. 115: Panama City, St. Andrew Bay, FL					
Observer			NOS		
Longitude			85.67 W		
Latitude			30.15 N		
Simulation Results					
	333K	95K	60K	53K	48K
Ph [º]	14.4	23.3	28.2	24.4	21.1
R^2 [-]	0.86	0.87	0.85	0.86	0.87

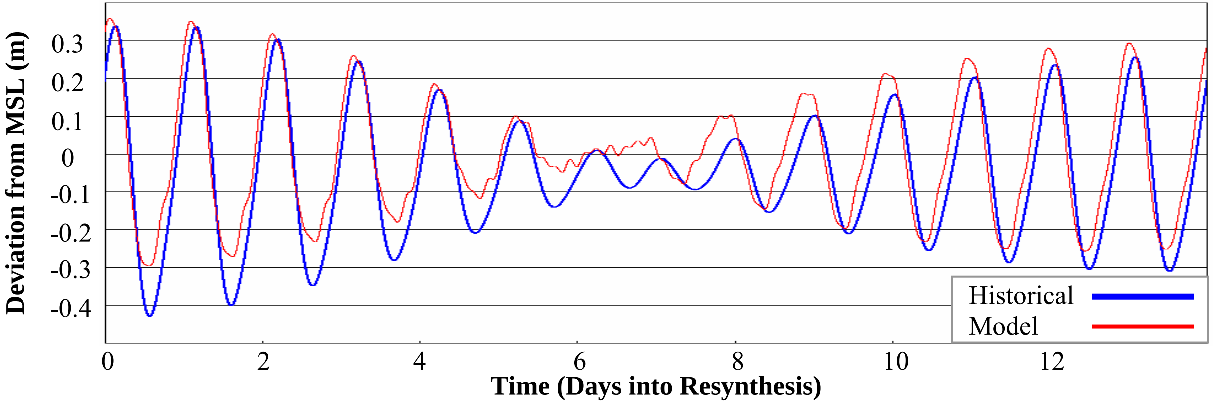

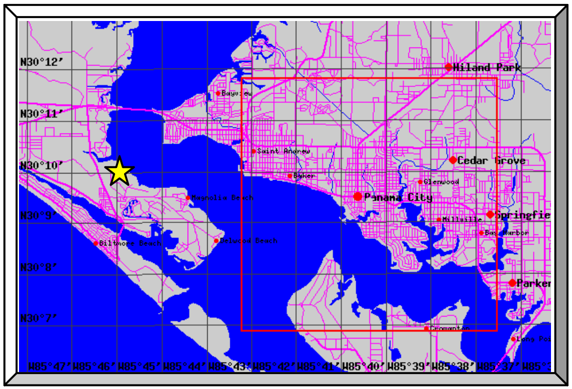

St. 116: Alligator Bayou, FL					
Observer			IHO		
Longitude			85.75 W		
Latitude			30.17 N		
Simulation Results					
	333K	95K	60K	53K	48K
Ph [º]	13.7	22.0	20.3	20.1	21.6
R^2 [-]	0.97	0.97	0.98	0.98	0.97

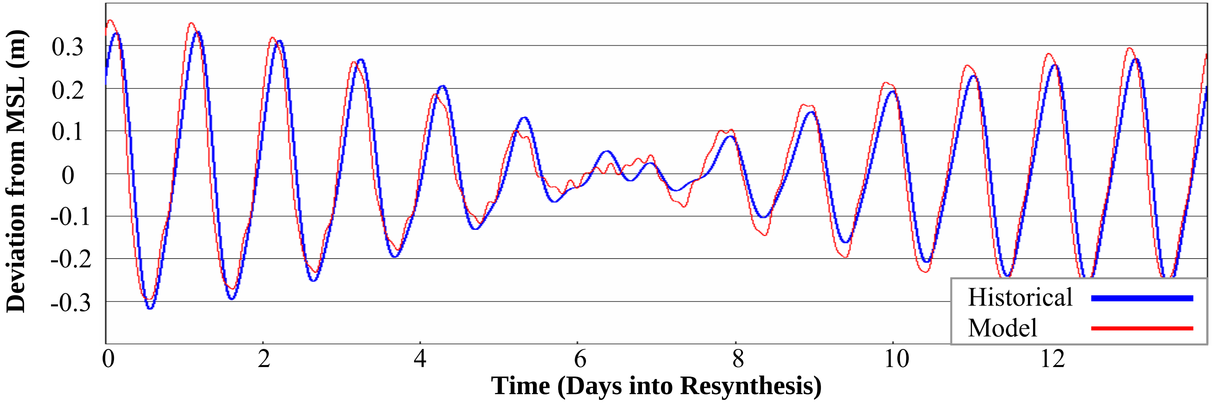

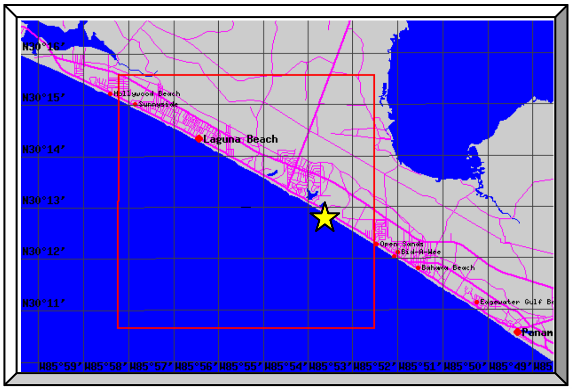

St. 117: Panama City Beach, Gulf of Mexico, FL					
Observer			NOS		
Longitude			85.88 W		
Latitude			30.21 N		
Simulation Results					
	333K	95K	60K	53K	48K
Ph [º]	1.1	3.6	8.7	4.9	5.8
R^2 [-]	0.86	0.86	0.84	0.85	0.85

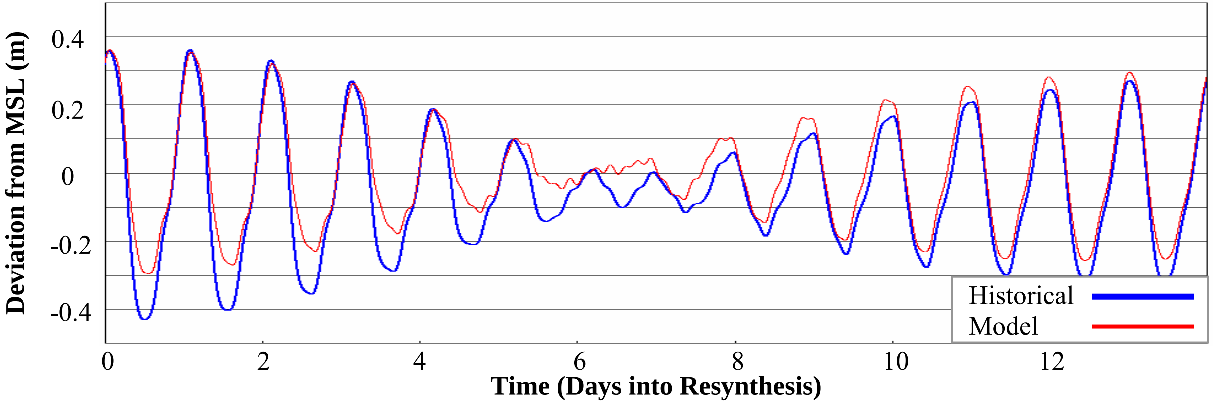

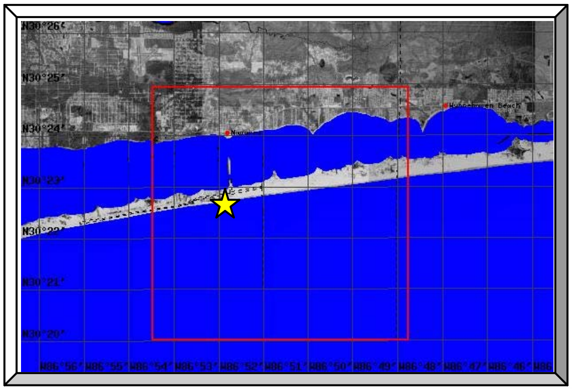

<table>
<tr><th colspan="6">St. 118: Navarre Beach, FL</th></tr>
<tr><td colspan="3">Observer</td><td colspan="3">NOS</td></tr>
<tr><td colspan="3">Longitude</td><td colspan="3">86.87 W</td></tr>
<tr><td colspan="3">Latitude</td><td colspan="3">30.38 N</td></tr>
<tr><td colspan="6">Simulation Results</td></tr>
<tr><td></td><td>333K</td><td>95K</td><td>60K</td><td>53K</td><td>48K</td></tr>
<tr><td>Ph [º]</td><td>1.2</td><td>1.8</td><td>9.0</td><td>4.4</td><td>3.2</td></tr>
<tr><td>R^2 [-]</td><td>0.81</td><td>0.81</td><td>0.79</td><td>0.80</td><td>0.81</td></tr>
</table>

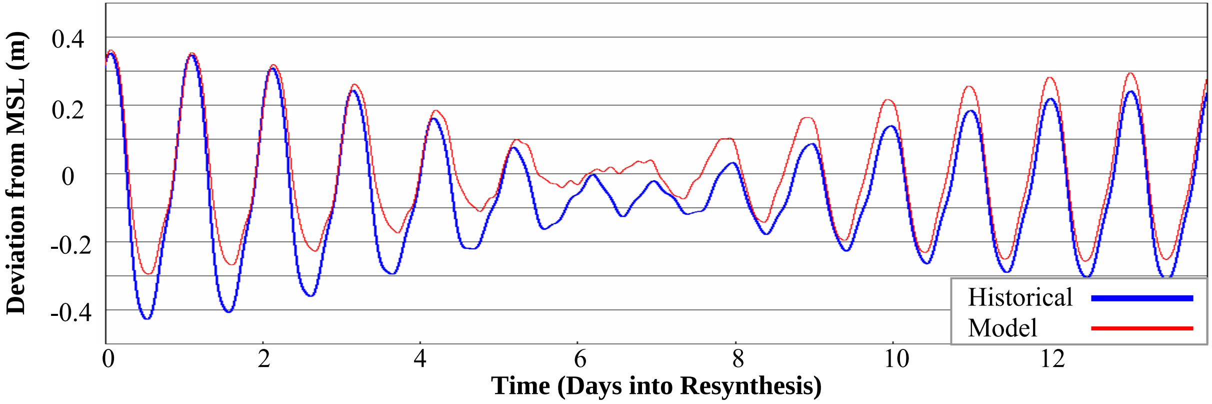

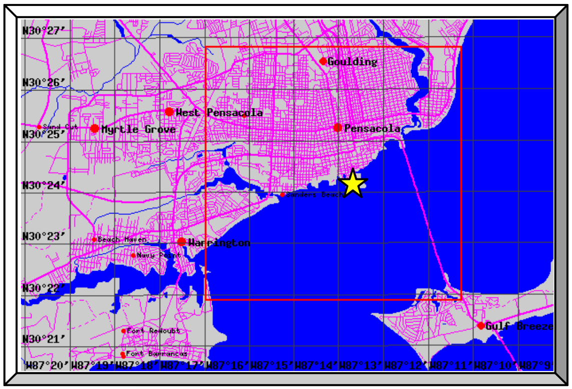

<table>
<tr><th colspan="6">St. 119: Pensacola, Pensacola Bay, FL</th></tr>
<tr><td colspan="3">Observer</td><td colspan="3">NOS</td></tr>
<tr><td colspan="3">Longitude</td><td colspan="3">87.21 W</td></tr>
<tr><td colspan="3">Latitude</td><td colspan="3">30.40 N</td></tr>
<tr><td colspan="6">Simulation Results</td></tr>
<tr><td></td><td>333K</td><td>95K</td><td>60K</td><td>53K</td><td>48K</td></tr>
<tr><td>Ph [º]</td><td>31.8</td><td>32.5</td><td>33.9</td><td>33.5</td><td>33.2</td></tr>
<tr><td>R^2 [-]</td><td>0.92</td><td>0.92</td><td>0.92</td><td>0.92</td><td>0.92</td></tr>
</table>

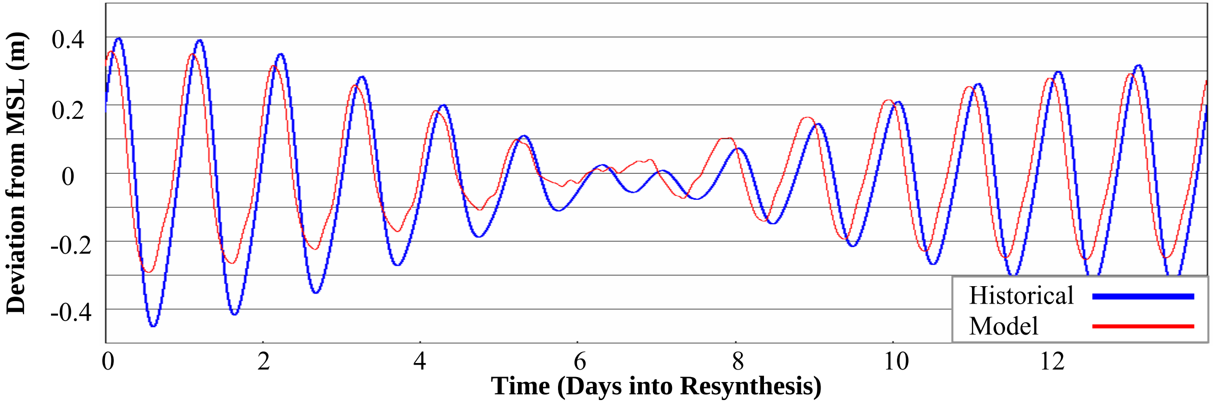

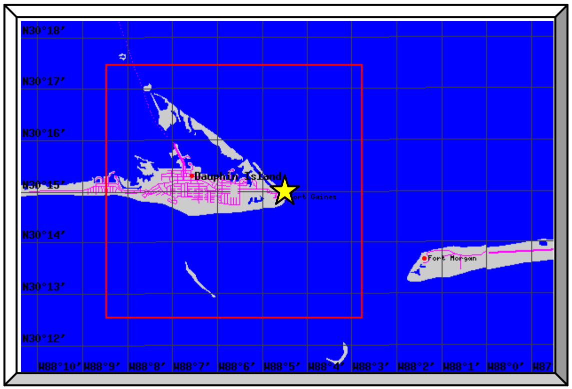

St. 120: Dauphin Island, Mobile Bay, AL					
Observer			NOS		
Longitude			88.08 W		
Latitude			30.25 N		
Simulation Results					
	333K	95K	60K	53K	48K
Ph [º]	10.7	7.4	13.8	12.0	10.8
R^2 [-]	0.92	0.85	0.92	0.91	0.91

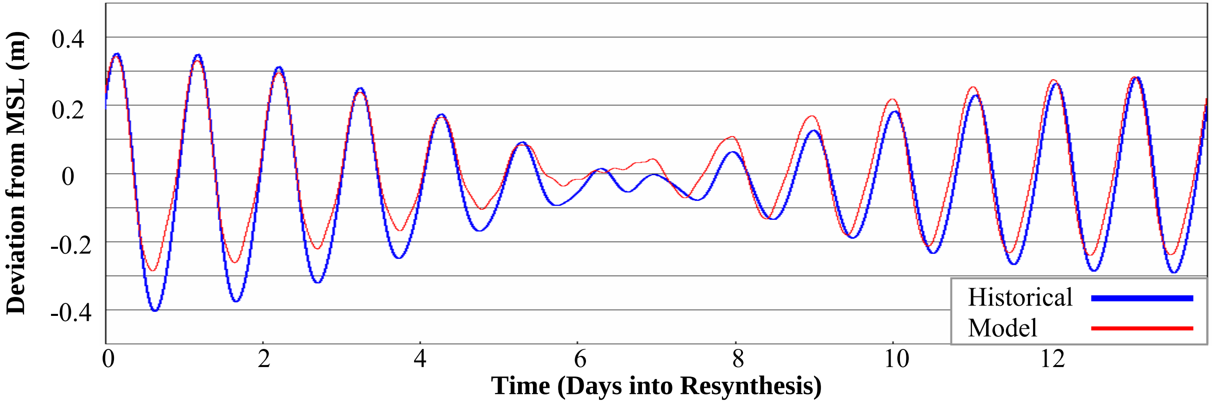

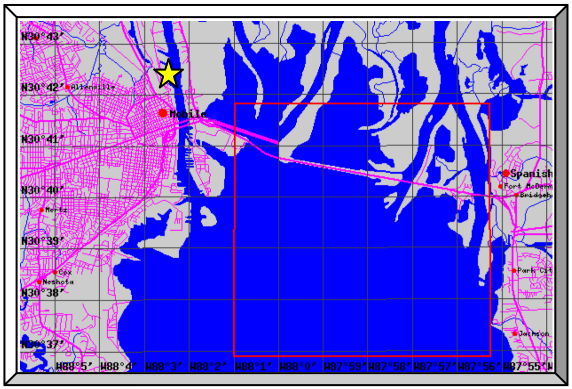

St. 121: Mobile State Docks, Mobile River, AL					
Observer			NOS		
Longitude			88.04 W		
Latitude			30.71 N		
Simulation Results					
	333K	95K	60K	53K	48K
Ph [º]	28.1	7.2	27.5	20.7	20.3
R^2 [-]	0.88	0.86	0.88	0.88	0.88

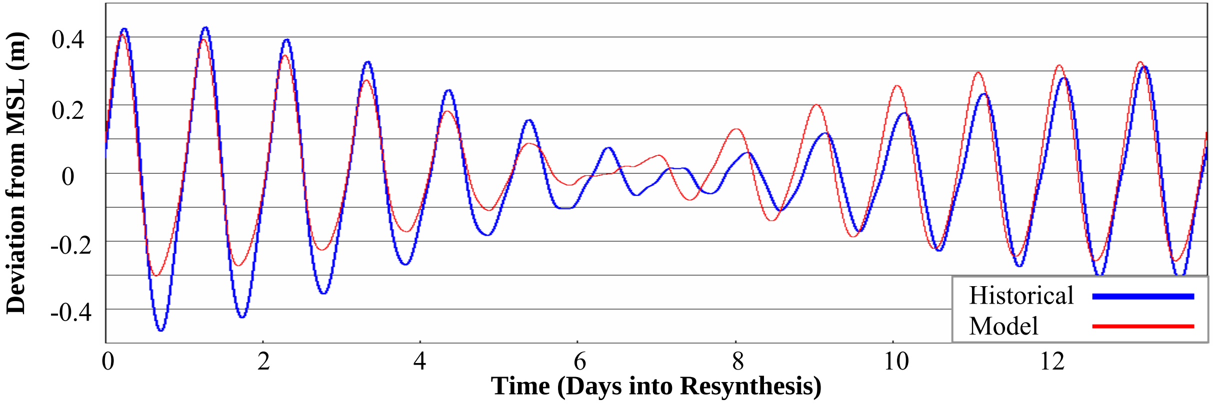

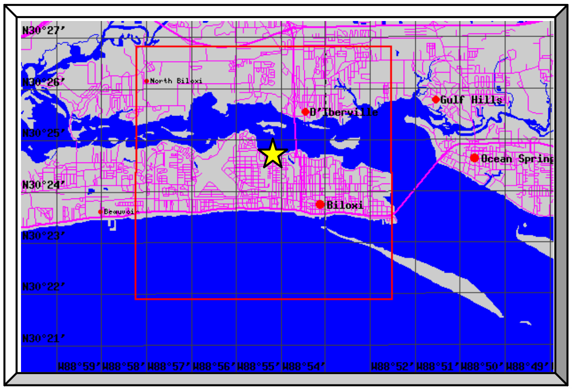

St. 122: Biloxi, Bay of Biloxi, MS					
Observer	NOS				
Longitude	88.90 W				
Latitude	30.41 N				
Simulation Results					
	333K	95K	60K	53K	48K
Ph [º]	27.2	23.6	24.5	24.9	29.0
R^2 [-]	0.93	0.94	0.94	0.94	0.93

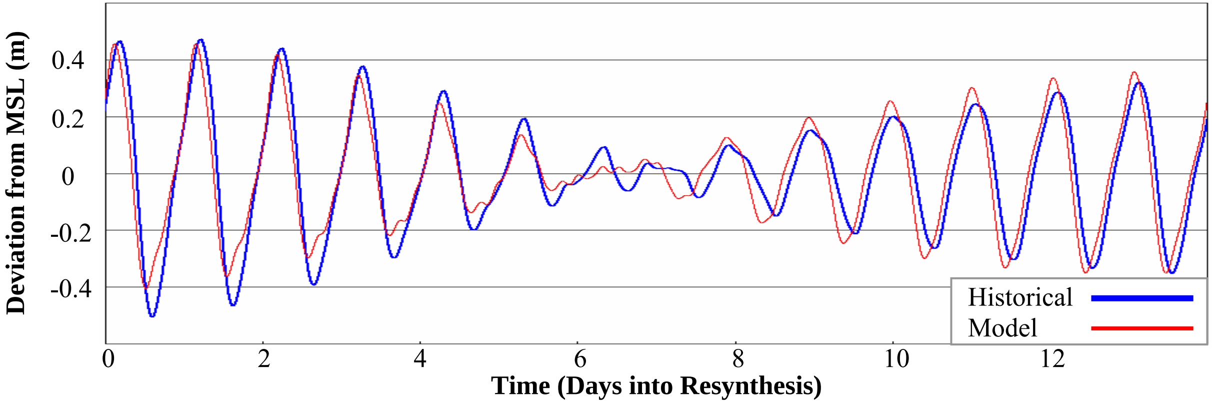

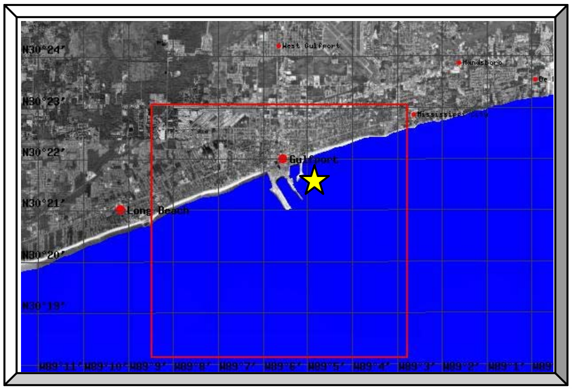

St. 123: Gulfport Harbor, Mississippi Sound, MS					
Observer	NOS				
Longitude	89.08 W				
Latitude	30.36 N				
Simulation Results					
	333K	95K	60K	53K	48K
Ph [º]	23.8	22.8	22.0	21.6	30.3
R^2 [-]	0.90	0.90	0.90	0.91	0.90

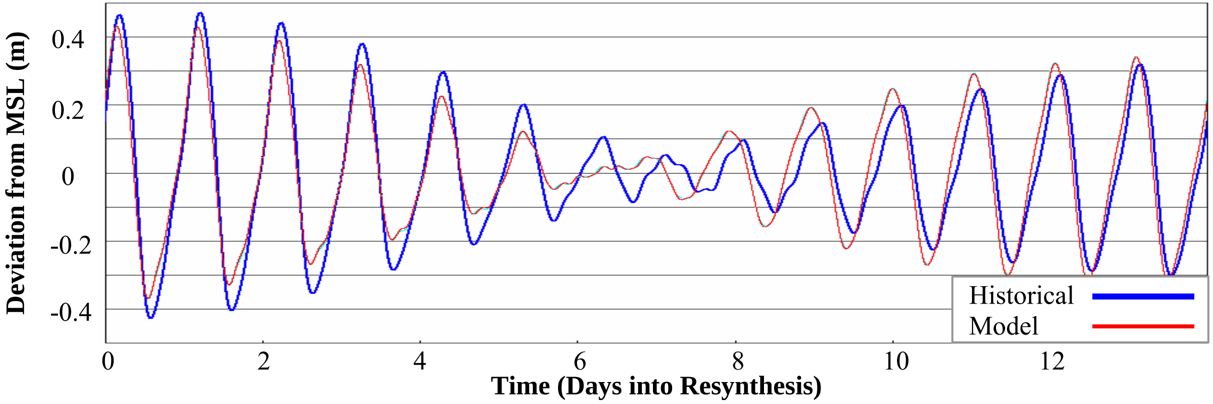

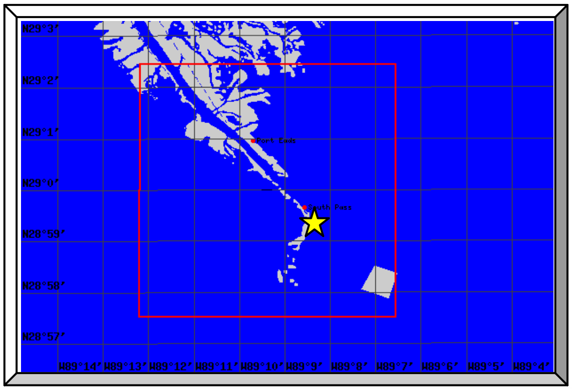

St. 128: South Pass, LA					
Observer			NOS		
Longitude			89.14 W		
Latitude			28.99 N		
Simulation Results					
	333K	95K	60K	53K	48K
Ph [º]	2.3	2.3	2.0	2.4	2.5
R^2 [-]	0.92	0.93	0.93	0.93	0.93

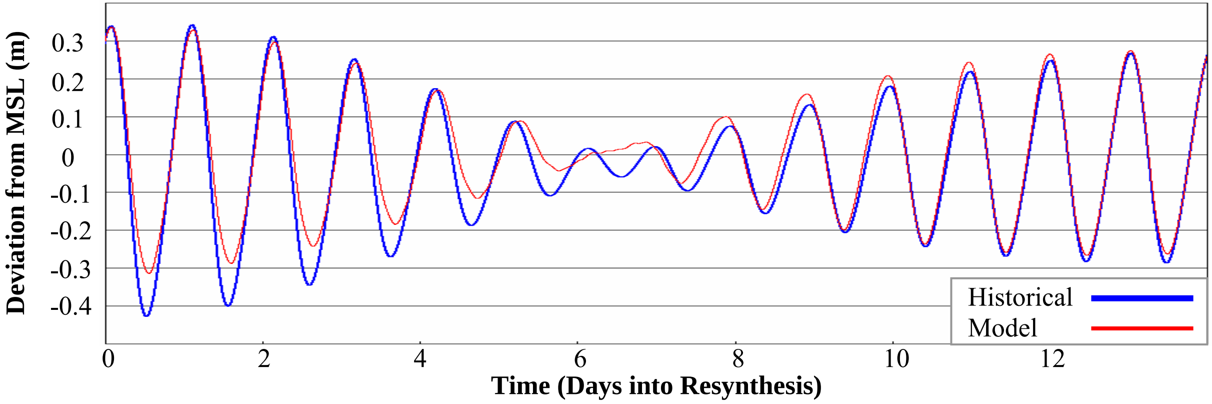

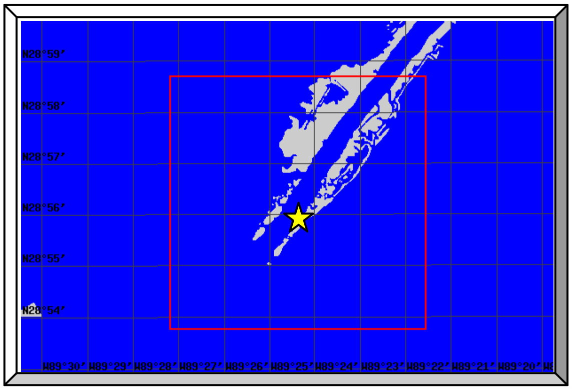

St. 129: Pilots Station East, Southwest Pass, LA					
Observer			NOS		
Longitude			89.41 W		
Latitude			28.93 N		
Simulation Results					
	333K	95K	60K	53K	48K
Ph [º]	3.9	4.0	3.9	3.6	3.5
R^2 [-]	0.92	0.92	0.92	0.92	0.92

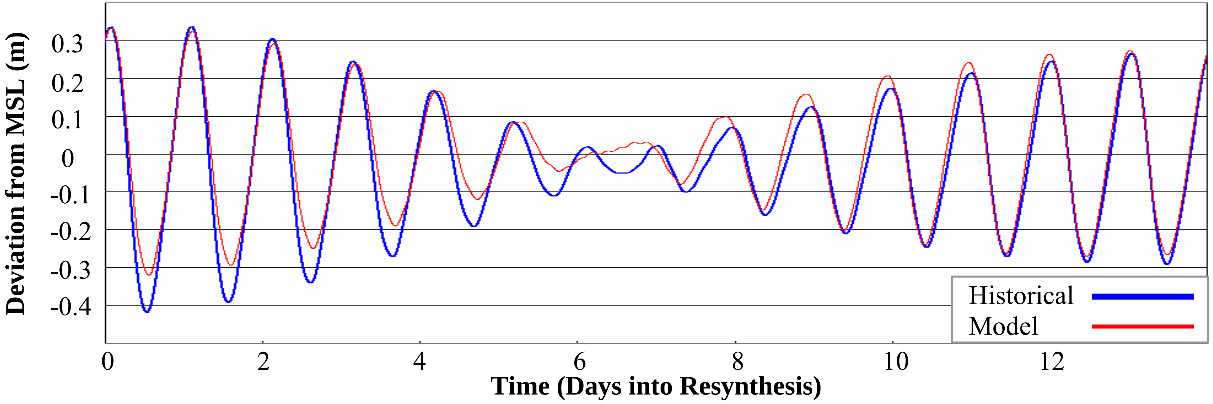

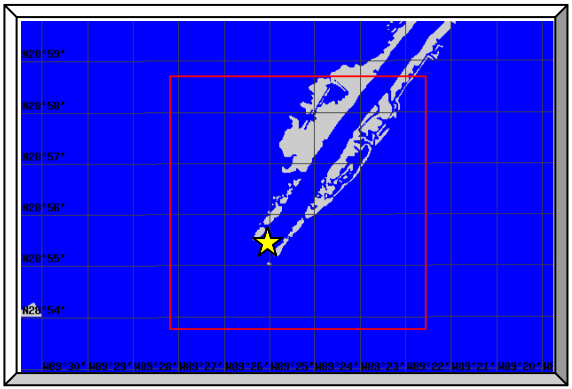

St. 130: Pilot Station, SW Pass, LA					
Observer			NOS		
Longitude			89.42 W		
Latitude			28.93 N		
Simulation Results					
	333K	95K	60K	53K	48K
Ph [º]	0.6	1.2	0.2	1.3	0.8
R^2 [-]	0.92	0.92	0.92	0.92	0.92

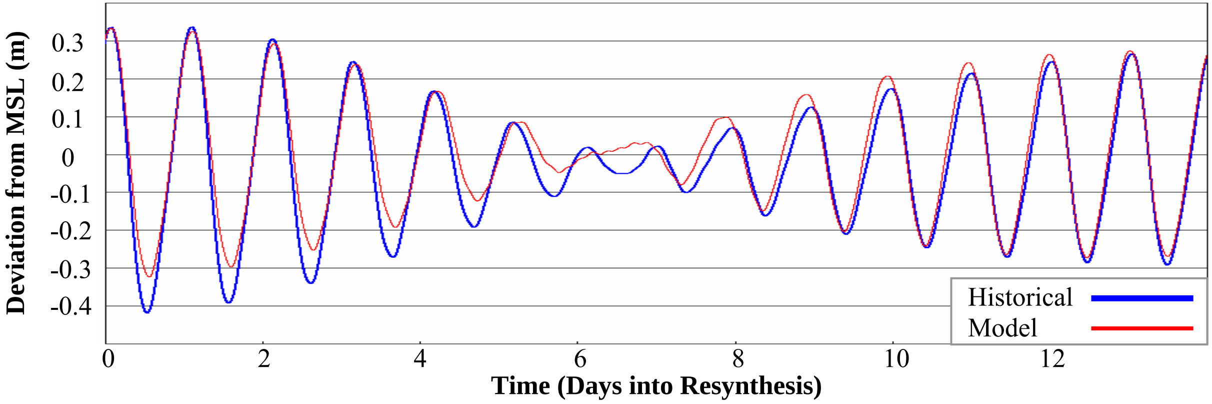

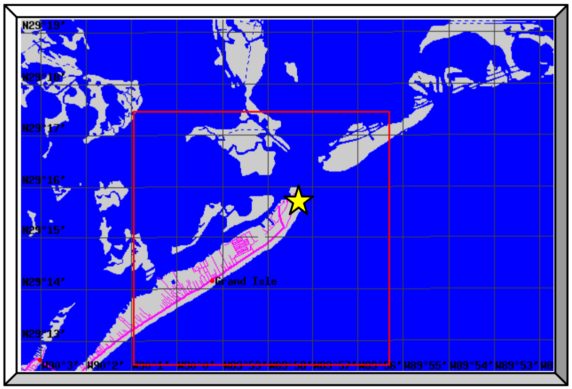

St. 131: Grand Isle, East Point, LA					
Observer			NOS		
Longitude			89.96 W		
Latitude			29.26 N		
Simulation Results					
	333K	95K	60K	53K	48K
Ph [º]	5.4	5.1	6.9	5.6	4.5
R^2 [-]	0.92	0.93	0.92	0.92	0.92

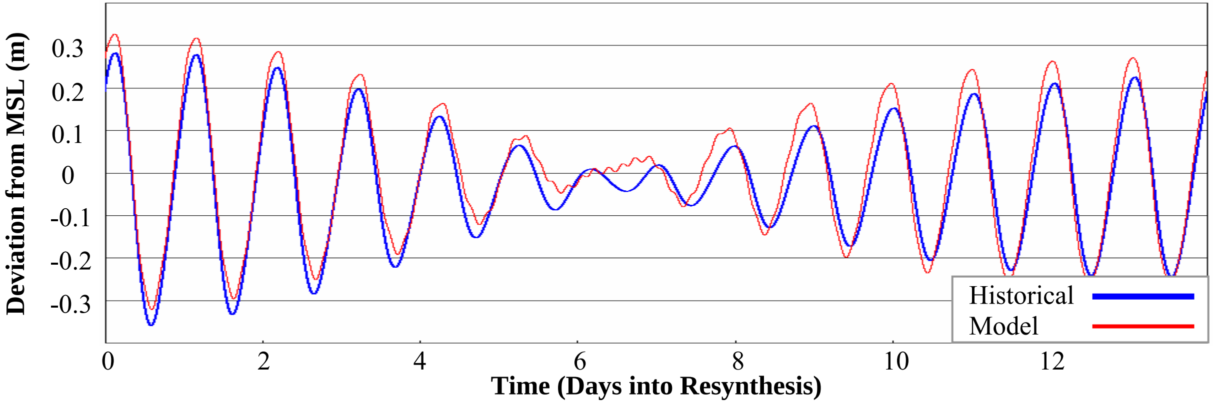

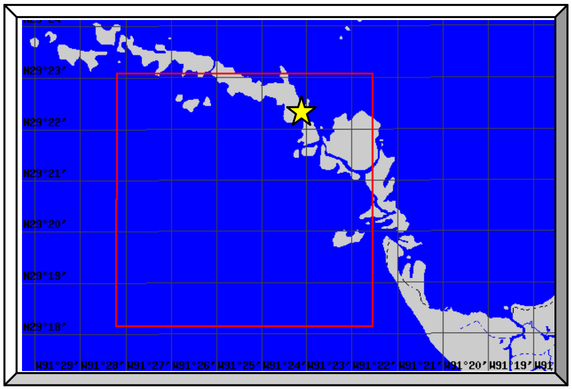

St. 134: Eugene Island, LA					
Observer		NOS			
Longitude		91.39 W			
Latitude		29.37 N			
Simulation Results					
	333K	95K	60K	53K	48K
Ph [º]	3.3	6.1	0.1	3.1	0.4
R^2 [-]	0.89	0.89	0.89	0.89	0.90

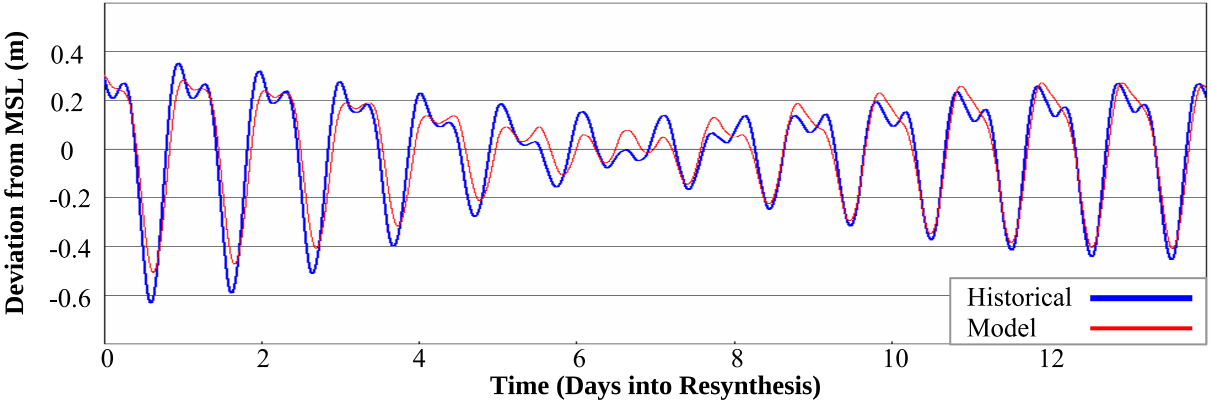

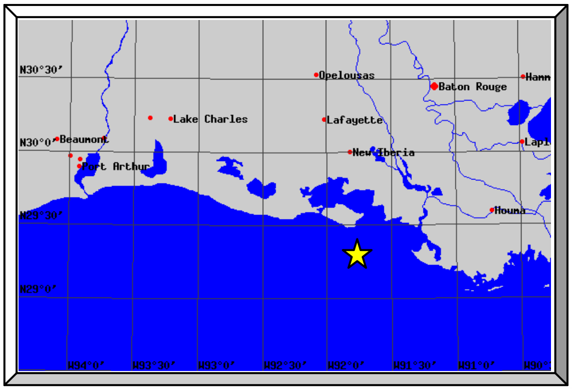

St. 135: Point au Fer, LA					
Observer		IHO			
Longitude		91.75 W			
Latitude		29.29 N			
Simulation Results					
	333K	95K	60K	53K	48K
Ph [º]	10.1	13.1	1.9	8.3	12.3
R^2 [-]	0.98	0.98	0.98	0.98	0.98

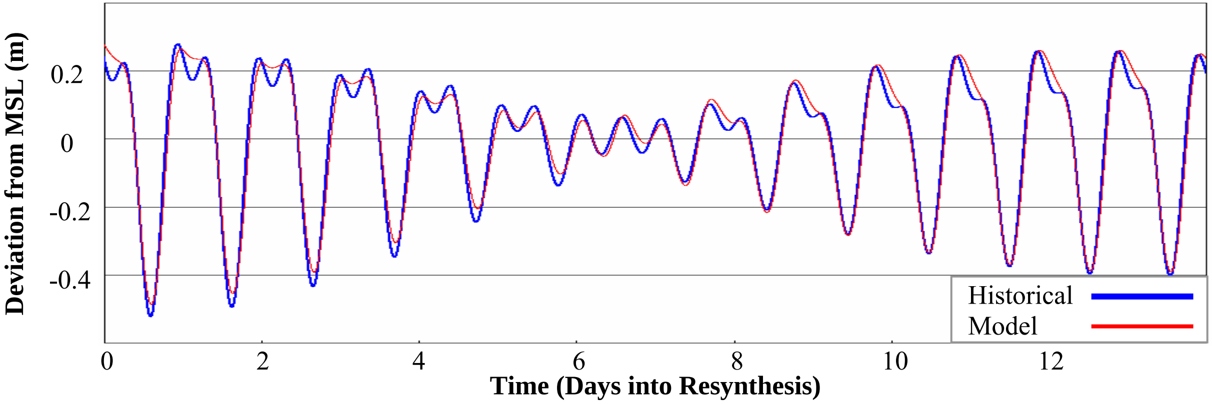

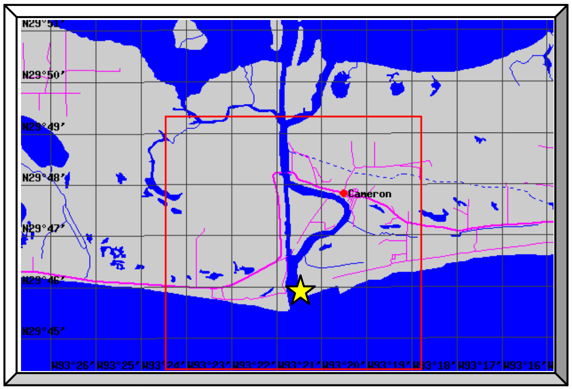

St. 136: Calcasieu Pass, East Jetty, LA					
Observer			NOS		
Longitude			93.34 W		
Latitude			29.77 N		
Simulation Results					
	333K	95K	60K	53K	48K
Ph [°]	7.9	4.8	5.3	9.2	7.8
R^2 [-]	0.92	0.91	0.92	0.91	0.92

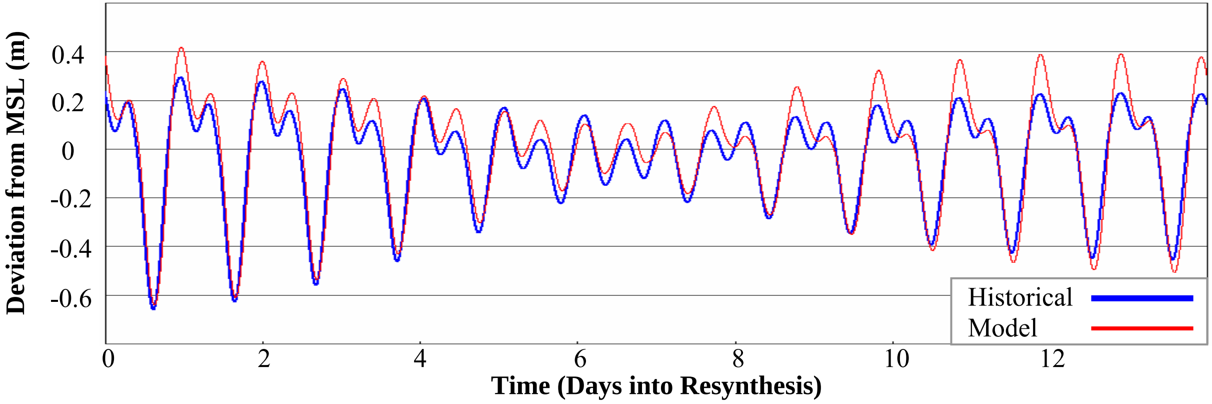

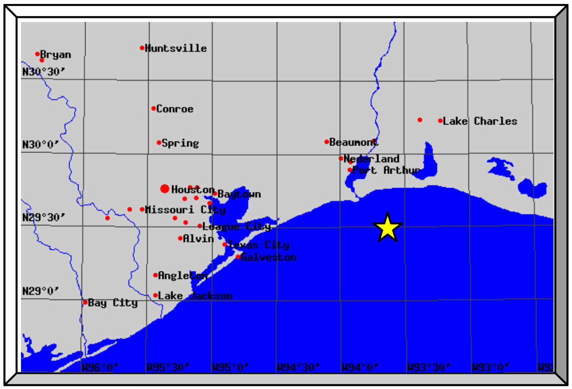

St. 137: Sabine Offshore, TX					
Observer			NOS		
Longitude			93.64 W		
Latitude			29.50 N		
Simulation Results					
	333K	95K	60K	53K	48K
Ph [°]	6.8	9.1	5.6	5.6	8.1
R^2 [-]	0.92	0.92	0.92	0.92	0.92

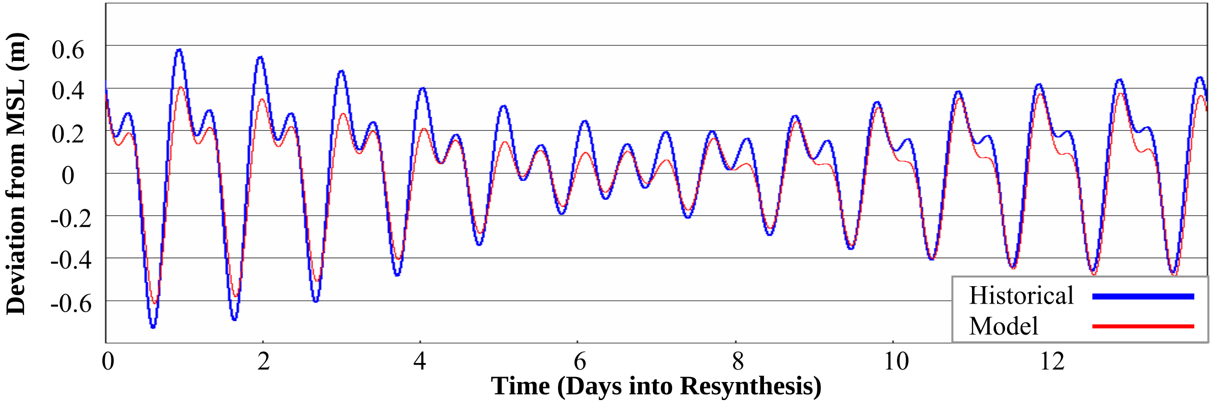

St. 140: Galveston Bay Entrance, North Jetty, TX	
Observer	NOS
Longitude	94.73 W
Latitude	29.36 N

Simulation Results					
	333K	95K	60K	53K	48K
Ph [º]	0.2	2.9	0.4	1.9	2.6
R^2 [-]	0.95	0.94	0.95	0.95	0.94

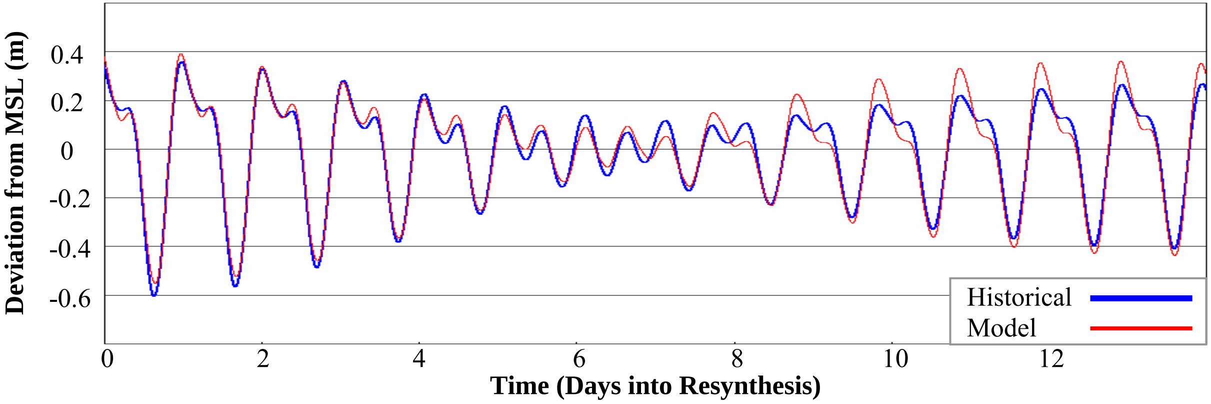

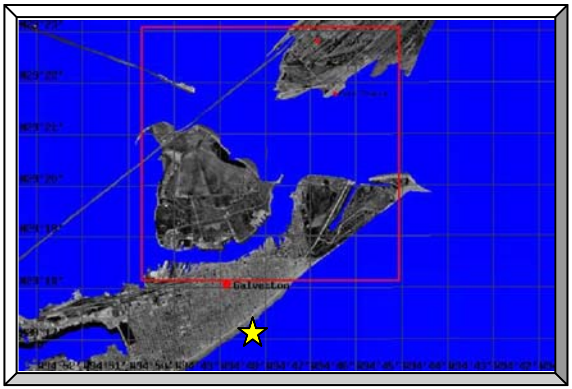

St. 143: Galveston Pleasure P., Gulf of Mexico, TX	
Observer	NOS
Longitude	94.79 W
Latitude	29.29 N

Simulation Results					
	333K	95K	60K	53K	48K
Ph [º]	21.8	23.9	21.5	20.8	22.9
R^2 [-]	0.91	0.91	0.91	0.91	0.91

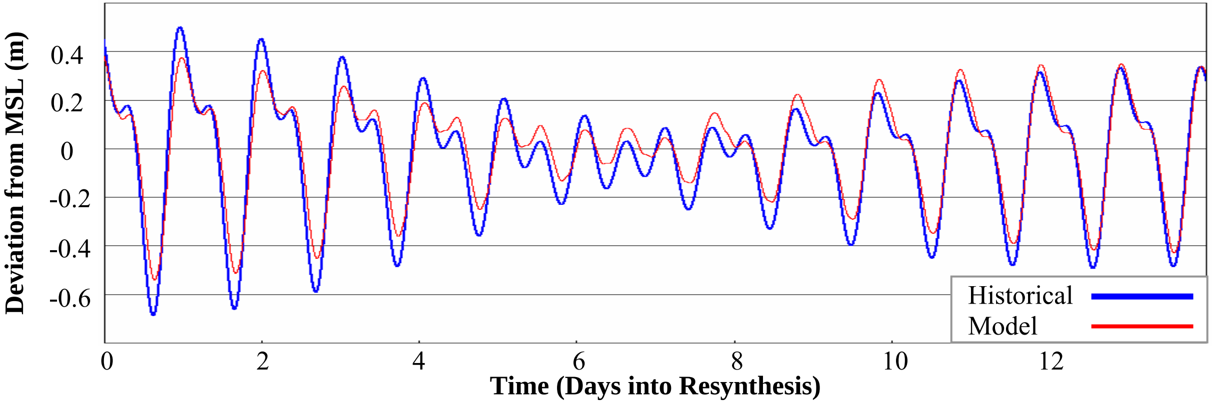

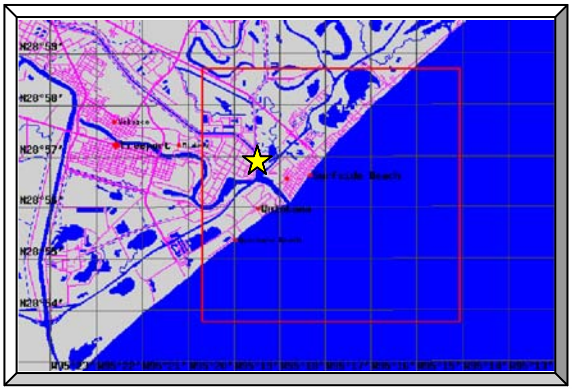

St. 144: Freeport, Dow Barge Canal, TX					
Observer			NOS		
Longitude			95.31 W		
Latitude			28.95 N		
Simulation Results					
	333K	95K	60K	53K	48K
Ph [º]	4.2	5.1	3.6	3.7	4.6
R^2 [-]	0.97	0.97	0.97	0.97	0.97

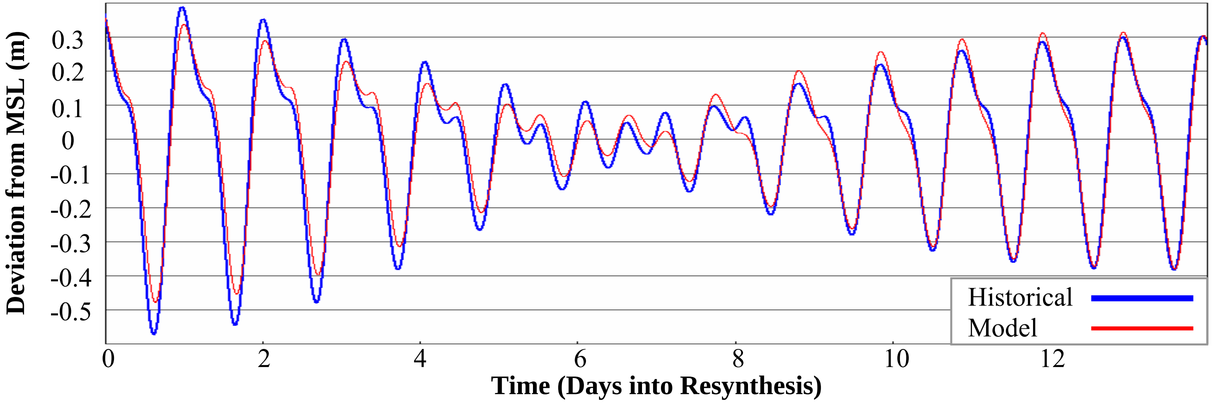

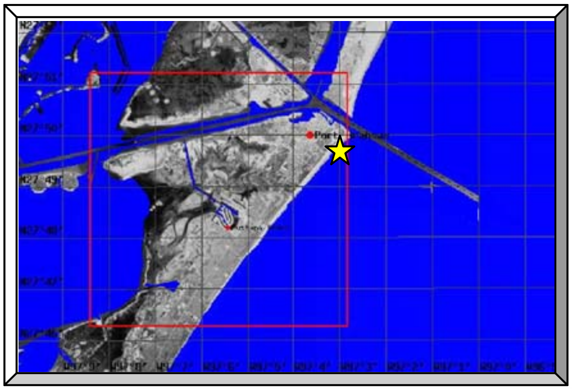

St. 147: Port Aransas, H. Caldwell Pier, TX					
Observer			NOS		
Longitude			97.05 W		
Latitude			27.83 N		
Simulation Results					
	333K	95K	60K	53K	48K
Ph [º]	4.8	5.0	3.8	3.5	4.2
R^2 [-]	0.90	0.90	0.91	0.91	0.90

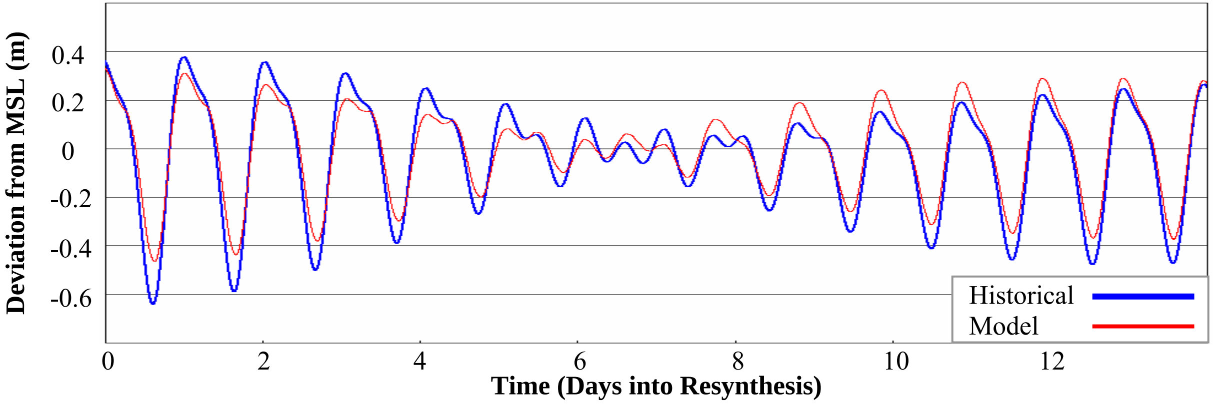

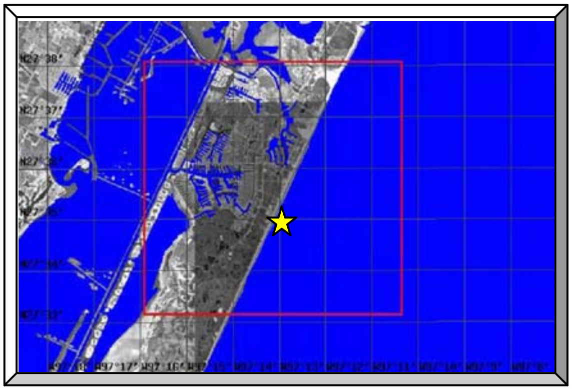

St. 149: Corpus Christi, Gulf of Mexico, TX					
Observer			NOS		
Longitude			97.22 W		
Latitude			27.58 N		
Simulation Results					
	333K	95K	60K	53K	48K
Ph [º]	4.8	4.9	3.7	3.5	3.9
R^2 [-]	0.96	0.96	0.96	0.96	0.96

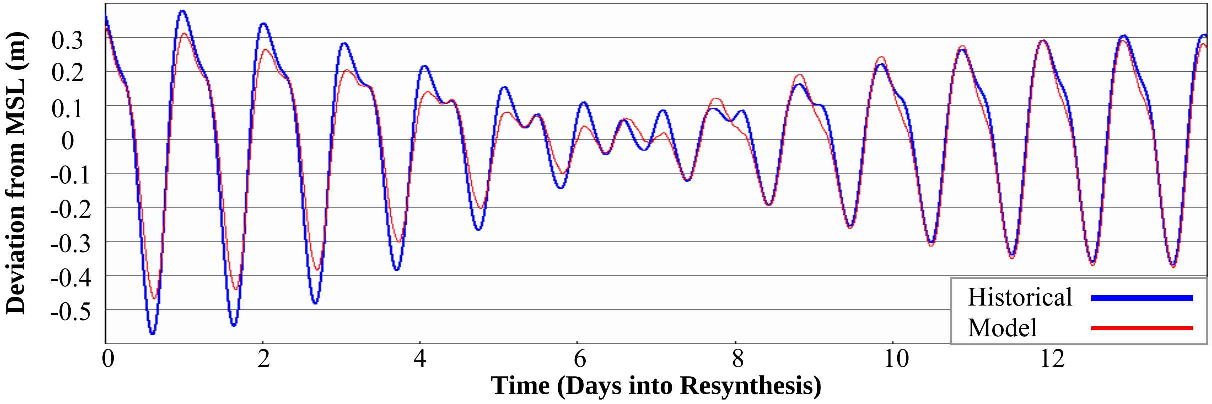

St. 151: Padre Island, Brazos Santiago Pass, TX					
Observer			NOS		
Longitude			97.16 W		
Latitude			26.07 N		
Simulation Results					
	333K	95K	60K	53K	48K
Ph [º]	1.7	2.3	1.1	0.9	1.3
R^2 [-]	0.90	0.91	0.91	0.91	0.91

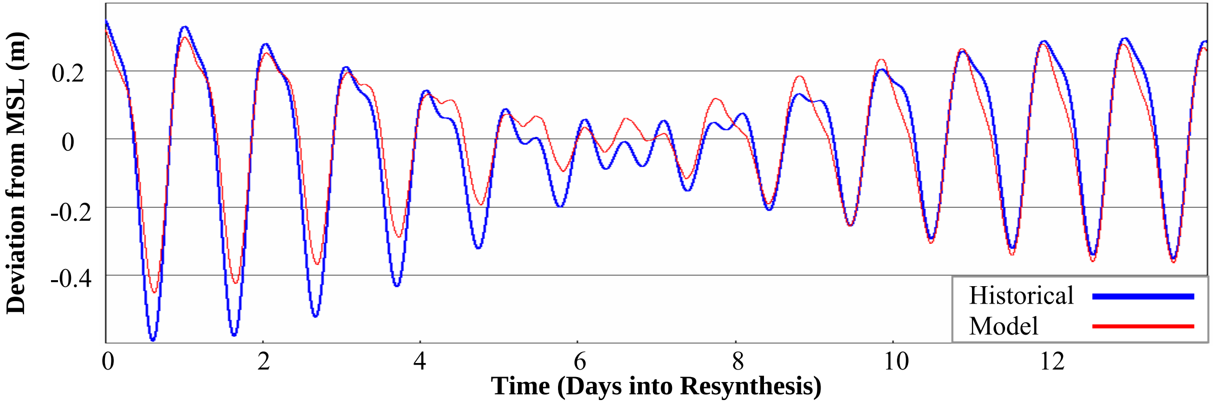

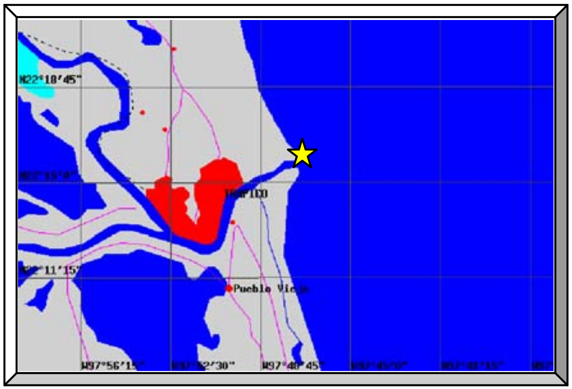

St. 153: Madero, Tampico Harbor, MT					
Observer			NOS		
Longitude			97.80 W		
Latitude			22.26 N		
Simulation Results					
	333K	95K	60K	53K	48K
Ph [º]	3.8	4.0	3.3	3.4	3.8
R^2 [-]	0.95	0.94	0.95	0.95	0.94

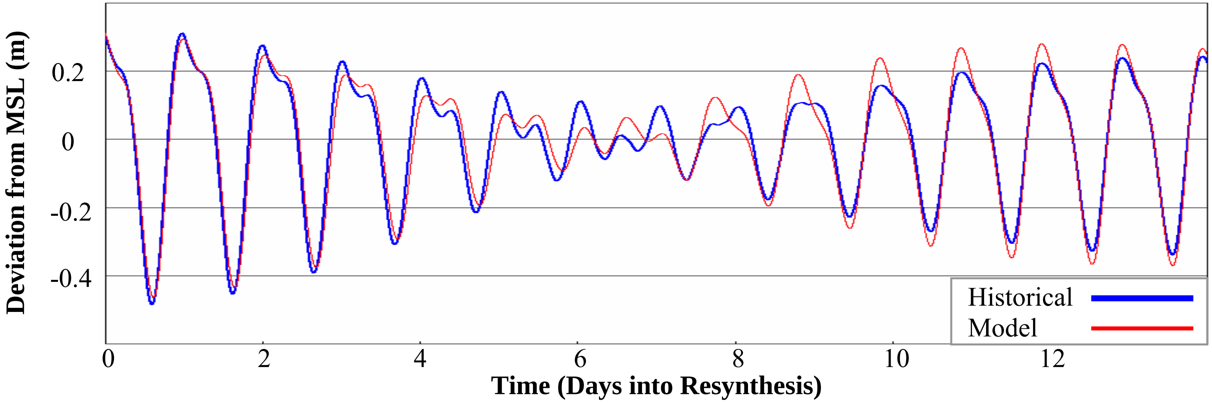

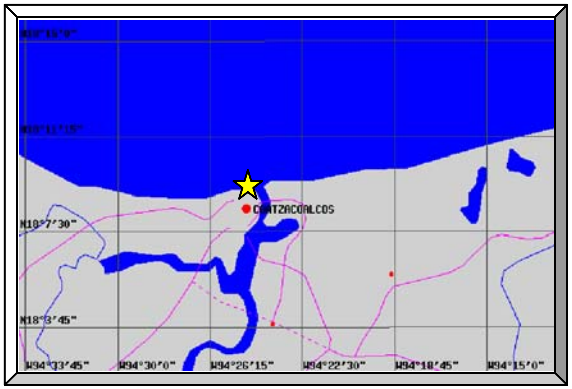

St. 155: Coatracoalcos, Mexico					
Observer			IHO		
Longitude			94.41 W		
Latitude			18.15 N		
Simulation Results					
	333K	95K	60K	53K	48K
Ph [º]	9.9	7.7	7.7	6.3	9.8
R^2 [-]	0.91	0.92	0.91	0.92	0.91

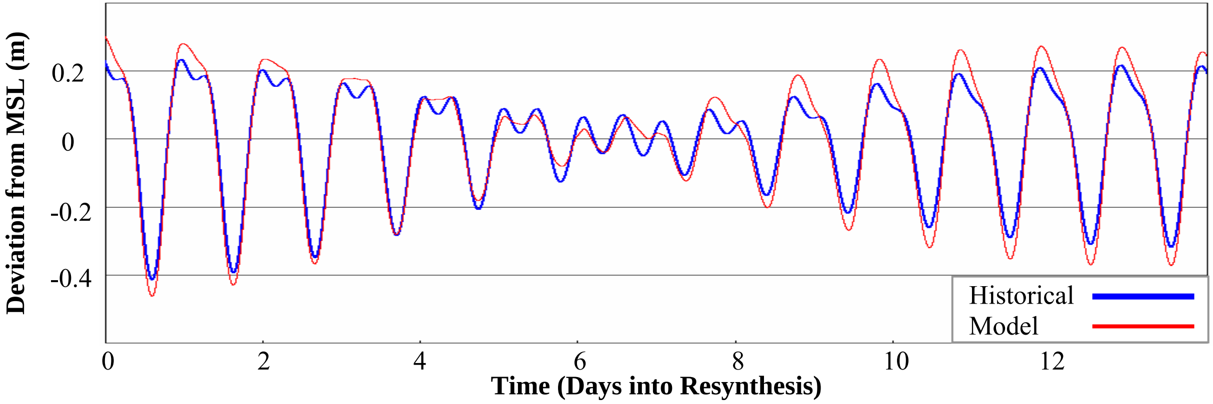

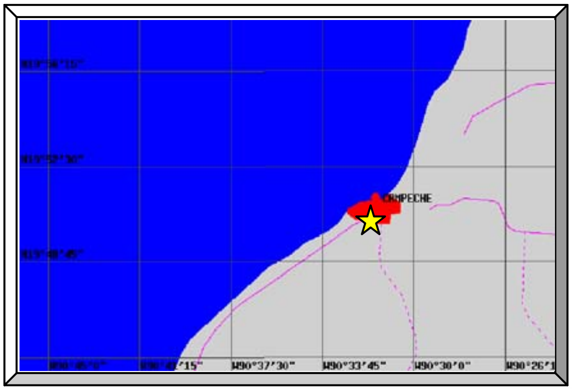

St. 156: Campeche, Mexico	
Observer	IHO
Longitude	90.53 W
Latitude	19.83 N

Simulation Results

	333K	95K	60K	53K	48K
Ph [º]	7.7	3.9	10.3	1.8	10.4
R^2 [-]	0.86	0.87	0.88	0.85	0.85

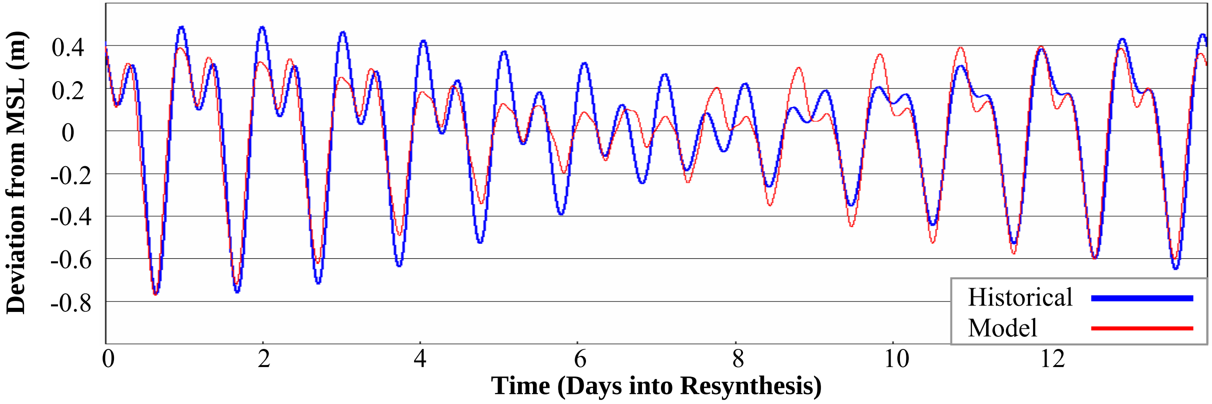

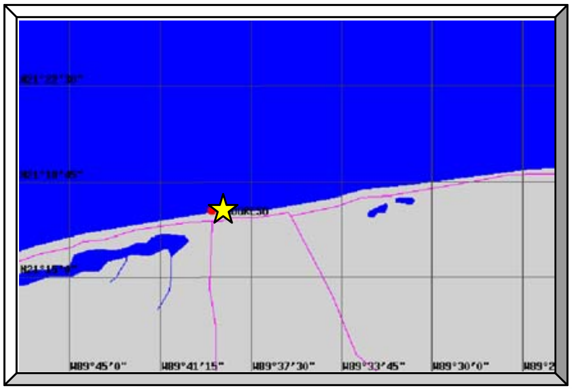

St. 157: Progreso, Yucatan, Mexico	
Observer	IHO
Longitude	89.65 W
Latitude	21.30 N

Simulation Results

	333K	95K	60K	53K	48K
Ph [º]	10.2	12.5	9.1	7.5	15.4
R^2 [-]	0.95	0.93	0.95	0.96	0.91

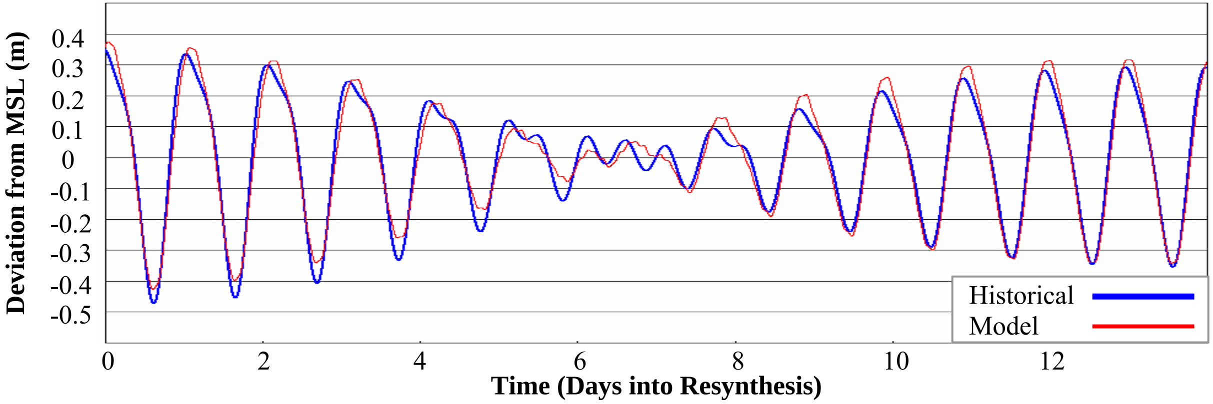

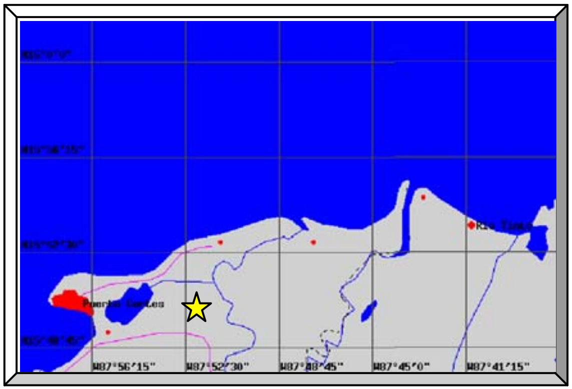

St. 158: Puerto Cortes					
Observer			NOS		
Longitude			87.87 W		
Latitude			15.84 N		
Simulation Results					
	333K	95K	60K	53K	48K
Ph [°]	27.2	30.5	27.4	29.2	20.4
R^2 [-]	0.90	0.89	0.90	0.90	0.89

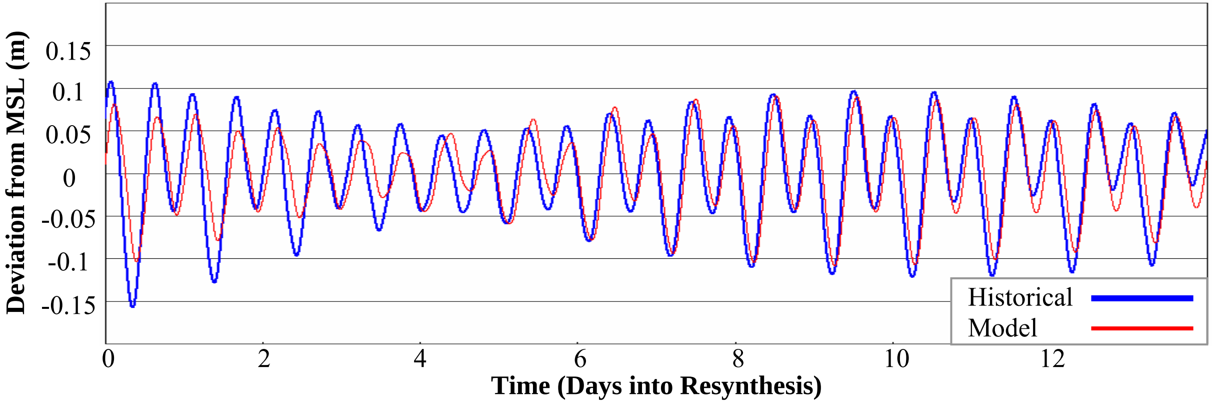

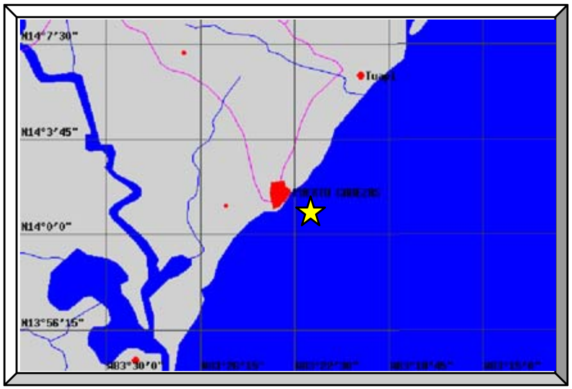

St. 159: Puerto Cabezas, Nicaragua					
Observer			IHO		
Longitude			83.37 W		
Latitude			14.02 N		
Simulation Results					
	333K	95K	60K	53K	48K
Ph [°]	12.2	15.9	13.6	13.6	13.9
R^2 [-]	0.80	0.77	0.79	0.80	0.79

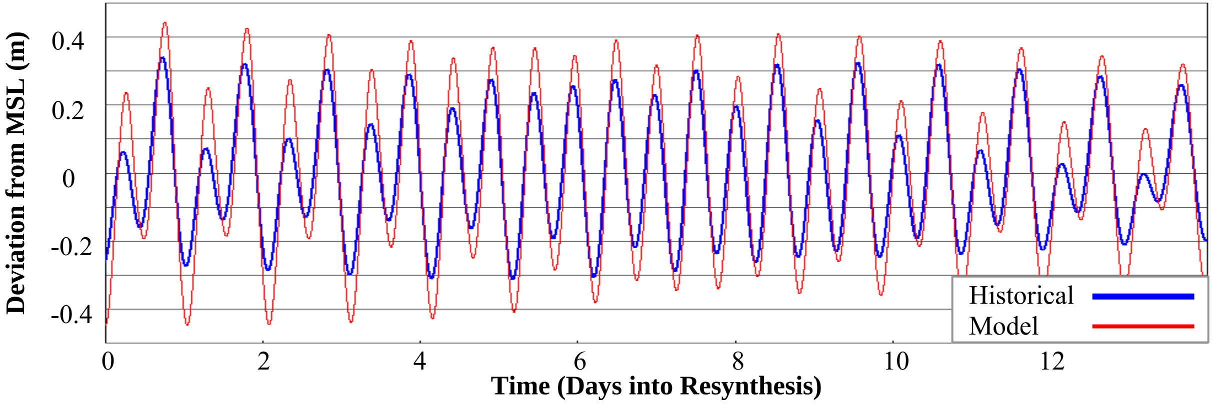

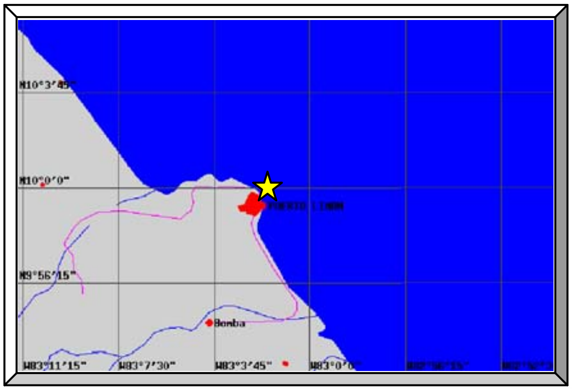

St. 160: Puerto Limon, Costa Rica					
Observer			IHO		
Longitude			83.03 W		
Latitude			10.00 N		
Simulation Results					
	333K	95K	60K	53K	48K
Ph [º]	2.2	1.7	2.4	1.9	1.7
R^2 [-]	0.94	0.93	0.94	0.93	0.93

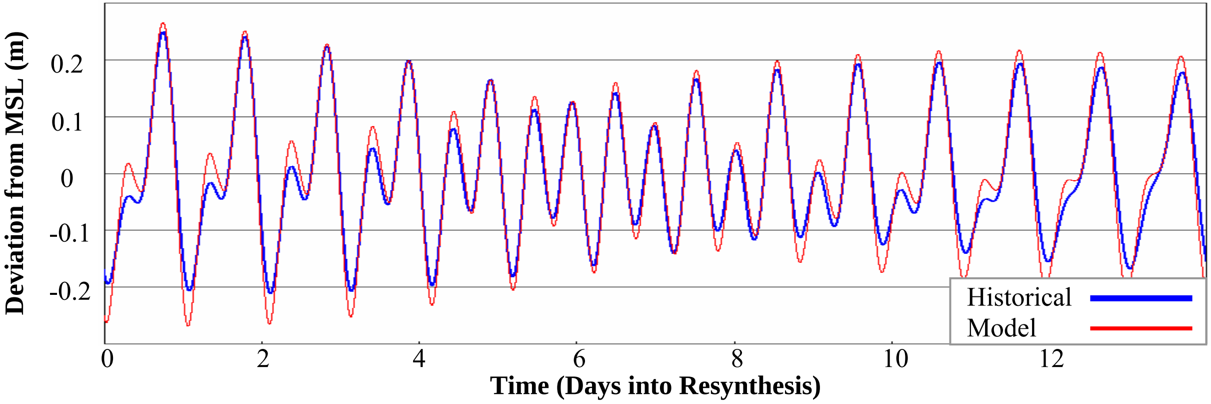

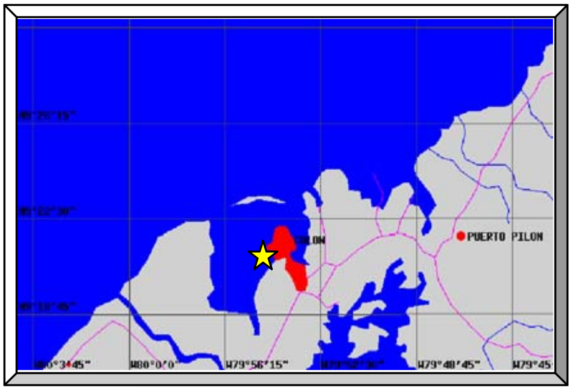

St. 161: Cristobal, Panama					
Observer			IHO		
Longitude			79.92 W		
Latitude			9.35 N		
Simulation Results					
	333K	95K	60K	53K	48K
Ph [º]	3.2	3.2	2.9	3.2	3.3
R^2 [-]	0.94	0.94	0.94	0.94	0.93

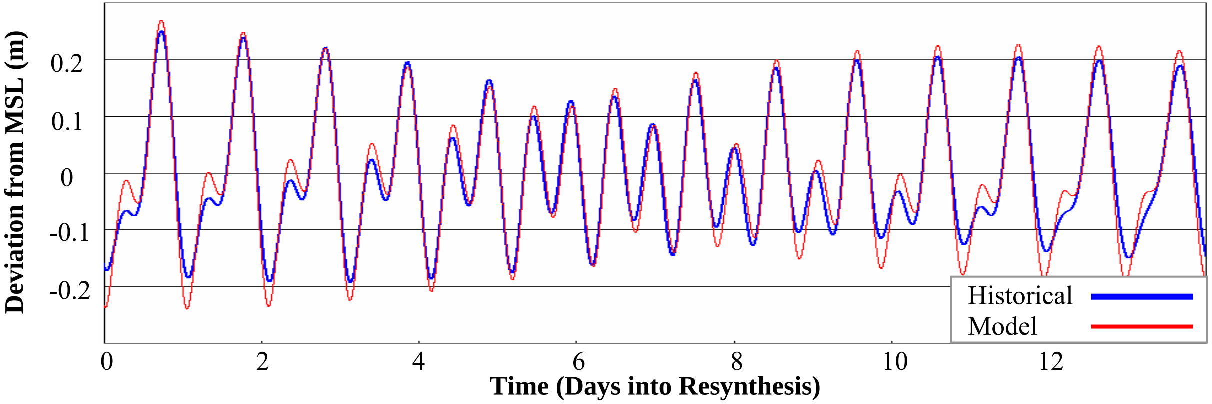

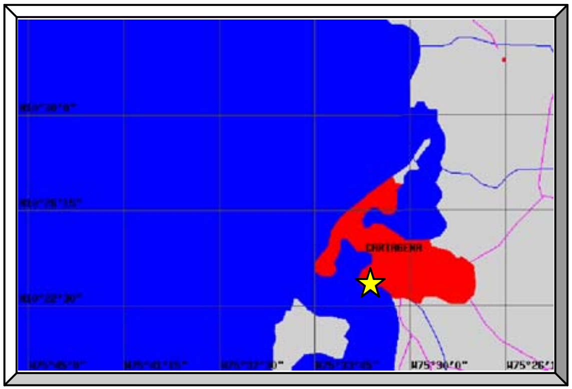

St. 162: Cartagena, Colombia					
Observer	IHO				
Longitude	75.53 W				
Latitude	10.38 N				
Simulation Results					
	333K	95K	60K	53K	48K
Ph [º]	17.5	17.0	17.0	16.9	17.0
R^2 [-]	0.92	0.92	0.92	0.92	0.92

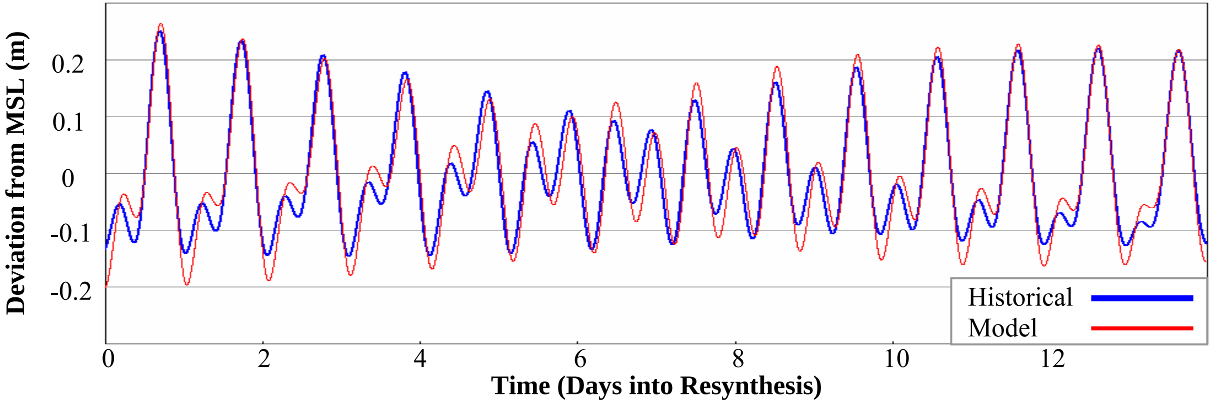

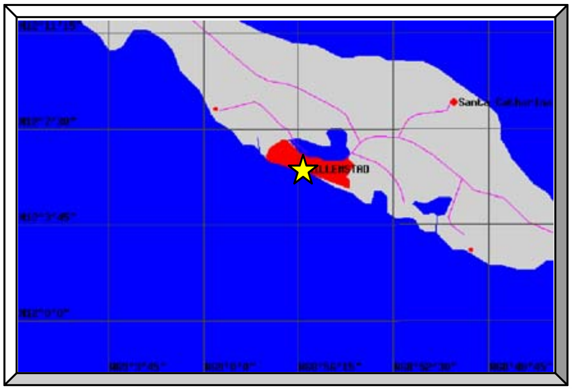

St. 163: Willemstad, Curacao Antilles					
Observer	IHO				
Longitude	68.93 W				
Latitude	12.10 N				
Simulation Results					
	333K	95K	60K	53K	48K
Ph [º]	1.2	0.8	1.2	1.0	1.1
R^2 [-]	0.93	0.93	0.93	0.93	0.93

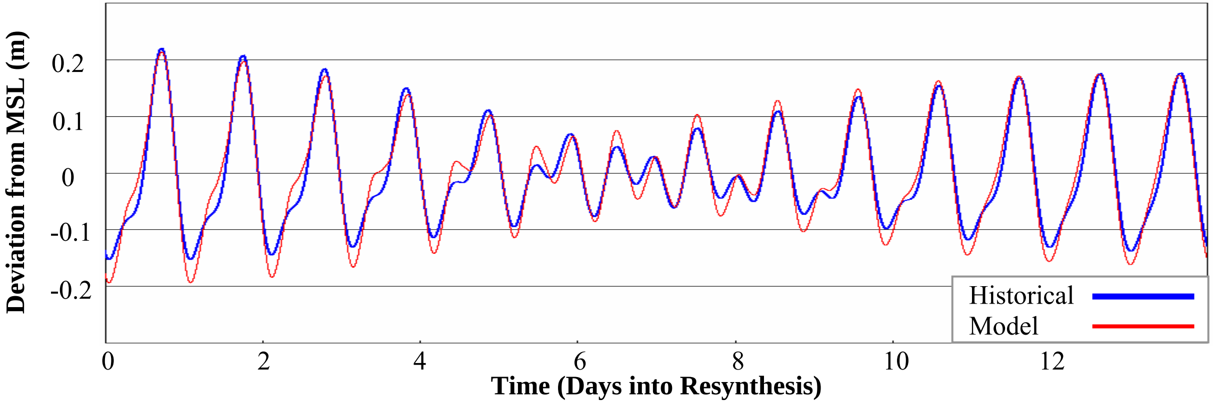

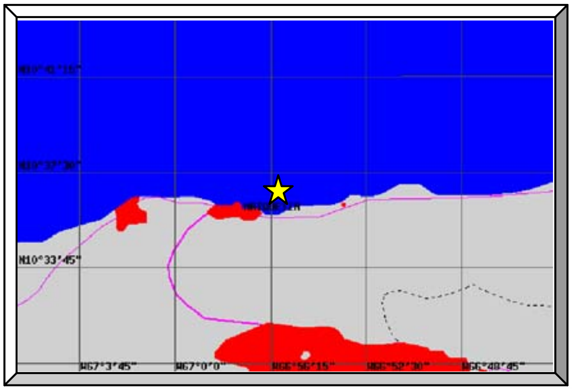

St. 164: La Guaira, Venezuela					
Observer	IHO				
Longitude	66.93 W				
Latitude	10.62 N				
Simulation Results					
	333K	95K	60K	53K	48K
Ph [º]	3.8	3.1	4.0	4.1	4.1
R^2 [-]	0.95	0.95	0.95	0.95	0.95

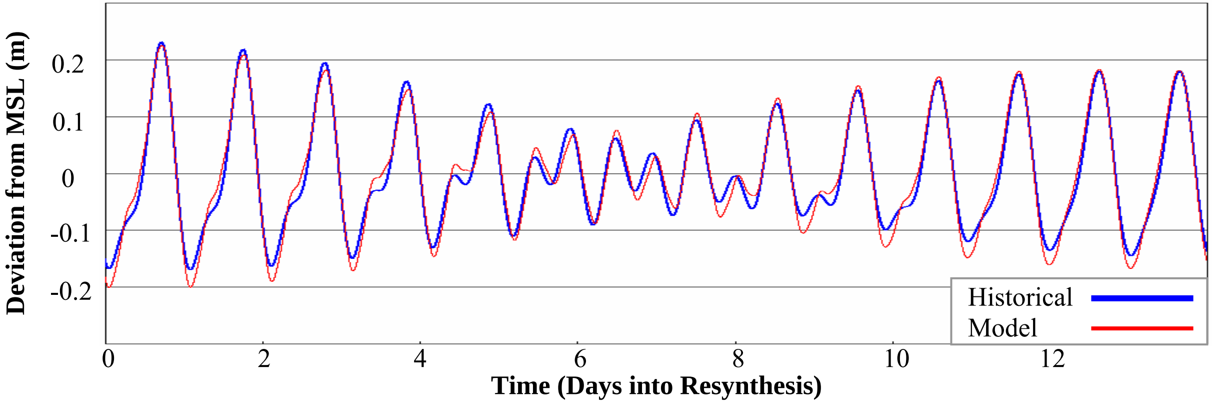

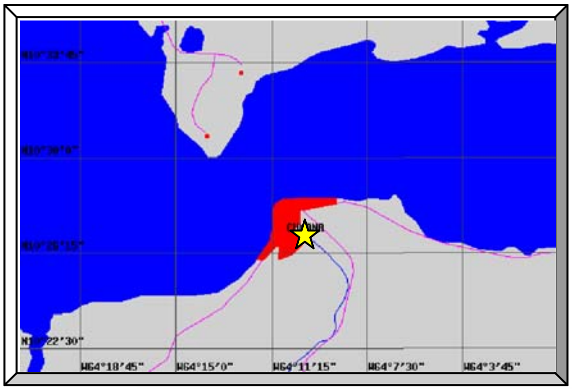

St. 165: Cumana, Venezuela					
Observer	IHO				
Longitude	64.17 W				
Latitude	10.45 N				
Simulation Results					
	333K	95K	60K	53K	48K
Ph [º]	3.2	3.7	3.5	3.5	3.6
R^2 [-]	0.95	0.95	0.95	0.95	0.95

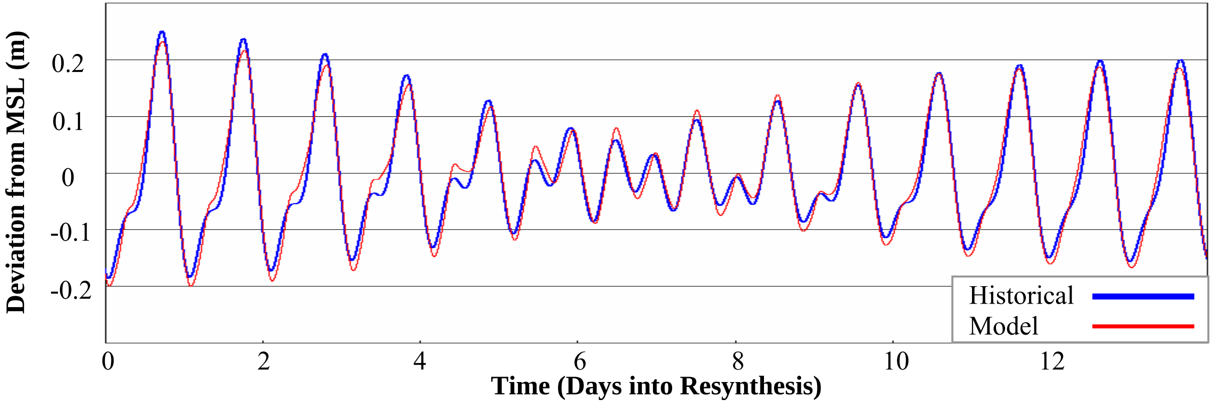

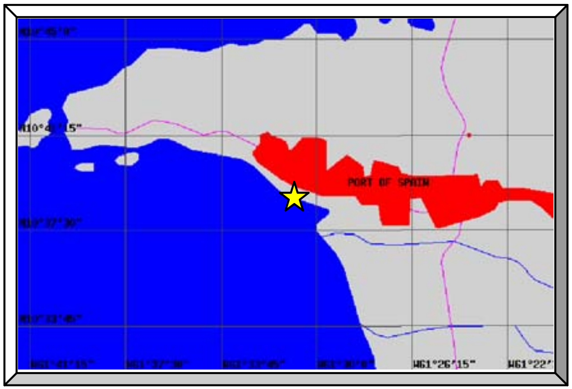

St. 166: Port of Spain Trinidad and Tobago					
Observer		IHO			
Longitude		61.52 W			
Latitude		10.65 N			
Simulation Results					
	333K	95K	60K	53K	48K
Ph [º]	20.8	11.7	21.9	17.9	17.6
R^2 [-]	0.93	0.92	0.93	0.93	0.94

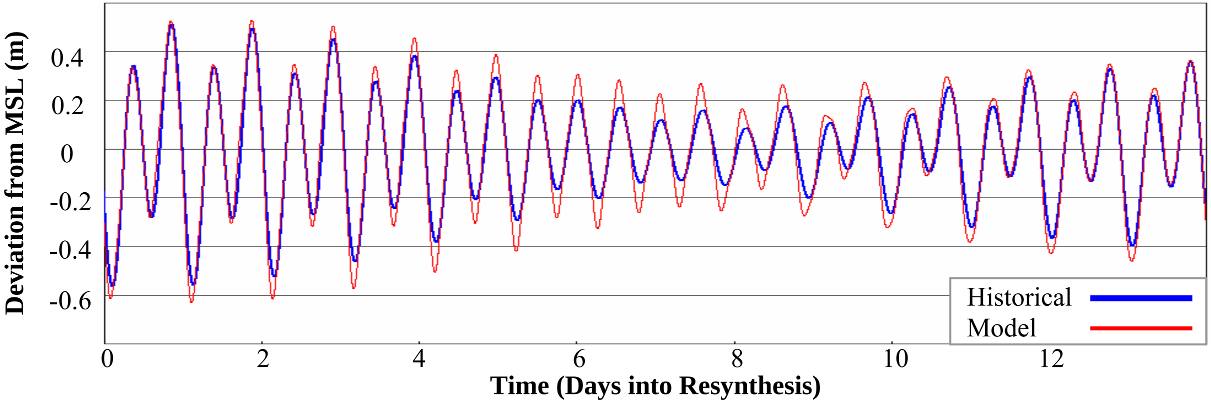

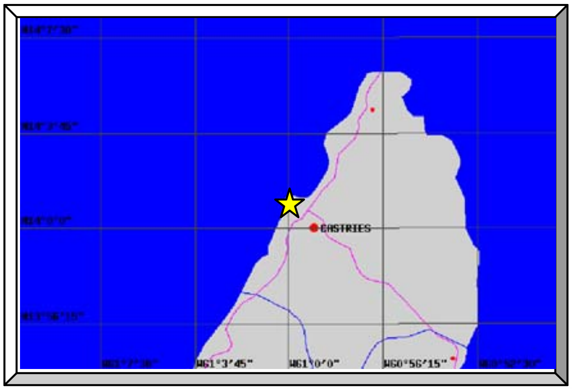

St. 167: Castries, St. Lucia, B.W.I.					
Observer		IHO			
Longitude		61.00 W			
Latitude		14.02 N			
Simulation Results					
	333K	95K	60K	53K	48K
Ph [º]	21.4	21.3	21.8	21.7	22.1
R^2 [-]	0.95	0.95	0.95	0.95	0.95

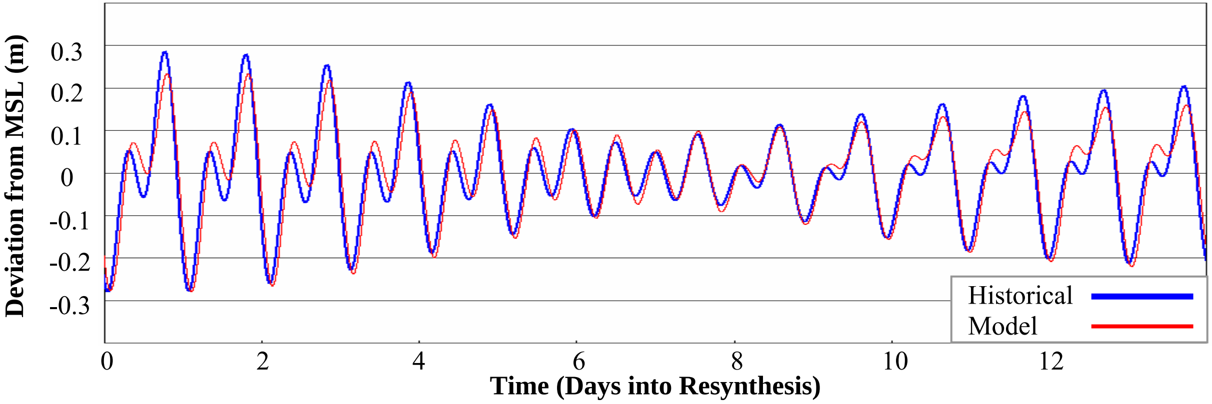

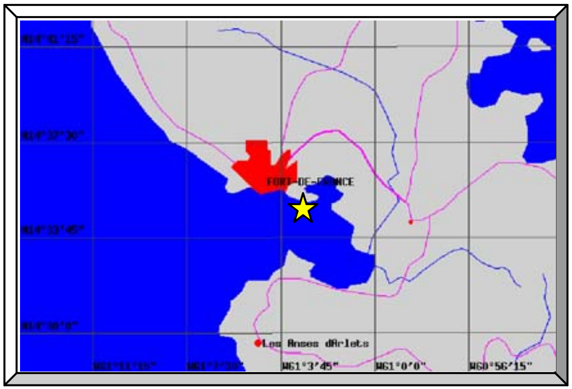

St. 168: Fort-de-France, Martinique					
Observer	IHO				
Longitude	61.05 W				
Latitude	14.58 N				
Simulation Results					
	333K	95K	60K	53K	48K
Ph [º]	18.3	17.4	18.0	10.7	17.8
R^2 [-]	0.83	0.86	0.83	0.87	0.84

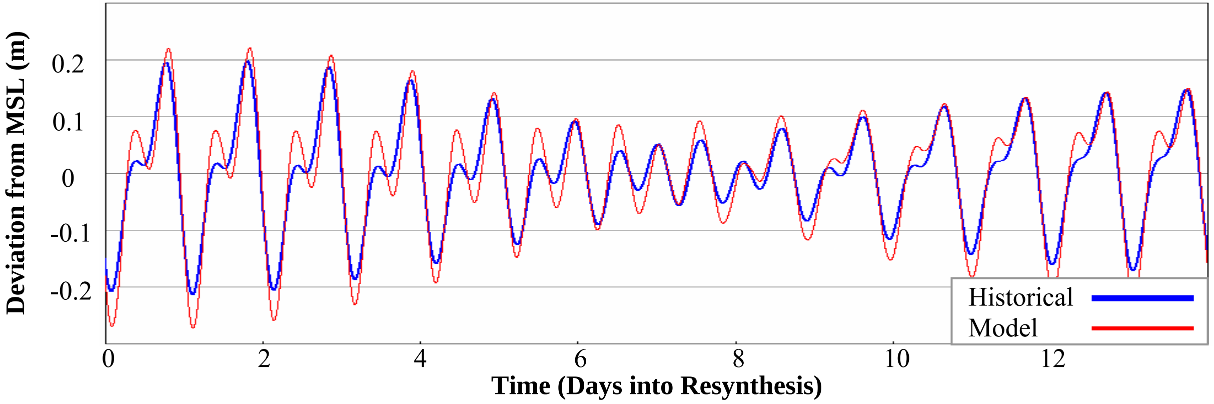

In the Ocean

St. 169: East Caribbean Sea					
Observer	IHO				
Longitude	64.88 W				
Latitude	16.53 N				
Simulation Results					
	333K	95K	60K	53K	48K
Ph [º]	2.8	0.3	2.6	0.8	2.9
R^2 [-]	0.97	0.96	0.96	0.95	0.97

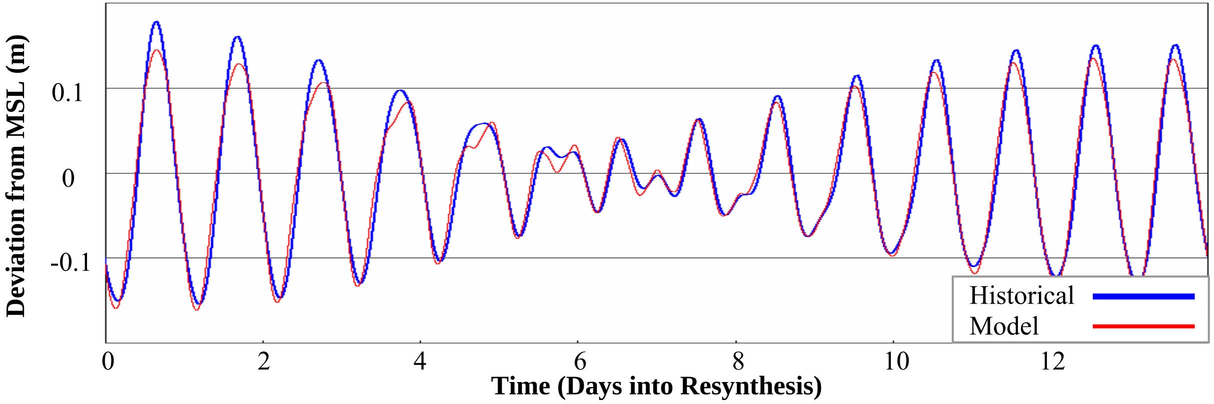

St. 170: Lime Tree Bay, St. Croix, VI					
Observer	NOS				
Longitude	64.75 W				
Latitude	17.70 N				
Simulation Results					
	333K	95K	60K	53K	48K
Ph [º]	14.6	14.2	15.1	14.5	14.5
R^2 [-]	0.65	0.65	0.65	0.65	0.65

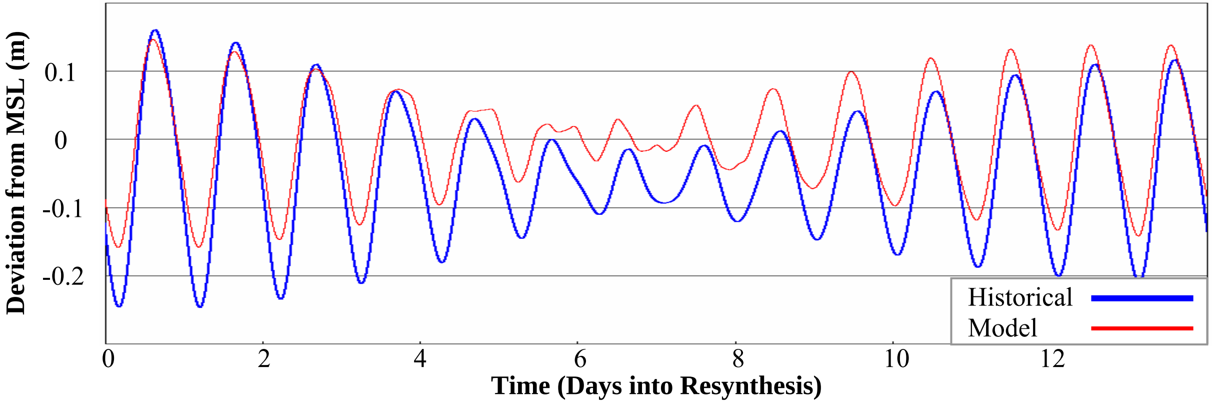

St. 171: Benner Bay					
Observer	NOS				
Longitude	64.87 W				
Latitude	18.32 N				
Simulation Results					
	333K	95K	60K	53K	48K
Ph [º]	8.2	10.0	7.3	13.9	14.3
R^2 [-]	0.94	0.94	0.94	0.91	0.90

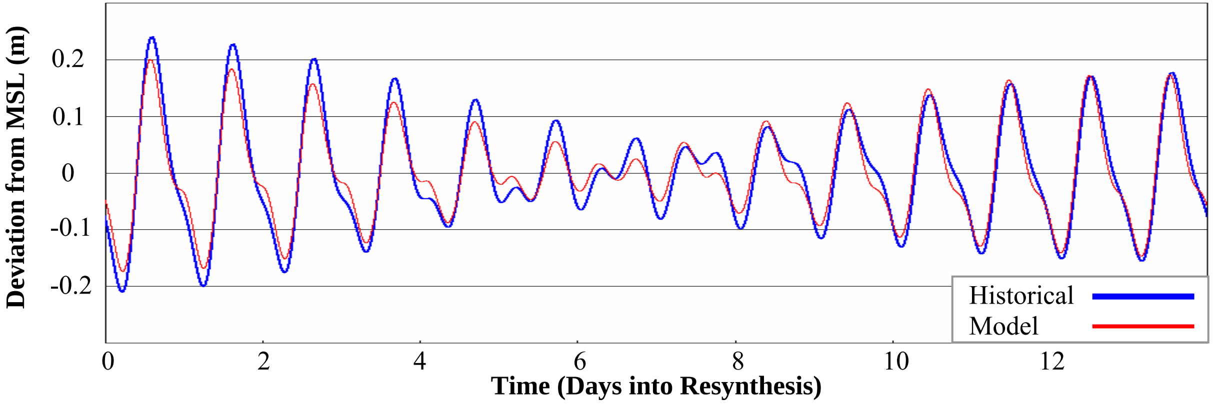

St. 172: Charlotte Amalie, St. Thomas, VI					
Observer			NOS		
Longitude			64.92 W		
Latitude			18.34 N		
Simulation Results					
	333K	95K	60K	53K	48K
Ph [º]	10.1	14.0	15.1	10.4	9.9
R^2 [-]	0.68	0.61	0.65	0.66	0.66

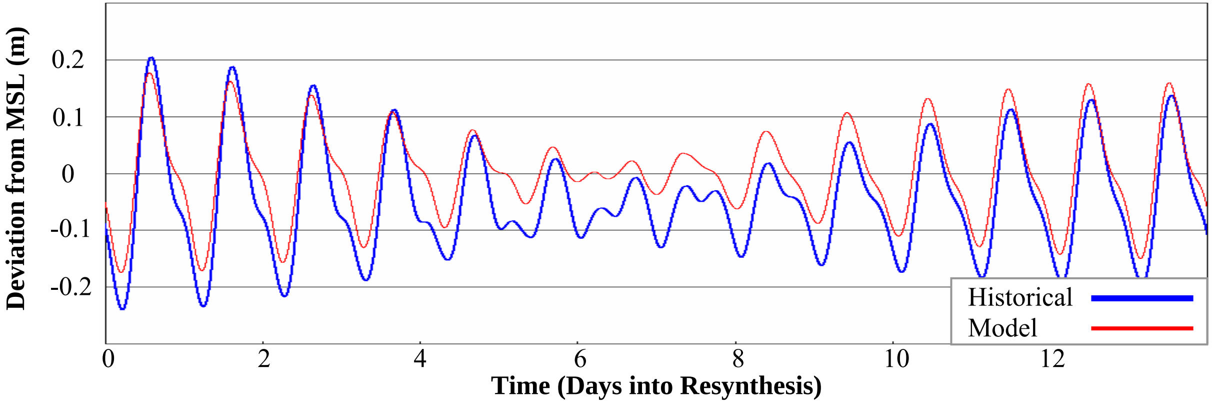

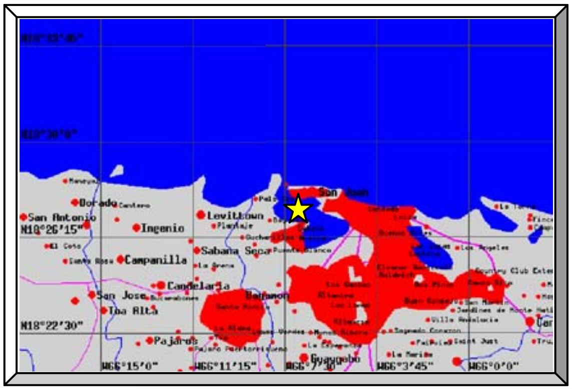

St. 173: San Juan, la Puntilla, San Juan Bay, PR					
Observer			NOS		
Longitude			66.12 W		
Latitude			18.46 N		
Simulation Results					
	333K	95K	60K	53K	48K
Ph [º]	13.9	14.0	14.1	14.0	14.5
R^2 [-]	0.90	0.89	0.90	0.90	0.90

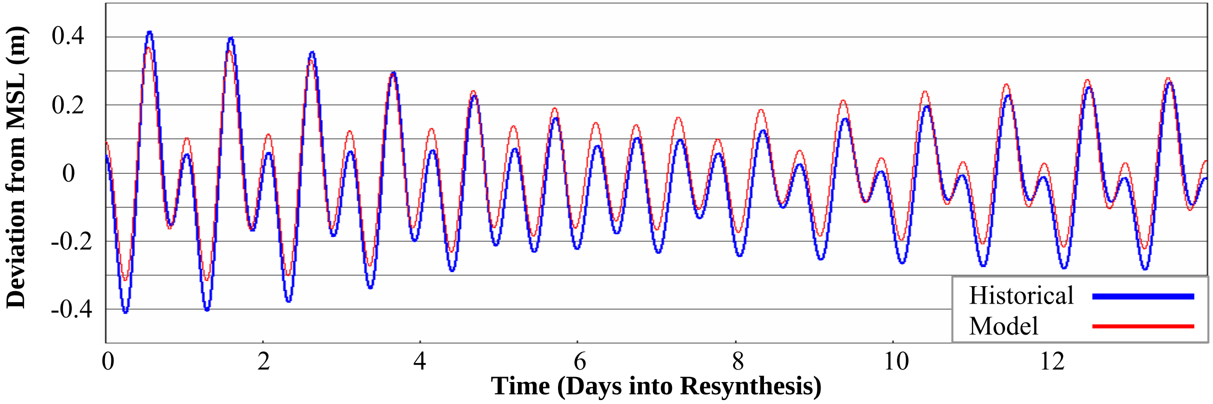

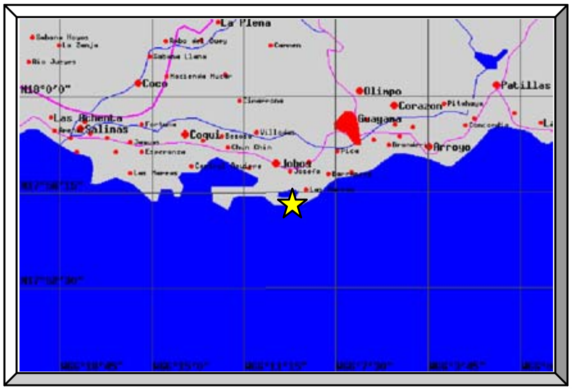

St. 174: Las Mareas, PR	
Observer	NOS
Longitude	66.16 W
Latitude	17.93 N

Simulation Results					
	333K	95K	60K	53K	48K
Ph [º]	13.0	13.0	12.6	12.7	12.8
R^2 [-]	0.93	0.93	0.93	0.93	0.93

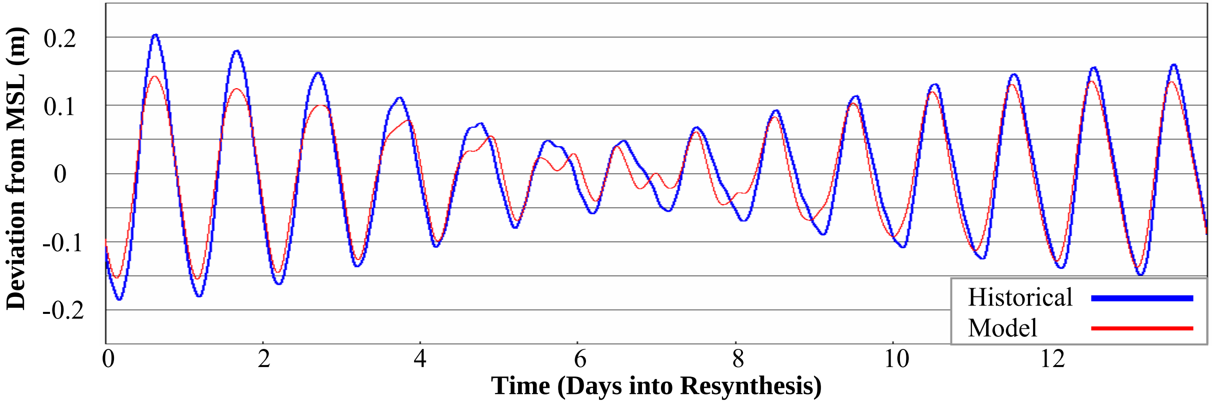

St. 175: Punta Guayanilla, PR	
Observer	NOS
Longitude	66.76 W
Latitude	17.98 N

Simulation Results					
	333K	95K	60K	53K	48K
Ph [º]	10.4	10.7	10.2	10.4	10.3
R^2 [-]	0.58	0.59	0.58	0.58	0.58

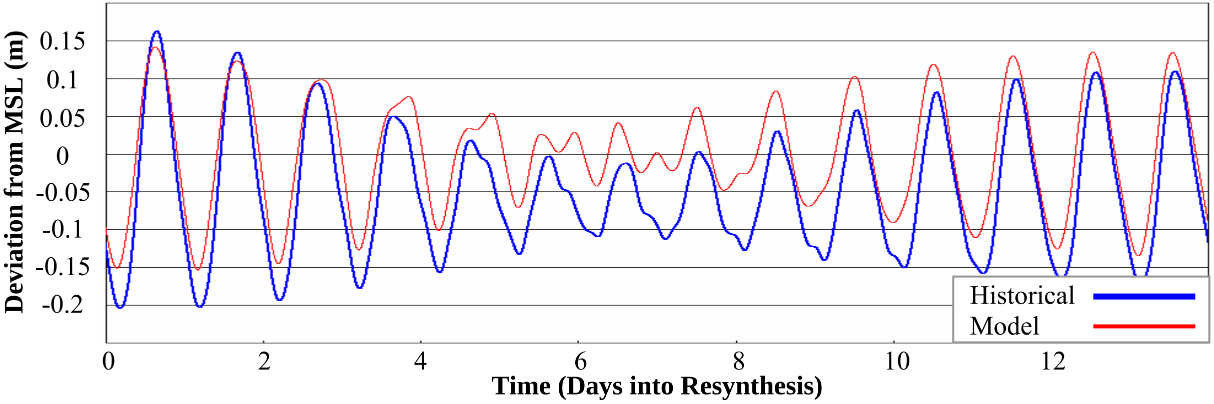

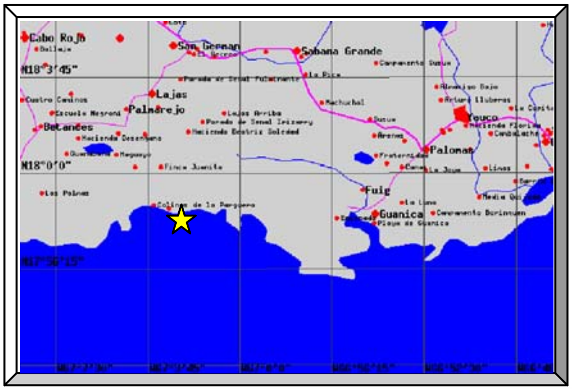

St. 176: Magueyes Island, Caribbean Sea, PR					
Observer			NOS		
Longitude			67.05 W		
Latitude			17.97 N		
Simulation Results					
	333K	95K	60K	53K	48K
Ph [°]	9.8	8.8	8.8	9.5	9.5
R^2 [-]	0.61	0.62	0.61	0.61	0.61

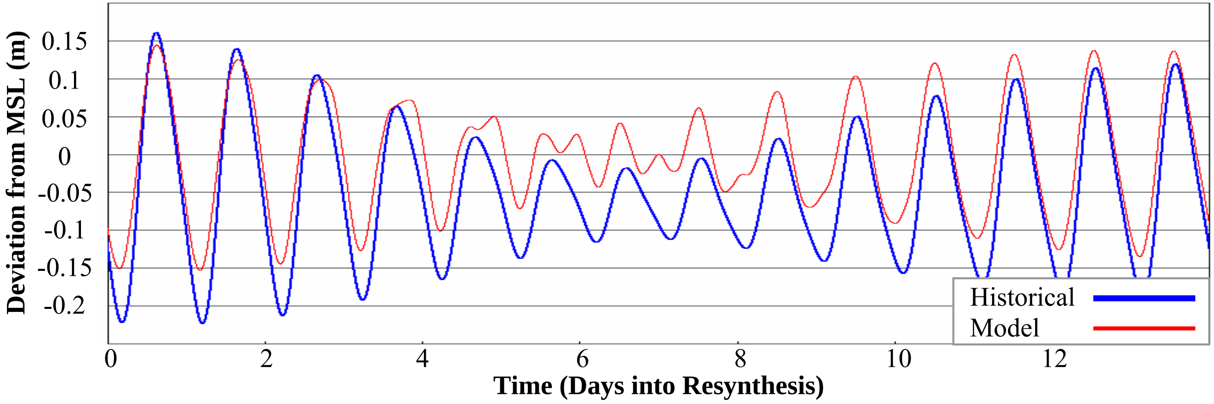

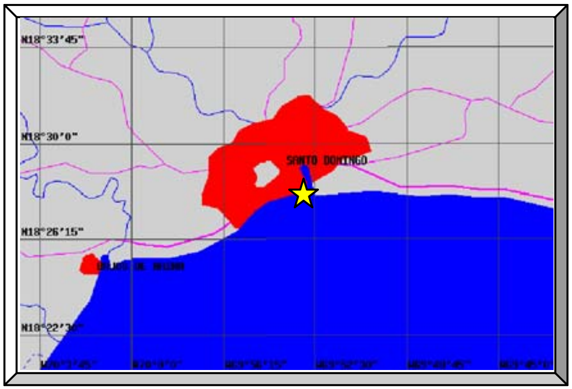

St. 177: Ciudad, Dominican Republic					
Observer			IHO		
Longitude			69.88 W		
Latitude			18.47 N		
Simulation Results					
	333K	95K	60K	53K	48K
Ph [°]	5.9	6.7	5.9	6.4	6.3
R^2 [-]	0.93	0.93	0.93	0.93	0.93

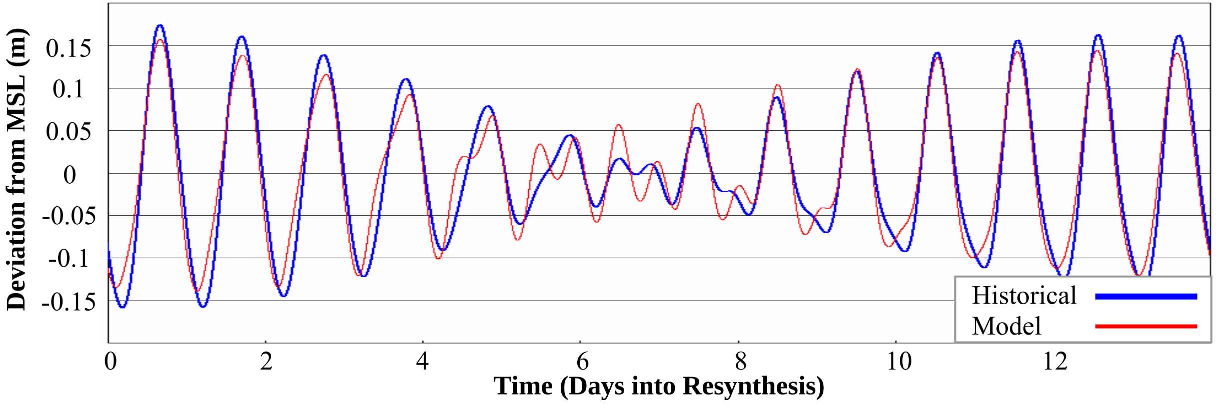

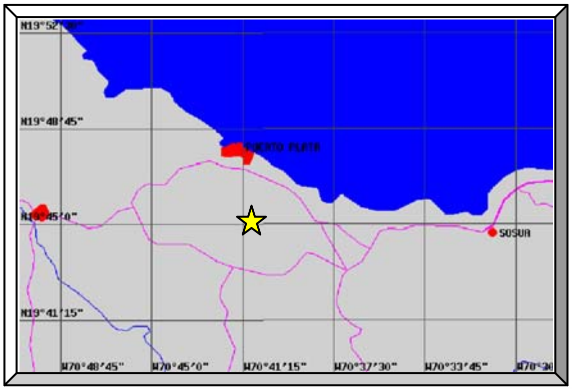

St. 178: Puerto Plato, Dominican Republic	
Observer	IHO
Longitude	70.68 W
Latitude	19.75 N

Simulation Results

	333K	95K	60K	53K	48K
Ph [º]	5.9	5.9	5.8	5.7	6.3
R^2 [-]	1.00	1.00	1.00	1.00	1.00

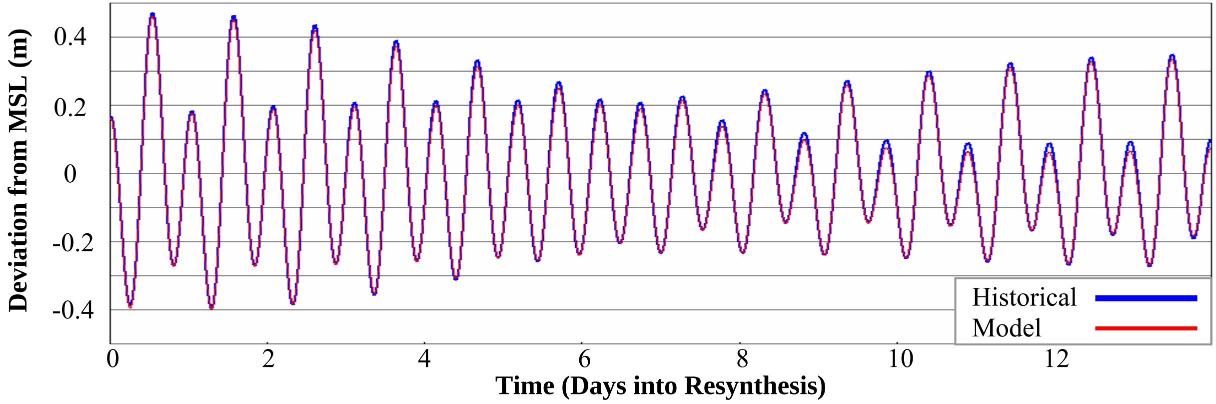

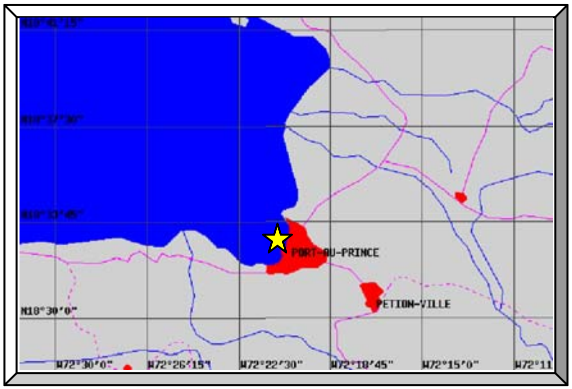

St. 179: Port-au-Prince, Haiti	
Observer	IHO
Longitude	72.35 W
Latitude	18.55 N

Simulation Results

	333K	95K	60K	53K	48K
Ph [º]	14.7	14.5	15.0	15.3	14.5
R^2 [-]	0.97	0.96	0.96	0.96	0.97

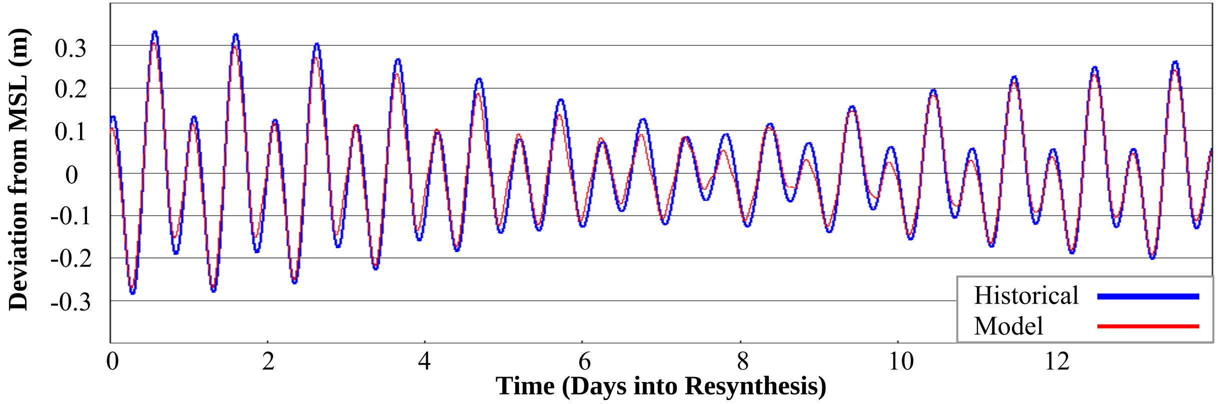

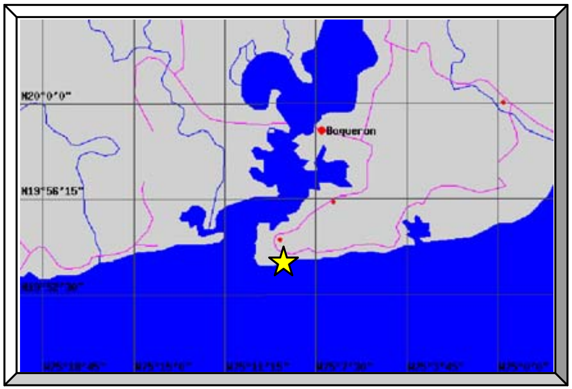

St. 180: Guantanomo Bay, Cuba					
Observer		IHO			
Longitude		75.15 W			
Latitude		19.90 N			
Simulation Results					
	333K	95K	60K	53K	48K
Ph [º]	0.4	1.0	0.2	0.7	0.1
R^2 [-]	0.86	0.85	0.86	0.85	0.85

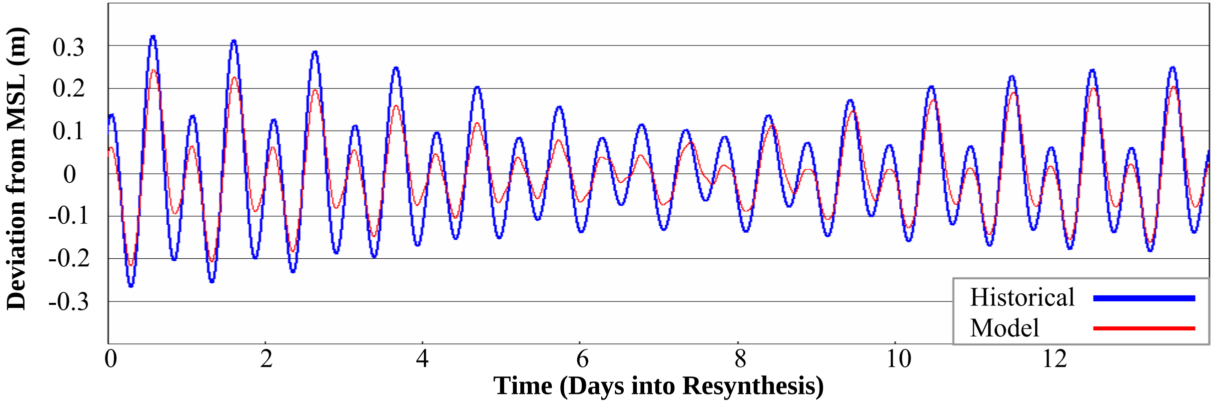

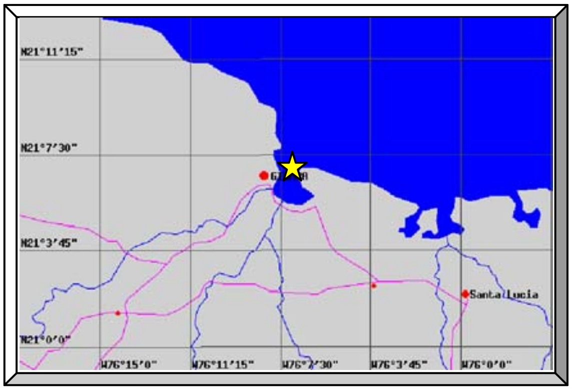

St. 181: Gibara, Cuba					
Observer		IHO			
Longitude		76.12 W			
Latitude		21.10 N			
Simulation Results					
	333K	95K	60K	53K	48K
Ph [º]	8.6	8.8	9.2	8.5	9.3
R^2 [-]	0.99	0.99	0.99	0.99	0.99

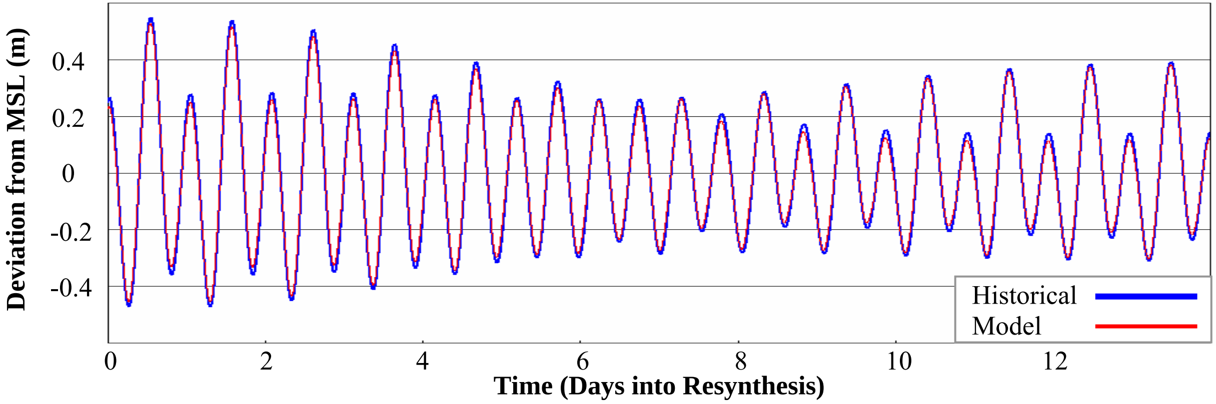

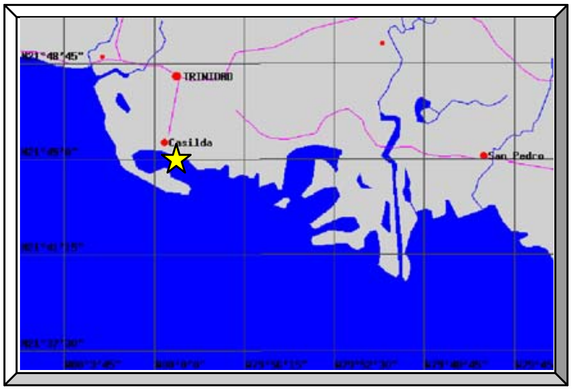

St. 182: Casilda, Cuba					
Observer	IHO				
Longitude	79.98 W				
Latitude	21.75 N				
Simulation Results					
	333K	95K	60K	53K	48K
Ph [º]	16.3	19.4	16.6	18.6	18.1
R^2 [-]	0.87	0.86	0.87	0.87	0.87

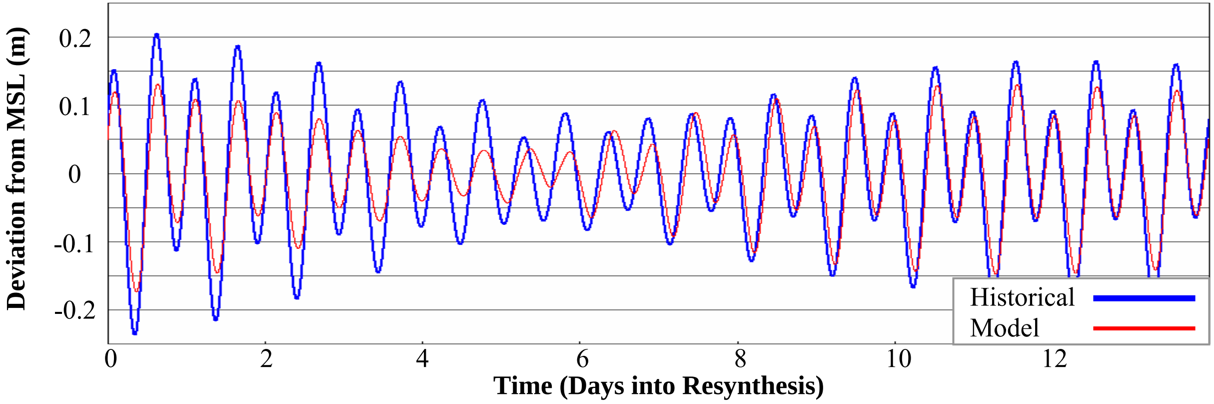

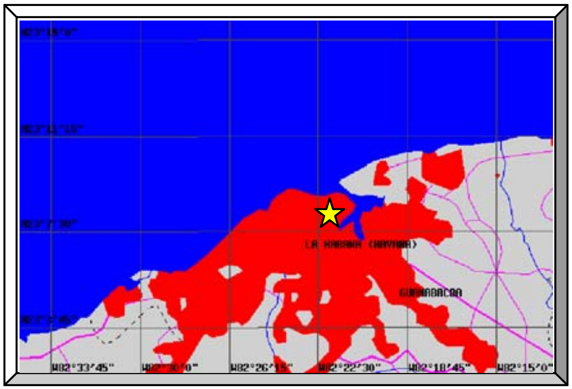

St. 183: Havana, Cuba					
Observer	IHO				
Longitude	82.37 W				
Latitude	23.13 N				
Simulation Results					
	333K	95K	60K	53K	48K
Ph [º]	1.4	0.5	0.7	0.5	0.7
R^2 [-]	0.98	0.98	0.98	0.98	0.98

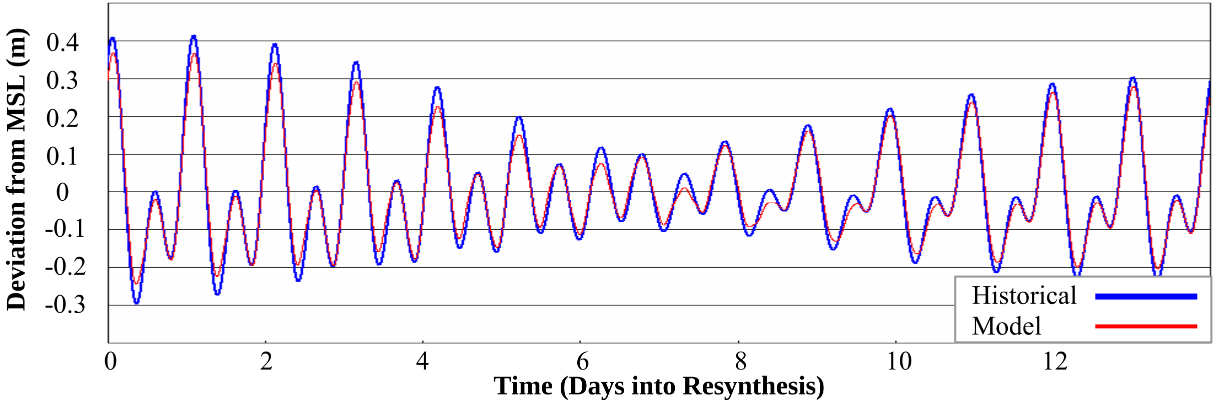

St. 184: Settlement Point, Grand Bahamas, BA					
Observer			NOS		
Longitude			79.00 W		
Latitude			26.71 N		
Simulation Results					
	333K	95K	60K	53K	48K
Ph [º]	7.6	8.1	8.3	7.8	8.2
R^2 [-]	0.96	0.96	0.96	0.96	0.96

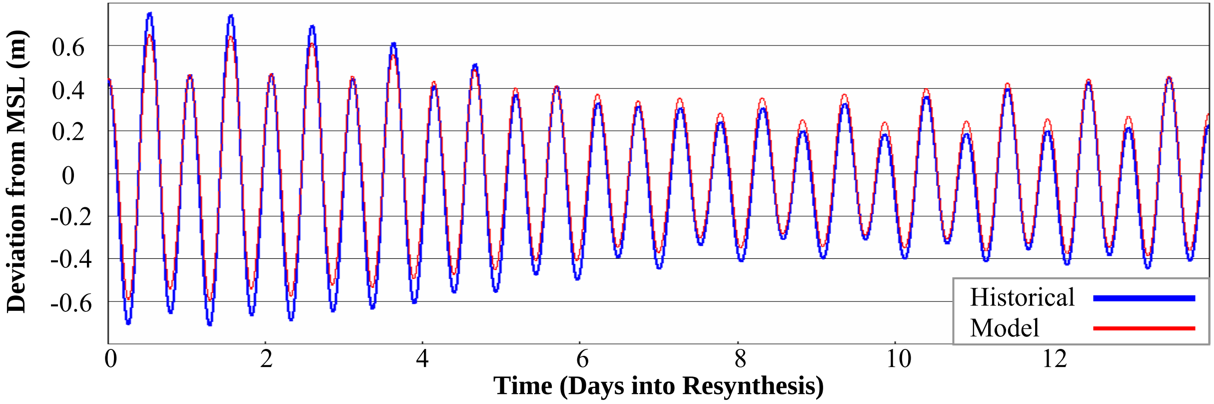

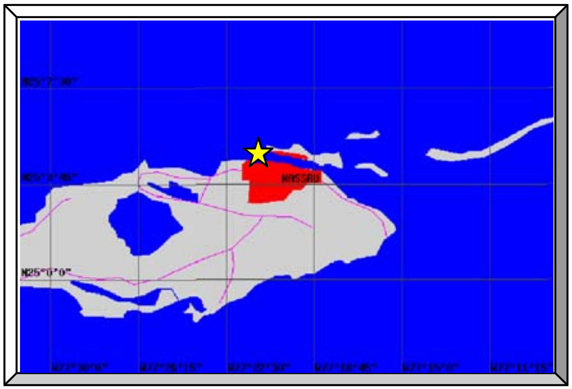

St. 185: Nassau, Bahamas					
Observer			IHO		
Longitude			77.35 W		
Latitude			25.08 N		
Simulation Results					
	333K	95K	60K	53K	48K
Ph [º]	7.0	7.0	7.4	6.7	7.7
R^2 [-]	0.99	0.99	0.99	0.99	0.99

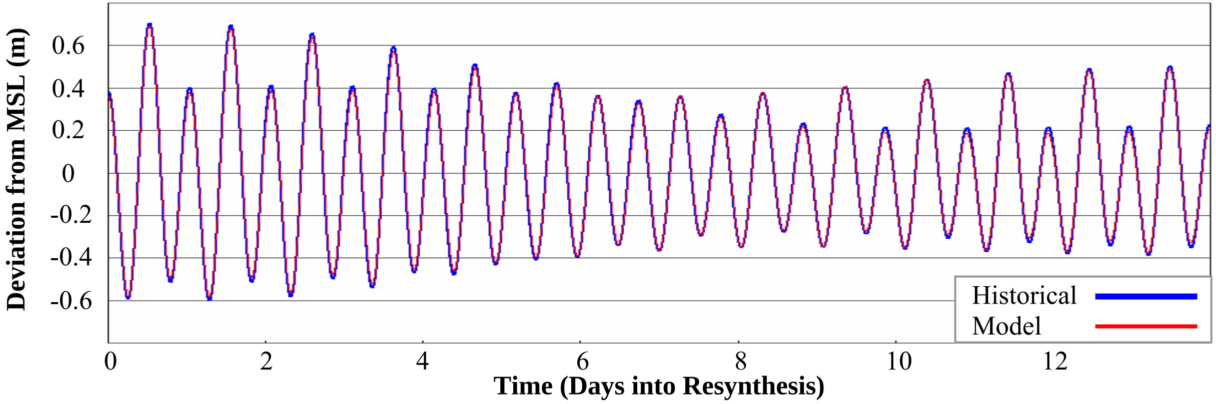

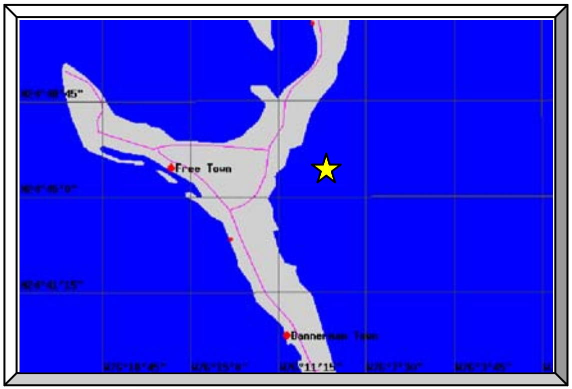

St. 186: Eleuthera, Bahamas	
Observer	IHO
Longitude	76.15 W
Latitude	24.77 N

Simulation Results					
	333K	95K	60K	53K	48K
Ph [º]	18.9	19.2	19.1	19.1	19.5
R^2 [-]	1.00	1.00	1.00	1.00	1.00

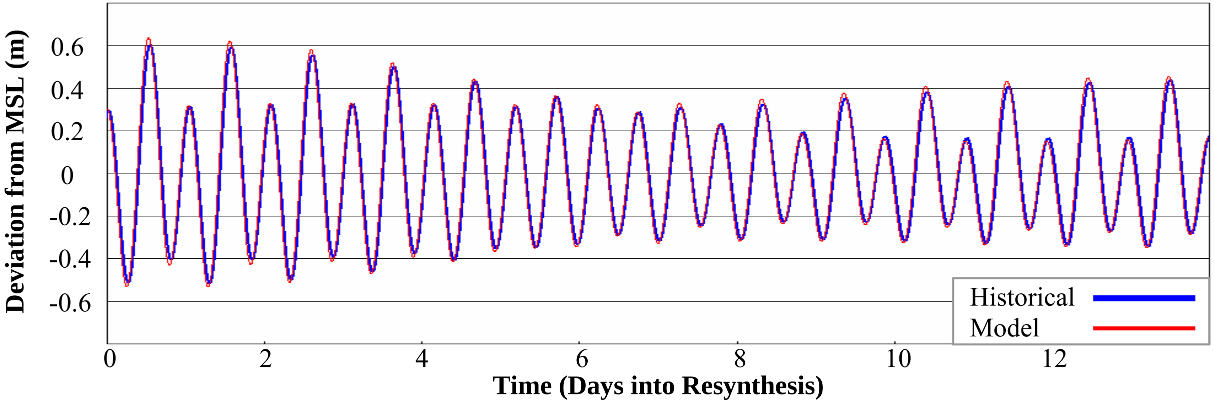

In the Ocean

St. 187: Atlantic Ocean	
Observer	IHO
Longitude	70.90 W
Latitude	40.30 N

Simulation Results					
	333K	95K	60K	53K	48K
Ph [º]	3.1	3.4	4.1	3.5	4.6
R^2 [-]	1.00	0.99	1.00	1.00	1.00

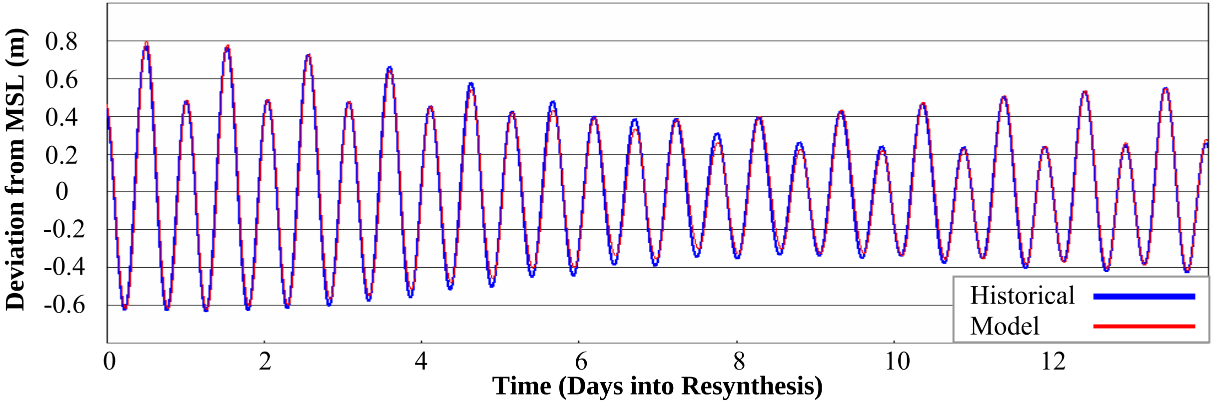

In the Ocean

<table>
<tr><th colspan="6">St. 188: Atlantic Ocean</th></tr>
<tr><td colspan="3">Observer</td><td colspan="3">IHO</td></tr>
<tr><td colspan="3">Longitude</td><td colspan="3">71.37 W</td></tr>
<tr><td colspan="3">Latitude</td><td colspan="3">39.17 N</td></tr>
<tr><td colspan="6">Simulation Results</td></tr>
<tr><td></td><td>333K</td><td>95K</td><td>60K</td><td>53K</td><td>48K</td></tr>
<tr><td>*Ph* [º]</td><td>0.3</td><td>0.0</td><td>0.6</td><td>0.2</td><td>0.9</td></tr>
<tr><td>R^2 [-]</td><td>0.98</td><td>0.98</td><td>0.98</td><td>0.98</td><td>0.98</td></tr>
</table>

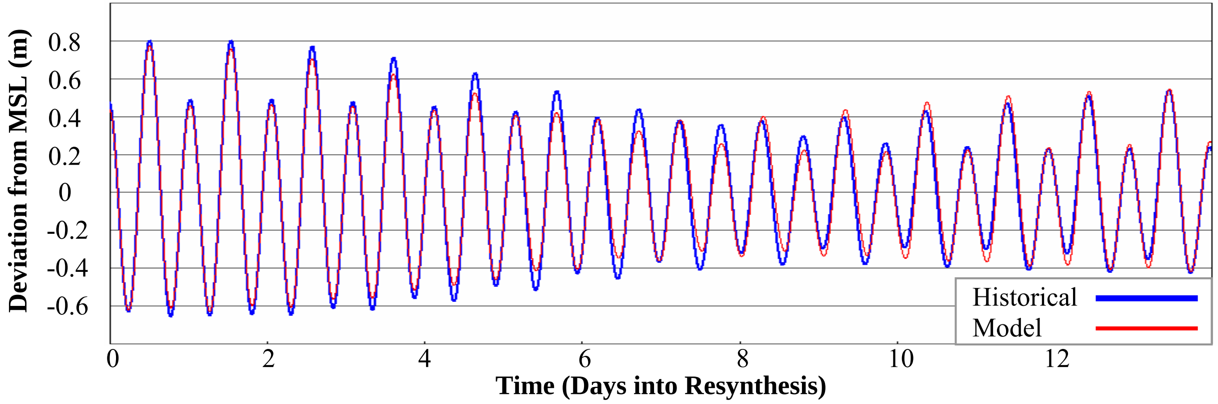

In the Ocean

<table>
<tr><th colspan="6">St. 189: Atlantic Ocean</th></tr>
<tr><td colspan="3">Observer</td><td colspan="3">IHO</td></tr>
<tr><td colspan="3">Longitude</td><td colspan="3">72.17 W</td></tr>
<tr><td colspan="3">Latitude</td><td colspan="3">39.22 N</td></tr>
<tr><td colspan="6">Simulation Results</td></tr>
<tr><td></td><td>333K</td><td>95K</td><td>60K</td><td>53K</td><td>48K</td></tr>
<tr><td>*Ph* [º]</td><td>5.8</td><td>6.1</td><td>6.8</td><td>6.0</td><td>7.1</td></tr>
<tr><td>R^2 [-]</td><td>1.00</td><td>1.00</td><td>1.00</td><td>1.00</td><td>1.00</td></tr>
</table>

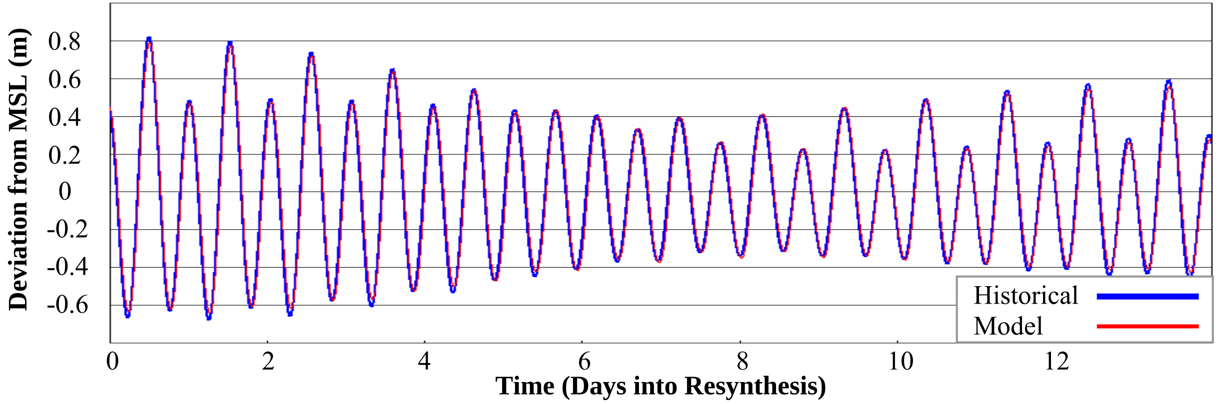

In the Ocean

St. 190: Atlantic Ocean					
Observer			IHO		
Longitude			73.08 W		
Latitude			37.37 N		
Simulation Results					
	333K	95K	60K	53K	48K
Ph [º]	12.0	12.1	12.7	11.8	12.9
R^2 [-]	1.00	1.00	1.00	1.00	1.00

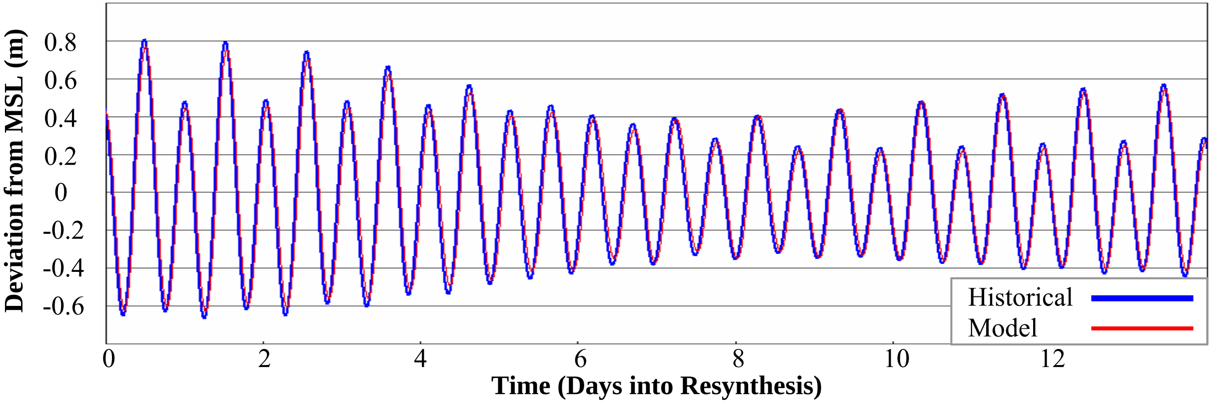

In the Ocean

St. 191: Atlantic Ocean					
Observer			IHO		
Longitude			75.62 W		
Latitude			32.68 N		
Simulation Results					
	333K	95K	60K	53K	48K
Ph [º]	0.2	0.2	0.4	0.5	0.3
R^2 [-]	0.97	0.97	0.97	0.97	0.97

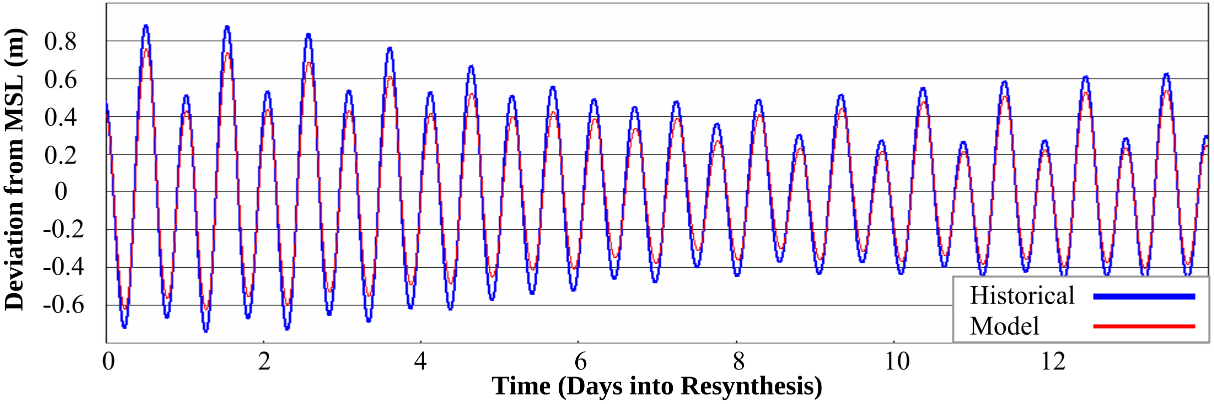

In the Ocean

St. 192: Atlantic Ocean	
Observer	IHO
Longitude	76.42 W
Latitude	30.43 N

Simulation Results

	333K	95K	60K	53K	48K
Ph [º]	3.0	3.4	3.1	3.5	3.2
R^2 [-]	0.99	0.99	0.99	0.99	0.99

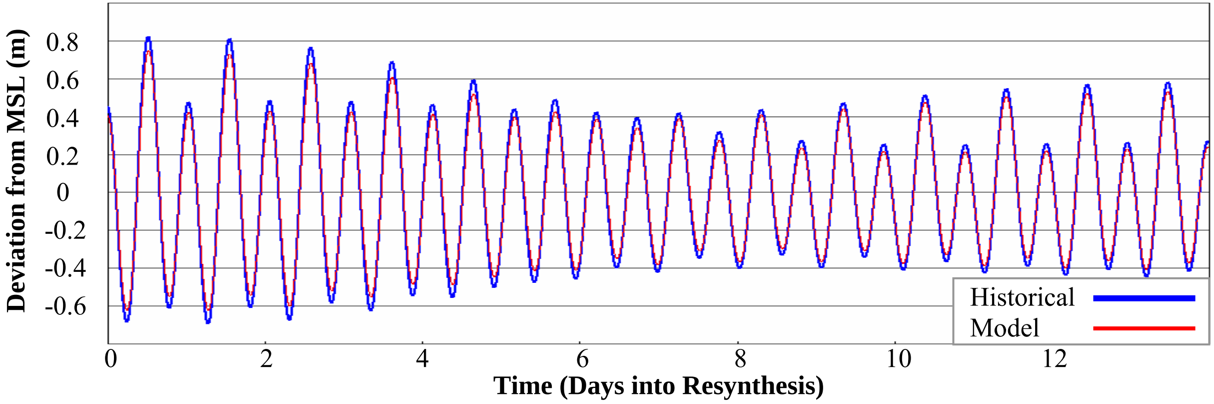

In the Ocean

St. 193: Atlantic Ocean	
Observer	IHO
Longitude	76.80 W
Latitude	28.45 N

Simulation Results

	333K	95K	60K	53K	48K
Ph [º]	4.8	5.2	5.0	5.2	5.1
R^2 [-]	0.99	0.99	0.99	0.99	0.99

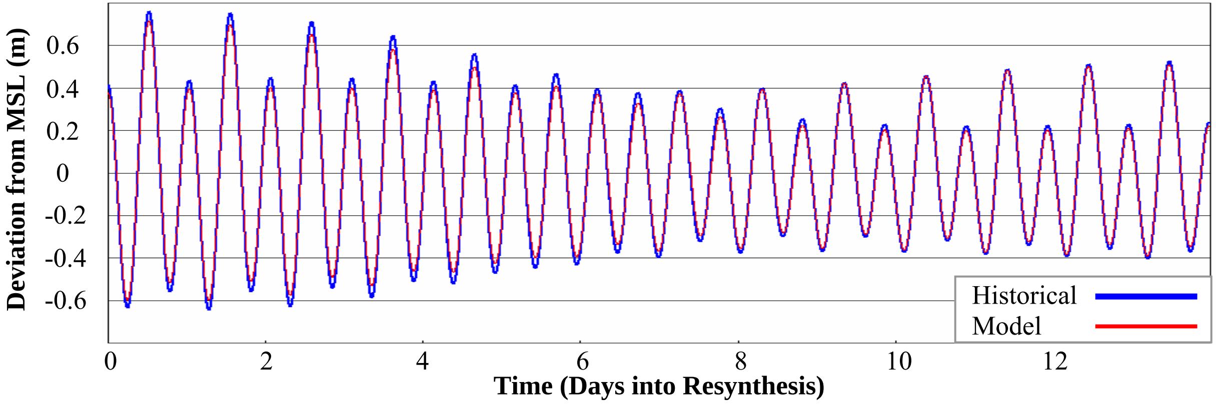

In the Ocean

St. 194: Atlantic Ocean					
Observer	IHO				
Longitude	76.78 W				
Latitude	28.02 N				
Simulation Results					
	333K	95K	60K	53K	48K
Ph [º]	11.2	11.7	11.4	11.6	11.7
R^2 [-]	0.99	0.99	0.99	0.99	0.99

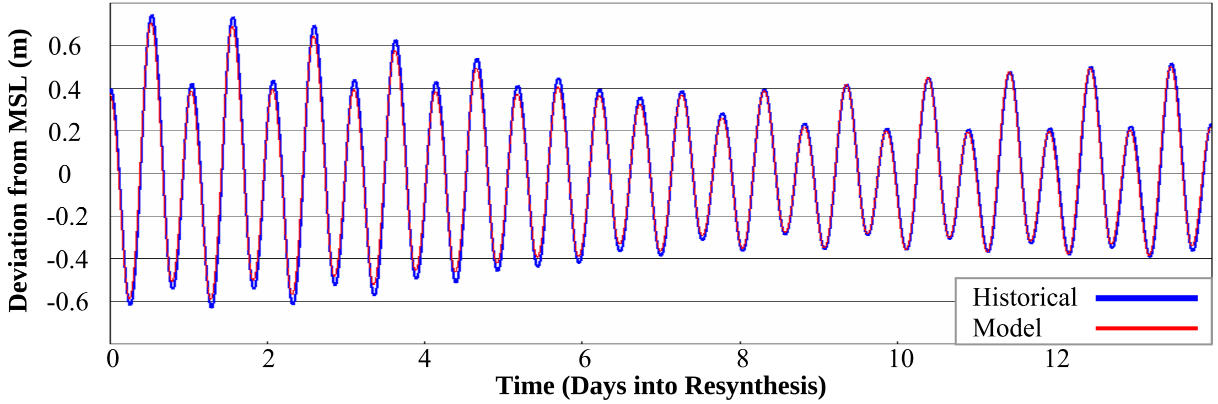

In the Ocean

St. 195: Atlantic Ocean					
Observer	IHO				
Longitude	69.33 W				
Latitude	26.47 N				
Simulation Results					
	333K	95K	60K	53K	48K
Ph [º]	4.2	4.4	4.2	4.3	4.5
R^2 [-]	0.99	0.99	0.99	0.99	0.99

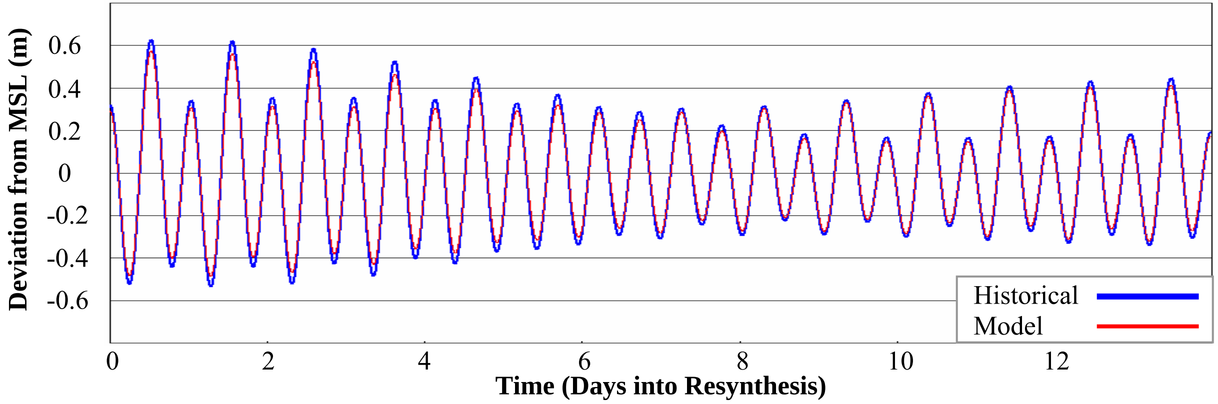

In the Ocean

St. 196: Atlantic Ocean					
Observer			IHO		
Longitude			67.53 W		
Latitude			28.23 N		
Simulation Results					
	333K	95K	60K	53K	48K
Ph [º]	2.1	2.2	2.0	2.1	2.1
R^2 [-]	0.99	0.99	0.99	0.99	0.99

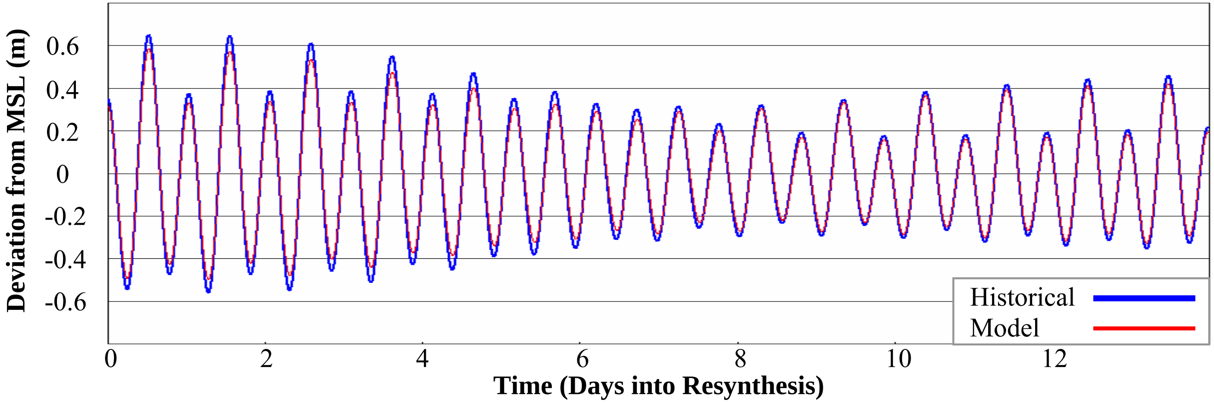

In the Ocean

St. 197: Atlantic Ocean					
Observer			IHO		
Longitude			69.75 W		
Latitude			28.13 N		
Simulation Results					
	333K	95K	60K	53K	48K
Ph [º]	3.4	3.6	3.3	3.5	3.5
R^2 [-]	0.99	0.99	0.99	0.99	0.99

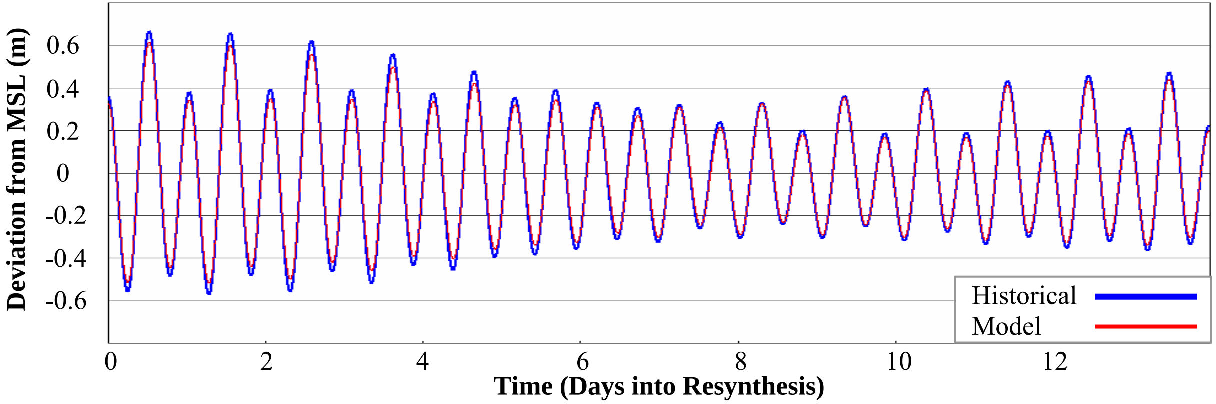

In the Ocean

St. 198: Florida Bank					
Observer			IHO		
Longitude			84.25 W		
Latitude			26.70 N		
Simulation Results					
	333K	95K	60K	53K	48K
Ph [º]	2.7	2.7	1.9	2.6	2.3
R^2 [-]	0.97	0.97	0.97	0.97	0.97

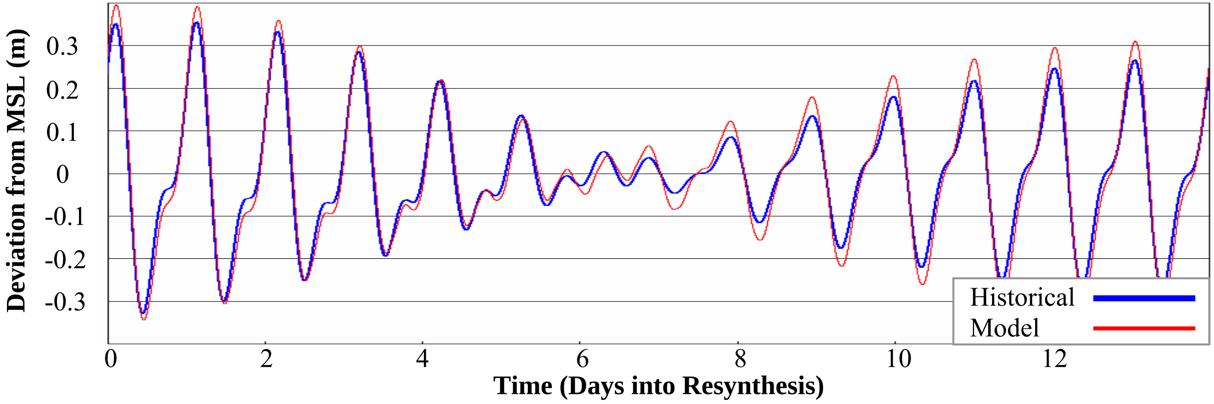

In the Ocean

St. 199: Middle of GOM					
Observer			IHO		
Longitude			89.65 W		
Latitude			24.77 N		
Simulation Results					
	333K	95K	60K	53K	48K
Ph [º]	1.7	1.7	1.6	1.8	1.8
R^2 [-]	0.98	0.98	0.98	0.98	0.98

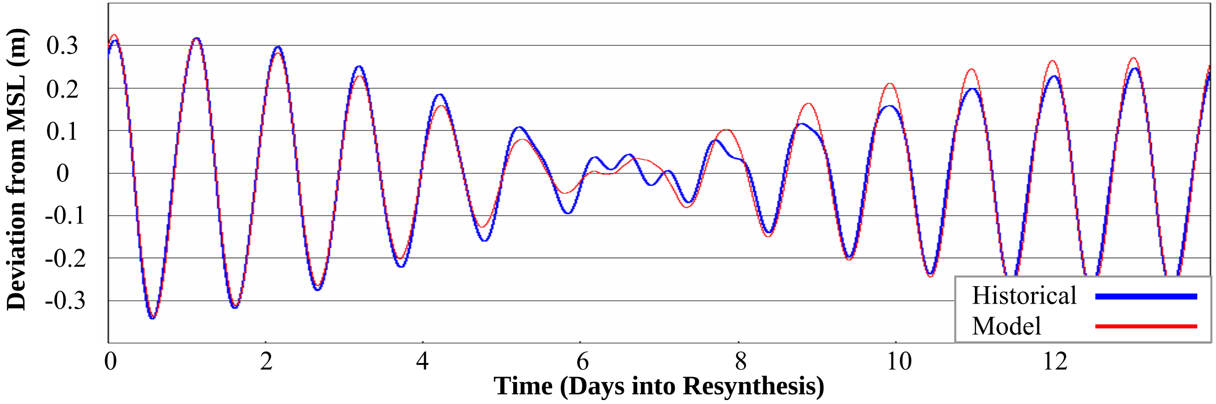

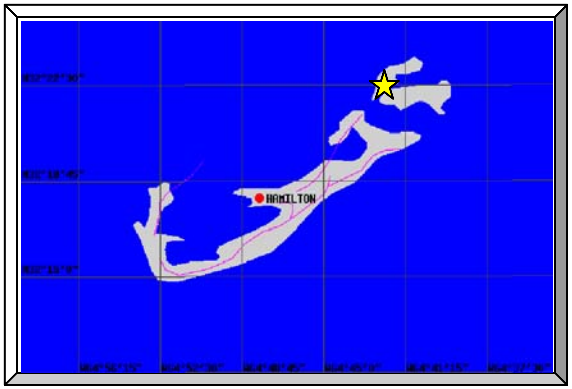

St. 200: Bermuda Esso Pier, St. Georges Island	
Observer	NOS
Longitude	64.70 W
Latitude	32.37 N

Simulation Results					
	333K	95K	60K	53K	48K
Ph [º]	4.6	4.4	4.2	4.5	4.2
R^2 [-]	0.95	0.95	0.95	0.95	0.95

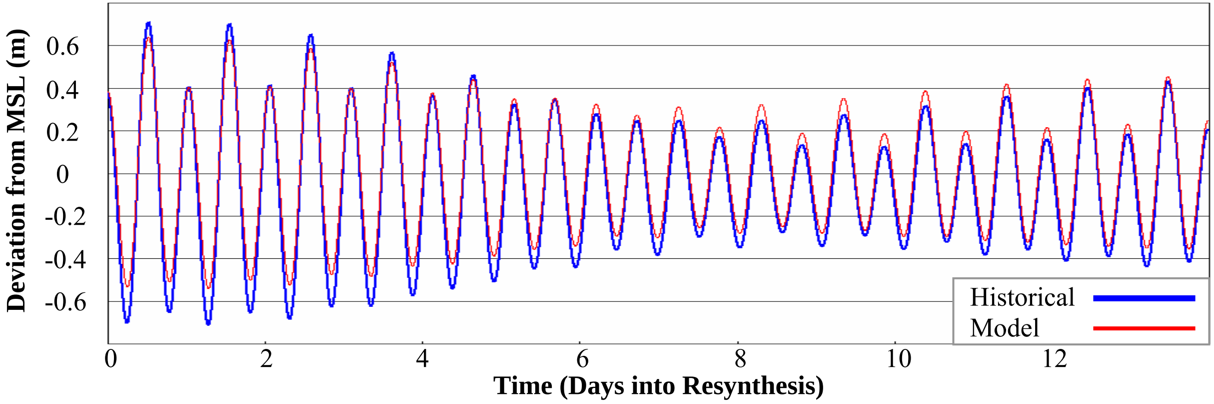

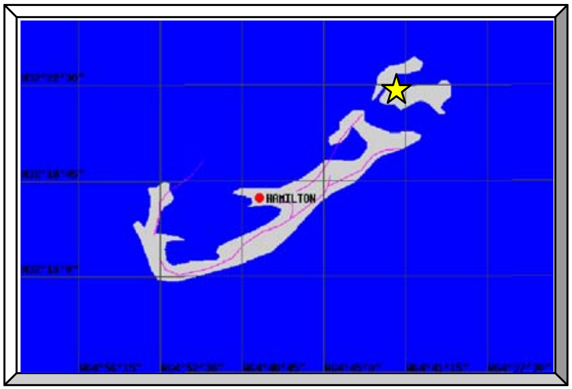

St. 201: St. Davids Island, Bermuda	
Observer	IHO
Longitude	64.70 W
Latitude	32.37 N

Simulation Results					
	333K	95K	60K	53K	48K
Ph [º]	1.0	1.3	1.5	1.3	1.5
R^2 [-]	0.99	0.99	0.99	0.99	0.99

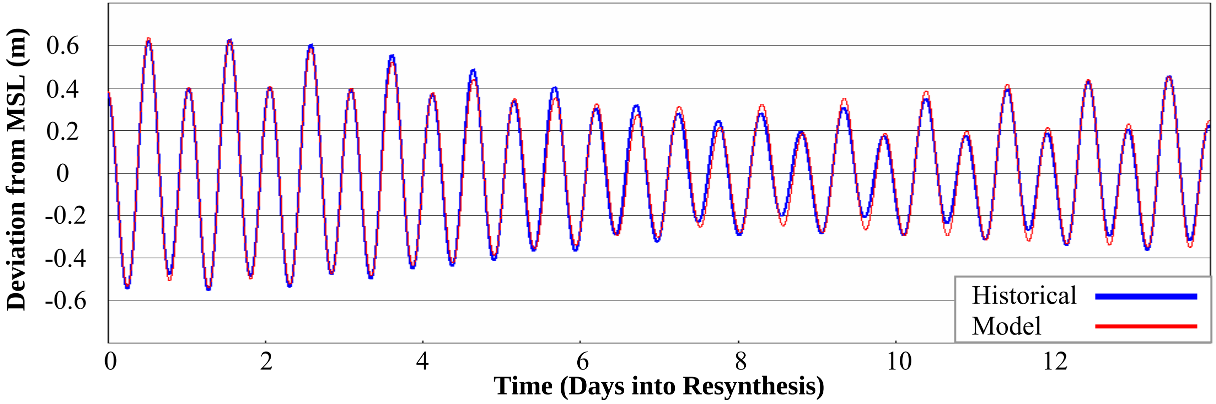

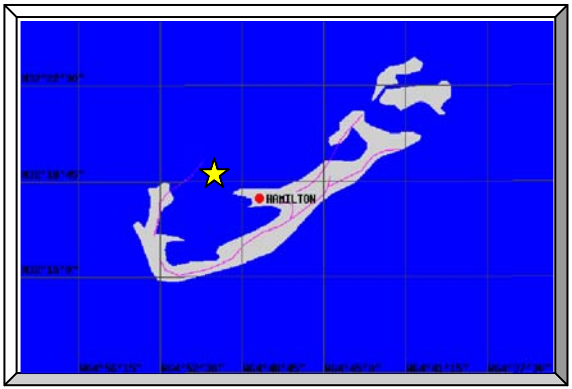

St. 202: Ireland Island, Bermuda	
Observer	IHO
Longitude	64.83 W
Latitude	32.32 N

Simulation Results					
	333K	95K	60K	53K	48K
Ph [º]	11.3	11.3	11.0	11.4	11.1
R^2 [-]	0.99	0.99	0.99	0.99	0.99

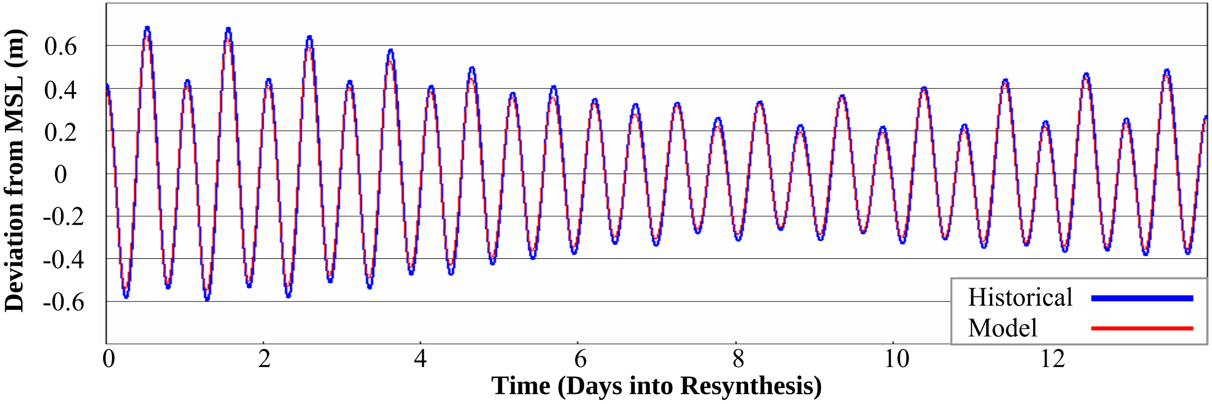

In the Ocean

St. 203: Atlantic Ocean near Bermuda	
Observer	IHO
Longitude	64.43 W
Latitude	32.02 N

Simulation Results					
	333K	95K	60K	53K	48K
Ph [º]	2.3	2.3	2.1	2.4	2.1
R^2 [-]	0.98	0.98	0.98	0.98	0.98

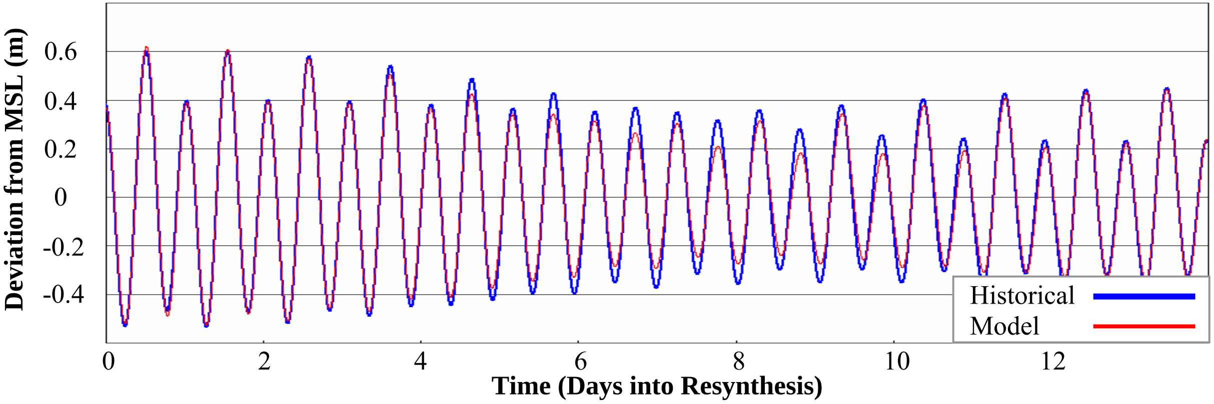

LIST OF REFERENCES

Berger, M. J. and Colella, P. (1986)
"Local adaptive mesh refinement for shock hydrodynamics." *Journal of Computational Physics*, 82, 64–84.

Blain, C. A., Westerink, J. J., and Luettich, R. A. Jr. (1994a)
"The influence of domain size on the response characteristics of a hurricane storm surge model." *Journal of Geophysical Research*, 99(C9), 18467–18479.

Blain, C. A., Westerink, J. J., and Luettich, R. A. Jr. (1994b)
"Domain and grid sensitivity studies for hurricane storm surge predictions." *Proceedings of the 10th International Conference on Computational Methods in Water Resources*, Delft, The Netherlands.

Blain, C. A., Westerink, J. J., and Luettich, R. A. Jr. (1995)
"Application of a domain size and gridding strategy for the prediction of hurricane storm surge." *Proceedings of the 2nd International Conference on Computer Modelling of Seas and Coastal Regions*, Cancun, Mexico.

Blain, C. A., Westerink, J. J., Luettich, R. A. Jr., and Scheffner, N. W. (1994c)
"ADCIRC: An advanced three-dimensional circulation model for shelves, coasts, and estuaries, IV: Hurricane storm surge modeling using large domains." *Technical Report DRP-92-6*, U.S. Army Corps of Engineers, Waterways Experiment Station, Vicksburg, Mississippi.

Braddock, R. D. (1969)
"Tsunami propagation over large distances." *Proceedings of the International Symposium on Tsunamis and Tsunami Research*, Honolulu, Hawaii.

Canann, S. A., Muthukrishna, S. N., and Phillips, R. K. (1996)
"Topological refinement procedures for triangular finite element meshes." *Engineering with Computers 1996; 12(3-4): 243-255*

Cartwright, D. E. (1999)
"Tides: A scientific history." Cambridge University Press, Cambridge, United Kingdom.

Cartwright, D. E., Edden, A. C., Spencer, R., and Vassie, J. M. (1980)
"The tides of the northeast Atlantic Ocean." *Philosophical Transactions of the Royal Society of London*, 298(A), 87–139.

Chelton, D. B., Schlax, M. G., Witter, D. L., and Richman, J. G. (1990)
"Geosat altimeter observations of the surface circulation of the Southern Ocean." *Journal of Geophysical Research*, 95(C10), 17877–17903.

Compaq Water Resources Simulations (CWRS) Laboratory
University of Central Florida, Orlando, Florida, USA (http://cwrsl.cecs.ucf.edu/)

Darwin, G. H. (1911)
"The tides and kindred phenomena in the solar system." John Murray, London, United Kingdom.

Deacon, M. (1997)
"Scientists and the sea, 1650-1900: A study of marine science." Ashgate Publishing Ltd., Hampshire, United Kingdom.

Defant, A. (1960)
"Physical oceanography, II." Pergamon Press, Oxford, United Kingdom.

Dietrich, G., and Kalle, K. (1963)
"General oceanography: An introduction." John Wiley & Sons, Inc., New York, New York.

Dietsche, D. (2004)
"Storm Tide Simulations for Hurricane Hugo (1989): On the Significance of Including Inland Flooding Areas." A thesis submitted in partial fulfillment for the requirements for the degree of Master of Science in the Department of Civil and Environmental Engineering in the College of Engineering and Computer Science at the University of Central Florida Orlando, Florida

Doodson, A. T. (1928)
"The analysis of tidal observations." *Philosophical Transactions of the Royal Society of London*, 227, 223–279.

Emile-Geay, Julien (2003)
"Tides: a quick review." "OK, go to tides. How do they work? Why are tides important? How do they increase mixing?"

Flather, R. A. (1987)
"Estimates of extreme conditions of tide and surge using a numerical model of the North-west European continental shelf." *Estuarine, Coastal and Shelf Science*, 24, 69–93.

Foreman, M. G. G. (1977)
"Manual for tidal heights analysis and prediction." *Pacific Marine Science Report 77-10*, Institute of Ocean Sciences, Patricia Bay, Victoria, British Columbia.

Foreman, M. G. G. (1986)
"An accuracy analysis of boundary conditions for the forced shallow water equations." *Journal of Computational Physics*, 64, 334–367.

Foreman, M. G. G. (1988)
"A comparison of tidal models for the southwest coast of Vancouver Island." *Proceedings of the 7th International Conference on Computational Methods in Water Resources*, Cambridge, Massachusetts.

Foreman, M. G. G., and Henry, R. F. (1979)
"Tidal analysis based on high and low water observations." *Pacific Marine Science Report 79-15*, Institute of Ocean Sciences, Victoria, British Columbia.

Forrester, W. D. (1983)
"Canadian tidal manual." Department of Fisheries and Oceans, Ottawa, Canada.

Frey, W. H. (1987)
"Selective refinement: A new strategy for automatic node placement in graded triangular meshes." *International Journal for Numerical Methods in Engineering*, 24, 2183–2200.

Fugal, A. (2000)
"Two-Dimensional Finite Element Density Meshing." MS thesis, Brigham Young University, Prove, Utah, U.S.A. 2000

Fu, L. -L., and Cazenave, A. (2001)
"Satellite altimetry and earth sciences." Academic Press, New York, New York.

Funakoshi, Y., Hagen, S. C., Zundel, A. K., and Kojima, S. (2004)
"Driving an integrated surface water, three-dimensional model." *Proceedings of the 6th International Conference on Hydro-Science and -Engineering*, Brisbane, Australia.

Garland, G. D. (1965)
"The earth's shape and gravity." Pergamon Press, Oxford, United Kingdom.

George, P.L. and Seveno, E. (1994)
"The advancing-front mesh generation method revisited." *International Journal for Numerical Methods in Engineering Nov 1994; 37(21): 3605-3619*

George, P.L., Hecht, R., and Saltel, E. (1991)
"Automatic mesh generator with specified boundary." *Computer Methods in Applied Mechanics and Engineering Nov 1991; 92(3): 269-288*

Gerritsen, H., and Bijlsma, A. C. (1988)
"Modelling of tidal and winddriven flow: The Dutch continental shelf model." *Computer Modelling in Ocean Engineering*, B. A. Schrefler and O. C. Zienkiewicz, eds., Balkema, Rotterdam, The Netherlands.

Godin, G. (1972)
"The analysis of tides." University of Toronto, Toronto, Canada.

Gray, W. G. (1989)
"A finite element study of tidal flow data for the North Sea and English channel." *Advances in Water Resources*, 12, 143–154.

Hagen, S. C. (1998)
"Finite Element Grids based on a Localized Truncation Error Analysis." A dissertation submitted to the graduate school of the University of Notre Dame in partial fulfillment of the requirements for the degree of doctor of philosophy: Department of Civil Engineering and Geological Sciences: Notre Dame, Indiana

Hagen, S. C. (2001)
"Estimation of the truncation error for the linearized, shallow water momentum equations." *Engineering with Computers*, 17, 354–362.

Hagen, S. C., Horstmann, O., and Bennett, R. J. (2002)
"An unstructured mesh generation algorithm for shallow water modeling." *International Journal of Computational Fluid Dynamics*, 16(2), 83–91.

Hagen, S. C., and Parrish, D. M. (2004)
"Unstructured mesh generation for the western North Atlantic tidal model domain." *Engineering with Computers*, 20, 136–146.

Hagen, S. C., and Westerink, J. J. (1995)
"Finite element grid resolution based on second- and fourth-order truncation error analysis." *Proceedings of the 2nd International Conference on Computer Modelling of Seas and Coastal Regions*, Cancun, Mexico.

Hagen, S. C., Westerink, J. J., and Kolar, R. L. (2000)
"One-dimensional finite element grids based on a localized truncation error analysis." *International Journal for Numerical Methods in Fluids*, 32, 241–261.

Hagen, S. C., Westerink, J. J., Kolar, R. L., and Horstmann, O. (2001)
"Two-dimensional, unstructured mesh generation for tidal models." *International Journal for Numerical Methods in Fluids*, 35, 669–686.

Hendershott, M.C. (1981)
"Long waves and ocean tides." Evolution of physical oceanography, B.A. Warren and C. Wunsch, ed., MIT Press, Cambridge, MA, 292-341

Ho-Le, K. (1988)
"Finite element mesh generation methods: A review and classification." *Computer-Aided Engineering Journal*, 20, 27–38.

Horn, W. (1960)
"Some recent approaches to tidal problems." *International Hydrographic Review*, 37(2), 65–88.

Howarth, M. J., and Pugh, D. T. (1983)
"Observations of tides over the continental shelf of northwest Europe." *Physical Oceanography of Coastal and Shelf Seas*, B. Johns, ed., Elsevier, Amsterdam, The Netherlands.

Howlett, J.D. (2005)
"Function Based Mesh Relaxation." MS thesis, Brigham Young University, Provo, Utah, U.S.A. 2005

International Hydrographic Organization (IHO)
The International Hydrographic Organization
(http://www.iho.shom.fr/)

Japan Meteorological Agency (JMA)
Japan Meteorological Agency [in Japanese]
(http://www.jma.go.jp/JMA_HP/jma/index.html)

Jeffreys, H. (1976)
"The earth, its origin, history and physical constitution." 6th edn., Cambridge University Press, Cambridge, United Kingdom.

Johnston, B.P. and Sullivan, J.M. (1992)
"Fully-automatic 2-dimensional mesh generation using normal offsetting." *International Journal for Numerical Methods in Engineering Jan1992; 33(2): 425-442*

Jones, N. L., and Richards, D. R. (1992)
"Mesh generation for estuarine flow modeling." *Journal of Waterway, Port, Coastal, and Ocean Engineering*, 118, 599–614.

Kashiyama, K., and Okada, T. (1992)
"Automatic mesh generation method for shallow water flow analysis." *International Journal for Numerical Methods in Fluids*, 15, 1039–1057.

King-Hele, D. G., Brookes, C. J., and Cook, G. E. (1980)
"The pear-shaped section of the earth." *Nature*, 286, 377–378.

Kinnmark, I.P.E. (1984)
"The shallow water wave equations." Formulation, analysis, and application, Ph.D. diss., Department of Civil Engineering, Priceton University, NJ

Knauss, J. A. (1978)
"Introduction to physical oceanography." Prentice-Hall, Inc., Englewood Cliffs, New Jersey.

Knupp, P., and Steinberg, S. (1994)
"Fundamentals of grid generation." CRC Press, Boca Raton, Florida.

Kojima, S., Hagen, S. C., and Zundel, A. K. (2005)
"Automatic, unstructured mesh generation for tidal calculations in a large domain." *International Journal for Numerical Methods in Engineering*, in review.

Kolar, R. L., Gray, W. G., and Westerink, J. J. (1994b)
"Normal flow boundary conditions in shallow water models – influence on mass conservation and accuracy." *Proceedings of the 10th International Conference on Computational Methods in Water Resources*, Delft, The Netherlands.

Kolar, R. L., Gray, W. G., and Westerink, J. J. (1996)
"Boundary conditions in shallow water models – an alternative implementation for finite element codes." *International Journal for Numerical Methods in Fluids*, 22, 603–618.

Kolar, R. L., Westerink, J. J., Cantekin, M. E., and Blain, C. A. (1994a)
"Aspects of nonlinear simulations using shallow-water models based on the wave continuity equation." *Computers and Fluids*, 23(3), 523–538.

Le Provost, C., and Vincent, P. (1986)
"Some tests of precision for a finite element model of ocean tides." *Journal of Computational Physics*, 65, 273–291.

Le Provost, C., Lyard, F., Molines, J.M., Genoco, M.L., and Rabilloud, F. (1998)
'A hydrodynamic ocean tide model improved by assimilating a satellite altimeter-derived data set." *Journal of Geophysical Research* 1998; 103(C3): 5513-5529

LeBlond, P. H., and Mysak, L. A. (1978)
"Waves in the ocean." Elsevier, New York, New York.

Lennon, G. W. (1971)
"Sea level instrumentation, its limitations and the optimisation of the performance of conventional gauges in Great Britain." *International Hydrographic Review*, 48(2), 129–147.

Li, X., and Gotze, H. (2001)
"Ellipsoid, geoid, gravity, geodesy, and geophysics." *Geophysics*, 66(6), 1660–1668.

Lohner, R. (1987)
"An adaptive finite element scheme for transient problems in CFD." *Computer Methods in Applied Mechanics and Engineering*, 61, 323–338.

Lohner, R. (1996)
"Progress in grid generation via the advancing front technique." *Engineering with Computers 1996; 12(3-4): 186-210*

Loomis, H. G. (1978)
"Tsunami." *Geophysical Predictions*, National Academy of Sciences, Washington, DC.

Luettich, R. A. Jr., and Westerink, J. J. (1995)
"Continental shelf scale convergence studies with a barotropic tidal model." *Coastal and Estuarine Studies, 47, Quantitative Skill Assessment for Coastal Ocean Models*, D. R. Lynch and A. M. Davies, eds., AGU Press, Washington, DC, 349–371.

Luettich, R.A. Jr. and Westerink, J.J. (2000)
ADCIRC: A (Parallel) Advanced Circulation Model for Oceanic, Coastal and Estuarine Waters

Luettich, R.A. Jr., Westerink, J.J., and Scheffner, N.W. (1992)
ADCIRC: An Advanced Three-Dimensional Circulation Model for Shelves, Coasts, and Estuaries; Report 1 Theory and Methodology of ADCIRC-2DDI and ADCIRC-3DL; Department of the Army US Army Corps of Engineers, Washington, DC 20314-1000 under Work Unit No. 32466

Lynch, D. R. (1983)
"Progress in hydrodynamic modeling, review of U.S. contributions, 1979–1982." *Reviews of Geophysics and Space Physics*, 21(3), 741–754.

Lynch, D.R. and Gray, W.G. (1979)
"A wave equation model for finite element tidal computations." *Comp. Fluids* 7, 207-28

Macmillan, D. H. (1966)
"Tides." Elsevier, New York, New York.

Marine Information Research Center (MIRC)
Japan Hydrographic Association [in Japanese]
(http://www.mirc.jha.or.jp/index.html)

McLellan, H. J. (1965)
"Elements of physical oceanography." Pergamon Press, New York, New York.

Mukai, A.Y., Westerink, J.J., and Luettich, R.A (2002)
"Guidelines for Using Eastcoast 2001 Database of Tidal Constituents within Western North Atlantic Ocean, Gulf of Mexico and Caribbean Sea." *ERDS/CHETN-IV-40 March 2002*

Munk, W., and Cartwright, D. (1966)
"Tidal spectroscopy and prediction." *Philosophical Transactions of the Royal Society of London*, 259, 553–581.

Murray, J. (1911)
"The Tides and Kindred Phenomena in the Solar System." The substance of lectures delivered in 1897 at the Lowell Institute, Massachusetts: By Sir George Howard Darwin, K.C.B.: Plumian professor and fellow of trinity college in the University of Cambridge: Third Edition

Murray, R.R. (2003)
"A Sensitivity Analysis for a Tidally-Influenced Riverine System." A thesis submitted in partial fulfillment for the requirements for the degree of Master of Science in the Department of Civil and Environmental Engineering in the College of Engineering and Computer Science at the University of Central Florida Orlando, Florida

Murty, T. S. (1977)
"Seismic sea waves and tsunamis." *Bulletin No. 198*, Department of Fisheries and the Environment, Fisheries and Marine Service, Ottawa, Canada.

Nekrasov, A. V. (1969)
"Transformation of tsunamis on the continental shelf." *Proceedings of the International Symposium on Tsunamis and Tsunami Research*, Honolulu, Hawaii.

Neumann, G., and Pierson, W. J. Jr. (1966)
"Principles of physical oceanography." Prentice Hall, Inc., Englewood Cliffs, New Jersey.

National Ocean Service (NOAA)
Center for Operational Oceanographic Products and Services
(http://co-ops.nos.noaa.gov/)

Noye, B. J. (1974)
"Tide-well systems, 3: Improved interpretation of tide-well records." *Journal of Marine Research*, 32, 183–194.

O'Loughlin, K. F., and Lander, J. F. (2003)
"Caribbean tsunamis, a 500-year history from 1498-1998." Kluwer Academic Publishers, Dordrecht, The Netherlands.

Open University (2000)
"Waves, tides and shallow-water processes." 2nd edn., Butterworth-Heinemann/Open University, Oxford, United Kingdom.

Palmer, H. R. (1831)
"Description of graphical register of tides and winds." *Philosophical Transactions of the Royal Society of London*, 121, 209–213.

Parrish, D.M. (2001)
"Development of a Tidal Constituent Database for the St. Johns River Water Management District." A thesis submitted in partial fulfillment for the requirements for the degree of Master of Science in the Department of Civil and Environmental Engineering in the College of Engineering and Computer Science at the University of Central Florida Orlando, Florida

Phillips, O. M. (1966)
"The dynamics of the upper ocean." Cambridge University Press, Cambridge, United Kingdom.

Parrish, D.M. and Hagen, S.C. (2002)
"Verification of a Tidal Constituent Database of the Western North Atlantic, Gulf of Mexico, and Caribbean Sea." Proceeding of the 21st Southeastern Conference on theoretical and applied Mechanics. Orlando, FL

Pickard, G. L. (1975)
"Descriptive physical oceanography." Pergamon Press, Oxford, United Kingdom.

Podyapolsky, G. S. (1969)
"Generation of the tsunami wave by the earthquake." *Proceedings of the International Symposium on Tsunamis and Tsunami Research*, Honolulu, Hawaii.

Pond, S., and Pickard, G. L. (1978)
"Introductory dynamic oceanography." Pergamon Press, Oxford, United Kingdom.

Proudman, J. (1953)
"Dynamical oceanography." Methuen and Co., London, United Kingdom.

Pugh, D. T. (1972)
"The physics of pneumatic tide gauges." *International Hydrographic Review*, 49(2), 71–97.

Pugh, D. T. (1987)
"Tides, surges and mean sea-level: A handbook for engineers and scientists." John Wiley & Sons, Inc., New York, New York.

Pugh, D. T. (2004)
"Changing sea levels: Effects of tides, weather and climate." Cambridge University Press, Cambridge, United Kingdom.

Ramaswamy, B., and Akin, J. E. (1990)
"Design of an optimal grid for finite element methods in incompressible fluid flow problems." *Engineering with Computers*, 7, 311–326.

Reid, R. O. (1990)
"Tides and storm surges." *Handbook of Coastal and Ocean Engineering, I: Wave Phenomena and Coastal Structures*, J. B. Herbich, ed., Gulf Publishing Co., Houston, Texas, 533–590.

Reid, R.O. and Whitaker, R.E. (1981)
"Numerical model for astronomical tides in the Gulf of Mexico." Technical report for the U.S. Army Corps of Engineers, Department of Oceanography, Texas A&M University

Roache, P. J. (1994)
"Perspective: A method for uniform reporting of grid refinement studies." *Journal of Fluids Engineering*, 116, 405–413.

Robinson, I. S. (1985)
"Satellite oceanography." Ellis Horwood, Chichester, United Kingdom.

Schwiderski, E.W. (1980)
"On charting global ocean tides." Reviews in Geophysics and Space Physics 18, 243-68

Seelig, W. N. (1977)
"Stilling well design for accurate water level measurement." *Technical Paper No. 77-2*, U.S. Army Coastal Engineering Research Center, Coastal and Hydraulics Laboratory, Washington, DC.

Simpson, R. (2003)
"Hurricane: Coping with disaster." American Geophysical Union, Washington, DC.

Sullivan, J.M. and Zhang, J.Q.Y. (1997)
“Adaptive mesh generation using a normal offsetting technique.” Finite Elements in Analysis and Design Apr 1997; 25(3-4): 275-295

Taniguchi, T., Holz, K. P., and Ohta, C. (1992)
“Grid generation for 2D flow problems.” *International Journal for Numerical Methods in Fluids*, 15, 985–997.

Thacker, W. C., Gonzalez, A., and Putland, G. E. (1990)
“A method for automating the construction of irregular computational grids for storm surge forecast models.” *Journal of Computational Physics*, 37, 371–387.

Turner, P. J., and Baptista, A. M. (1993)
“Software for semi-automatic generation of two-dimensional finite element grids.” ACE/gredit User’s Manual.

Vincent, P., and Le Provost, C. (1988)
“Semidiurnal tides in the northeast Atlantic from a finite element numerical model.” *Journal of Geophysical Research*, 93(C1), 543–555.

Wahr, J.M. (1981)
“Body tides on an elliptical, rotating, elastic and ocean-less earth.” *Geophysical Journal of the Royal Astronomical Society 64, 677-703*

Walters, R. A., and Werner, F. E. (1989)
“A comparison of two finite element models of tidal hydrodynamics using a North Sea data set.” *Advances in Water Resources*, 12, 184–193.

Werner, F. E., and Lynch, D. R. (1989)
“Harmonic structure of English channel/southern bight tides from a wave equation simulation.” *Advances in Water Resources*, 12, 121–142.

Westerink, J. J., and Gray, W. G. (1991)
“Progress in surface water modeling.” *Reviews in Geophysics*, 29, 210–217.

Westerink, J. J., Luettich, R. A. Jr., Baptista, A. M., Scheffner, N. W., and Farrar, P. (1992a)
“Tide and storm surge predictions using finite element model.” *Journal of Hydraulic Engineering*, 118, 1373–1390.

Westerink, J. J., Luettich, R. A. Jr., Blain, C. A., and Hagen, S. C. (1995)
“Surface elevation and circulation in continental margin waters.” *Finite Element Modeling of Environmental Problems*, G. F. Carey, ed., John Wiley & Sons, Inc., New York, New York, 39–59.

Westerink, J. J., Luettich, R. A. Jr., and Hagen, S. C. (1994c)
"Meshing requirements for large scale coastal ocean tidal models." *Proceedings of the 10th International Conference on Computational Methods in Water Resources*, Delft, The Netherlands.

Westerink, J. J., Luettich, R. A. Jr., and Muccino, J. C. (1992b)
"Resolution requirements for a tidal model of the Western North Atlantic and Gulf of Mexico." *Proceedings of the 9th International Conference on Computational Methods in Water Resources*, Denver, Colorado.

Westerink, J. J., Luettich, R. A. Jr., and Muccino, J. C. (1994a)
"Modeling tides in the western North Atlantic using unstructured graded grids." *Tellus*, 46A, 178–199.

Westerink, J.J., Luettich, R.A. Jr., and Scheffner, N.W. (1994)
"ADCIRC: An Advanced Three-Dimensional Circulation Model for Shelves, Coasts, and Estuaries; Report 2 User's Manual for ADCIRC-2DDI." *Department of the Army US Army Corps of Engineers, Washington, DC 20314-1000 under Work Unit No. 32466*

Westerink, J. J., Luettich, R. A. Jr., and Scheffner, N. (1993)
"ADCIRC: An advanced three-dimensional circulation model for shelves, coasts and estuaries, Report 3: Development of a tidal constituent database for the western North Atlantic and Gulf of Mexico." *Technical Report DRP-92-6*, U.S. Army Corps of Engineers, Waterways Experiment Station, Vicksburg, Mississippi.

Westerink, J. J., Luettich, R. A. Jr., Wu, J. K., and Kolar, R. L. (1994b)
"The influence of normal flow boundary conditions on spurious modes in finite element solutions to the shallow water equations." *International Journal for Numerical Methods in Fluids*, 18, 1021–1060.

Westerink, J. J., Muccino, J. C., and Luettich, R. A. Jr. (1991)
"Tide and hurricane storm surge computations for the western North Atlantic and Gulf of Mexico." *Proceedings of the 2nd International Conference on Estuarine and Coastal Modeling*, Tampa, Florida.

Zundel, A.K. (2005)
"Users Manual for the Surface-water modeling System, Version 9.0, 2005." Brigham Young university, Provo, Utah, U.S.A. 2005